

Infrasound and the Dynamical Stratosphere
A new application for operational weather and climate prediction

Smets, Pieter

DOI

[10.4233/uuid:517f8597-9c24-4d01-83ed-0f430353e905](https://doi.org/10.4233/uuid:517f8597-9c24-4d01-83ed-0f430353e905)

Publication date

2018

Document Version

Final published version

Citation (APA)

Smets, P. (2018). *Infrasound and the Dynamical Stratosphere: A new application for operational weather and climate prediction*. [Dissertation (TU Delft), Delft University of Technology].
<https://doi.org/10.4233/uuid:517f8597-9c24-4d01-83ed-0f430353e905>

Important note

To cite this publication, please use the final published version (if applicable).
Please check the document version above.

Copyright

Other than for strictly personal use, it is not permitted to download, forward or distribute the text or part of it, without the consent of the author(s) and/or copyright holder(s), unless the work is under an open content license such as Creative Commons.

Takedown policy

Please contact us and provide details if you believe this document breaches copyrights.
We will remove access to the work immediately and investigate your claim.

Infrasound and the Dynamical Stratosphere

A new application for operational
weather and climate prediction

Infrasound and the Dynamical Stratosphere

A new application for operational
weather and climate prediction

Dissertation

for the purpose of obtaining the degree of doctor
at Delft University of Technology,
by the authority of the Rector Magnificus, prof. dr. ir. T.H.J.J. van der Hagen,
chair of the Board for Doctorates,
to be defended publicly on
Wednesday, 28 March 2018 at 15.00 o'clock

by

Pieter Steven Maarten SMETS

Master of Science in Aerospace Engineering, Delft University of Technology
born in Wilrijk, Belgium

This dissertation has been approved by the promotor.

Composition of the doctoral committee:

Rector Magnificus	chairman
Prof. dr. L. G. Evers	Delft University of Technology, promotor

Independent members:

Prof. dr. ir. C. P. A. Wapenaar	Delft University of Technology
Prof. dr. W. A. Mulder	Delft University of Technology
Prof. dr. ir. E. C. Slob	Delft University of Technology
Prof. dr. P. J. Espy	Norwegian University of Science and Technology
dr. D. N. Green	AWE, United Kingdom
dr. A. J. Charlton-Perez	University of Reading, United Kingdom



Keywords: stratosphere infrasound array propagation temperature wind SSW

Cover illustration: Michael Tritsmans.

ISBN 978-94-6186-909-8

Copyright © 2018 by P. S. M. Smets.

All rights reserved. No part of the material protected by this copyright may be reproduced, or utilised in any other form or by any means, electronic or mechanical, including photocopying, recording or by any other information storage and retrieval system, without the prior permission of the author.

Typesetting system: L^AT_EX.

Printed in The Netherlands by Gildeprint B.V., Enschede.

An electronic version of this dissertation is available at
<http://repository.tudelft.nl/>.



*For Albert and Justin,
my grandfathers*

Preface

*“We live at a very special time . . . the only time
when we can observationally verify that
we live at a very special time”*

Lawrence M. Krauss

The journey that led to the publication of this work started back in 2010. I can vividly remember my first introduction to infrasound by Láslo Evers, during my master course in acoustic remote sensing. I was totally amazed by the fact that you can hear how the stratospheric winds reverse by season. It feels great to realise and understand, some years later, the beauty of it. Intrigued by the relationship between infrasound and the atmosphere, I was well pleased I could continue in the field after my internship and master thesis project.

The real journey of this work started at the beginning of January 2012 at the Abbaye des Vaux de Cernay, France, with the kickoff meeting of the *Atmosphere Dynamics Research Infrastructure* in Europe – ARISE – project. ARISE is a collaborative infrastructure Design Study project, gathering various middle atmosphere observation techniques (infrasound, lidar, radars, wind radiometers and ionospheric sounders) to study atmospheric disturbances of interest for improving stratosphere resolving climate and weather forecasting models. For the next three years, I would be involved in the utilisation of ARISE-data for model use and development: a challenging but interesting work package, co-lead by the University of Reading and KNMI, that formed the basis of this thesis. Although it was not planned initially, our work in the project evolved into a doctoral plan and eventually this dissertation. The work continued in ARISE2, now focusing on the road towards data assimilation of ARISE-data in operational weather and climate models. What followed after that first meeting in 2012 is an incredible list of project meetings, workshops, summer

schools, courses, conferences, and discussions: Andøya, Boston, Brussels, Collioure, Cologne, Florence, Grainau, Haute-Provence, Paris, Pittsburgh, Reading, Reunion Island, Vienna, Delft, and De Bilt. It has been a long road from the beginning of this journey to where I am now. I will stick to naming the places that played a key role in my journey, because naming all people I have met would be an impossible assignment. Nevertheless, the realisation of this doctoral thesis would not have been possible without the ARISE project, all the meetings, and without all the people involved in the project. I would like to emphasise the various visits to Reading. Although Reading could not compete with all other locations, I much appreciated visiting the university, the European weather centre, and the Met Office. I not only learned a lot from our meetings and open discussion but even gained many research ideas from these. Visiting the weather centres was the key element to bridge the observation based ARISE community and the modelling world of numerical weather prediction. The importance of speaking the same language and how to interpret an atmospheric model are two things I will not easily forget. It was only when standing between modellers and observers that I realised how different two closely connected scientific worlds can be. I became aware of the fact that it is not just science that is important, but the scientific language as well. The past years, data assimilation has been the word I tried to avoid the most. Even though it is the connection between the two scientific worlds, it is simply not that easy to setup. Assimilation of new observations requires a long pathway, something I did not realise in the beginning of the project. The magic solution to please both communities was to insistently add the phrase *the road towards* to it. Despite that we aim towards the implementation of ARISE for weather and climate monitoring in the next 10 to 20 years, significant progress has been made during the past five years. This doctoral thesis primarily focusses on short-term goals for infrasound data assimilation: to develop new methods, applications, for the utilisation of infrasound by weather and climate prediction centres. However, hopefully it does contribute to the long-term impacts as well. Goals that require more time and which results are hardly noticeable in the beginning. Being involved in the weather and climate community is the key element to guarantee long-term existence.

For me, the value of this doctoral thesis is much more than its scientific value. I do hope that it does convey some useful knowledge for certain experts in some field of research. To me, this doctoral thesis represents a magnificent journey in science and in life.

Dear prof. dr. L. G. Evers, thanks a million for this journey, starting from the introductory course into infrasound to everything that followed along: an internship and M.Sc. graduation project, a research position and even this doctoral opportunity. I have to admit, I did not gain much experience in job interviews over the past six years. Notwithstanding, I got something way more important in return. Láslo, I gratefully thank you for all the inspiration, support and opportunities! I enjoyed how you insist on simplicity to explain complex things and to approach new challenges. This is an expertise you seek to carry on to all of your students, which I appreciated a lot when guiding M.Sc. students together.

Many thanks to prof. dr. ir. C. P. A. Wapenaar for the warm welcome at the

department of Geoscience and Engineering. Although my research topic is kind of odd compared to the ideal world of synthetic seismic interferometry, I never had felt like an outsider. Kees, thank you very much for your support and attentiveness.

I would like to thank all my colleagues of the KNMI R&D department of Seismology and Acoustics and TU Delft department of Geoscience and Engineering. Thank you all for the tremendous support, rewarding discussions and litres of coffee during many coffee breaks. Special thanks to Jelle Assink, partner in crime on various studies we accomplished and a lot more ideas we have planned to execute. Cornelis Weemstra, I much appreciated all our routinely walks to the coffee machine and even more the fruitful discussions we had along the way. Although we often got lost near the machine, talking way too long, I really enjoyed it. Thank you Julius Fricke, for all the fun times in the office or during one of our multiple road trips to the infrasound stations of LOFAR.

I am grateful to the ARISE project for making this research possible. Thank you Elisabeth Blanc for hosting this great project, and many thanks to all my fellow ARISE colleagues and plenty of researchers I met during one of the various workshops or meetings. In particular, I would like to thank our work package's co-leader, the meteorology department of the University of Reading. It was a pleasure to visit Reading and the UK-based weather centres. Many thanks to Prof. Giles Harrison, Andrew Charlton-Perez, Christopher Lee and Graeme Marlton for guiding me in the world of numerical weather prediction and the stratosphere. Christopher, you deserve some special thanks. I will never forget how we paved the way together during the first project, the issues we came upon and the proud moments we shared. Thanks for all the lovely dinners and late-night drinks. Thank you Steven Gibbons, Thormod Kværna and Sven-Peter Näsholm from NORSAR for the much appreciated discussions, exchanges and collaborations over the past years.

I would like to thank the European weather centre for its generosity. Special thanks to Adrian Simmons for the fruitful comments and helpful contacts. There was not a single question that did not get answered by you or any of your colleagues. That is really astonishing and was very helpful, which I admire a lot. I really enjoyed the course on predictability and ocean-atmosphere ensemble forecasting, inspiring me for the probabilistic infrasound propagation study.

Thank you Roger Waxler for your inspiration and discussions on microbarom modelling. I would not have achieved these ambient noise simulations without your prior effort. Thank you David Green and David Fee for your highly valued reviews.

Marijke, I could not have achieved this thesis without your support. Thanks for always being there. A big hug and kiss. Sorry to all for interrupted plans and moments due to time spent on my research and thesis.

Thank you mum and dad for the everlasting support, opportunities and love. Thank you to all friends and family for your endless encouragement, even though I was not available.

The past six years both my research and leisure activity have been dominated by the abbreviation *SSW*. The first definition is a Sudden Stratospheric Warming, one of the key elements of my doctoral thesis. The second meaning is, in Dutch, *samenscholingsweek*: the yearly gathering week of our former youth organisation

Jozib. Together with finalizing my thesis, this wonderful period came to an end as well. Thank you Anke, Maarten and many others for all the magnificent moments and, yes it is possible, briefly making me forget about my research.

This work was performed during the course of the ARISE design study project: part one (2012-2014) funded by European Union FP7 program (grant number 284387) and part two (2015-2017) funded by the European Commission H2020 program (grant number 653980). Láslo Evers' contribution is partly funded through a VIDI project from the Netherlands Organisation for Scientific Research (NWO), project number 864.14.005.

CTBTO and station operators are thanked for guaranteeing the high quality of the IMS data and products. Most graphs in this thesis have been made with the Generic Mapping Tools [*Wessel and Smith, 1991*].

Pieter Smets,
De Bilt/Delft,
November 2017

Summary

Infrasound and the dynamical stratosphere: a new application for operational weather and climate prediction

Sudden stratospheric warmings (SSWs) are important features of the winter atmosphere in the northern hemisphere. During such events, the strongest transient forcing of the stratosphere on the troposphere is observed, influencing weather conditions and their predictability in the troposphere. Significant effort has been made by numerical weather prediction (NWP) to improve the predictability of stratospheric variability, such as SSWs. However, additional upper atmospheric observations are required in a region which is notoriously difficult to monitor. Hence, beyond the middle stratosphere direct information of wind is missing.

Infrasound, part of the *Atmospheric Dynamics Research Infrastructure in Europe* – ARISE – project, has shown its ability in probing the upper atmosphere. Infrasound is low-frequency inaudible sound (< 20 Hz) which propagates efficiently over long distances, since attenuation is in general relatively low. Accordingly, infrasound is used as one of the waveform verification techniques for the Comprehensive Nuclear-Test-Ban Treaty (CTBT). A key benefit of infrasound is the sensitivity to both temperature and wind in a region where atmospheric observations are scarce. Currently, infrasound is primarily a monitoring technique with data gathered from a sparse global network of national and CTBT infrasound arrays. Despite the capabilities of infrasound, a direct use in operational weather and climate modelling, e.g., assimilation, is not for the near future. Therefore, this thesis contributes to the development of methods to allow infrasound to be used by weather and climate prediction centres, making the first pathway to assimilation.

As atmospheric conditions in the lower and middle atmosphere are routinely used in a wide variety of atmospheric sciences and applications, accurate representation of the atmosphere is important to a broad community and a wide variety of applications, such as the verification of the CTBT. Knowledge of stratospheric

(and middle atmospheric) variability is equally important for infrasound monitoring purposes.

Three research objectives form the basis of this thesis:

- To use passive ambient infrasound signals as an atmospheric probe. To extract relevant parameters from continuous waveforms by signal detectors and array processing techniques.
- To develop a technique to use infrasound in current atmospheric models. To demonstrate how infrasound data, both observations and simulations, can be of use for operational weather and climate modelling in the stratosphere.
- To apply knowledge of stratospheric variability to problems of infrasonic detection and propagation modelling. To utilise knowledge of the dynamical stratosphere when undertaking infrasound analysis, in order to benefit CTBT verification efforts.

In this thesis, it is shown that infrasound can provide useful additional information in regions where data coverage is sparse, especially during a SSW. It is demonstrated that infrasound has the potential to contribute to operational weather prediction applications by validation of atmospheric analysis and forecast products, in particular in regions above 30 km altitude. Evaluating the forecast in the middle atmosphere can act as an early indicator of a possible upcoming loss of forecast skill in the troposphere. In this thesis, observed and simulated infrasound wavefront parameters are compared, i.e., back azimuth, apparent velocity, or travel time. The theoretical basis of this method relies on the assertion that sound propagates through a particular atmospheric state. The state that is closest to reality will then lead to simulated values that are closest to the observed values. Wavefront information is extracted from the continuous waveform recordings using beamforming and the Fisher coherence analysis and simulated by ray theory using various atmospheric conditions.

For the first time, middle atmospheric numerical weather forecasts are evaluated using infrasound. A year of near continuous infrasound from the volcano Mount Tolbachik (Kamchatka, Russian Federation) is compared with simulations using high-resolution deterministic forecasts of the European Centre for Medium-range Weather Forecasts (ECMWF). For the entire time span the nowcast generally performs best, indicated by a higher continuity of the predicted wavefront characteristics with a minimal back azimuth difference. Best performance for all forecasts is obtained in summer. The difference between the infrasound observations and the predictions based on the forecasts is significantly larger during the 2013 SSW period for all forecasts. Simulations show that the SSW onset is better captured by the ten-day forecast while the recovery is better captured by the nowcast. The proposed method for the evaluation of middle atmospheric weather forecasts using near-continuous infrasound detections can directly be applied to similar setups, making use of other IMS or even national infrasound arrays.

Microbarom observations are evaluated to study the life cycle of the 2009 major sudden stratospheric warming. Knowledge of the atmospheric ducting condition of

the observed microbaroms is obtained from the infrasonic amplitudes only, without any a priori atmospheric information. The observed microbarom amplitudes show more details on the life cycle of a sudden stratospheric warming, with differences in the warming onset and offsets, than can be explained by ECMWF's operational analysis. The type of vortex disturbance, split or reversal, can be deduced from the combined effect of the change in back-azimuth direction and solar tidal signature of the observed microbarom amplitudes. Expanding towards ambient noise observations provides the ability to probe larger parts of the stratosphere. This is highly important for NWP, since improved knowledge of the global stratosphere leads to a gain in tropospheric forecast skill but only when incorporated in global observations.

Probabilistic infrasound propagation modelling using ensembles of physically realistic perturbed analyses is successfully demonstrated. A significant improvement in propagation modelling is obtained without the need of adding random fluctuations. Error variance profiles at the array show that the yearly mean effective sound speed variation can reach up to 8 m s^{-1} in the stratosphere, occasionally exceeding 25 m s^{-1} for a single ensemble set. The latter value is in the order of what has been proposed previously to explain infrasound observations, often dedicated to missing small-scale fluctuations and gravity waves or model discrepancies.

The underground nuclear tests conducted by the Democratic People's Republic of Korea (DPRK) generated detectable atmospheric infrasound, both in 2013 and 2016. Clear detections were made in the Russian Federation (IS45) and Japan (IS30) in 2013 at stations from the International Monitoring System. Both tropospheric and stratospheric refractions arrived at the stations. In 2016, only a weak return was potentially observed at IS45. Data analysis and propagation modelling show that the noise level at the stations and the stratospheric circumpolar vortex were different in 2016 compared to 2013. However, amplitude modelling led to the hypothesis that the 2016 test was about 1.5 times deeper than the 2013 test.

In summary, this thesis demonstrates that infrasound can be used by operational weather and climate prediction as an evaluation method for the middle atmosphere by simulating observed wavefront parameters, making the first pathway to assimilation. In addition, knowledge of stratospheric variability is beneficial for advanced infrasound propagation, of importance for infrasound monitoring purposes, e.g., treaty verification.

Samenvatting

Infrageluid en de dynamische stratosfeer: een nieuwe toepassing voor operationele weer- en klimaatvoorspelling

Abrupte opwarming van de stratosfeer, zogenaamde *sudden stratospheric warmings* (SSWs), zijn belangrijke kenmerken van de winterse atmosfeer op het noordelijk halfrond. Tijdens dit kortstondig fenomeen vindt de sterkste invloed van de stratosfeer op de troposfeer plaats, wat het weer en zijn voorspelling in de troposfeer beïnvloedt. Numerieke weersvoorspelling (NWP) heeft de laatste jaren grote inspanningen geleverd om de voorspelling van de stratosferische variabiliteit te verbeteren. Echter vraagt dit extra observaties van de hogere atmosfeer, een regio die gekenmerkt is als zijnde zeer moeilijk te observeren. Windobservaties ontbreken in weermodellen voorbij het midden van de stratosfeer hoger dan zo'n 30 km.

Infrageluid, onderdeel van het *Atmospheric Dynamics Research Infrastructure in Europe* – ARISE – project, biedt mogelijkheden voor het doorgronden van de hogere atmosfeer. Infrageluid zijn onhoorbare laag frequente geluidsgolven (< 20 Hz) die efficiënt over lange afstanden kunnen reizen doorheen de atmosfeer omdat ze weinig demping ondervinden. Infrageluid maakt deel uit als golfvorm verificatie techniek van het alomvattende kernstopverdrag (Comprehensive Nuclear-Test-Ban Treaty, CTBT). Een vitaal voordeel van infrageluid ten opzichte van NWP is de gevoeligheid voor zowel wind als temperatuur in dat deel van de atmosfeer waar observaties beperkt zijn. Momenteel is infrageluid in de eerste plaats een waarnemingsmethode bestaande uit een global netwerk van nationale en CTBT gerelateerde arrays. Hoewel de capaciteiten van infrageluid reeds jaren bekend zijn biedt het nog geen directe toepassing in operationele weer- en klimaatmodellen. Assimilatie van infrageluid observaties bijvoorbeeld, is niet voor de nabije toekomst. Net daarom draagt dit proefschrift bij aan het ontwikkelen van methodes om het gebruik van infrageluid in huidige weer- en klimaatmodellen te promoten, als zijnde een eerste stap op de weg tot assimilatie.

Modelrepresentaties van de lage en middelatmosfeer worden frequent gebruikt door een brede waaier van atmosferisch onderzoek en toepassingen. Een realistisch beeld van de atmosfeer is belangrijk voor diverse vakgebieden met verscheidene toepassingen, zoals onder andere de verificatie van het kernstopverdrag. Kennis van de stratosferische variabiliteit is dus van even groot belang voor infrageluid observatie toepassing als voor weers- en klimaatvoorspelling.

In dit proefschrift staan drie onderzoeksdoelen centraal:

- Het gebruik van passief omgevingsruis voor het doorgronden van de atmosfeer. In het bijzonder het verkrijgen van extra informatie over de atmosfeer uit de gemeten signalen, gebruik te maken van detectie algoritmen en array analyse technieken.
- Het ontwikkelen van een methode voor het gebruik van infrageluid in huidige weermodellen. Aantonen hoe infrageluid observaties en simulaties van nut zijn voor de voorspelling in de stratosfeer.
- Het toepassen van kennis over de stratosferische variabiliteit op de detectie en propagatie van infrageluid. Het toepassen van dit voordeel in kennis over de stratosfeer voor verificatie van het kernstopverdrag.

Dit proefschrift laat zien dat infrageluid bijkomende informatie van de atmosfeer kan voorzien daar waar metingen beperkt zijn, van belang tijdens een SSW. Het is aangetoond dat infrageluid potentieel heeft om bij te dragen tot weersvoorspelling met validatie toepassingen van atmosferische analyses en verwachtingen, in het bijzonder in de regio boven de 30 km. Het evalueren van weersvoorspellingen in de middelatmosfeer kan worden gebruikt als een indicator van het mogelijke verlies van voorspelbaarheid in de troposfeer. De gebruikte methode in dit proefschrift vergelijkt gemeten en voorspelde golfkarakteristieken zoals richting, schijnbare snelheid en reistijd. De theoretische basis van de methode is gebaseerd op de verklaring dat geluid reist door een specifieke staat van de atmosfeer. De modelweergave die deze staat het beste benadert levert simulaties op die het meeste overeenkomen met de observaties. Golfkarakteristieken zijn afgeleid uit de ruwe opnames door middel van bundelvorming en Fisher coherentie analyse, en gesimuleerd door stralen theorie gebruik makende van verscheidene atmosferische modelrepresentaties.

Voor de eerste keer zijn middel atmosferische weersvoorspelling geëvalueerd met infrageluid. Een jaar van bijna continu infrageluid van de vulkaan Mount Tolbachik, (Kamchatka, Russische Federatie) is vergeleken met simulaties door middel van hoog resolutie deterministische voorspelling van het Europees Centrum voor Weersverwachtingen op Middellange Termijn (ECMWF) met verschillende aanvangstijden. De nowcast, de voorspelling met de kortste aanvangstijd, verricht de beste voorspelling doorheen de ganse tijdsperiode, aangetoond door een hogere continuïteit van de gesimuleerde golfkarakteristieken en een minimale afwijking in richting. Het beste resultaat voor alle voorspelling is verkregen tijdens de zomer. Tijdens de 2013 SSW periode neemt het verschil in richting tussen de observaties en voorspellingen significant toe. Simulaties tonen aan dat de SSW aanvang beter overeenkomt voor de tiendaagse voorspelling en het herstel met de nowcast. De voorgestelde methode

voor het evalueren van weersvoorspellingen in de middelatmosfeer aan de hand van bijna continu infrageluid kan direct toegepast worden op soortgelijke opstellingen, zoals andere CTBT of zelfs nationale infrageluid arrays.

Omgevingsruis van oceaangolven is gebruikt als signaal voor het bestuderen van de levensloop van de 2009 SSW. Kennis over de atmosferische golfgeleiding is bestudeerd aan de hand van slechts amplitude variaties van het omgevingsruis, zonder nodige voorafgaande informatie over de atmosfeer. Geobserveerde amplitude variaties tonen meer details over de levensloop van de SSW, met verschillen in aanvang en herstel, dat niet kan worden verklaard met de analyse data van het ECMWF. Het verstoringstype van de stratosferische wervelwind, gesplitst of verplaatst, kan worden verkregen door de combinatie van de verandering van richting en zonnegetijde signatuur van de amplitudes van het omgevingsruis. Uitbreiding van de evaluatiemethode naar omgevingsruis biedt infrageluid de mogelijkheid om grotere delen van de atmosfeer te doorgronden. Dit is zeer belangrijk voor NWP omdat extra observaties van de stratosfeer alleen een voordeel opleveren voor de weersvoorspelling in de troposfeer bij globale metingen.

Het gebruik van kennis van stratosferische variabiliteit voor bevorderde simulatie van infrageluid voortplanting is aangetoond. Dit is met name belangrijk voor de verificatie van het kernstopverdrag. Probabilistisch infrageluid modellering door middel van een pluim van realistisch verstoorde analyses is met succes gedemonstreerd. Een veelbetekenend voordeel in propagatiemodellering is verkregen zonder de noodzaak om bijkomende kleine fluctuaties bij te moeten voegen. Variantie profielen voor de locatie van het array tonen aan dat de jaarlijkse gemiddelde effectieve geluidssnelheid variatie verschillen tot 8 m s^{-1} behaalt in de stratosfeer, en zelfs af en toe 25 m s^{-1} overschrijden voor een enkele pluim. Laatstgenoemde variatie is van dezelfde orde wat nodig is om infrageluid observaties te verklaren met atmosferedata, vaak toegewijd aan ontbrekende kleine fluctuaties en zwaartegolven of tegenstrijdigheden in het atmosfeermodel.

De ondergrondse nucleaire testen uitgevoerd door de Democratische Volksrepubliek Korea bracht in zowel 2013 als 2016 atmosferisch infrageluid voort. Duidelijke observaties werden gemaakt in de Russische Federatie (IS45) en Japan (IS30) in 2013 op infrageluid arrays van het internationale observatie systeem van het kernstopverdrag. Zowel de troposferische als stratosferische refracties zijn geobserveerd op beide arrays. In 2016 is er enkel een zwak signaal gemeten op IS45. Data analyse en propagatiemodellering laten zien dat het ruisniveau voor beide arrays en de stratosferische wervelwind verschilde in 2016 vergeleken met 2013. Echter resulteert amplitude modellering tot de hypothese dat de 2016 test ongeveer 1.5 keer dieper was dan de test in 2013.

Dit proefschrift toont aan dat infrageluid kan worden toegepast in operationele weeren klimaatvoorspelling als middelatmosferische evaluatietechniek door het simuleren van geobserveerde golfkarakteristieken. Het gebruik van kennis van stratosferische variabiliteit bevordert propagatiemodellering van infrageluid, wat met name belangrijk is voor de verificatie van het kernstopverdrag.

Contents

Preface	i
Summary	v
Samenvatting	ix
1 Introduction	1
1.1 Dynamical stratosphere	2
1.1.1 Composition and classification of the middle atmosphere	2
1.1.2 Stratospheric circulation	2
1.1.3 Sudden stratospheric warmings	3
1.1.4 Importance to weather and climate	5
1.2 Infrasound and sudden stratospheric warmings	6
1.2.1 Sensitivity of infrasound to SSWs	7
1.2.2 Importance to infrasound monitoring	8
1.3 Overview of studies	9
1.3.1 From the 1970's to 2009	9
1.3.2 The 2009 major SSW: an infrasonic game changer	10
1.3.3 Anomalous infrasound propagation in a warm stratosphere	13
1.3.4 Bidirect infrasonic ducts associated with a minor SSW	14
1.4 Statement of problems	18
1.5 Research objectives	19
1.6 Outline of the thesis	19
2 Processing and modelling of infrasound	21
2.1 Infrasound array measurements	21
2.1.1 Plane wave beamforming	22
2.1.2 Fisher detector	26

2.2	Infrasound propagation in a dynamic medium by ray theory	31
2.2.1	Adiabatic, absolute, and effective speed of sound	31
2.2.2	Acoustic wave equation in a dynamic medium	35
2.2.3	Eikonal approximation of the wave equation	37
2.2.4	Asymptotic ray solution of the eikonal equation	39
2.2.5	Ray pressure field by geometrical spreading	41
2.2.6	Implementation and example	45
2.3	Infrasonic ambient noise from atmospheric microbaroms	51
2.3.1	Origin of deep ocean standing surface waves	51
2.3.2	Microbarom radiation of the atmosphere-ocean interface	55
2.3.3	Microbarom source spectrum for a finite ocean depth	57
2.3.4	Implementation and examples	59
3	The life cycle of a sudden stratospheric warming from infrasonic ambient noise observations	65
3.1	Introduction	66
3.2	Data	68
3.2.1	Arctic infrasound observations	68
3.2.2	Ocean wave data	70
3.2.3	Atmospheric specifications	70
3.3	Model	71
3.3.1	Microbarom source model	71
3.3.2	Atmospheric propagation	72
3.3.3	Simulated microbarom observations	73
3.4	Results	75
3.4.1	Infrasound observations	75
3.4.2	Stratospheric versus thermospheric return heights	78
3.4.3	Simulated microbarom observations	81
3.5	The life cycle of a SSW	84
3.6	Discussion and conclusions	85
4	Sudden stratospheric warming forecast evaluation using infrasound	87
4.1	Introduction	88
4.2	Background	89
4.2.1	The relationship between wind, temperature and infrasound	89
4.2.2	Signature of SSW events on infrasound recordings	92
4.3	Methods	93
4.3.1	Infrasound observations	93
4.3.2	Propagation modelling	93
4.3.3	Atmospheric forecasts	94
4.4	Observations	97
4.5	Evaluating ECMWF forecasts	99
4.5.1	Entire observation period	101
4.5.2	2013 SSW	101
4.6	Discussion and Conclusions	104

5	Using stratospheric variability for advanced infrasound propagation	107
5.1	Probabilistic infrasound propagation using realistic atmospheric perturbations	107
5.1.1	Introduction	107
5.1.2	Realistic atmospheric perturbations	108
5.1.3	Infrasound propagation modelling	110
5.1.4	Case study: 1 year of reference events	110
5.1.5	Atmospheric error variance profiles	112
5.1.6	Deterministic versus probabilistic simulations	113
5.1.7	Discussion and Conclusions	115
5.2	On the infrasound detected from the 2013 and 2016 DPRK's underground nuclear tests	117
5.2.1	Introduction	117
5.2.2	Atmospheric propagation of infrasound in 2013 and 2016	118
5.2.3	Infrasound detections of the 2013 and 2016 tests	122
5.2.4	Discussion and conclusions	124
6	Conclusions and recommendations	129
6.1	Conclusions	129
6.2	Recommendations and outlook	132
A	Additional theory	135
A.1	Ideal signal-to-noise ratio increase using array measurements	135
A.2	Pressure gradient force	136
A.3	Hamilton's canonical equations	137
A.4	Ray equations in spherical coordinates	139
B	Additional spectral amplitude variations for the 2010–2014 winters	143
C	Preliminary analysis of the relative source depth of DPRK's 2013 and 2016 underground nuclear tests	151
C.1	Propagation efficiency and pressure ratios	151
C.2	Stratospheric propagation	152
C.3	Estimating relative depth from the pressure ratio	152
	Bibliography	155
	List of symbols and abbreviations	167
	Curriculum Vitæ	173

1

Introduction

“Stratospheric sudden warmings are the clearest and strongest manifestation of dynamical coupling in the stratosphere-troposphere system.”

Charlton and Polvani, 2007

Sudden stratospheric warmings (SSWs) are important features of the winter atmosphere in the Northern Hemisphere [Charlton and Polvani, 2007]. During such events, the strongest transient forcing of the stratosphere on the troposphere is observed [Gerber *et al.*, 2009; Tripathi *et al.*, 2014], influencing weather conditions and its predictability in the troposphere [Jung *et al.*, 2010]. Consequentially, improving the predictability of stratospheric variability, such as during SSWs, is important to Numerical Weather Prediction (NWP). Infrasound, part of the Atmospheric Dynamics Research Infrastructure in Europe - ARISE - project, has shown its ability in probing the upper atmosphere [e.g. Donn and Rind, 1971; Le Pichon *et al.*, 2009]. Further ARISE techniques to probe the middle atmosphere (10-100 km) are ground based lidars, radars, wind radiometers and ionospheric sounders (see arise-project.eu). Infrasound is low-frequency inaudible sound (< 20 Hz), used as a waveform verification technique for the Comprehensive Nuclear-Test-Ban Treaty (CTBT). A key benefit of infrasound is the sensitivity to both temperature and wind in a region where atmospheric observations are scarce. Infrasound has a long history for monitoring SSWs. Several pioneering studies have focused on the various effects of a major warming on the propagation of infrasound. For that reason, studying SSWs using infrasound is part of the ARISE roadmap demonstrating the use of infrasound data for weather and climate monitoring [Smets *et al.*, 2014].

Published as: Smets, P. S. M., J. D. Assink, and L. G. Evers (2018), The study of sudden stratospheric warmings using infrasound, In: Le Pichon A., Blanc E., Hauchecorne A. (eds) *Infrasound Monitoring for Atmospheric Studies: Challenges and New Perspectives*, Springer, Dordrecht. Note that minor changes have been introduced to make the text consistent with the other chapters.

1.1 Dynamical stratosphere

■ 1.1.1 Composition and classification of the middle atmosphere

The Earth's dry atmosphere, named *air*, is a mixture of gases primarily existing of diatomic nitrogen (N_2) and oxygen (O_2). These two gases account for 98.65% of the total mass of the dry atmosphere, accompanied by noble argon (Ar, 1.28%) [Andrews *et al.*, 1987]. A small but important fraction are trace species ($< 0.1\%$), predominantly carbon dioxide (CO_2 , 0.04%). Important trace species for the atmosphere's thermodynamic and radiative heat balance are water vapour, carbon dioxide, and ozone (O_3). Note that, these three trace species together with methane (CH_4) and nitrous oxide (N_2O) form the most abundant greenhouse gases in the Earth's atmosphere. Motions of the atmosphere tend to produce uniform mixing of the atmosphere, except for constituents with significant sources or sinks. The mass of the atmosphere is proportional to pressure, decreasing exponentially with height.

The atmosphere can be divided in layers, classified by their temperature stratification based on the kinetic energy of the molecules [Holton, 2004], shown in Figure 1.1 as a function of geopotential height¹. The lowest layer is the *troposphere*, containing about 80–90% of the total mass of the atmosphere and nearly all water vapour. Most weather occurs in this lower layer. The troposphere is warmest near the surface, due to radiation of solar heat by the ground, and regularly cools by height² up to the *tropopause* (~ 10 km). The tropopause is an inversion layer in between the troposphere and stratosphere, where the air temperature remains constant. In the *stratosphere*, the temperature increases with height up to the *stratopause* (~ 45 km) due to the absorption of solar ultraviolet radiation by ozone. Ozone absorption in the long-wave (i.e. thermal) radiation is also an important contributor to the stratification. The stratosphere contains about 10–20% of the total mass of the atmosphere, and everything above the stratopause, just 0.1%. At the stratopause the temperature remains constant. Above, in the *mesosphere*, the temperature reduces by height due to the decrease in ozone and very strong radiative cooling of carbon dioxide, reaching a minimum at the *mesopause* (~ 90 km). From the *thermosphere* the temperature increases due to absorption of highly energetic solar radiation causing photoionization of the atmosphere's molecules in the ionosphere (> 85 km).

■ 1.1.2 Stratospheric circulation

The unequal solar insolation induces a temperature gradient from the warm summer pole to the cold winter pole, driving the stratospheric circumpolar vortex. For this induced geostrophic circulation, the Coriolis force balances the horizontal pressure gradient whereas the thermal-wind balance relates the vertical wind shear to the horizontal temperature gradient [Muench, 1965; Kriester, 1972]. The temperature

¹Geopotential height $Z_g(h) = \Phi(h)/g_0$ is a vertical coordinate referencing the geopotential Φ at geometric height h to the Earth's standard gravity g_0 at mean sea level.

²The dry adiabatic lapse rate (DALR = $-dT/dz$) of the free troposphere is approximately $g_0/c_p = 9.8 \text{ K km}^{-1}$. The average environmental lapse rate (ELR) by the International Standard Atmosphere equals 6.5 K km^{-1} from sea level up to 11 km.

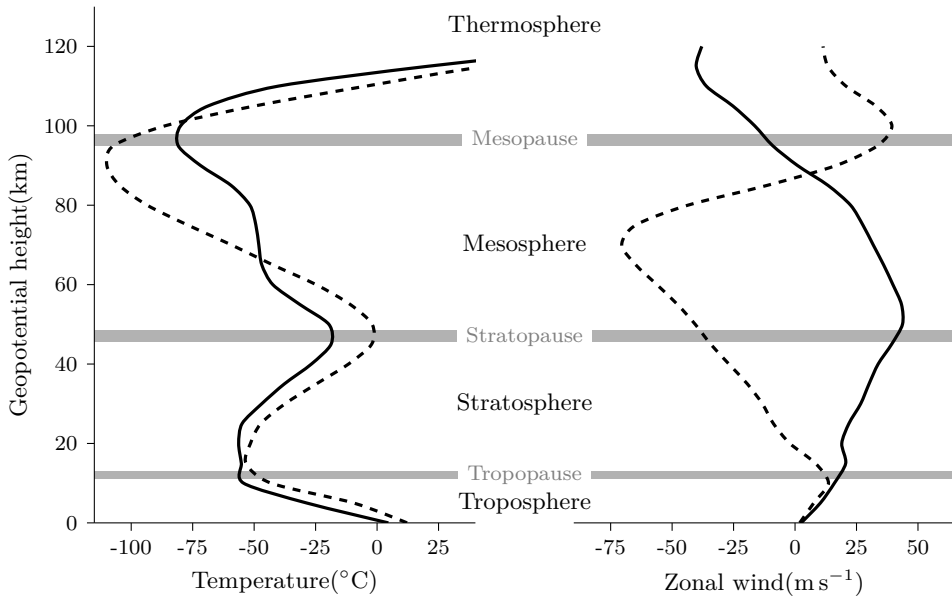


Figure 1.1: Zonal mean vertical profile based on the (solid) January and (dashed) July temperature and zonal wind at 50°N from the Committee on Space Research (COSPAR) International Reference Atmosphere 1986 empirical model (CIRA-86) [Fleming et al., 1990].

gradient is minimum at the equator and maximum at the summer pole and near midlatitudes for the winter pole.

The seasonal variation in the atmosphere's heat balance changes the direction of the polar vortex, typically around the vernal and autumnal equinoxes. In summer, during polar day, the circumpolar vortex is easterly, characterized by a stable stratospheric wind and temperature structure [McIntyre and Palmer, 1984]. In winter, the westerly circumpolar vortex is stronger but unstable. The zonal mean circulation is strongly influenced by vertical propagating planetary waves, predominantly by Kelvin and Rossby waves, breaking in the stratosphere [McIntyre and Palmer, 1983]. These waves interact with the flow forcing a long period oscillation (quasi biennial oscillation) yielding large year-to-year variation of the zonal circulation [Labitzke and van Loon, 1999]. At the winter pole, a meridional circulation around the midlatitude temperature peak yields zonal mean transport from the equator tropopause to the polar night tropopause.

■ 1.1.3 Sudden stratospheric warmings

Sudden stratospheric warmings (SSWs) are regularly occurring features in winter in the Northern Hemisphere (NH) [Charlton and Polvani, 2007] characterized by dramatic changes in the stratospheric wind and temperature. SSWs are the strongest

transient manifestation of the stratosphere-troposphere interaction [Charlton and Polvani, 2007; Shaw and Shepherd, 2008; Gerber *et al.*, 2009].

During polar night, the high-latitude westerly jets provide a waveguide for vertical propagation of quasi stationary planetary waves, primarily of zonal wave numbers 1 and 2, caused by selective filter by the mean state [Holton, 2004]. Rossby waves propagate vertically from the troposphere up into the stratosphere and break at the top of the westerly polar vortex, around 50 km altitude, which can trigger a SSW [Matsuno, 1971]. This planetary wave breaking decelerates the westerly zonal mean flow, reducing the pole-to-equator mean temperature gradient [Charney and Drazin, 1961]. The effect increases with height as the vertically-propagating Rossby wave amplitude increases because of the reduced air density. Due to the repeated Rossby wave breaking the stratospheric polar vortex gets highly distorted, breaks down and eventually reverses to an easterly flow. As the zonal mean flow is to remain geostrophic, air descends adiabatically into the easterly polar vortex which strongly increases the polar stratospheric temperature up to 50°C in a few days. As the easterly circulation is no longer affected by the vertically propagating waves, the disruption migrates down into the stratosphere by the next planetary wave disturbances, reversing the flow underneath. When these stratospheric changes are severe it is known as a sudden stratospheric warming and can be classified in four characteristic scales (see grey box). Throughout a major stratospheric warming, two types of vortex disturbances can be observed: a displacement of the cold vortex away from the pole or a vortex split into two separate daughter vortices [Charlton

Sudden stratospheric warmings can be classified in four characteristic scales, however, various definitions exist for each. The definition according to the World Meteorological Organisation (WMO) and Labitzke and van Loon [1999] is specified by their strength.

Major A latitudinal mean temperature increase poleward of 60° latitude with an associated easterly circulation around 10 hPa accompanied with either a vortex displacement or vortex split. Major warmings occur mostly in January–February.

Minor Zonal winds in the stratosphere weaken, reversing the temperature gradient between the poles and midlatitudes, but do not lead to a breakdown nor reversing of the polar vortex.

Canadian An early winter warming with strong non-zonal character solely occurring in the Northern Hemisphere. The net zonal winds briefly change but are not strong enough to cause a breakdown of the polar vortex.

Final A major warming which appears at the end of the winter indicating the transition from a cold winter system to a warm high-pressure system due to the change from polar night to polar day.

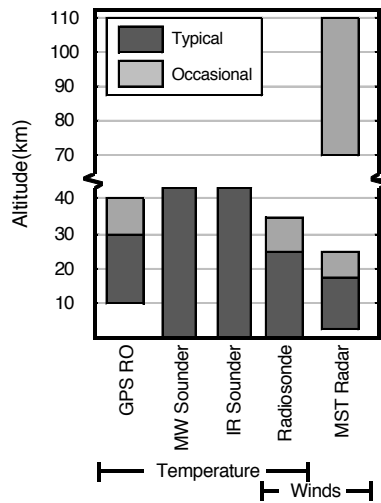


Figure 1.2: Typical and occasional altitude ranges of instruments probing the middle atmosphere commonly assimilated by NWP models. Figure adapted from [Lee et al., 2018].

and Polvani, 2007]. SSWs occur mainly in the NH since the enhanced upward propagation of Rossby waves is primarily induced by continental blocking [Kodera et al., 2013].

■ 1.1.4 Importance to weather and climate

The importance of the middle atmosphere upon weather and climate has been increasingly appreciated following evidence indicating that processes in the stratosphere couple to the troposphere [Baldwin and Dunkerton, 2001; Limpasuvan et al., 2004; Charlton et al., 2004; Shaw and Shepherd, 2008]. Progress has been made towards a more comprehensive representation of the atmosphere in order to better capture the stratospheric-tropospheric coupling [Randel et al., 2004; Charlton-Perez et al., 2013].

Significant effort has been made by numerical weather prediction (NWP) models to better characterize SSWs. Accurate SSW prediction is justified due to its delayed impact up to two months on the weather as experienced on the Earth's surface [Sigmond et al., 2013; Tripathi et al., 2015]. Recently, a significant update has been made to the numerical scheme in the stratosphere of the Integrated Forecast System (IFS) at the European Centre for Medium-range Weather Forecasts (ECMWF) [Diamantakis, 2014], leading to an improved characterisation of SSWs. However, the stratospheric region is notoriously difficult to monitor.

In the past, frequent in-situ wind observations were retrieved by rocket sounding [e.g. Seibert, 2006]. Currently, radiosonde and aircraft are the main sources of information about the upper-air wind up to 30 km altitude [WMO, 2013]. Beyond

the middle stratosphere, direct information of wind is lacking. In this region, NWP is limited to observations of the thermal structure by Global Positioning System (GPS) radio occultation and satellite based sounding (microwave and high-spectral-resolution infrared³). From the stratopause upward no data is assimilated (see Figure 1.2). In the past, frequent in-situ observations of wind were retrieved by rocket sounding, usually by campaigns, [e.g. *Seibert, 2006*], yet these have significantly reduced in the last three decades. Currently, the only upcoming mission designed for global wind-component-profile observations is ESA's ADM-Aeolus Earth observation satellite [e.g. *Källén, 2008; Straume et al., 2016*]. However, in continuous operating mode it will not report higher than 30 km. Hence, filling the vast gap in the global observing system with new wind observations can have a big impact on weather forecasting. Radiance observations are dominated by Advanced Microwave Sounding Unit type A (AMSU-A), but other⁴ microwave sounders are now taking its place.

The quality of both the stratospheric analysis and forecast during a stratospheric warming can be inadequate, as discussed by *Diamantakis [2014]* and *Smets et al. [2016]* for the 2013 SSW. AMSU-A is capable of capturing the fast temperature variations related to a SSW. However, due to these very rapid changes, the NWP model first-guess field and assimilated observations can differ significantly at the onset of a warming. Significant discrepancies can result in a possible rejection of all good AMSU-A data, hence affecting the stratospheric predictability. At the European weather centre, improved stratospheric forecast skill during a SSW is obtained by a refined numerical scheme, noticeably increasing in the number of assimilated satellite observations. Further improvements in SSW predictions can be obtained from better resolving the stratosphere [*Gerber et al., 2009; Roff et al., 2011*] and mesosphere [*Coy et al., 2011*] together with assimilating data using additional techniques.

1.2 Infrasound and sudden stratospheric warmings

Infrasound is low-frequency inaudible sound, used as a waveform verification technique for the Comprehensive Nuclear-Test-Ban Treaty (CTBT). The infrasound spectrum (0.002–20 Hz) comprises acoustic waves, restored solely by pressure, and acoustic-gravity waves ($< 0.02 \text{ Hz}^5$), and are restored by both pressure and gravity [*Gossard and Hooke, 1975*]. Below 0.002 Hz signals are no longer acoustic waves, restoring only by gravity. To produce these low-frequency acoustic signals a powerful source is required to displace large volumes of air, for example, a nuclear explosion.

Infrasound has notably progressed in its ability as a remote sensing technique for the upper atmosphere [e.g. *Le Pichon et al., 2010*]. Since the CTBT opened for

³Example of infrared sounder instruments are: Atmospheric Infrared Sounder (AIRS), Infrared Atmospheric Sounding Interferometer (IASI), Cross-track Infrared Sounder (CrIS)

⁴Advanced Technology Microwave Sounder (ATMS) on NOAA's National Polar-orbiting Operational Environmental Satellite System (NPOESS) and the temperature and humidity sounders (MWTs and MWHS) and radiation imager (MWTs) on CMA/NSMC FengYun-3 (FY-3) polar orbiting meteorological satellite series.

⁵The critical frequency above which no gravity waves exists, named acoustic cut-off frequency.

signing in 1996 [Dahlman et al., 2009], there has been a renaissance in exploiting ground-based infrasound arrays for upper atmospheric remote sensing [e.g. Lalande et al., 2012; Assink et al., 2013; Fricke et al., 2014; Chunchuzov et al., 2015]. The International Monitoring System (IMS), in place for the verification of the CTBT, will consist of 60 infrasound arrays, of which 49 have currently been certified (status July 2017). Furthermore, many national arrays, not part of the IMS, exist, which are often part of seismo-acoustic measurement systems. Examples of these are the LOFAR array [Fricke et al., 2014] in the Netherlands, the USArray [Hedlin et al., 2012; de Groot-Hedlin and Hedlin, 2014] in the United States and various seismo-acoustic arrays in South Korea [Che et al., 2002].

■ 1.2.1 Sensitivity of infrasound to SSWs

Infrasound propagation strongly depends on the state of the atmosphere, which may result in changes in the wave vector direction (e.g. reflection, refraction) and attenuation of the signal. The low frequency signals propagate efficiently over long distances, since attenuation is in general relatively low (f^{-2}). In a horizontally layered atmosphere, infrasound propagation can be approximated to the first order by the effective speed of sound $c_{\text{eff}} = c_T + w_a$, a function of the adiabatic speed of sound $c_T \approx 20.04\sqrt{T} \text{ m s}^{-1}$ for absolute temperature (T) and the horizontal wind in direction of propagation (w_a) [Godin, 2002]. Refraction of the infrasonic signals is constrained by variations in the speed of sound gradient [Brekhovskikh and Godin, 1999]. In a negative vertical sound speed gradient propagating sound waves will refract upwards such that they have a larger vertical velocity component, while in a positive sound speed gradient propagation will tend toward being more horizontal. Since most sources of interest and almost all receivers are ground based, of interest is predominantly ground-to-ground propagation; e.g. ducting is considered between the ground and the top of the waveguide aloft. The refractivity or ducting of the atmosphere can be indicated by the ratio of the effective speed of sound at an altitude with respect to the effective speed of sound at the ground. Signals refract back to the ground when the effective speed of sound ratio is approximately one or larger; indicating an atmospheric waveguide or duct. Infrasound is most sensitive when the vertical velocity component is minimal: at the refracting or return altitude.

In general, three different atmospheric waveguides can be differentiated: signals refracting in either the troposphere, stratosphere, or thermosphere. The tropospheric waveguide is mainly bound by wind, i.e., the mid-latitude jet stream around the tropopause ($\sim 10 \text{ km}$). The stratospheric waveguide depends on the increase of both wind and temperature, induced by the temperature increase due to the presence of ozone driving the stratospheric polar vortex. Both tropospheric and stratospheric waveguides are predominantly anisotropic due to the strong wind jets. Propagation in directions opposite to the tropospheric and stratospheric wind is possible, but ducting is not. The thermospheric waveguide is dominated by a strong positive temperature gradient above the mesopause, causing more isotropic ducting. However, infrasound from these return altitudes is strongly attenuated due to the highly rarified atmosphere at these altitudes [Sutherland and Bass, 2004; Assink et al., 2012]. During SSWs, the top of the stratospheric waveguide may extend from

the lower stratosphere to the lower mesosphere. In addition, a SSW affects the atmospheric waveguide due to rapidly changing wind and temperature conditions, ranging from minor variations to dramatic changes, detectable in the infrasound observations at the ground [e.g. *Donn and Rind*, 1971; *Evers and Siegmund*, 2009; *Hedlin et al.*, 2010; *Assink et al.*, 2014a].

■ 1.2.2 Importance to infrasound monitoring

Improved knowledge and observations of stratospheric warmings is not only of great interest to Numerical Weather Prediction but as well to infrasound monitoring purposes, e.g., CTBT treaty verification.

Capabilities of the CTBT International Monitoring System (IMS) infrasound network considering long range propagation aspects are determined by the state of the stratosphere. Stratospheric variability, e.g., during equinox periods and stratospheric warmings, strongly influences the detectability of infrasound [*Le Pichon et al.*, 2008, 2010; *Tailpied et al.*, 2017]. During the last decade, the number of studies coming across unexpected atmospheric conditions related to SSWs has increased significantly.

On 19 February 2008 a large bolide was observed by several hundreds of broadband seismic stations in the U.S. Pacific Northwest. *Hedlin et al.* [2010] found an unexpected predominant easterly propagation direction of the acoustic coupled to seismic signals related to a sudden stratospheric warming event. Infrasound propagation simulations using ECMWF and G2S (Ground-to-Space⁶) atmospheric conditions were unable to explain the observation. The study of *Hedlin et al.* [2010] indicates for the first time discrepancies in atmospheric models by infrasound during a stratospheric warming.

In 2009 and 2011, two large-scale infrasound calibration experiments consisting of three explosions were conducted to test the International Monitoring System (IMS) infrasound network of the CTBT and provide ground truth data for infrasound propagation studies [*Fee et al.*, 2013]. For the 2011 experiments, portable infrasound arrays in the source region were deployed to the east of the source, aiming to take advantage of the typical winter westerly tropospheric and stratospheric winds. However, prior to the 2011 tests a minor stratospheric warming occurred (see Subsection 1.3.4) affecting the stratospheric duct. Infrasound propagation and detectability were strongly influenced. The results of the Sayarim experiments, designed to test the IMS, would have been significantly different if the explosions had occurred a week earlier.

The study of *De Angelis et al.* [2012] demonstrates an automatic infrasound and seismo-acoustic eruption detection algorithm for real-time volcano monitoring operations in remote regions. Acoustic propagation modelling shows how strong tropospheric ducting allows infrasound to travel long distances across the Aleutian Arc. For the stratospheric signals, *De Angelis et al.* [2012] point out an unusual winter

⁶Whole atmosphere conditions of the U.S. Naval Research Laboratory (NRL) obtained by a combination of various atmospheric products from NOAA and NASA, vertically extended by empirical modelling of the upper atmosphere using HWM/MSIS [*Picone et al.*, 2002; *Drob et al.*, 2015].

stratospheric jet characterized by easterly winds, identified as a sudden stratospheric warming event in NWP analyses.

More recently, the study of *Assink et al.* [2016] analysed the atmospheric infrasound of the underground nuclear tests by the Democratic People's Republic of Korea (DPRK) of 12 February 2013 and 6 January 2016. During the 2013 and 2016 tests, the stratospheric waveguide was in a very different state. Clear detections were made in the Russian Federation (IS45) and Japan (IS30) in 2013 at stations from the International Monitoring System. Both tropospheric and stratospheric refractions arrived at the stations. In 2016, only one weak return was potentially observed at IS45 due to the presence of an early stage SSW. Despite the stratospheric variability, the 2016 event could be simulated using the ECMWF HRES (High Resolution) deterministic forecast. Observations and the modelled parameters associate this arrival to both the tropospheric and stratospheric propagation paths.

Therefore, understanding the detectability of infrasound and its dependencies is crucial for successfully applying infrasound as a verification technique.

1.3 Overview of studies

■ 1.3.1 From the 1970's to 2009

The first infrasound signature of a stratospheric warming goes back to the pioneering studies by both Donn and Rind, intrigued by the ability of natural infrasound to probe the upper atmosphere. Their studies are characterized by the use of ambient noise from interacting ocean waves, microbaroms and microseisms, as a continuously natural source for exploring the atmosphere. Fundamental to their studies of the SSW is the identification of a characteristic diurnal variation in the amplitude of the ambient noise observations. *Donn and Rind* [1971] relate amplitude changes to the state of the atmosphere, independent of any variation in the source. In winter, high amplitudes with a strong semidiurnal variation are denoted while summer amplitudes are lower with a weak diurnal variation. They associate typical amplitude variations to viscous dissipation associated with refraction height variation, described more thoroughly in *Rind and Donn* [1975]. More important is the link between abnormal microbarom intensities in the early winter of 1967-1968 to variations in the stratosphere; the first infrasonic signature of a stratospheric warming. As the winds turn, around the equinoxes and during SSWs, the amplitude of ambient coherent infrasound noise increases due to the formed stratospheric waveguide between the Atlantic and Palisades.

The stratospheric warming of December 1967 is studied more elaborately in *Donn and Rind* [1972], including early propagation simulations. In addition to amplitude variations, *Rind et al.* [1973] made use of microbarom apparent velocities⁷ for estimating upper air wind speeds. The latter led to the studies of *Rind and Donn* [1975, 1978], utilising sound intensity variations from infrasound-seismic ambient noise variations as a preliminary atmospheric probe. These studies came to a stop

⁷Apparent velocity is the propagation velocity of the (plane) wave across the infrasound array.

Microbaroms are atmospheric pressure oscillations radiated from non-linear ocean surface wave interaction at double the ocean wave frequency [Gutenberg, 1939; Longuet-Higgins, 1950; Posmentier, 1967]. Interacting large regions of high-energetic ocean waves of similar frequency with opposite directions, e.g., ocean swell and marine storms, radiate acoustic energy almost continuously well characterized by a radiation frequency of 0.2 ± 0.1 Hz. Microbaroms dominate the infrasound and seismic ambient noise field due to their continuous presence, making them a preferred source for passive atmospheric probing.

when nuclear tests were diverted to the subsurface under the Limited or Partial Test Ban Treaty in 1963. Nevertheless, the excellent work of Donn and Rind paved the path for using natural ambient noise as a comprehensive technique for monitoring several upper atmospheric parameters.

■ 1.3.2 The 2009 major SSW: an infrasonic game changer

In January 2009, a major sudden stratospheric warming caused drastic changes in the stratosphere. The midwinter westerly stratospheric vortex quickly displaced and elongated, followed by a full vortex split and an increased amplitude of the zonal wavenumber 2 planetary wave. For several days, two vortices and reversed winds characterize the stratosphere (see Figure 1.3). By the beginning of February 2009 the stratosphere recovered to its typical midwinter state.

The infrasonic signature of the 2009 SSW is described by *Evers and Siegmund* [2009], exploiting back azimuths of oceanic noise at the IMS infrasound arrays on the NH. For the first time, passive infrasonic observations at the surface provided detailed information on upper atmospheric processes on a global scale. IMS arrays north of 15°N detect a large amount of coherent ambient infrasound noise, as long as the local wind speeds are low. High local wind speed causes coherent wind noise at the instrument which reduces the signal-to-noise-ratio and detection capability [Walker and Hedlin, 2009]. Sensitivity of infrasound arrays to sources located in specific directions is controlled by the atmospheric state, described in Subsection 1.2.1. Therefore, variations in the direction and intensity of the stratospheric polar vortex, such as during a SSW, seriously affects the microbarom's detectability in terms of back azimuth. Figure 1.3 illustrates the stratospheric wind and temperature at 50 km prior to the SSW and during the vortex split. The SSW caused ambient noise observations to arrive from the opposite direction than expected during regular midwinter conditions at multiple infrasound arrays, marked in Figure 1.3. In normal winter conditions, westerly ambient noise observations are expected, since the stratospheric duct is favourable to downwind conditions. However, throughout the major SSW the polar vortex breaks down and reverses which alters the duct from westerly to easterly. This dramatic change is clearly observable in the microbarom observations by an altered or apparently (dis)appeared microbarom source region, leading up to the infrasonic signature of a SSW. *Evers and Siegmund* [2009] indicate clear infrasonic signatures of the stratospheric warming observed in Greenland

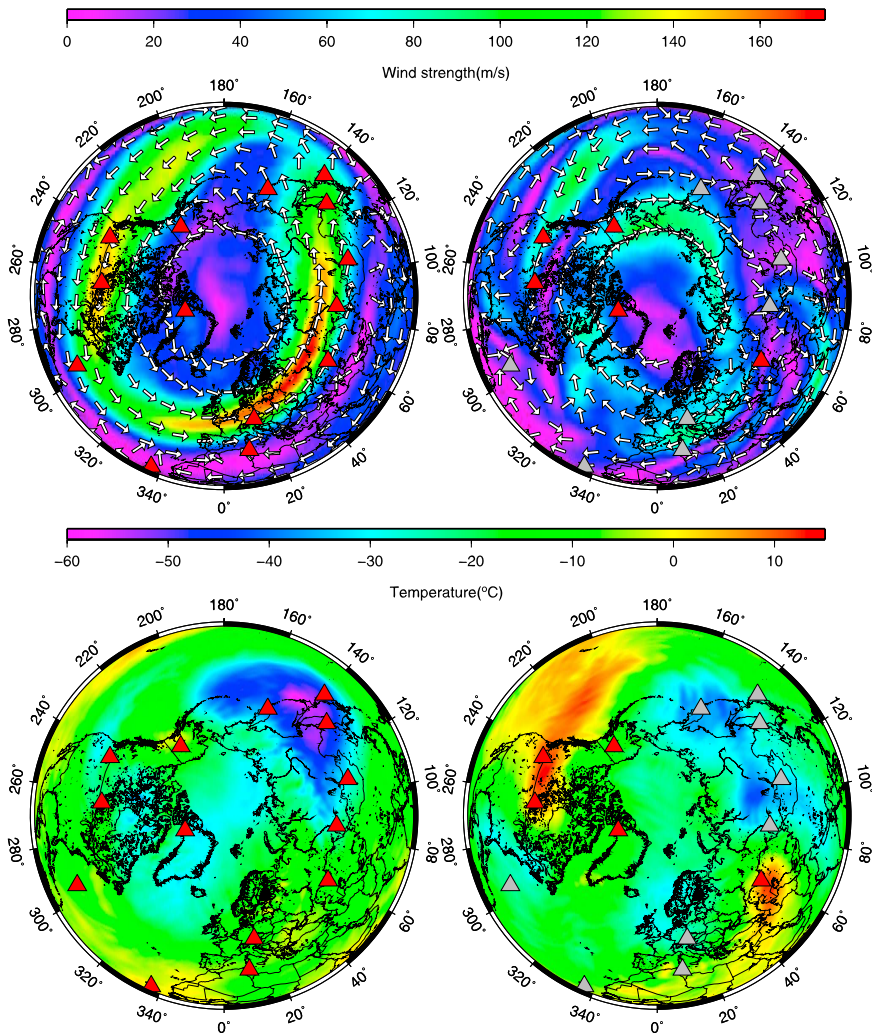


Figure 1.3: (top) wind and (bottom) temperature at 50 km altitude from ECMWF analyses. (left) Valid for 2009, January 2 at 00 UTC, prior to the SSW; (right) values during the vortex split phase of the SSW on January 23 at 00 UTC. The red triangles in the right column indicate arrays which sensed the SSW, the grey triangles represent arrays where no clear signature was found in the observed back azimuths. Figure adapted from Evers and Siegmund [2009].

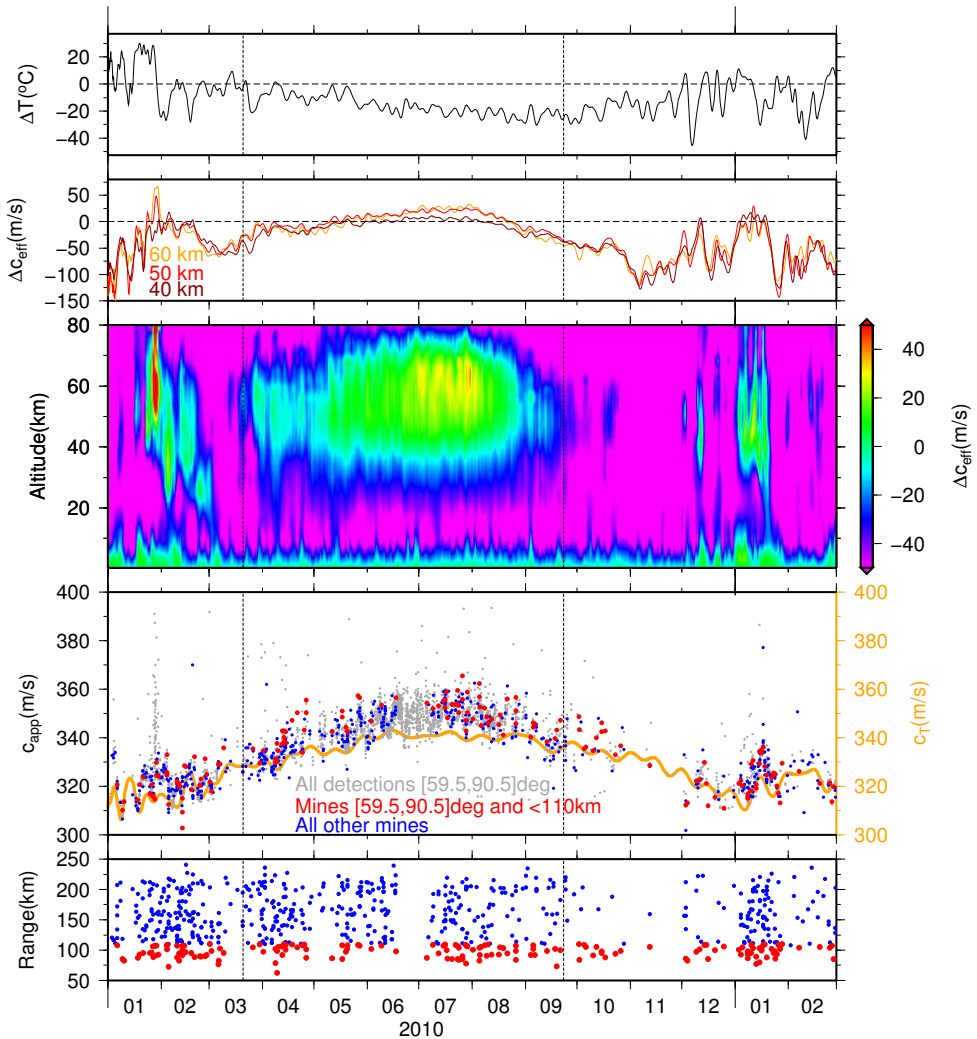


Figure 1.4: From top to bottom are listed; atmospheric conditions and REB detections at IMS infrasound array IS46 (Russian Federation) from seismic ground-truth locations. Only associated infrasound detections within the back azimuthal interval between 59.5° to 90.5° are used. Vertical dashed lines indicate the vernal and autumnal equinox. (first panel) The temperature difference between 50 km altitude and the surface, ΔT . The c_T , Δc_T and ΔT curves are smoothed with a polynomial fit. (second panel) Cross sections from Δc_{eff} at an altitude of 40, 50 and 60 km. (third panel) The difference between the effective sound speed at a certain altitude and near the surface, colour coded as Δc_{eff} . The latter are derived from ECMWF analyses at 54.0° N, 85.5° E. (fourth panel) The apparent sound speed, c_{app} , of the detections. The red and blue dots are seismic locations from the REB assumed to correlate with mining activity, i.e., blasting. Mines at a distance of less than 110 km are denoted by red dots, all other detections within the back azimuth range are added as grey dots. The surface sound speed c_T is given as orange line and calculated from the temperature. (fifth panel) The distances of the mining activity sources with respect to IS46 as function of time. Figure adapted from Evers et al. [2012].

(IS18), Alaska (IS53), over the western US (IS56) and central Canada (IS10). Even in Kazakhstan (IS31) slight changes in the retrieved back azimuths are notable. At the Russian arrays (IS44, IS45 and IS46) no pronounced changes in the observed back azimuths are visible. Similar results are also found for the German (IS26), Japanese (IS30), Mongolian (IS34) and Tunisian (IS48) arrays.

■ 1.3.3 Anomalous infrasound propagation in a warm stratosphere

So far, less attention had been paid to stratospheric temperature variations than to the wind variations. *Evers et al.* [2012] studied the temperature effect in the stratosphere on infrasound propagation. A case study of an explosion indicates a significant reduction of the size of the classical stratospheric shadow zone. The reduction corresponds with a lowering of the return height following the stratospheric temperature increase. During the January 2010 SSW, the extent of the classical stratospheric shadow zone (~ 200 km) reduces by a factor of 2, leading to extremely small shadow zones. When the temperature in the vicinity of the stratopause is higher than the Earth's surface temperature, for example throughout a SSW, pure temperature gradient induced refractions can occur.

The occurrence of such conditions is quantified by analysing ten years of ECMWF analyses, four times per day. The stratospheric shadow zone is simulated by ray theory in a one-dimensional model in direction of the wind at 50 km. A minimum value in stratospheric shadow is obtained by using the steepest gradient in c_{eff} . Stratospheric returns occurred 62% of the time and mostly in winter (51%). Hardly any returns are observed around the equinoxes due to the lack of significant downwind component at 50 km altitude. Very small shadow zones of less than 100 km occurred 3% of the time. For 1% of the time no additional downwind component w_a is necessary to enable refraction back to the Earth's surface, mostly associated with SSWs.

The existence of small shadow zones is confirmed by infrasound from mining blasts in southwestern Siberia, Russia, observed by IMS infrasound array IS46 (Russian Federation). Events are obtained from the Reviewed Event Bulletin (REB) from the International Data Centre (IDC) for verification of the CTBT. Locations are seismically determined using IMS seismic data in the Russian Federation detected at at least two arrays. Locations errors are of the order of a couple of kilometres. Selected events in this low-seismic area, within the back azimuthal interval between 59.5° to 90.5° of IS46 at a maximum distance of 250 km, most likely correspond to open pit mining. Stratospheric conditions of wind and temperature correspond to the number of detections at IS46, see Figure 1.4, and consequently to the variation in the apparent velocity c_{app} of the events. c_{app} is the horizontal projection of the propagation velocity vector. For a layered medium, the apparent velocity is invariant [*Pierce, 1981*]. Minimal c_{app} values are predominantly controlled by the near surface temperature (and not the stratospheric conditions). The range of c_{app} is defined by the propagation conditions (i.e. the inclination angle), related to the both the return height and strength of the gradient in c_{eff} . The infrasound signals correspond to stratospheric refractions, indicated by the agreement of the structure of c_{app} to the structure of the stratosphere. This would not have been the case for

tropospheric arrivals. During the equinoxes hardly any detections are made and during winter conditions, summer-like apparent velocities appear which could only be caused by SSWs. However, it should be noted that more stratospheric arrivals are observed than predicted by the modelling. Fine-scale structure in the wind and temperature caused by internal gravity waves, not resolved by, e.g., the ECMWF models, may be responsible for generating additional arrivals in the classical shadow zone, as predicted by ray theory [Kulichkov *et al.*, 2010; Revelle, 2010; Chunchuzov *et al.*, 2011].

Some observed c_{app} lay below the c_T curve at the surface, which is physically impossible (see Figure 1.4, fourth panel). The adiabatic speed of sound c_T is the lowest possible propagation velocity (in the absence of wind) and should correspond to the minimal c_{app} . Too low values of c_{app} are in first order attributed to uncertainties in array processing (timing and c_{app} , especially for low SNR events), surface temperature estimates and the impact of ignoring wind. The temperature is obtained from NWP specifications and is not an actual measurement at the station. Nevertheless, the general trends of near-surface and stratospheric variations, i.e., summer versus winter characteristics are reflected in the observed c_{app} . Lower surface temperatures and stronger gradients in c_{eff} during winter explain the lower values of c_{app} with respect to summer. Observations at IS46 deliver the proof for the existence of extremely small shadow zones, less than 100 km in size, for stratospheric arrivals. These results are applicable to a broad latitudinal range defined as the stratospheric surf zone, i.e., 20°N to 60°N where a rather stationary flow of stratospheric air occurs.

■ 1.3.4 Bidirect infrasonic ducts associated with a minor SSW

Donn and Rind [1972, Subsection 1.3.1] and Evers and Siegmund [2009, Subsection 1.3.2] reported on significant azimuthal reversal due to the reversal of the zonal jet as a result of a major warming event. Nevertheless, Assink *et al.* [2014a] denoted simultaneous arrivals from two nearly opposite stratospheric ducts during a minor warming. In January 2011, a bidirectional stratospheric duct persisted for two weeks in the wake of a minor SSW. This situation occurred just prior to the 2011 Sayarim experiments [Fee *et al.*, 2013], which took place on 24 and 26 January 2011 (see Subsection 1.2.2). The existence of bidirectional ducting during stratospheric warming events has not been considered in the past.

The development of a bidirectional duct had significant effects on infrasound propagation in the middle atmosphere, which is typically expected to be unidirectional. Such ducting significantly improves infrasound detection capability during these periods, since the anisotropy is strongly reduced. In general, the detectability is determined by the convolution of the source strength, distance to the source, atmospheric wind and temperature, and the ambient noise conditions near the receiving array [Evers and Siegmund, 2009].

The existence of the bidirectional duct has been demonstrated at IMS infrasound array IS48 (Tunisia). The bidirectional ducting effect is clearly captured at IS48, due to its favourable location with respect to microbarom sources at both sides of the station. Two microbarom signals, from nearly opposite back azimuth directions

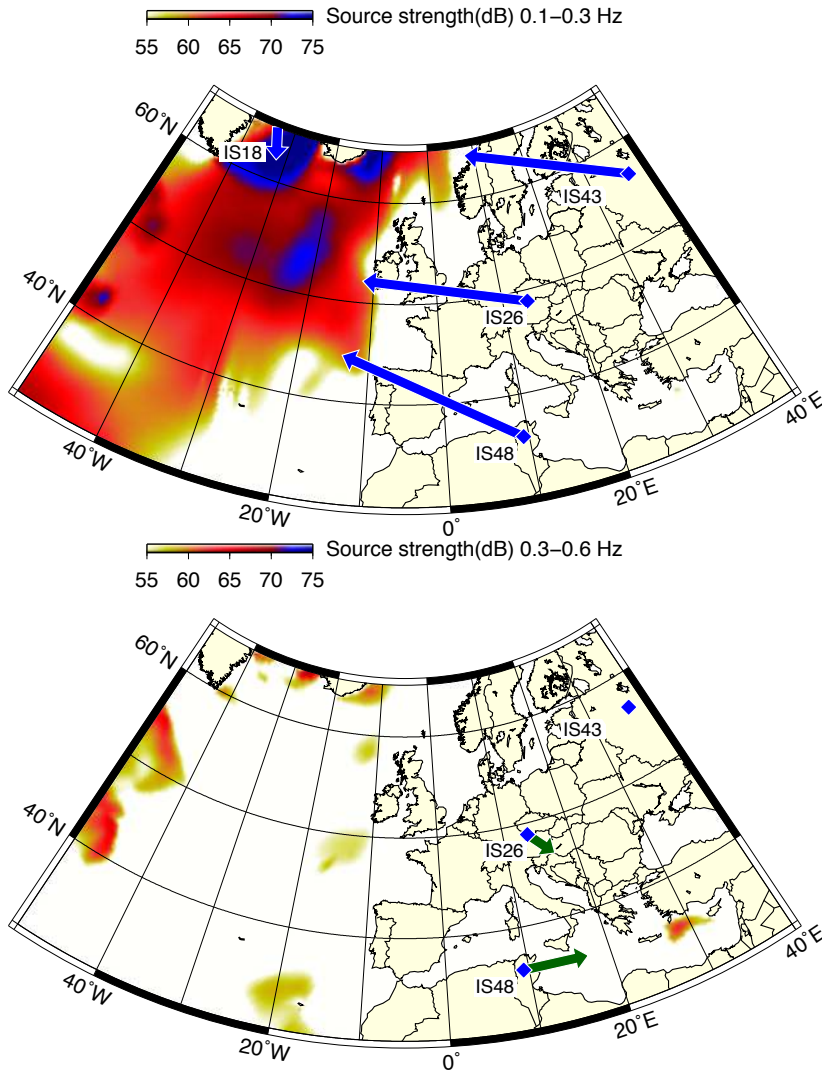


Figure 1.5: Microbarom source region predictions for two distinct frequency bands, computed using the source model described by Waxler and Gilbert [2006] and ECMWF HRES-WAM two-dimensional ocean wave spectra, for 17 January 2011 00 UTC for the (top) 0.1–0.3 Hz and (bottom) 0.3–0.6 Hz frequency bands. Blue and green arrows correspond to observed back azimuth directions at IMS infrasound arrays for the specific frequency ranges. Figure adapted from Assink et al. [2014a].

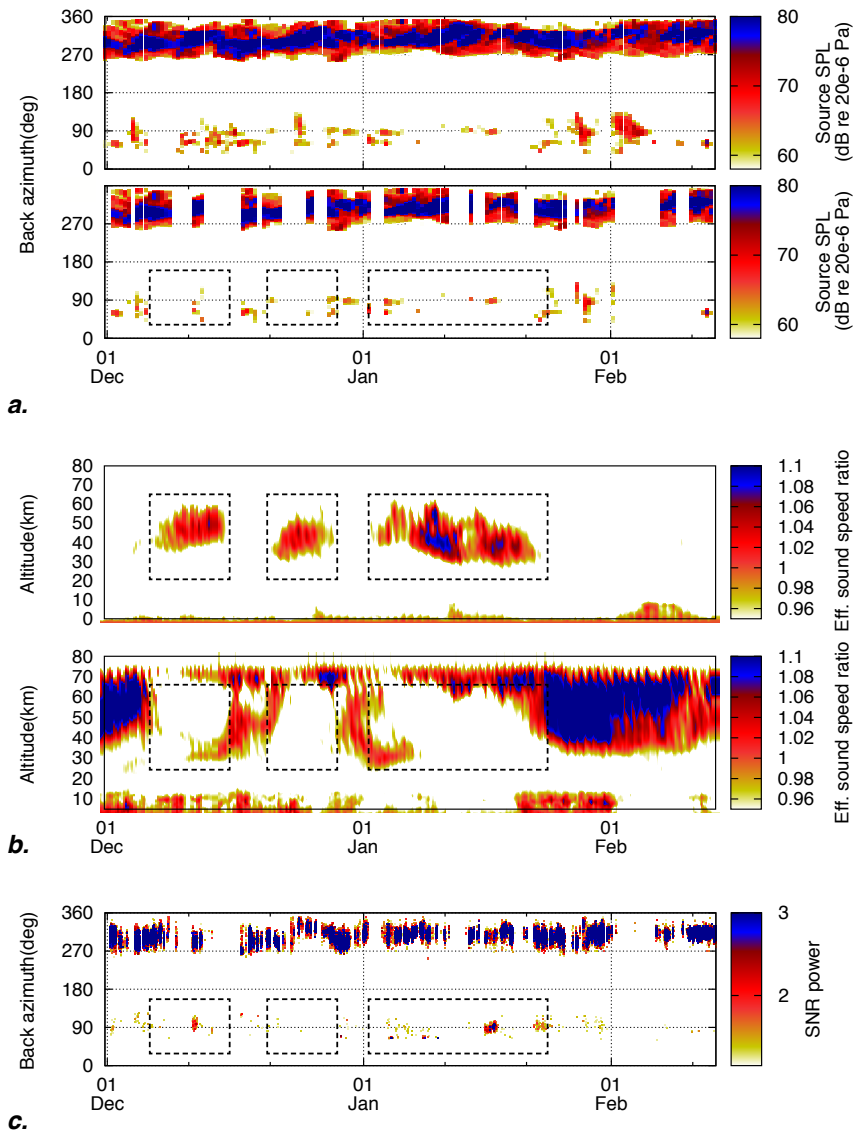


Figure 1.6: (a) Microbarom source activity in the Atlantic and Mediterranean Basins, modelled using ECMWF HRES-WAM wave spectra and the Waxler and Gilbert [2006] source model. The back azimuths with respect to IS48 (Tunisia) and the source intensity is given as a function of time. The top frame shows all sources, the bottom frame shows the source activity for when local winds are less than 1 m s^{-1} , leading to low wind noise conditions and increased infrasound detectability. (b) Effective sound speed ratio as a function of altitude and time for (top) westward and (bottom) eastward propagation. (c) Infrasound detections during the winter of 2010–2011. Intervals of bidirectional ducting conditions are indicated with dashed rectangles; the eastward duct nearly always exists. During favourable conditions, microbarom signals from two opposite directions are detected at IS48. Figure adapted from Assink et al. [2014a].

are observed in January 2011. A strong and persistent signal from the northwest, with frequencies around 0.2 Hz, is detected with a weaker signal from the east, in the 0.2–0.6 Hz band. The observed microbarom sources, induced by non-linear ocean surface wave interaction, are explained by source modelling [Waxler and Gilbert, 2006] based on two-dimensional ocean wave spectra from the ECMWF operational HRES-WAM (High RESolution WAVE Model) analysis. Source modelling, see Figure 1.5, reveals a previously unidentified microbarom source region in the eastern Mediterranean besides the more typical microbarom source region in the Atlantic Ocean. Figure 1.6a shows microbarom source activity in the northern Atlantic and eastern Mediterranean Basins in terms of back azimuth with respect to IS48 as a function of time. The detectability is mostly constrained by the local noise conditions due to wind, assuming efficient propagation conditions and a relatively nearby microbarom source. Low wind noise conditions are defined as local winds less than 1 m s^{-1} , similar to *Le Pichon et al.* [2005], shown in Figure 1.6a (bottom frame). Figure 1.6b shows the ducting conditions throughout the winter of 2010–2011 in direction of the northern Atlantic and Mediterranean in terms of effective sound speed ratio as a function of altitude. Several intervals of bidirectional ducting conditions exist throughout the winter of 2010–2011, indicated in Figure 1.6 by the dashed rectangles. The most significant interval occurs during January 2011. Note that the eastward duct would have disappeared if a major SSW had occurred. While a continuous, broadband energetic microbarom source is present in the northern Atlantic Basin, the eastern Mediterranean activity is more sporadic and weaker.

The observed directions (Figure 1.6c) correspond well with the predicted source locations for low wind noise conditions (Figure 1.6a, bottom frame). While the frequency bands of the two source directions overlap, the Mediterranean signal is coherent up to about 0.6 Hz. This observation is consistent with the predicted sources. Microbarom source predictions indicate various high-intensity sources regions are present in the Atlantic Ocean in the classic microbarom band 0.1–0.3 Hz. At higher frequencies, the deep ocean Atlantic source regions weaken and shallower source regions appear in the eastern Mediterranean Sea, in between Crete and Cyprus. As the Mediterranean signal is typically much weaker than the Atlantic signal, such events are predominantly detected when beam forming specifically toward the east to minimize the contribution of other sources.

Signals from both directions are detected when all criteria are fulfilled. During intervals of bidirectional ducting with low local noise conditions and when microbarom sources are sufficiently strong. Around 10 December and 17 January 2011 the most significant eastward detections occur, indicated by the first and third dashed rectangle in Figure 1.6, respectively. These detections correspond with the onset and offset of bidirectional ducting conditions throughout December 2010 to February 2011. Only very few detections from the east are made during the second anomalous period in December 2010, likely due to the presence of strong local winds that masked the microbarom sources in the eastern Mediterranean (see Figure 1.6a). Around 17 January, the signal intensity of both signals is about equal.

1.4 Statement of problems

The importance of improving the representation of the middle atmospheric conditions and the predictability of sudden stratospheric warmings in specific is stated in Subsection 1.1.4. To improve NWP in this region, additional upper atmospheric observations are required. Particularly observation of wind are important. Infrasound has shown its ability in probing the middle and upper atmosphere, being sensitive to both wind and temperature. Currently, infrasound is primarily applied as a monitoring technique using a global network of national and CTBT IMS infrasound arrays. Although the capabilities of infrasound to probe the middle atmosphere, a direct use in operational weather and climate modelling, e.g., assimilation, is not for the near future. Therefore, in what extent can infrasound now contribute to NWP to better resolve a SSW? How can infrasound progress from a monitoring technique towards a new application for NWP? So far, this has not been examined explicitly. An important side question is why is NWP not yet aware of or attracted by the potential of infrasound? Do both research fields speak a common language? Hence, it is important to step into the field of NWP when presenting new achievements from the specific area of infrasound research.

Knowledge on stratospheric (and middle atmospheric) variability is equally important for infrasound monitoring purposes, as discussed in Subsection 1.2.2. The state of the atmosphere is of utmost importance for infrasound propagation modelling. In infrasound propagation modelling, still, the true state of the atmosphere is usually represented by the analysis. The analysis is the best deterministic estimate of the atmosphere using a data assimilation system consisting of a General Circulation Model (GCM). Both the treaty verification as well as atmospheric probing, e.g., inversion studies, make significant use of infrasound propagation modelling that still relies on the best deterministic estimate of the atmosphere, the analysis. Usually, the analysis is used, but occasionally modelling is based on free running atmospheric models that are not constrained by assimilating atmospheric observations. However, two typical problems related to atmospheric conditions occur. First, stratospheric variability strongly influences infrasound propagation, during equinox periods and stratospheric warmings, for example. At these moments, the stratospheric predictability, in specific for the deterministic representation, can be poor [Assink *et al.*, 2014b; Smets and Evers, 2014]. Second, GCMs are smooth, designed to suppress unbalanced motion associated with, e.g., internal gravity waves, to allow longer model integration time steps [Shutts *et al.*, 2011]. Consequentially, GCM limitations influence the simulation of infrasound propagation, resulting in the lack of simulated arrivals due to fine-scale structure in wind and temperature [Chunchuzov *et al.*, 2005, 2011; Kulichkov *et al.*, 2008, 2010; Revelle, 2010]. A current trend in improving infrasound propagation modelling is adding fine-scale structure and unresolved gravity waves to one-dimensional vertical profiles of horizontal wind [e.g. Drob *et al.*, 2013]. However, these modifications do not obey the physical laws acting in the atmosphere, for example, the thermal wind relation. How can infrasound modelling be improved to include more stratospheric variability without adding random fluctuations?

1.5 Research objectives

Based on the statement of problems, the following objectives have been identified:

- To use passive ambient infrasound signals as an atmospheric probe. To extract relevant parameters from continuous waveforms by signal detectors and array processing techniques.
- To develop a technique to use infrasound in current atmospheric models. To demonstrate how infrasound data, both observations and simulations, can be of use for operational weather and climate modelling in the stratosphere.
- To apply knowledge of stratospheric variability to problems of infrasonic detection and propagation modelling. To utilise knowledge of the dynamical stratosphere when undertaking infrasound analysis, in order to benefit CTBT verification efforts.

1.6 Outline of the thesis

This thesis describes the synergy of infrasound and the dynamical stratosphere, focussing on a stratospheric warmings.

Chapter 2 explains the fundamental theory used throughout this thesis. Section 2.1 explains the detection of coherent signals by array processing of infrasound data. This includes the use of beamforming and the Fisher coherence analysis to extract relevant information from the continuous waveform recordings. Section 2.2 describes propagation modelling of infrasound in a dynamical atmosphere. Infrasound propagation is approximated by ray theory, including transmission loss by geometrical spreading. A brief overview of the implementation in spherical coordinates and an example are given. Section 2.3 describes the dominant ambient infrasound source: microbaroms. This section explains both the source mechanism, non-linear interacting ocean surface waves, and how these signals are predicted using oceanic wave models. For each of the three sections, packages are coded in modern Fortran providing various processing and plotting routines.

The use of passive ambient noise as an atmospheric probe is discussed in detail in Chapter 3. In this chapter, a method is presented to study the life cycle of a SSW using infrasonic ambient noise observations only. The potential of infrasound is shown to provide the missing observations required by numerical weather prediction to better resolve the upper atmosphere. Microbarom observations are evaluated to identify detections that cannot be explained by the analysis of the ECMWF.

In Chapter 4, for the first time middle atmospheric numerical weather forecasts are evaluated using infrasound. A year of near continuous infrasound from the volcano Mount Tolbachik (Kamchatka, Russian Federation) is compared with simulations using high resolution deterministic ECMWF forecasts.

The use of knowledge on stratospheric variability for advanced infrasound propagation is applied in Chapter 5. In this chapter, two applications are given. Firstly, Chapter 5 demonstrates probabilistic infrasound propagation modelling using realistic atmospheric perturbations. One year of large mining explosions in the Aitik

mine, northern Sweden, observed at infrasound array IS37 in northern Norway are simulated using three-dimensional ray tracing. Probabilistic propagation modelling using the ensembles demonstrates that small-scale fluctuations are not always necessary to improve the match between predictions and observations. Secondly, Chapter 5 explains the observed atmospheric infrasound generated by the 2013 and 2016 underground nuclear tests conducted by the Democratic People's Republic of Korea (DPRK). Data analysis and propagation modelling shows that the noise level at the stations and the stratospheric circumpolar vortex were different in 2016 compared to 2013. Incorporating knowledge of these significant differences is vital when attempting to deduce information about a source from infrasound signals, and is therefore of great value for CTBT verification.

Chapter 6 concludes with summarizing the major findings described in this thesis. Furthermore, possible topics of further research and new applications of infrasound on the path towards data assimilation are given in an outlook.

2

Processing and modelling of infrasound

This chapter describes the processing and modelling of infrasound. Section 2.1 describes the detection of coherent infrasound signals using beamforming and the Fisher coherence analysis. Next, propagation modelling of infrasound through the atmosphere is explained. Section 2.2 starts with how to obtain the acoustic wave equation in a dynamic medium followed by the derivation of the approximating ray and amplitude equations. Finally, Section 2.3 describes the dominant ambient infrasound source, microbaroms, by explaining the source mechanism and how it can be modelled. For each of the three sections, packages are coded in modern Fortran¹ providing various processing and plotting routines.

2.1 Infrasound array measurements

Infrasound is recorded using surface based arrays of microbarometers consisting of three or more instruments. The infrasound sensors have a typical flat frequency response in the pass band between 0.08 and 4 Hz and are sensitive to amplitudes of several mPa up to tens of pascals. The use of microbarometer arrays has two main advantages.

Firstly, arrays are able to resolve the wave vector of a propagating coherent signal by beamforming. Beamforming is a signal summation process of delayed traces yielding an average array signal or the beam. Signal delaying alters the array interference pattern. Shifting the traces in a way that the coherent signal amplitudes of the array beam are maximum gives the event's slowness or back azimuth and apparent velocity, which describe the wave vector.

Secondly, signal summation over the various array elements increases the signal gain by suppressing uncorrelated noise. The infrasonic noise field is dominated

¹Packages are available at <http://www.pietersmets.eu>

by frequent, large, uncorrelated bursts of wind. The correlation length of wind is much smaller than that of the infrasonic waves. For an array of N elements, signal summation ideally leads to an increased signal-to-noise-ratio (SNR) by \sqrt{N} (see Appendix A.1). In addition to signal summation, wind noise filters are used to reduce the noise levels over the infrasonic frequency band at each sensor. Wind noise filters, for example, porous hoses or solid pipe arrays, are used to spatially average the local pressure field in the vicinity of the infrasound sensor.

Coherent signal within a finite time window is detected and characterized by the combination of plane wave beamforming and the Fisher detector. A predefined set of wave vectors is analysed for each time window since multiple coherent signals can occur. Therefore, the quality of each beam is evaluated by correlation analysis in terms of the Fisher (F-) ratio. The maximum Fisher ratio yields the array best-beam and corresponding wave vector.

■ 2.1.1 Plane wave beamforming

Consider a three-dimensional planar wavefield τ with position $\mathbf{x} = (x, y, z)$ at time t and an arbitrary array of N receivers on the horizontal xy -plane Γ , i.e., the Earth's surface, with receiver positions $\mathbf{r} = (x, y)$. The array has a zero mean centred around $(0, 0)$. An illustration is given in Figure 2.1. The propagating wavefield is discretely sampled by this limited aperture array.

Let the infinite plane wave of frequency f_0 be defined by,

$$a(\mathbf{x}, t) = Ae^{-i(\mathbf{k}_0 \cdot \mathbf{x} - \omega_0 t)}, \quad (2.1.1)$$

with wave vector \mathbf{k}_0 , angular frequency $\omega_0 = 2\pi f_0$, and complex amplitude $A = A_0 e^{-i\varphi}$ as a function of wave amplitude A_0 and phase φ .

Propagation of the wave is described by wave vector \mathbf{k}_0 , normal to the wavefront, and is related to the wave slowness vector \mathbf{p}_0 by,

$$\mathbf{p} = \omega^{-1} \mathbf{k}. \quad (2.1.2)$$

For a monochromatic plane wave with unitary amplitude, equation (2.1.1) reduces to,

$$g(\mathbf{x}, t) = e^{-i(\mathbf{k}_0 \cdot \mathbf{x} - \omega_0 t)}. \quad (2.1.3)$$

The frequency transform of the monochromatic plane wave in equation (2.1.3) is defined as

$$G(\mathbf{x}, f) = \int_{-\infty}^{\infty} g(\mathbf{x}, t) e^{-i2\pi f_0 t} dt, \quad (2.1.4)$$

and yields,

$$G(\mathbf{x}, f) = \delta(f - f_0) e^{-i\mathbf{k}_0 \cdot \mathbf{x}}. \quad (2.1.5)$$

The wavefront is characterized by wavelength λ and propagation velocity c , related

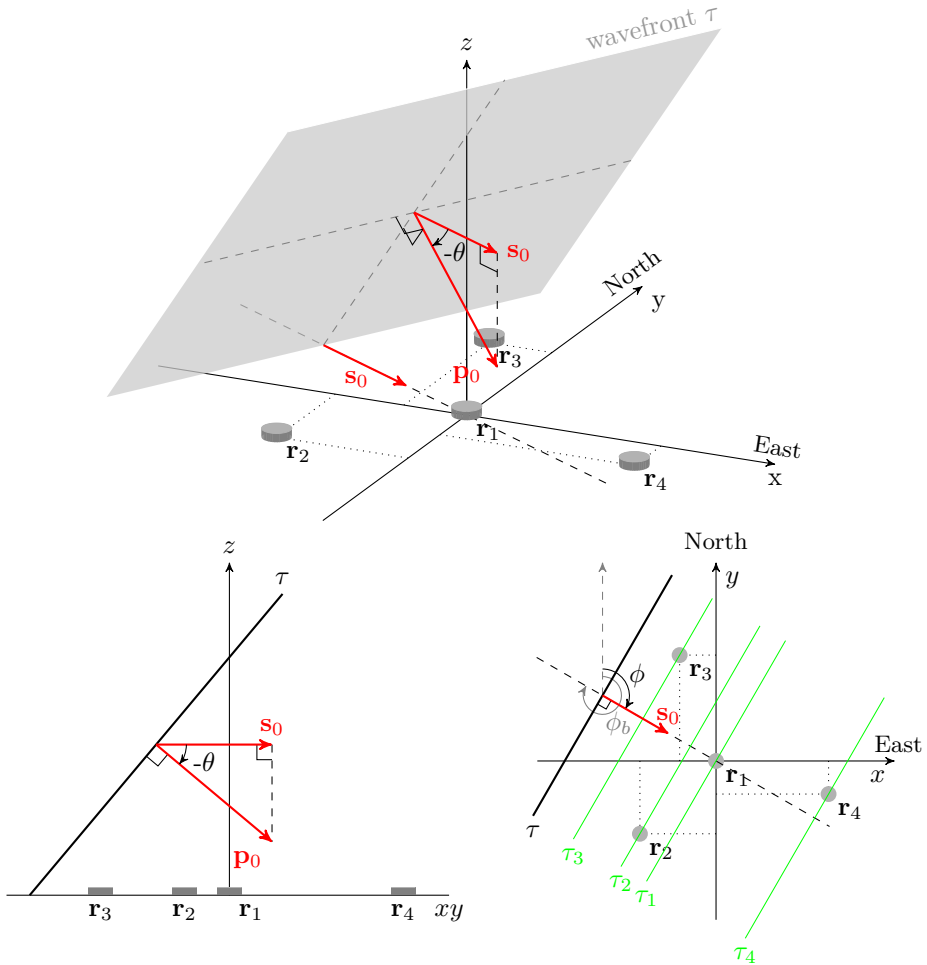


Figure 2.1: An inclined three-dimensional planar wavefront τ traveling over an array of four microbarometers located in the xy -plane Γ , i.e., the earth's surface. The wave propagates with slowness \mathbf{p}_0 normal to the wavefront and is characterized by magnitude c^{-1} , grazing angle θ with respect to the local horizon, and azimuth ϕ clockwise from north. Note the minus sign for grazing angle θ , since upward is positive. c is the true propagation velocity of the wave. The wavefront in the receiver plane Γ propagates with slowness \mathbf{s}_0 yielding the apparent velocity $c_{\text{app}} \geq c$ with direction of propagation azimuth ϕ . The origin of propagation is indicated by back azimuth $\phi_b = \phi \pm \frac{\pi}{2}$. Green lines in the top-view indicate the wavefront at receiver locations \mathbf{r}_n corresponding with delay times τ_n .

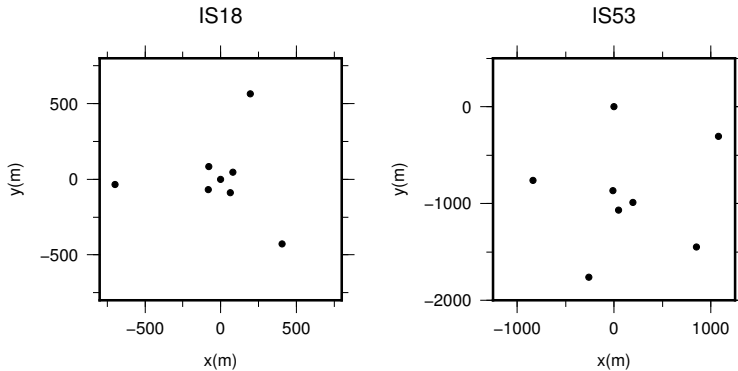


Figure 2.2: Array layout of two 8-element IMS Infrasound arrays (left) IS18 in Qaanaaq, Greenland, and (right) IS53 in Fairbanks, Alaska.

to the magnitude of \mathbf{k} and \mathbf{p} by,

$$\lambda = \frac{2\pi}{\|\mathbf{k}\|} = \frac{f^{-1}}{\|\mathbf{p}\|}, \quad (2.1.6)$$

$$c = \frac{\omega}{\|\mathbf{k}\|} = \frac{1}{\|\mathbf{p}\|}, \quad (2.1.7)$$

with

$$c = \lambda f. \quad (2.1.8)$$

The local orientation of the three-dimensional wave or slowness vector is defined by grazing angle θ with respect to the local horizon and azimuth angle ϕ clockwise from north. The slowness vector \mathbf{p} as a function of direction and magnitude denotes,

$$\mathbf{p} := \begin{pmatrix} p_x \\ p_y \\ p_z \end{pmatrix} = c^{-1} \begin{pmatrix} \cos \theta \cos \phi \\ \cos \theta \sin \phi \\ \sin \theta \end{pmatrix}, \quad (2.1.9)$$

or in terms of back azimuth $\phi_b = \phi \pm \frac{\pi}{2}$ to point towards the event origin. The projected slowness vector \mathbf{p} onto the receiver plane Γ is given by $\mathbf{p}^\Gamma = \mathbf{s}$

$$\mathbf{s} := \begin{pmatrix} s_x \\ s_y \end{pmatrix} = c_{\text{app}}^{-1} \begin{pmatrix} \cos \phi \\ \sin \phi \end{pmatrix}. \quad (2.1.10)$$

The magnitude of the horizontal slowness \mathbf{s} yields the apparent velocity c_{app} which is related to the true propagation velocity of the wave c by,

$$c_{\text{app}} = \frac{c}{\cos \theta}. \quad (2.1.11)$$

ranging from c up to infinity depending on the incidence angle θ .

The time difference $\tau = t_2 - t_1$ of the plane wave over the distance $d = \|\mathbf{x}_2 - \mathbf{x}_1\|$ can be written as

$$\begin{aligned}\tau &= \mathbf{p}_0 \cdot (\mathbf{x}_2 - \mathbf{x}_1), \\ &= \mathbf{s}_0 \cdot (\mathbf{x}_2^\Gamma - \mathbf{x}_1^\Gamma).\end{aligned}\quad (2.1.12)$$

From equation (2.1.12) follows the time difference or delay time from the plane wave to a receiver,

$$\tau_n = \mathbf{s}_0 \cdot (\mathbf{r}_n - \mathbf{x}^\Gamma), \quad (2.1.13)$$

which simplifies to,

$$\tau_n = \mathbf{s}_0 \cdot \mathbf{r}_n, \quad (2.1.14)$$

for a plane wave at the zero mean array centre \mathbf{x}_0 . As such, delay time τ_1 in Figure 2.1 will be equal to zero.

If the actual wave is not planar, for example, in the near field of a source, this can result in significant errors in receiver delay estimates. The curved wavefront will be approximated by a plane wave, over estimating the delay times. The corresponding slowness will have a similar direction, since the normal vector of both planes has a similar direction, yielding an adequate azimuth. However, the apparent velocity of the corresponding slowness will be too low.

The wavefield can be characterized as a function of frequency and wavenumber in terms of a spectral density. The analytical f - \mathbf{k} power spectral density function for the two-dimensional array in Γ is defined by [e.g. *Denholm-Price and Rees, 1999*],

$$E(\mathbf{k}^\Gamma, f) = \int_{\Gamma} G(\mathbf{r}, f) e^{i\mathbf{k}_0^\Gamma \cdot \mathbf{r}} d\mathbf{r}, \quad (2.1.15)$$

with $G(\mathbf{r}, f)$ the frequency transform of the plane wave of equation (2.1.5) at the surface Γ . Equation (2.1.15) yields,

$$E(\mathbf{k}^\Gamma, f) = \delta(\mathbf{k}^\Gamma - \mathbf{k}_0^\Gamma) \delta(f - f_0). \quad (2.1.16)$$

The power spectral density $E(\mathbf{k}^\Gamma, f)$ is maximum for frequency f_0 with wave vector \mathbf{k}_0^Γ , the plane wave. The latter forms the fundamental lemma of beamforming the array towards the wavefront.

The discrete frequency-wavenumber f - \mathbf{k} spectra follows from the cross-spectra between the individual sensors [*Smart and Flinn, 1971; Evers, 2008*],

$$E(\mathbf{k}^\Gamma, \omega) = \left| \sum_{n=1}^N G(\mathbf{r}_n, \omega) e^{-i\mathbf{k}_0^\Gamma \cdot \mathbf{r}_n} \right|^2. \quad (2.1.17)$$

Substituting the resulting frequency transform of the plane wave of equation (2.1.5) at the surface Γ the wavefield is discretely sampled by N sensors, which leads to spatial aliasing, and yields the array response R ,

$$R(\mathbf{s}, \omega) = \left| \frac{1}{N} \sum_{n=1}^N e^{-i\omega(\mathbf{s} - \mathbf{s}_0) \cdot \mathbf{r}_n} \right|^2. \quad (2.1.18)$$

R is a theoretical measure for the best estimate or sensitivity of receivers \mathbf{r}_n to plane wave \mathbf{s}_0 with frequency f_0 represented by an infinite aperture array regularly sampled in \mathbf{s} .

The array can be focussed or steered towards an arbitrary \mathbf{s} for a certain f or band of frequencies. However, the ability to resolve the plane wave depends on the number of array elements, its geometry and the sample rate Δ . Equation (2.1.18) states an inverse relation between array aperture and beamwidth, the larger the aperture the narrower the beam. This is theoretically true, however, in practise the wave coherency is limited and determines the aperture (and is a function of frequency). An infinite number of sensors is preferable to avoid spatial aliasing, the aperture however is limited by signal coherency along and perpendicular to the wavefront [Mack and Flinn, 1971; Fricke *et al.*, 2014]. For high frequencies, aliasing within the slowness domain becomes an issue. A possible solution to suppress side lobes, without altering the array geometry, is broadband processing. This is achieved by time domain processing, or in the frequency domain by averaging multiple frequency bands. The array layout for two eight element infrasound arrays of the IMS, IS18 and IS53, with an aperture of 1170 and 1980 m, respectively, is given in Figure 2.2. Note the opposite array design. Figures 2.3 and 2.4 show the array response. The smaller aperture of IS18, with the pentagram core and triangular outer array, is more beneficial for high frequencies. The larger aperture of IS53, with a triplet core and pentagram outer shape, yields a better sensitivity for low frequencies.

The illustrated azimuth–velocity representation does not cover the entire slowness domain. Near vertical plane waves, yielding an infinite apparent velocity, are not resolved. However, if only far field low elevation (often ground based) sources are of interest, processing in the azimuth–velocity domain is more efficient. Less beams are required compared to the regular slowness grid to obtain a similar resolution.

Note that non-planar infrasound arrays exist, and processing them assuming flat arrays ($z = 0$) can generate small biases in both backazimuth and apparent velocity estimation [Edwards and Green, 2012]. Beamforming with interarray elevation differences can cause errors that are a function of the arrival azimuth and become increasingly large for steeply inclined arrivals.

■ 2.1.2 Fisher detector

Correlation analysis is either realized in the time domain [e.g. Melton and Bailey, 1957; Jacobson, 1957; Olson, 2004; Evers, 2008] or frequency domain [e.g. Smart and Flinn, 1971; Shumway, 1971; McKisic, 1996; Evers, 2008]; this section describes both approaches.

Time domain

Let $y_n(\mathbf{r}_n, t)$ be the recording of array element n at time t . Beamforming is applied by time shifting the recordings according to τ_n in equation (2.1.14) for an arbitrary slowness \mathbf{s} . The time shifted recordings are denoted by $y_n(t + \tau_n)$ for a certain recording at r_n .

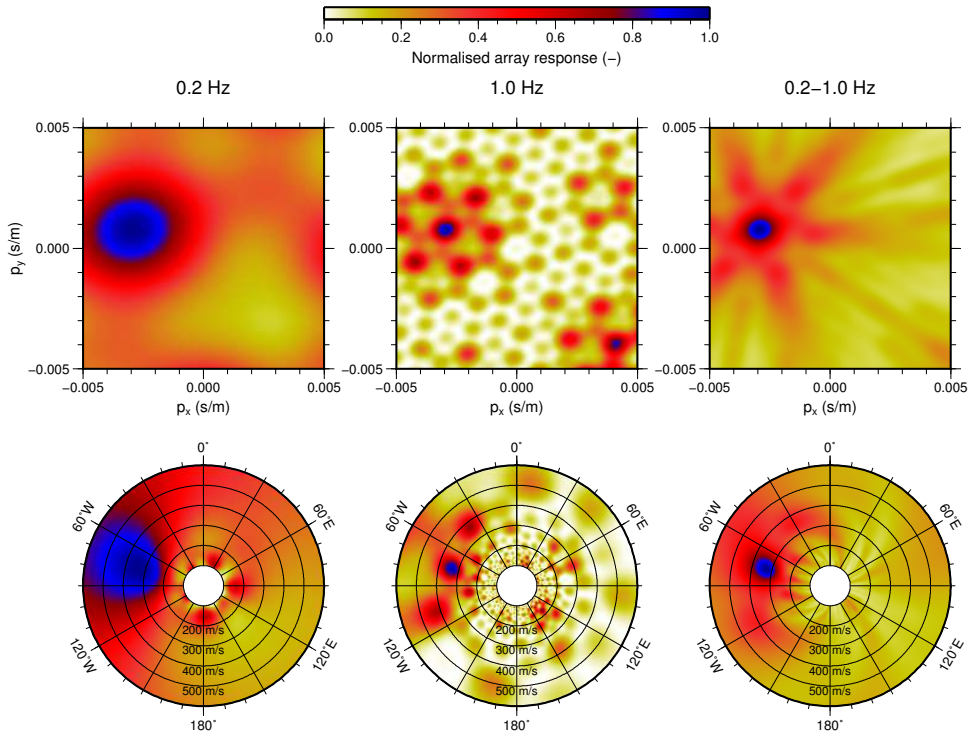


Figure 2.3: Array response for IS18, an 8 element infrasound array of the CTBT IMS, for a propagating plane wave with 285° back azimuth and 330 m s^{-1} apparent velocity. Three different frequencies (columns) are given, represented in both (top) slowness and (bottom) azimuth-velocity domain. Note that regular sampling in slowness yields exponential sampling for azimuth-velocity and vice versa. First two columns from left show the response for the plane wave with a frequency of 0.2 Hz and 1.0 Hz. Last column corresponds to an integrated response for a broadband signal ranging from 0.2 to 1.0 Hz with 0.05 Hz increments. The array layout of IS18 is given in Figure 2.2 (left).

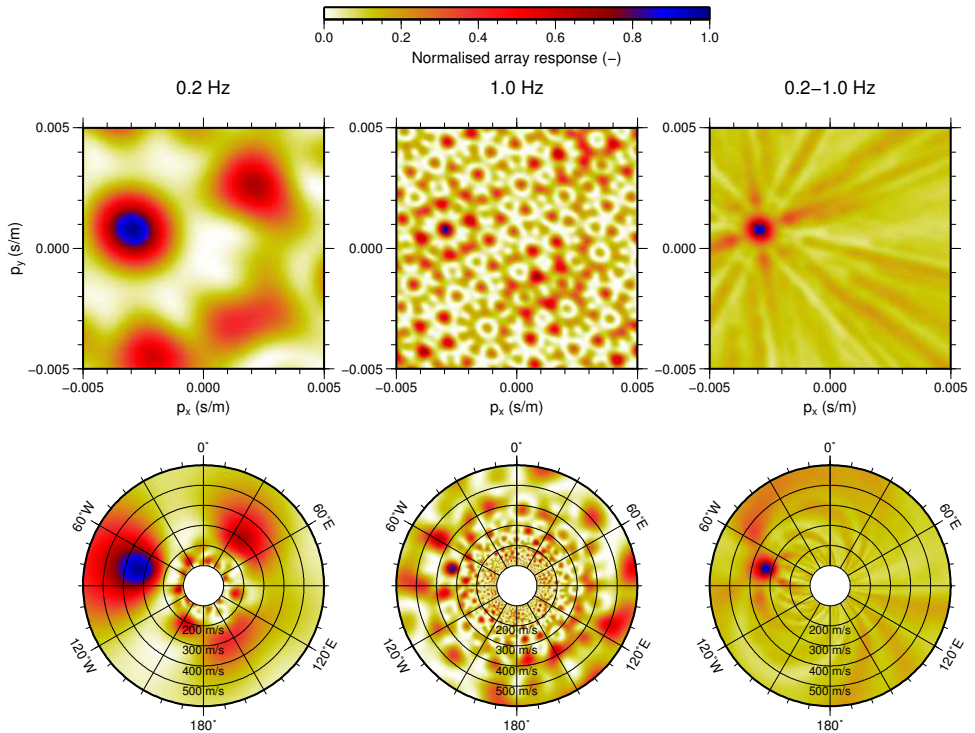


Figure 2.4: Array response for IS53, an 8 element infrasound array of the CTBT IMS, for a propagating plane wave with 285° back azimuth and 330 m s^{-1} apparent velocity. Three different frequencies (columns) are given, represented in both (top) slowness and (bottom) azimuth-velocity domain. Note that regular sampling in slowness yields exponential sampling for azimuth-velocity and vice versa. First two columns from left show the response for the plane wave with a frequency of 0.2 Hz and 1.0 Hz. Last column corresponds to an integrated response for a broadband signal ranging from 0.2 to 1.0 Hz with 0.05 Hz increments. The array layout of IS53 is given in Figure 2.2 (right).

The array beam or average array output is defined as

$$\mu_t = \frac{1}{N} \sum_{n=1}^N y_n(t + \tau_n), \quad (2.1.19)$$

and the total average,

$$\mu = \frac{1}{NT} \sum_{t=1}^T \sum_{n=1}^N y_n(t + \tau_n). \quad (2.1.20)$$

A measure for the coherence of time-aligned recordings y during a period of length T in the presence of uncorrelated noise is the Fisher ratio as defined by *Melton and Bailey* [1957]. The Fisher detector is based on the analysis of variances of both signal s and noise ϵ . The total variation in the recordings during the period T is defined as

$$\sigma^2 = \sum_{t=1}^T \sum_{n=1}^N (y_n(t + \tau_n) - \mu)^2. \quad (2.1.21)$$

Equation (2.1.21) can be written as

$$\sigma^2 = \sigma_s^2 + \sigma_\epsilon^2, \quad (2.1.22)$$

with the variation between recordings σ_s^2 representing the amount of coherent signal,

$$\sigma_s^2 = N \sum_{t=1}^T (\mu_t - \mu)^2, \quad (2.1.23)$$

and the variation within a recording σ_ϵ^2 as a measure for the amount of noise

$$\sigma_\epsilon^2 = \sum_{t=1}^T \sum_{n=1}^N (y_n(t + \tau_n) - \mu_t)^2. \quad (2.1.24)$$

The Fisher ratio F is a measure of the signal-to-noise ratio (SNR). For an unbiased true-positive signal estimate of σ_s^2 using equations (2.1.24) and (2.1.23) it holds that

$$F(\mathbf{s}) = \frac{\sigma_s^2 T (N - 1)}{\sigma_\epsilon^2 T - 1}, \quad (2.1.25)$$

with the presence of signal defined as an expected value $\langle F \rangle > 1$ and

$$F = N \cdot \text{SNR}^2 + 1. \quad (2.1.26)$$

The maximum Fisher ratio value F_{\max} for a given grid of slownesses yields the detection best slowness estimate $\mathbf{s}_{F_{\max}}$. The slowness $\mathbf{s}_{F_{\max}}$ is not necessarily the true slowness \mathbf{s}_0 due to the chosen slowness grid and the presence of noise. The array's best-beam or best average array output is obtained from equation (2.1.19) by time shifting the recordings with time delays consistent with $\mathbf{s}_{F_{\max}}$.

Frequency domain

The Fisher ratio in the frequency domain is based on the f - \mathbf{k} spectra [Smart and Flinn, 1971] in equation (2.1.17) in terms of the horizontal slowness \mathbf{s} for a plane wave at the zero mean array centre \mathbf{x}_0 .

Let $Y_n(\mathbf{r}_n, \omega)$ be the Fourier transform of the recording $y_n(\mathbf{r}_n, t)$ of array element n at time t for a time window of duration T convolved with a window function to suppress spectral leakage. The amount of phase aligned signal in the recorded window after beamforming equals

$$E(\mathbf{s}, \omega) = \left| \frac{1}{N} \sum_{n=1}^N Y_n(\mathbf{r}_n, \omega) e^{-i\omega \mathbf{s} \cdot \mathbf{r}_n} \right|^2, \quad (2.1.27)$$

by applying a phase shift $\omega \mathbf{s} \cdot \mathbf{r}_n$ to the individual recordings. The total amount of energy in the window holds,

$$E(\omega) = \frac{1}{N} \sum_{n=1}^N |Y_n(\mathbf{r}_n, \omega)|^2. \quad (2.1.28)$$

Since the Fisher ratio is a measure for the signal-to-noise power ratio, the Fisher ratio for a single frequency yields [Shumway, 1971]

$$F(\mathbf{s}, \omega) = (N - 1) \frac{E(\mathbf{s}, \omega)}{E(\omega) - E(\mathbf{s}, \omega)}. \quad (2.1.29)$$

The Fisher ratio in the time domain for a time window of duration T corresponds to a broad range of frequencies ω . Pre-processing in the time domain with, for example, a bandpass filter can be approximated by selecting a frequency band (from cutoff frequencies ω_1 to ω_2) in the frequency domain. As such, the Fisher ratio in the frequency domain for the frequency band from ω_1 to ω_2 is obtained by integrating $E(\mathbf{s}, \omega)$ and $E(\omega)$ before calculating the power ratio,

$$F(\mathbf{s}, \omega) \Big|_{\omega_1}^{\omega_2} = (N - 1) \frac{\sum_{\omega_1}^{\omega_2} E(\mathbf{s}, \omega)}{\sum_{\omega_1}^{\omega_2} E(\omega) - \sum_{\omega_1}^{\omega_2} E(\mathbf{s}, \omega)}. \quad (2.1.30)$$

Note that the Fourier coefficients Y_n in Equation(2.1.30) should be multiplied with a filter $h(\omega)$ to obtain a gradual frequency response between cutoff frequencies ω_1 to ω_2 .

2.2 Infrasound propagation in a dynamic medium by ray theory

Sound is a pressure disturbance propagating through a medium, for example, air. Sound waves are elastic waves that, after disturbing a medium, allow the medium to relax to its undisturbed state after passing through. Such waves, also named compressional waves, are defined by a particle oscillation parallel to the direction of propagation. Propagation through the medium is affected by the medium itself, which may result in changes in the wave vector direction (e.g. reflection, refraction) and attenuation of the signal.

Sound propagation through the atmosphere is mathematically described by the wave equation given atmospheric conditions describing the state of the atmosphere. A numerical approximation of the wave equation can be obtained by a variety of acoustic propagation models. In general, five types of acoustic modelling techniques can be distinguished [Jensen *et al.*, 2011]. First of all, direct finite-difference or finite-element solutions of the full wave equation [e.g. de Groot-Hedlin *et al.*, 2011; de Groot-Hedlin, 2016]. Next are full wave approximations in terms of spectral, normal mode, or parabolic equation models [e.g. Lingeitch *et al.*, 2002; Assink *et al.*, 2014b, 2017]. And finally ray theory, the infinite-frequency or geometrical approximation of the wave equation [e.g. Lalande *et al.*, 2012; Blom and Waxler, 2012; Lonzaga *et al.*, 2015].

Ray theory does not describe full wave theory phenomena such as interference and diffraction from small-scale structure, e.g., from gravity waves [Chunchuzov *et al.*, 2015]. However, ray theory is exact when atmospheric variations are small over an acoustic wavelength [Brekhovskikh and Godin, 1999]. Full waveform techniques do require significant computational effort for acoustic propagation modelling in a moving non-homogeneous medium such as the atmosphere. Therefore, additional approximations are applied to the wave equation and atmosphere in order to obtain a numerical solution. Typically, full waveform computations are limited to in-plane effects using a two-dimensional range-dependent cross section of the atmosphere [e.g. Assink *et al.*, 2014a]. Other common simplifications of the atmosphere include projecting the horizontal wind in the direction of propagation, hence assuming a static atmosphere, or even assuming a laterally constant atmosphere. As such, horizontal movement such as drifting of the sound is constrained, which can be an issue for long-range infrasound propagation. Vertical motions in the atmosphere are often neglected. This is valid, since vertical motions in the atmosphere are far less than the horizontal ones (about 1/10 or more), except for synoptic weather phenomena. Large low-pressure areas, e.g. extratropical cyclones, can generate severe downdrafts near their frontal zone which can induce vertical motions larger than horizontal movements. In order to capture the effects of the atmospheric variability with minimal computational cost infrasound propagation is described by linear ray theory.

■ 2.2.1 Adiabatic, absolute, and effective speed of sound

In a non-dispersive medium the speed of sound is independent of the frequency of the sound wave. Energy transport and sound propagation are the same for all

frequencies. For a dispersive medium the speed of sound becomes a function of frequency. In such a medium, each frequency component propagates at its own speed, called the phase velocity, whereas the total energy propagates at the group velocity. In general, the atmosphere is non-dispersive. However, wave guides, like low velocity layers, in the atmosphere are dispersive.

Adiabatic speed of sound

Propagation of an acoustic wave through the atmosphere can be defined as a thermodynamic process that is both adiabatic and reversible. There is no transfer of heat or matter and work transfers are frictionless.

Consider an infinitesimal parcel $V(\mathbf{x}, t)$ of an ideal gas of uniform composition at position $\mathbf{x}(x, y, z)$ and time t with intrinsic properties density (ρ), absolute pressure (P), and absolute temperature (T). The volume of the infinitesimal element is defined by the ideal gas law assuming a constant composition,

$$PV = NR^*T = mRT, \quad (2.2.1)$$

with $R^* = 8.314 \text{ J kg}^{-1} \text{ mol}^{-1}$ the ideal or universal gas constant, R the specific gas constant, N the amount of moles and molar mass M such that mass $m = NM$ and $R = R^*/M$.

Substituting $m = \rho V$ into equation (2.2.1) yields the ideal gas law independent of the quantity of considered gas

$$P = \rho RT. \quad (2.2.2)$$

The molar mass of a moist air parcel in the Earth's atmosphere can be defined in components of dry air and water vapour,

$$M_{\text{air}} = \frac{P_d}{P} M_d + \frac{P_v}{P} M_v, \quad (2.2.3)$$

with indices d and v denoting dry air and water vapour, respectively. Dry air, mainly a mixture of nitrogen and oxygen, is assumed to be of constant composition throughout the atmosphere. From Dalton's law of partial pressures, the total pressure of the air parcel yields,

$$P = P_v + P_d. \quad (2.2.4)$$

In meteorology, pressure and density of a moist air parcel are commonly scaled to a dry air in the ideal gas law by virtual temperature (T_v),

$$T_v = T \frac{q + \epsilon}{\epsilon + (1 + q)}. \quad (2.2.5)$$

where q is specific humidity or the mixing ratio, defining the mass of water vapour per unit mass of air, and ϵ the ratio of specific heats for dry air and water vapour,

$$\epsilon = \frac{R_d}{R_v} \approx 0.622$$

with $R_d = 287.056 \text{ J kg}^{-1} \text{ K}^{-1}$ and $R_v = 461.495 \text{ J kg}^{-1} \text{ K}^{-1}$. The virtual temperature of an air parcel is the temperature that dry air would have if its pressure and density were equal to those of moist air. T_v is thus always higher than the dry air temperature. The difference between T_v and T is usually on the order of a few degrees Celsius for warm and moist conditions. At low humidity, differences between T_v and T are negligible.

The ideal gas law (2.2.2) of a moist air parcel in terms of virtual temperature becomes,

$$P = \rho R_d T_v. \quad (2.2.6)$$

The adiabatic speed of sound c_T at constant entropy S is often expressed by the equation of state,

$$c_T^2 = \left(\frac{\partial P}{\partial \rho} \right)_S, \quad (2.2.7)$$

obtained from the relativistic Euler equations.

Equation (2.2.7) relates the propagation speed to the medium's compressibility and density, which can be related to the isentropic bulk modulus or stiffness coefficient $\kappa > 0$. The bulk modulus yields the resistance against a uniform compression given an infinitesimal change in volume or density

$$\kappa = -V \frac{dP}{dV}, \quad (2.2.8a)$$

$$\kappa = \rho \frac{dP}{d\rho}. \quad (2.2.8b)$$

For an ideal gas the bulk modulus can be expressed as

$$\kappa = \gamma P, \quad (2.2.9)$$

with adiabatic index $\gamma = c_P/c_V$ defined by the ratio of the heat capacity at constant pressure c_P to the heat capacity at constant volume c_V .

The equation of state (2.2.7) can be expressed in terms of the isentropic bulk modulus κ by substituting equation (2.2.8b)

$$c_T^2 = \frac{\kappa}{\rho}, \quad (2.2.10)$$

formerly known as the Newton–Laplace equation. Substituting equations (2.2.6) and (2.2.9) into equation (2.2.10) yields the adiabatic speed of sound for an ideal gas

$$c_T = \sqrt{\gamma \frac{P}{\rho}} = \sqrt{\gamma R_d T_v}. \quad (2.2.11)$$

For moist air the ideal adiabatic speed of sound becomes

$$c_{T,\text{air}} \approx 20.04 \sqrt{T_v} \text{ m s}^{-1},$$

with $\gamma = 1.4$. Henceforth, c_T indicates $c_{T,\text{air}}$.

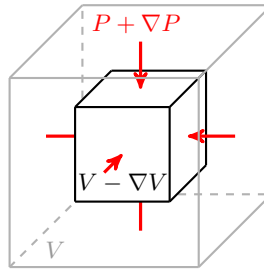


Figure 2.5: Uniform compression of the infinitesimal air parcel V .

Absolute speed of sound

In a moving medium such as the atmosphere, phase velocity c equals the sum of the intrinsic phase velocity and the flow velocity in direction of propagation, represented by the adiabatic speed of sound and the projected wind, respectively.

Since V depends on both position and time, the total (or convective) time derivative applying the chain rule is defined as

$$\frac{d}{dt} = D_t = \left(\frac{\partial}{\partial t} + \dot{\mathbf{x}} \cdot \nabla \right), \quad (2.2.12)$$

where $\dot{\mathbf{x}} = \partial \mathbf{x} / \partial t$ equals the flow velocity of the dynamic medium, hereinafter referred to as wind \mathbf{w} .

The phase velocity in a moving medium, the absolute speed of sound, yields

$$c = \|\mathbf{p}\|^{-1} = \mathbf{w} \cdot \hat{\mathbf{n}} + c_T, \quad (2.2.13)$$

with three-dimensional wind field $\mathbf{w} = \partial \mathbf{x} / \partial t$, the flow velocity of the dynamic medium, and slowness \mathbf{p} with unit vector $\hat{\mathbf{n}}$. Unit vector $\hat{\mathbf{n}}$ indicates the direction of propagation, characterized in three dimensions by elevation θ and azimuth ϕ . In Cartesian coordinates, unit vector $\hat{\mathbf{n}}$ denotes

$$\hat{\mathbf{n}} = \frac{\mathbf{p}}{\|\mathbf{p}\|} = \begin{pmatrix} \cos \theta \cos \phi \\ \cos \theta \sin \phi \\ \sin \theta \end{pmatrix}. \quad (2.2.14)$$

Effective speed of sound

In a horizontally layered atmosphere, the effective sound speed c_{eff} can be used to approximate the absolute speed of sound [Godin, 2002] to first order effects of temperature T and horizontal wind in the direction of propagation $\mathbf{w}_{\text{uv}} \cdot \hat{\mathbf{n}}_{xy}$,

$$c_{\text{eff}} = c_T + \mathbf{w}_{\text{uv}} \cdot \hat{\mathbf{n}}_{xy} = c_T + w_a. \quad (2.2.15)$$

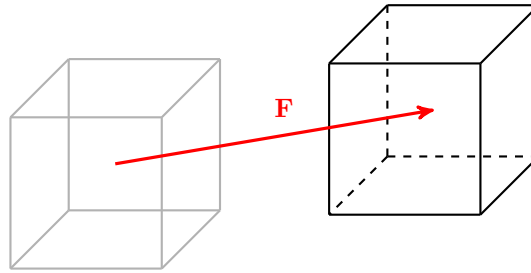


Figure 2.6: Lateral movement of the infinitesimal air parcel V by a net force \mathbf{F} due to an acoustic wavefront.

In equation (2.2.15) the vertical wind is neglected, which is valid in the absence of synoptic weather, since vertical motions are typically far less than horizontal ones.

The along-track wind w_a and cross-wind w_c are obtained by rotating the zonal w_u and meridional w_v components of the horizontal wind vector $\mathbf{w}_{\mathbf{uv}}$ with horizontal propagation direction azimuth,

$$\begin{pmatrix} w_a \\ w_c \end{pmatrix} = \begin{pmatrix} \sin \phi & \cos \phi \\ \cos \phi & -\sin \phi \end{pmatrix} \begin{pmatrix} w_u \\ w_v \end{pmatrix}. \quad (2.2.16)$$

Note that propagation azimuth ϕ is clockwise relative to the north.

■ 2.2.2 Acoustic wave equation in a dynamic medium

Sound propagation, by longitudinal waves, in the absence of dissipation can be described by two processes: compression (Hooke's law in terms of the bulk modulus, Figure 2.5) and lateral movement in the direction of propagation (Newton's law, Figure 2.6).

Uniform compression of the volume V in an isentropic flow is described by the equation of state (2.2.7). Substituting the isentropic bulk modulus equation (2.2.8b) into the equation of state (2.2.10) yields

$$d\rho = \frac{1}{\gamma} \frac{\rho}{P} dP, \quad (2.2.17)$$

The spatial pressure gradient induces a net force \mathbf{F} acting on the infinitesimal volume V (see Figure 2.6) resulting in a lateral movement; \mathbf{F} can be expressed as (see Appendix A.2),

$$-\nabla P = \frac{\mathbf{F}}{V}. \quad (A.2.1)$$

The minus sign of the gradient causes a positive net effect from a high to a low pressure system, moving V towards the minima in order to reach an equilibrium.

The equilibrium of forces acting on V is described by Newton's second law,

$$\mathbf{F} = m\mathbf{a} = m\frac{d\mathbf{v}}{dt}, \quad (2.2.18)$$

with acceleration $\mathbf{a}(\mathbf{x}, t)$, the time derivative of the ambient velocity $\mathbf{v}(\mathbf{x}, t)$. As the infinitesimal volume should be in equilibrium, substituting equation (2.2.18) and $m = \rho V$ yields

$$-\nabla P = \rho\frac{d\mathbf{v}}{dt}, \quad (2.2.19)$$

known as the continuity equation of motion (EOM).

The full system of non-linear fluid dynamics equations, for a compressible fluid of uniform composition and in the absence of dissipation, can be written as:

$$D_t\mathbf{v} + \rho^{-1}\nabla P = 0, \quad (2.2.20a)$$

$$D_t\rho + \rho\nabla \cdot \mathbf{v} = 0, \quad (2.2.20b)$$

$$D_t S = 0. \quad (2.2.20c)$$

conserving momentum, mass and energy. Note the gravitational acceleration constant $g = 9.81 \text{ m s}^{-1}$ is neglected in equation (2.2.20a), as this is not influencing the continuity of momentum. Furthermore, gravity is not a restoring force for acoustic waves, down to the acoustic cut-off frequency ($\sim 0.02 \text{ Hz}$); acoustic waves are solely restored by gradients in pressure.

Substituting (2.2.17) into the mass continuity equation (2.2.20b) gives

$$D_t P + \gamma P \nabla \cdot \mathbf{v} = 0, \quad (2.2.21)$$

The intrinsic variables of the air parcel can be written in terms of the mean or basic state (represented by overbars) and a perturbation (denoted by primes)

$$\begin{aligned} P(\mathbf{x}, t) &= \bar{P} + P'(\mathbf{x}, t) \\ \rho(\mathbf{x}, t) &= \bar{\rho} + \rho'(\mathbf{x}, t), \\ \mathbf{v}(\mathbf{x}, t) &= \bar{\mathbf{v}} + \mathbf{v}'(\mathbf{x}, t) \end{aligned} \quad (2.2.22)$$

where P' denotes the acoustic wavefield. P' is in the order of (milli)pascals, compared to hundreds of hectopascals for P . The average atmospheric pressure at sea level equals 1013.25 hPa. Substituting (2.2.22) into (2.2.20a) and (2.2.21) gives

$$\left(\frac{\partial}{\partial t} + (\bar{\mathbf{v}} + \mathbf{v}') \cdot \nabla\right)(\bar{\mathbf{v}} + \mathbf{v}') + \frac{1}{\bar{\rho} + \rho'}\nabla(\bar{P} + P') = 0, \quad (2.2.23a)$$

$$\left(\frac{\partial}{\partial t} + (\bar{\mathbf{v}} + \mathbf{v}') \cdot \nabla\right)(\bar{P} + P') + \gamma(\bar{P} + P')\nabla \cdot (\bar{\mathbf{v}} + \mathbf{v}') = 0. \quad (2.2.23b)$$

Provided $|\rho'/\bar{\rho}| \ll 1$, density term can be approximated using the binomial expansion as

$$\frac{1}{\bar{\rho} + \rho'} = \frac{1}{\bar{\rho}}\left(1 + \frac{\rho'}{\bar{\rho}}\right)^{-1} \approx \frac{1}{\bar{\rho}}\left(1 - \frac{\rho'}{\bar{\rho}}\right). \quad (2.2.24)$$

Substituting (2.2.24) into the perturbation equations (2.2.23a–b), neglecting products of perturbation quantities (which are small compared to other terms) and derivatives of constant fields, yields

$$\bar{D}_t \mathbf{v}' + \bar{\rho}^{-1} \nabla P' = 0, \quad (2.2.25a)$$

$$\bar{D}_t P' + \gamma \bar{P} \nabla \cdot \mathbf{v}' = 0, \quad (2.2.25b)$$

known as the *linear perturbation equations* of the fluid dynamics equations, with linear perturbed time derivative,

$$\bar{D}_t = \left(\partial_t + \mathbf{w} \cdot \nabla \right), \quad (2.2.26)$$

and three-component wind vector $\mathbf{w} = \bar{\mathbf{v}}$.

The linear equation of motion (2.2.25a) is simplified by the divergence, mapping the vector field to a scalar,

$$\bar{D}_t \nabla \cdot \mathbf{v}' + \bar{\rho}^{-1} \nabla^2 P' = 0. \quad (2.2.27)$$

Applying the perturbation time derivative \bar{D}_t to equation (2.2.25b) yields

$$\bar{D}_t^2 P' + \gamma \bar{P} \bar{D}_t \nabla \cdot \mathbf{v}' = 0. \quad (2.2.28)$$

Substituting (2.2.27) and (2.2.11) into (2.2.28) one obtains a form of the *acoustic wave equation*,

$$c_T^2 \bar{D}_t^2 P' - \nabla^2 P' = 0. \quad (2.2.29)$$

assuming a local steady homogeneous flow. Equation (2.2.29) is valid for an inhomogeneous nonstationary atmosphere under the condition that intrinsic variations in the atmosphere with a length scale L are negligible over the distance of an acoustic wavelength ($\lambda \ll L$) and at frequencies above the acoustic cut-off.

If the background flow is zero ($\mathbf{w} = 0$), the wave equation reduces to

$$c_T^2 \nabla^2 P' - \partial_t^2 P' = 0. \quad (2.2.30)$$

■ 2.2.3 Eikonal approximation of the wave equation

The wave equation, a second-order partial differential equation (PDE), provides the paradigm for hyperbolic equations that can be solved by the method of characteristics [Stone and Goldbart, 2009]. For such an equation with non-Cauchy data the initial state of the system is part of the auxiliary data for a well-posed problem.

The hyperbolic PDE of order $n + 1$ for position and time has a well-posed initial value problem for the first n tangential derivatives (in space) but is ill-posed to solve in direction of the normal (propagation in time). However, the Cauchy problem can be locally approximated for arbitrary initial data along any non-characteristic hypersurface. Therefore, to solve the hyperbolic PDE, the wave equation is reduced in complexity to a second-order time-independent ordinary differential equation (ODE) assuming Cauchy data. As such, time is parameterized by position, allowing the

advance the initial solution through space. The approximating ODE yields the characteristic surface or geometrical approximation of the wave equation.

Expand the wave equation (2.2.29),

$$(c_T^2 - \mathbf{w} \cdot \mathbf{w}) \nabla^2 P' - 2\mathbf{w} \cdot \nabla \partial_t P' - \partial_t^2 P' = 0. \quad (2.2.31)$$

The wave equation admits a harmonic solutions of the general form

$$P'(\mathbf{x}, t) = A(\mathbf{x}) \cos(\omega \Phi(\mathbf{x}, t) + \varphi), \quad (2.2.32)$$

existing of the smooth functionals A and Φ describing amplitude and phase as a function of \mathbf{x} and t . Phase functional Φ is described by

$$\Phi(\mathbf{x}, t) = \mathbf{p} \cdot \mathbf{x} - t = \tau(\mathbf{x}) - t. \quad (2.2.33)$$

The level curves of the phase functional Φ describes the propagating wave front $\tau(\mathbf{x})$ parameterising phase as a function of position \mathbf{x} by travel time $t \geq 0$. When the phase functional equals zero equation (2.2.33) yields,

$$\Phi = 0 \quad \therefore \quad \tau(\mathbf{x}) = t. \quad (2.2.34)$$

Consequentially, the general harmonic solution (2.2.32) describes a wave of constant phase or plane wave, which equals the characteristic of the wave equation. The gradient of (2.2.34) yields $\nabla \tau = \nabla t$, corresponding with the slowness of the wavefront.

Substituting the phase functional (2.2.33) into equation(2.2.32) in the absence of a phase shift ($\varphi = 0$) the harmonic solution becomes

$$P' = A \cos(\omega(\tau - t)), \quad (2.2.35)$$

or in the complex plane,

$$P' = \Re \left\{ A e^{-i\omega(\tau-t)} \right\}. \quad (2.2.36)$$

Note that the absence of a phase shift has implications for caustics (90 degrees phase shifts), when using the eikonal and corresponding ray equations to generate synthetic waveforms.

The gradient and the divergence of the harmonic solution (2.2.36) yield

$$\nabla P' = (\nabla A - i\omega A \nabla \tau) e^{-i\omega(\tau-t)}, \quad (2.2.37)$$

$$\nabla^2 P' = (\nabla^2 A - 2i\omega \nabla A \cdot \nabla \tau - i\omega A \nabla^2 \tau - \omega^2 A \nabla^2 \tau) e^{-i\omega(\tau-t)}. \quad (2.2.38)$$

The first and second derivative of (2.2.36) with respect to time are

$$\partial_t P' = i\omega A e^{-i\omega(\tau-t)}, \quad (2.2.39)$$

$$\partial_t^2 P' = -\omega^2 A e^{-i\omega(\tau-t)}. \quad (2.2.40)$$

The cross derivative becomes

$$\nabla \partial_t P' = (i\omega \nabla A + \omega^2 A \nabla \tau) e^{-i\omega(\tau-t)}. \quad (2.2.41)$$

Substituting the second order partial derivatives in the wave equation (2.2.31) with equations (2.2.38), (2.2.40) and (2.2.41) and removing the term $e^{-i\omega(\tau-t)}$ yields,

$$\begin{aligned} & (c_T^2 - \mathbf{w} \cdot \mathbf{w}) (\nabla^2 A - \omega^2 A \nabla^2 \tau) - 2\mathbf{w} \cdot \omega^2 A \nabla \tau + \omega^2 A \\ & + i[(c_T^2 - \mathbf{w} \cdot \mathbf{w}) (-2\omega \nabla A \cdot \nabla \tau - \omega A \nabla^2 \tau) - 2\mathbf{w} \cdot \omega \nabla A] \\ & = 0. \end{aligned} \quad (2.2.42)$$

The real part of equation (2.2.42) divided by $\omega^2 A$ gives,

$$\left(c_T^2 - \mathbf{w} \cdot \mathbf{w} \right) \left(\frac{1}{\omega^2 A} \nabla^2 A - \nabla^2 \tau \right) - 2\mathbf{w} \cdot \nabla \tau + 1 = 0. \quad (2.2.43)$$

which is still a function of both A and τ . Taking the infinite-frequency or plane wave approximation in the limit $\omega \rightarrow \infty$, which cancels the amplitude term, and reordering yields,

$$(1 - \mathbf{w} \cdot \mathbf{p})^2 - (c_T \mathbf{p})^2 = 0, \quad (2.2.44)$$

which is only valid when $\Phi \equiv 0$ so that the harmonic solution in equation (2.2.35), describing a plane wave, exists. Equation (2.2.44) is known as the eikonal equation, describing the kinematic or geometric propagation of a wavefront instead of the actual pressure disturbance. Similar to the wave equation, the eikonal equation (2.2.44) is only valid under the condition that variations in the atmosphere are negligible over the distance of an acoustic wavelength (i.e. $\lambda \ll L$).

■ 2.2.4 Asymptotic ray solution of the eikonal equation

The eikonal equation (2.2.44), an infinite-frequency plane wave approximation of the wave equation, is actually a geometric approach to the physical wave equation. It admits a local solution, however, due to non-linearity multiple solutions can exist. Caustics make a global smooth solution rather impossible. For that reason, an asymptotic solution is preferred. Wavefront propagation is described by geometric optics in terms of rays, e.g., *Arnold* [1989], tracing individual points on the wavefront in time.

The eikonal equation can be expressed in terms of the Hamilton-Jacobi equation, a non-linear partial differential equation, given by

$$\mathcal{H} + \frac{\partial \mathcal{S}}{\partial t} = 0, \quad (2.2.45)$$

with

$$\mathcal{H} \left(\mathbf{x}, \frac{\partial \mathcal{S}}{\partial \mathbf{x}}, t \right),$$

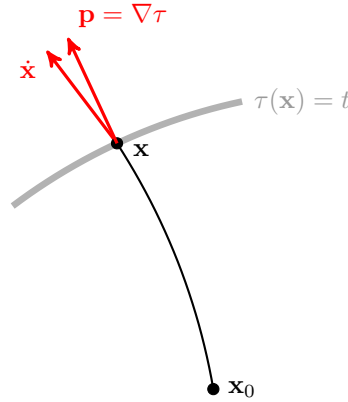


Figure 2.7: Huygens wave front and one of its corresponding ray paths. The wave front and ray path form mutually orthogonal families of curves. The gradient $\nabla\tau(\mathbf{x})$ is normal to the wave front τ and tangent to the ray through it at the point \mathbf{x} .

the Hamiltonian function which equals the total energy of the system $\mathcal{H} = E_{\text{kin}} + E_{\text{pot}}$, the sum of the kinetic and potential energy, and

$$\mathcal{S}(\mathbf{x}, t) = \int \mathcal{L}(\mathbf{x}, \dot{\mathbf{x}}, t) dt. \quad (2.2.46)$$

Hamilton's principal functional or action describing the time evolution of the dynamic system for position \mathbf{x} and time t , which is a function of the Lagrangian \mathcal{L} ,

$$\mathcal{L} = E_{\text{kin}} - E_{\text{pot}}. \quad (2.2.47)$$

Two fundamental notions of geometric optics are the extremal principle of Fermat or the principle of least time and Huygens' principle.

Let action \mathcal{S} be the optical path length from \mathbf{x}_0 to \mathbf{x} . Fermat's principle states that energy propagates from \mathbf{x}_0 to \mathbf{x} in the shortest possible time, which is not necessarily the shortest path. Therefore, the path \mathcal{S} is an extremum,

$$\delta\mathcal{S} = 0, \quad (2.2.48)$$

known in mechanics as Hamilton's stationary principle. In other words, Fermat's principle defines the wavefront $\tau(\mathbf{x})$ as the points \mathbf{x} to which a wave can propagate in time t and not faster.

Huygens' principle states the connection between propagating wavefronts in time. Huygens relates the gradient of the path function \mathcal{S} to the normal of the wavefront describing its direction. The gradient of \mathcal{S} yields,

$$\mathbf{p} = \frac{\partial\mathcal{S}}{\partial\mathbf{x}} = \nabla\tau, \quad (2.2.49)$$

known as the normal slowness vector of the wavefront by Hamilton or as the conjugate momenta in mechanics, which is related to position \mathbf{x} as

$$\mathbf{p} \cdot \dot{\mathbf{x}} = 1. \quad (2.2.50)$$

The time evolution of the system is uniquely defined by integrating Hamilton's canonical equations, relating the Hamiltonian to a set of first-order equations for position and momentum (see Appendix A.3).

$$\dot{\mathbf{x}} = \frac{\partial \mathcal{H}}{\partial \mathbf{p}} \quad \text{and} \quad \dot{\mathbf{p}} = -\frac{\partial \mathcal{H}}{\partial \mathbf{x}}, \quad (A.3.3)$$

with initial conditions for $t_0 = 0$,

$$\mathbf{x}(t_0) = \mathbf{x}_0 \quad \text{and} \quad \mathbf{p}(t_0) = \mathbf{p}_0 = \left. \frac{\partial \mathcal{S}_0}{\partial \mathbf{x}} \right|_{\mathbf{x}_0}. \quad (2.2.51)$$

For the eikonal equation (2.2.44) the Hamilton-Jacobi equation (2.2.45) reduces to,

$$\mathcal{H}(\mathbf{x}, \mathbf{p}) = -\frac{1}{2} \left((1 - \mathbf{w} \cdot \mathbf{p})^2 - c_T^2 \mathbf{p} \cdot \mathbf{p} \right) = 0, \quad (2.2.52)$$

which is the Hamiltonian that equals the total energy of the system. The kinematic ray equations describing the propagation in terms of time rates of change for position $\dot{\mathbf{x}}$ and slowness $\dot{\mathbf{p}}$ become,

$$\dot{\mathbf{x}} = \mathbf{w} \left(1 - \mathbf{w} \cdot \mathbf{p} \right) + c_T^2 \mathbf{p}, \quad (2.2.53a)$$

$$\dot{\mathbf{p}} = -c_T \frac{\partial c_T}{\partial \mathbf{x}} \left(\mathbf{p} \cdot \mathbf{p} \right) + \left(1 - \mathbf{w} \cdot \mathbf{p} \right) \left(-\mathbf{p} \cdot \frac{\partial \mathbf{w}}{\partial \mathbf{x}} \right). \quad (2.2.53b)$$

The initial conditions for \mathbf{x} and \mathbf{p} are not random, but need to obey both the eikonal equation (2.2.44) and Huygens principle (2.2.50). The initial conditions become,

$$\mathbf{x}(t=0) = \mathbf{x}_0 \quad \text{and} \quad \mathbf{p}(t=0) = \mathbf{p}_0 = \frac{\hat{\mathbf{n}}}{c_0}, \quad (2.2.54)$$

with c_0 the absolute speed of sound (2.2.13) for $c_{T,0} = c_T(\mathbf{x}_0)$ and $\mathbf{w}_0 = \mathbf{w}(\mathbf{x}_0)$.

■ 2.2.5 Ray pressure field by geometrical spreading

Whereas the assumed harmonic solution is only real, the imaginary part of equation (2.2.42) should be zero. The imaginary part of equation (2.2.42) divided by $-\omega$ and substituting the slowness definition yields the transport equation,

$$(c_T^2 - \mathbf{w} \cdot \mathbf{w}) (2\nabla A \cdot \mathbf{p} + A\nabla \cdot \mathbf{p}) + 2\mathbf{w} \cdot \nabla A = 0, \quad (2.2.55)$$

which can be rewritten as,

$$\nabla \cdot (A^2 \mathbf{p}) = 0, \quad (2.2.56)$$

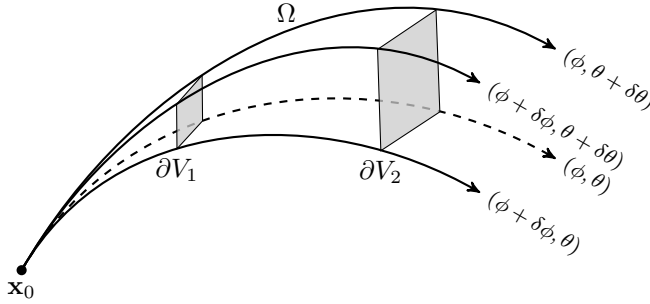


Figure 2.8: A ray tube of volume V with boundary Ω defined by a set of neighbouring rays. ∂V is the cross-sectional area at position \mathbf{x} with uniform amplitude A .

assuming a stationary atmosphere ($\mathbf{w} = 0$).

The transport equation is a frequency independent coefficient describing the amplitude along a ray path. Equation (2.2.56) describes the distribution of the wave energy over an increasing area, the flux variation, known as geometrical spreading.

Assume a set of neighbouring rays initiated at \mathbf{x}_0 with initial angles ϕ , $\phi + \delta\phi$, and θ , $\theta + \delta\theta$, for azimuth and elevation, respectively. Let V be the volume enclosed by the set of neighbouring rays defining the ray tube with cross-sectional area ∂V corresponding to the local wavefront τ . An illustration is given in Figure 2.8.

Gauss' divergence theorem for an arbitrary volume V with an arbitrary field F states that the flux with respect to the volume can be expressed in terms of the boundary Ω of that volume

$$\int_V \nabla \cdot F \, dV = \int_{\partial V} F \cdot \hat{\mathbf{n}} \, d\Omega, \quad (2.2.57)$$

where $\hat{\mathbf{n}}$ equals the outward normal to the surface ∂V in direction of propagation, the local wavefront τ . Applying Gauss's theorem and substituting equation (2.2.56) and the definition of the normal unit vector (2.2.14) yields

$$\int_{\partial V} A^2 \mathbf{p} \cdot \frac{\mathbf{p}}{\|\mathbf{p}\|} \, d\Omega = 0. \quad (2.2.58)$$

Rewriting in terms of the absolute speed of sound c (2.2.13) gives

$$\int_{\partial V} \frac{A^2}{c} \, d\Omega = 0, \quad (2.2.59)$$

The flux continuity of (2.2.59), based on the wave equation (2.2.29), does not depend on density. In the current form, ignoring density, the transport equation (2.2.59)

does not retain the continuity of momentum (2.2.25a). Hence, impedance contrasts due to variations in the background flow ($\lambda \ll L$ valid) are not taken into account. The transport equation multiplied with ρ^{-1} yields the following conservation of energy,

$$\int_{\partial V_1} \frac{A^2}{\rho c} d\Omega = \int_{\partial V_2} \frac{A^2}{\rho c} d\Omega = \text{constant}. \quad (2.2.60)$$

It is noted that ρc corresponds to the specific impedance of the wavefield.

Wavefronts ∂V_1 and ∂V_2 denote two areas of the ray tube (see Figure 2.8). In the limit of $\delta\theta \rightarrow 0$ and $\delta\phi \rightarrow 0$, the ray tube becomes infinitesimally small. As such, the area ∂V is described by the Jacobian determinant J .

The Jacobian determinant J relates the area at \mathbf{x} to changes of the ray path in terms of ray angles azimuth and elevation,

$$J(\mathbf{x}) = \left| \frac{\partial \mathbf{x}}{\partial(\phi, \theta, t)} \right|. \quad (2.2.61)$$

The Jacobian determinant requires four additional sets of ordinary differential equations. The ray equations (2.2.53) for position and slowness in terms of elevation are,

$$\begin{aligned} \partial_\phi \dot{\mathbf{x}} &= \frac{d}{dt} \frac{\partial \mathbf{x}}{\partial \phi} = \frac{\partial \mathbf{w}}{\partial \mathbf{x}} \frac{\partial \mathbf{x}}{\partial \phi} (1 - \mathbf{w} \cdot \mathbf{p}) - \mathbf{w} \left(\mathbf{p} \cdot \frac{\partial \mathbf{w}}{\partial \mathbf{x}} \frac{\partial \mathbf{x}}{\partial \phi} + \mathbf{w} \cdot \frac{\partial \mathbf{p}}{\partial \phi} \right) \\ &\quad + c_T^2 \frac{\partial \mathbf{p}}{\partial \phi} + 2c_T \mathbf{p} \frac{\partial c_T}{\partial \mathbf{x}} \frac{\partial \mathbf{x}}{\partial \phi}, \end{aligned} \quad (2.2.62a)$$

$$\begin{aligned} \partial_\phi \dot{\mathbf{p}} &= \frac{d}{dt} \frac{\partial \mathbf{p}}{\partial \phi} = - \left(\frac{\partial c_T}{\partial \mathbf{x}} \right)^2 \frac{\partial \mathbf{x}}{\partial \phi} (\mathbf{p} \cdot \mathbf{p}) - \frac{\partial^2 c_T}{\partial \mathbf{x}^2} \frac{\partial \mathbf{x}}{\partial \phi} (\mathbf{p} \cdot \mathbf{p}) - 2c_T \frac{\partial c_T}{\partial \mathbf{x}} \mathbf{p} \cdot \frac{\partial \mathbf{p}}{\partial \phi} \\ &\quad + \left(\mathbf{p} \cdot \frac{\partial \mathbf{w}}{\partial \mathbf{x}} \right)^2 \frac{\partial \mathbf{x}}{\partial \phi} + \left(\mathbf{p} \cdot \frac{\partial \mathbf{w}}{\partial \mathbf{x}} \right) \left(\mathbf{w} \cdot \frac{\partial \mathbf{p}}{\partial \phi} \right) \\ &\quad - (1 - \mathbf{w} \cdot \mathbf{p}) \frac{\partial \mathbf{p}}{\partial \phi} \cdot \frac{\partial \mathbf{w}}{\partial \mathbf{x}} - (1 - \mathbf{w} \cdot \mathbf{p}) \mathbf{p} \cdot \frac{\partial^2 \mathbf{w}}{\partial \mathbf{x}^2} \frac{\partial \mathbf{x}}{\partial \phi}, \end{aligned} \quad (2.2.62b)$$

and for azimuth,

$$\begin{aligned} \partial_\theta \dot{\mathbf{x}} &= \frac{d}{dt} \frac{\partial \mathbf{x}}{\partial \theta} = \frac{\partial \mathbf{w}}{\partial \mathbf{x}} \frac{\partial \mathbf{x}}{\partial \theta} (1 - \mathbf{w} \cdot \mathbf{p}) - \mathbf{w} \left(\mathbf{p} \cdot \frac{\partial \mathbf{w}}{\partial \mathbf{x}} \frac{\partial \mathbf{x}}{\partial \theta} + \mathbf{w} \cdot \frac{\partial \mathbf{p}}{\partial \theta} \right) \\ &\quad + c_T^2 \frac{\partial \mathbf{p}}{\partial \theta} + 2c_T \mathbf{p} \frac{\partial c_T}{\partial \mathbf{x}} \frac{\partial \mathbf{x}}{\partial \theta}, \end{aligned} \quad (2.2.63a)$$

$$\begin{aligned} \partial_\theta \dot{\mathbf{p}} &= \frac{d}{dt} \frac{\partial \mathbf{p}}{\partial \theta} = - \left(\frac{\partial c_T}{\partial \mathbf{x}} \right)^2 \frac{\partial \mathbf{x}}{\partial \theta} (\mathbf{p} \cdot \mathbf{p}) - \frac{\partial^2 c_T}{\partial \mathbf{x}^2} \frac{\partial \mathbf{x}}{\partial \theta} (\mathbf{p} \cdot \mathbf{p}) - 2c_T \frac{\partial c_T}{\partial \mathbf{x}} \mathbf{p} \cdot \frac{\partial \mathbf{p}}{\partial \theta} \\ &\quad + \left(\mathbf{p} \cdot \frac{\partial \mathbf{w}}{\partial \mathbf{x}} \right)^2 \frac{\partial \mathbf{x}}{\partial \theta} + \left(\mathbf{p} \cdot \frac{\partial \mathbf{w}}{\partial \mathbf{x}} \right) \left(\mathbf{w} \cdot \frac{\partial \mathbf{p}}{\partial \theta} \right) \\ &\quad - (1 - \mathbf{w} \cdot \mathbf{p}) \frac{\partial \mathbf{p}}{\partial \theta} \cdot \frac{\partial \mathbf{w}}{\partial \mathbf{x}} - (1 - \mathbf{w} \cdot \mathbf{p}) \mathbf{p} \cdot \frac{\partial^2 \mathbf{w}}{\partial \mathbf{x}^2} \frac{\partial \mathbf{x}}{\partial \theta}. \end{aligned} \quad (2.2.63b)$$

The initial conditions of equations (2.2.62a) and (2.2.63a) for \mathbf{x}_0 yield

$$\partial_\phi \mathbf{x}_0 = 0 \quad \text{and} \quad \partial_\theta \mathbf{x}_0 = 0, \quad (2.2.64)$$

since the initial ray coordinates are not yet changed by the ray angles elevation and azimuth. The initial conditions for (2.2.62b) and (2.2.63b) result from the derivative of initial slowness \mathbf{p}_0 for ϕ and θ ,

$$\partial_\phi \mathbf{p}_0 = -\frac{\hat{\mathbf{n}}}{c_0^2} \frac{\partial c_0}{\partial \phi} \quad \text{and} \quad \partial_\theta \mathbf{p}_0 = -\frac{\hat{\mathbf{n}}}{c_0^2} \frac{\partial c_0}{\partial \theta}. \quad (2.2.65)$$

The initial Jacobian determinant $J(\mathbf{x}_0)$ depends on the initial area described by $d\phi$ and $d\theta$. Assuming a regular increment in azimuth and elevation between the rays, the area only changes with elevation ϕ , yielding the initial Jacobian determinant,

$$J(\mathbf{x}_0) = \cos \theta. \quad (2.2.66)$$

From the conservation of energy in equation (2.2.60) in combination with the Jacobian determinant J it follows that ray amplitude A at location \mathbf{x} can be expressed in terms of the initial amplitude $A(\mathbf{x}_0)$ distributed over the area,

$$A(\mathbf{x}) = A(\mathbf{x}_0) \sqrt{\left| \frac{\rho c}{\rho_0 c_0} \frac{J(\mathbf{x}_0)}{J(\mathbf{x})} \right|}, \quad (2.2.67)$$

Geometrical spreading only is obtained when just taking into account the Jacobian determinant $\sqrt{|J|}$.

The pressure field $a(\mathbf{x})$ of a ray follows from the definition of a plane wave,

$$a(\mathbf{x}) = A(\mathbf{x}) e^{-i\omega(\tau-t)} = A(\mathbf{x}). \quad (2.2.68)$$

The accumulated decrease in pressure along the ray path can be expressed in terms of the transmission loss,

$$\text{TL}(\mathbf{x}) = -20 \log_{10} \left| \frac{a(\mathbf{x})}{a(\mathbf{x}_0)} \right|, \quad (2.2.69)$$

with units dB re 1m using the reference pressure for a point source in free space evaluated at a distance of 1 m. Thus,

$$a(\mathbf{x}_0) = A(\mathbf{x}_0) = \frac{1}{4\pi}. \quad (2.2.70)$$

Substituting (2.2.66) and (2.2.70) into (2.2.67) yields the amplitude variation along a ray,

$$A(\mathbf{x}) = \frac{1}{4\pi} \sqrt{\left| \frac{\rho c \cos \theta}{\rho_0 c_0 J(\mathbf{x})} \right|}. \quad (2.2.71)$$

■ 2.2.6 Implementation and example

Ray tracing in spherical coordinates

Ray tracing is performed in spherical coordinates to allow long range propagation, assuming the Earth is a perfect sphere. Although the Earth's ellipsoid has slight oblateness ($\sim 1/297$) this assumption is valid since atmospheric conditions from General Circulation Models, e.g., the ECMWF model, are defined on a perfect sphere. See Appendix A.4 for the ray equations for position and slowness in spherical coordinates, including the additional set of equations for the Jacobian determinant.

Realistic three-dimensional inhomogeneous fields for wind (zonal, meridional and vertical), temperature, pressure, and density are obtained from global Numerical Weather Prediction (NWP) data. Atmospheric conditions are provided by the Integrated Forecast System (IFS) of the European Centre for Medium-Range Weather Forecasts (ECMWF). The IFS consists of a global circulation model up to 1 Pa (~ 78 km) assimilating various ground, satellite and radiosonde based observations. The two upper levels are neglected. Those levels operate as a sponge layer, filtering wave reflections, which is required for model stability but provides an unrealistically representation of the atmosphere. As such, the maximum altitude is limited to 70 km. This is much lower than the thermospheric return height (~ 120 km). Consequently, thermospheric refractions cannot be resolved using IFS data. ECMWF's vertical hybrid model levels are first resampled to a regular grid using one dimensional piecewise cubic Hermite spline interpolation [*Fritsch and Carlson, 1980*] in the vertical with a low-pass filter to avoid aliasing. Subgrid atmospheric conditions and first and second order derivatives are obtained by three-dimensional cubic convolution interpolation with a smooth kernel [*Keys, 1981*].

The Earth's surface is assumed a perfect reflector, which is true for low-frequency acoustic waves. Rays bouncing on the Earth's surface reflect by Snell's law taking into account the slope of the topography, altering the slowness' reflection angle. Topography is retrieved from either ECMWF or a higher resolution digital elevation model (DEM).

All ray differential equations of position and slowness for time, azimuth and elevation are solved numerically by classical Runge-Kutta integration, generally referred to as RK4. A discrete set of ray is solved iteratively given a range of elevation and azimuth angles.

Eigenray grid search

Eigenrays are ray paths connecting source and receiver. Eigenrays yield various important simulated parameters, for example, travel time or array characteristics such as back azimuth and apparent velocity. Eigenrays are important for event analysis [e.g. *Evers et al., 2012; Smets et al., 2015; Assink et al., 2016*] and inversion studies [e.g. *Lalande et al., 2012; Assink et al., 2014a; Smets et al., 2016*], relating observations with atmospheric conditions. In a stratified atmosphere, an analytical solution of the eigenrays, contained within an azimuthal plane, can be determined [e.g. *Brekhovskikh and Godin, 1999; Assink et al., 2012*]. For the proposed ray

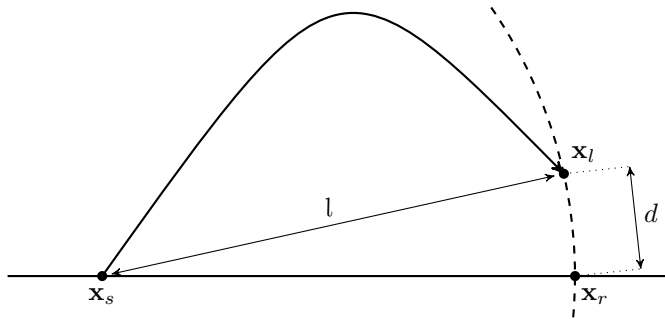


Figure 2.9: Illustration of the eigenray grid search method.

equations in a moving non-homogeneous atmosphere, an analytical solution is non-trivial. Since the propagation is non-planar, one searches for inclination and azimuth angles which produce a ray returning to the ground at a specified location [e.g. *Blom and Waxler, 2017*]. Therefore, a grid search is proposed to find approximate solutions within a given threshold. The method can be implemented iteratively to reduce the error from the true eigenray even further.

Assume a source at location \mathbf{x}_s and an arbitrary receiver \mathbf{x}_r , such that $\mathbf{x}_0 = \mathbf{x}_s$. Let l be the Euclidian distance between source and receiver,

$$l = \|\mathbf{x}_r - \mathbf{x}_s\|. \quad (2.2.72)$$

A ray S initiated from source \mathbf{x}_s with initial angles ϕ and θ in the direction of a receiver \mathbf{x}_r is shown in Figure 2.9. \mathbf{x}_l is the location when distance l is reached, resulting in the offset d from the receiver,

$$d = \|\mathbf{x}_r - \mathbf{x}_l\|. \quad (2.2.73)$$

Ray $S(\phi, \theta)$ is considered an eigenray when \mathbf{x}_l falls within a threshold offset of the array, $d < d_{\min}$, with minimum offset d_{\min} approximately the array aperture. Isolated eigenrays are retrieved by a local minimum search.

Example

Figures 2.10, 2.11, 2.12, and 2.13 illustrate anomalous infrasound propagation in a warm stratosphere by non-linear ray theory cast in spherical coordinates. Infrasound propagation corresponds to a domestic gas explosion in Liege, Belgium, of 27 January 2010 recorded at infrasound arrays DBN and TEX of KNMI located in De Bilt and Texel, respectively. A full discussion is given in *Evers et al. [2012]*.

Figures 2.10 and 2.11 illustrates the complexity of the wavefield by colour coded reflection points. Rays are traced from 0 to 360° azimuth and 0 to 45° elevation with

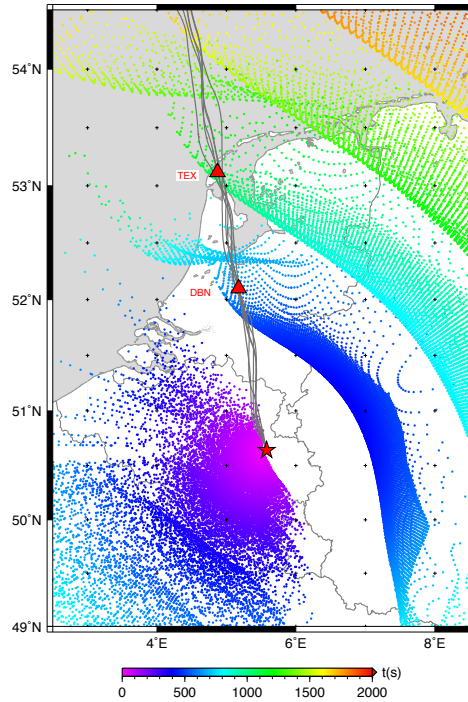


Figure 2.10: Three-dimensional ray tracing results for infrasound propagating from Liège, Belgium, to infrasound arrays DBN and TEX of KNMI (red triangles). Dots represent ray reflection points on the Earth's surface colour coded with travel time. The source location is indicated by the star. Grey rays indicate the eigenrays projected on the earth's surface. A vertical cross section of the source – receiver plane is shown in Figure 2.12.

1° and 0.5° increments, respectively. Note that both a tropospheric duct in south-westerly direction as well as a strong stratospheric in north-easterly direction are present, yielding wavefronts with two distinct directions. A vertical cross section of the source – receiver plane, with regard to a bearing of approximately 350° , is shown in Figure 2.12. The increasing negative offset indicates a westerly stratospheric duct. Eigenrays compensate the westerly drift by a negative back azimuth deviation, initiating slightly against the wind.

Eigenrays are obtained by a grid search, see Figure 2.13. Rays are traced from 330 to 360° azimuth and 0 to 30° elevation with 0.1° increments. The eigenray grid search yields three local minima in offset d for each array within 0.5 km of the array centre coordinate. These eigenrays are illustrated in Figures 2.10, 2.11 and 2.12.

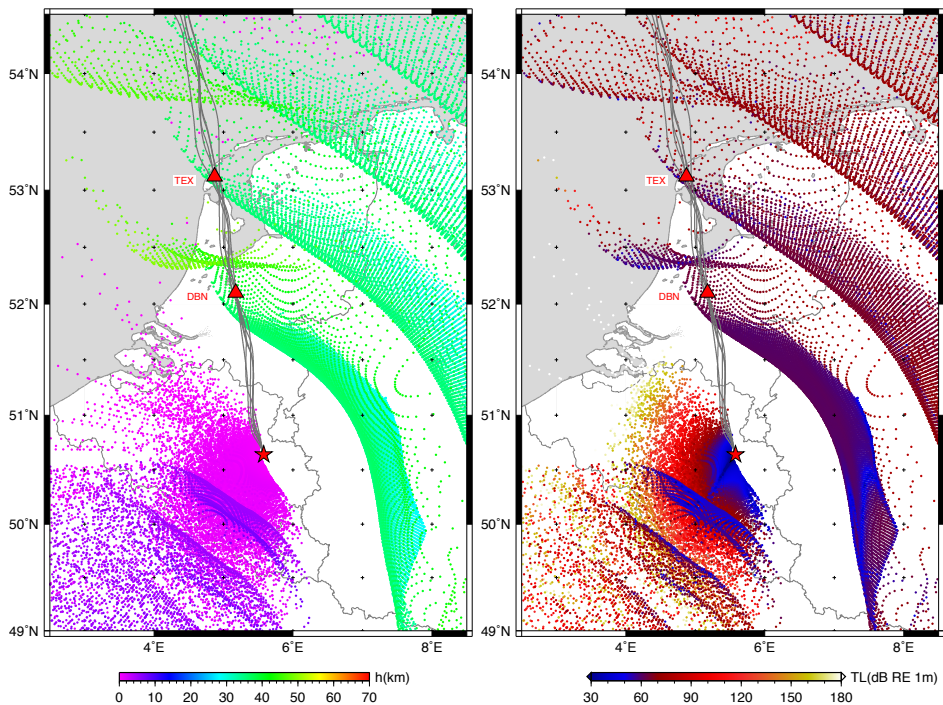


Figure 2.11: Three-dimensional ray tracing results for infrasound propagating from Liège, Belgium, to infrasound arrays DBN and TEX of KNMI (red triangles). Dots represent ray reflection points on the Earth's surface colour coded (left) return height, and (right) transmission loss. The source location is indicated by the star. Grey rays indicate the eigenrays projected on the earth's surface. A vertical cross section of the source – receiver plane is shown in Figure 2.12.

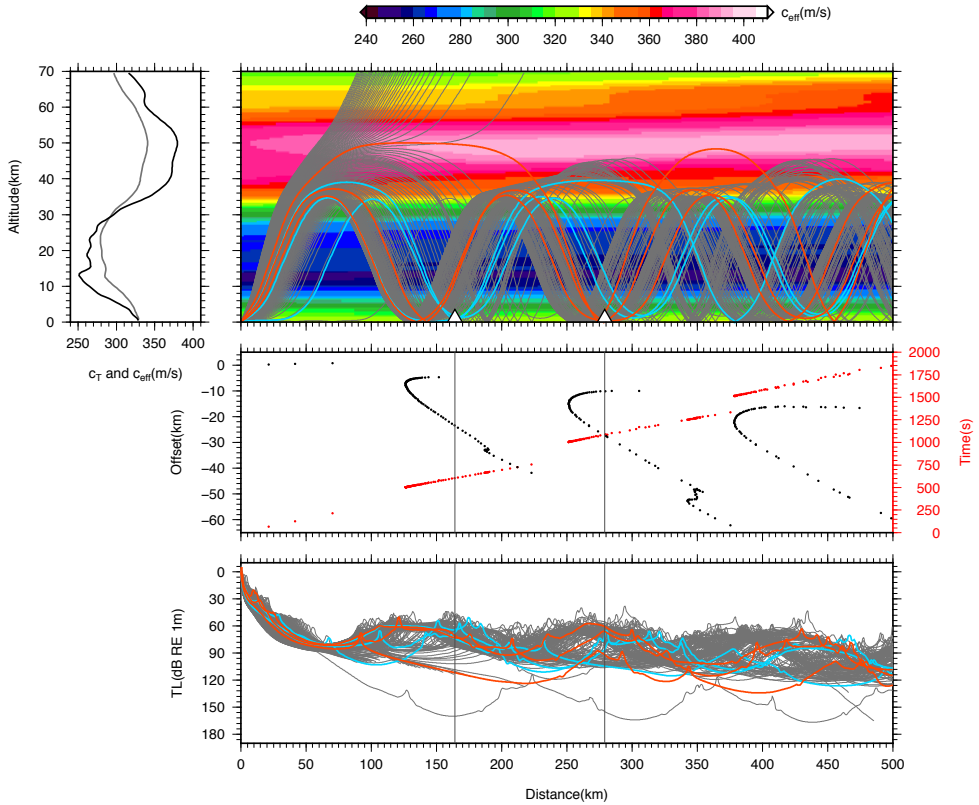


Figure 2.12: Vertical cross section along the bearing for infrasound propagating from Liège to DBN and TEX, for which the reflection points are given in Figure 2.11. (top left) Vertical profiles of the (grey) adiabatic (c_T) and (black) effective velocity (c_{eff}) at the source location. (top right) Rays (grey) initiated with the true bearing of approximately 350° . Elevation angles range from zero to 40° . Coloured rays are eigenrays to (blue) DBN and (orange) TEX. The effective velocity (c_{eff}) is colour coded in the background. (middle) Reflections on the Earth's surface (dots) of the (grey) rays with an azimuth of 350° . Colour coded are (red) travel time and (black) offset from the true bearing. The bottom frame shows the transmission loss.

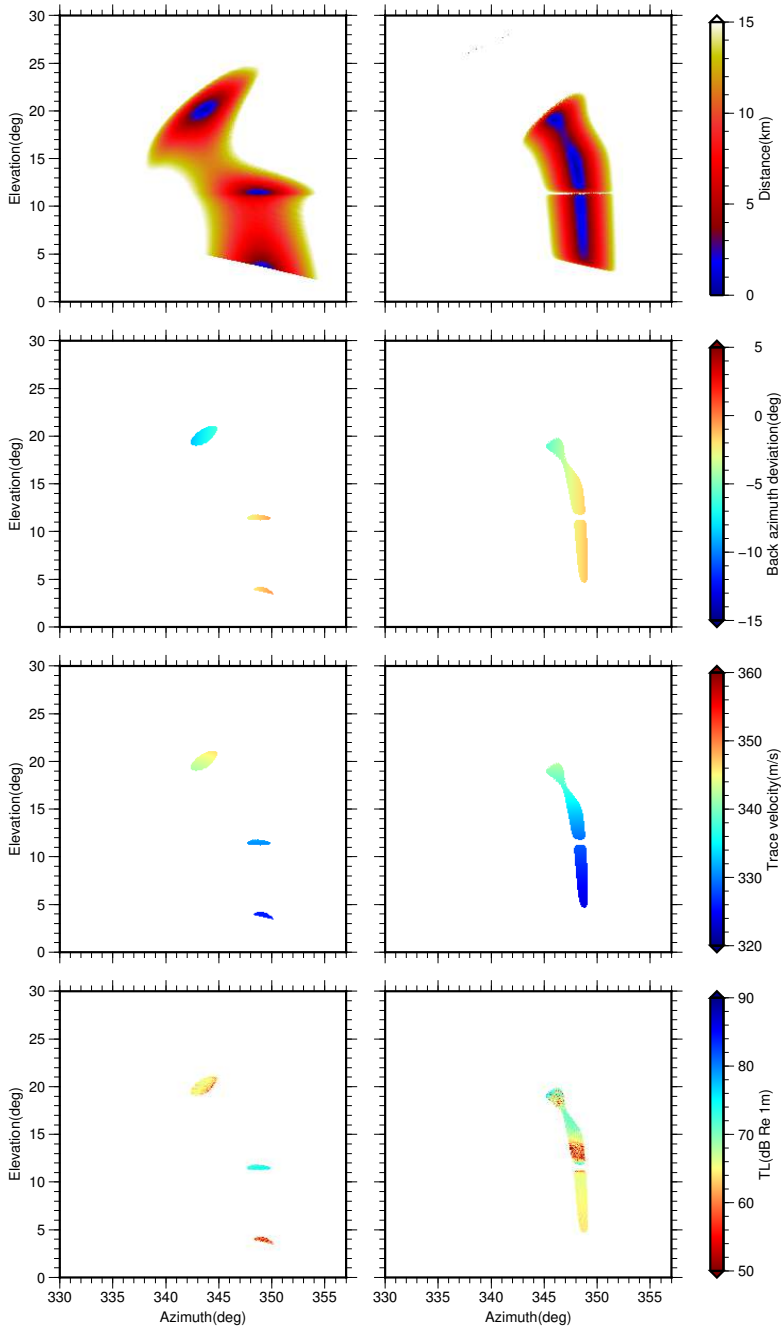


Figure 2.13: Example of eigenray grid search from Liège to (left) DBN and (right) TEX. From top to bottom are shown: offset, back azimuth deviation, apparent velocity and transmission loss. The lower three rows correspond to an offset of 2.5 km and less.

2.3 Infrasonic ambient noise from atmospheric microbaroms

Microbaroms are atmospheric pressure oscillations radiated from non-linear ocean surface wave interaction at double the ocean wave frequency [Gutenberg, 1939; Longuet-Higgins, 1950; Posmentier, 1967]. Interacting large regions of high-energetic oceanic waves of similar frequency with opposite directions, e.g., ocean swell and marine storms, radiate almost continuous acoustic energy well characterized by a radiation frequency of 0.2 ± 0.1 Hz. Microbaroms dominate the infrasound ambient noise field, making them a preferred source for passive atmospheric probing. Oceanic microbaroms couple to the ocean floor, generating seismic waves, referred to as microseisms.

■ 2.3.1 Origin of deep ocean standing surface waves

Ocean surface wave amplitudes and their classification are illustrated in Figure 2.14, briefly described according to Krauss [1973, pg. 95–96]. Wind and air pressure are the primary driving forces of the ocean surface spectrum; gravity is the main restoring force ($T_\zeta > 0.1$ s). Shorter waves are pure capillary waves ($T_\zeta < 0.1$ s), restored primarily by the ocean surface tension. Longer waves ($T_\zeta > 5$ min) are driven by earthquakes and solar and lunar forces for even longer periods. For these long periods the Coriolis force starts to dominate over gravity as the restoring force. These very long period waves either remain gravity waves, e.g., Kelvin waves, known as inertio-gravitational waves, or become pure inertial waves (like planetary waves in the atmosphere).

Gravity waves

Most energy of the ocean surface wave field is present within $1 \text{ s} < T_\zeta < 30 \text{ s}$, gravity waves (GWs), restored only by gravity. Surface tension is negligible at periods greater than 1 s. The GWs wave field is named *sea*, driven primarily by wind and air pressure. When the wave field is no longer driven by the external forces it is called *swell*. A steady atmospheric surface wind over long times and large areas of the sea surface deposits momentum into the sea surface, exciting sea waves. The duration and area is inversely related to the frequency of the sea wave. Energetic areas of low frequency waves are induced by, for example, severe marine storms.

Notice that the sea surface state, in terms of surface roughness, is equally important to the atmosphere [Janssen, 2009]. A rough sea induces an atmospheric drag, decelerating the atmospheric surface wind.

The phase speed c_ζ of a surface gravity wave is well approximated by [Komen *et al.*, 1996]

$$c_\zeta = \sqrt{\frac{g\lambda_\zeta}{2\pi} \tanh\left(\frac{2\pi D}{\lambda_\zeta}\right)}, \quad (2.3.1)$$

with D the depth of the water column, λ_ζ the wavelength, and $g = 9.81 \text{ m s}^{-2}$ the gravitational acceleration constant. In deep water, when $D \geq \lambda_\zeta/2$, the hyperbolic

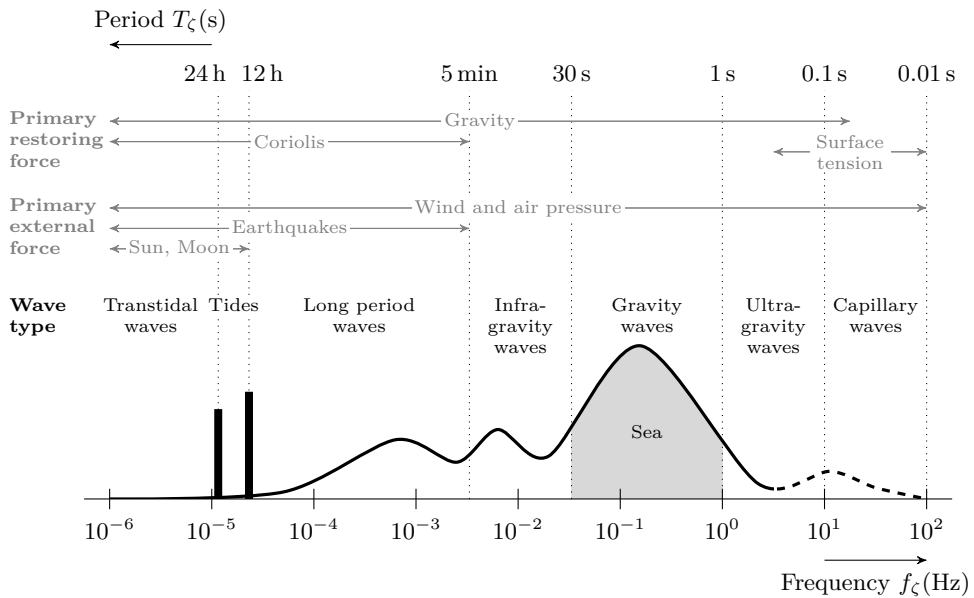


Figure 2.14: Schematic representation of ocean surface wave amplitudes and their classification on an arbitrary scale [Krauss, 1973, pg. 95]. The grey area indicates the wave field of interest, named sea.

tangent approaches one. At this depth, the influence of bathymetry on the surface waves is negligible. The phase speed c_ζ in deep water simplifies to

$$c_{\zeta,\text{deep}} = \sqrt{\frac{g\lambda_\zeta}{2\pi}}, \quad (2.3.2)$$

Equation (2.3.2) states that the longer the wavelength of the ocean surface wave, the faster it travels. On the contrary, when $\lambda_\zeta \gg D$, equation (2.3.1) becomes

$$c_{\zeta,\text{shallow}} = \sqrt{gD}, \quad (2.3.3)$$

which is independent of wavelength; nondispersive. The angular frequency of the surface gravity waves using (2.1.6) and (2.1.7) in deep water yields

$$\omega_{\zeta,\text{deep}} = \sqrt{g\|\mathbf{k}\|}, \quad (2.3.4)$$

with \mathbf{k} the two-dimensional horizontal wavenumber vector.

Deep sea gravity waves have a wavelength ranging from 1.5 m up to 1405 m (1 s to 30 s waves). Ocean wave spectra are typically peaked around 10 s (0.1 Hz), which results in an ocean surface wavelength of 156 m.

Sea state

Let $\zeta(\mathbf{r}, t)$ indicate the free-surface elevation at horizontal position \mathbf{r} and time t , defining the interface between the ocean and atmosphere. Altitude $z = \zeta$ is used to indicate the ocean ($z \leq \zeta$) or atmosphere ($z > \zeta$). When $\zeta = 0$ the sea surface is in equilibrium, named the *ambient* sea state.

In global and regional-scale wave predictions, prediction of the sea state is based on a statistical description of oceans waves in the GW spectrum [e.g. *Komen et al.*, 1996]. Air-sea coupling is crucial in prediction of the sea state due to the two-way interaction of surface winds and ocean waves [*Janssen*, 2009]. It is assumed that the sea wave field in a source region S can be represented as a zero-mean, quasi-homogeneous and quasi-stationary Gaussian process. Hence, the stochastic sea state is described by a slowly varying² two-dimensional variance density spectrum,

$$\langle \hat{\zeta}_S^2 \rangle = F(f_\zeta, \phi), \quad (2.3.5)$$

with wave frequency f_ζ and propagation direction ϕ clockwise to the north. F describes the distribution of the wave variance for a steady state by superposition of linear waves over different frequencies and directions.

$$\zeta_S(\mathbf{r}, t) = \Re \int \hat{\zeta}_S(\mathbf{k}) e^{\mathbf{k} \cdot \mathbf{r} - \omega_\zeta(\mathbf{k})t} d\mathbf{k}, \quad (2.3.6)$$

where $\hat{\zeta}_S$ denotes the mean sea state amplitude (Fourier coefficient) given a wave vector. The variance spectrum is related to the wave number spectral density \mathcal{F} by the dispersion relation $\omega_\zeta(\mathbf{k}) = 2\pi f_\zeta$ including the GW phase velocity (2.3.1),

$$F(f_\zeta, \phi) df_\zeta d\phi = \mathcal{F}(\mathbf{k}) d\mathbf{k}. \quad (2.3.7)$$

Equation (2.3.7) is related to the stochastic sea state (2.3.6) by

$$\langle \hat{\zeta}_S(\mathbf{k}) \hat{\zeta}_S(\mathbf{k}')^* \rangle_S = \mathcal{F}(\mathbf{k}) \delta(\mathbf{k} - \mathbf{k}'), \quad (2.3.8)$$

with

$$\langle \hat{\zeta}_S(\mathbf{k}) \hat{\zeta}_S(\mathbf{k}') \rangle_S = \langle \hat{\zeta}_S(\mathbf{k})^* \hat{\zeta}_S(\mathbf{k}')^* \rangle_S = 0$$

The integral of equation (2.3.5) over direction yields the sea mean energy spectrum

$$\bar{F}(f_\zeta) = \int_0^{2\pi} F(f_\zeta, \phi) d\phi. \quad (2.3.9)$$

and total integral of the spectrum defines the standard deviation of the wave field. Significant wave height, a measure of the excitation of the sea state, is defined as four times the standard deviation of the surface elevation (the zeroth-order moment of the wave spectrum),

$$H_S = 4 \sqrt{\int_0^\infty \bar{F}(f_\zeta) df}. \quad (2.3.10)$$

²Slow compared to the typical wave length and period thus considered constant over many ocean wavelengths.

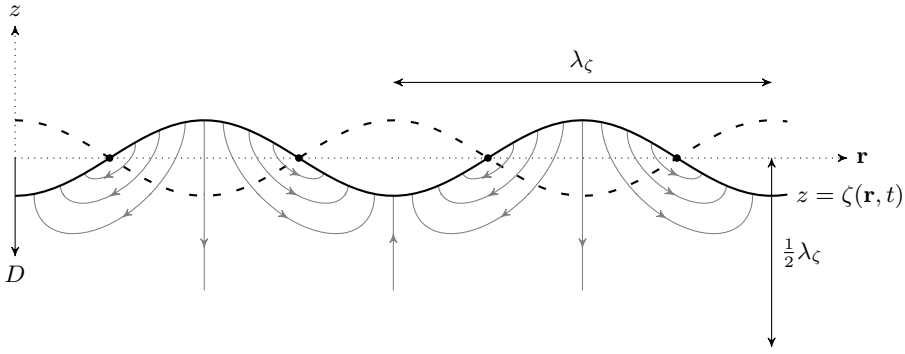


Figure 2.15: Deep ocean standing wave ($D \gg \lambda_\zeta$) with (black dots) nodes and (grey lines) particle velocity streamlines.

In practice, equation (2.3.10) is evaluated for the GW range (from 1 s to 30 s). It is noted that traditionally the significant wave height is defined as the mean wave height (trough to crest) of the highest third of the waves.

Standing ocean waves

Let ζ_1 and ζ_2 describe two progressive surface waves of same amplitude given by

$$\zeta_1 = A_0 \cos(\mathbf{k}_1 \cdot \mathbf{r} - \omega_1 t) \quad \text{and} \quad \zeta_2 = A_0 \cos(\mathbf{k}_2 \cdot \mathbf{r} - \omega_2 t).$$

Superposition of harmonic oscillations ζ_1 and ζ_2 yields

$$\zeta_{12} = 2A_0 \cos(\mathbf{k}' \cdot \mathbf{r} - \omega' t) \cos(\bar{\mathbf{k}} \cdot \mathbf{r} - \bar{\omega} t), \quad (2.3.11)$$

inducing a carrier wave of direction $\bar{\mathbf{k}}$ and a time dependent amplitude modulation of direction \mathbf{k}' , defined by

$$\begin{aligned} \bar{\mathbf{k}} &= (\mathbf{k}_1 + \mathbf{k}_2)/2, & \bar{\omega} &= (\omega_1 + \omega_2)/2, \\ \mathbf{k}' &= (\mathbf{k}_1 - \mathbf{k}_2)/2, & \omega' &= (\omega_1 - \omega_2)/2. \end{aligned}$$

The resulting wave is characterized by phase and modulation (or group) velocities

$$c_\zeta = \frac{\bar{\omega}}{\|\bar{\mathbf{k}}\|}, \quad \text{and} \quad c_{\zeta,g} = \frac{\omega'}{\|\mathbf{k}'\|}.$$

When ζ_1 and ζ_2 are ideal counter propagating waves, thus of same frequency and amplitude but of opposite direction,

$$\omega_1 = \omega_2 \rightarrow \omega' = 0, \quad \text{and} \quad \mathbf{k}_1 = -\mathbf{k}_2 \rightarrow \bar{\mathbf{k}} = 0.$$

Consequently, the amplitude modulation becomes stationary ($c_{\zeta,g} = 0$) and the phase velocity is infinite. The oscillation by superposition of ζ_1 and ζ_2 reduces to

$$\zeta_{12} = 2A_0 \cos(\mathbf{k}_1 \cdot \mathbf{r}) \cos(\omega_1 t), \quad (2.3.12)$$

describing a *standing wave* characterized by stationary minima of the oscillation, named *nodal points*. That is, when $\mathbf{k}_1 \cdot \mathbf{r} = \lambda_\zeta \|\mathbf{k}_1\| (1/4 + n/2)$ for any integer n . The resulting particle motion is an irrotational potential flow with velocities tangent to the stream lines [Krauss, 1973]. A schematic of a standing wave with particle velocity streamlines is given in Figure 2.15.

Hasselmann [1963] related the variance density spectrum, defined by the superposition of linear waves, to the statistical density spectrum of ideal counter propagating waves by

$$\mathcal{H}(f_\zeta) = \int_0^{2\pi} F(f_\zeta, \phi) F(f_\zeta, \phi - \pi) d\phi, \quad (2.3.13)$$

known as the *Hasselmann integral*. Hasselmann [1963] showed that microbaroms are only generated when discrete Fourier components of the random exciting sea state have the same phase velocities as free modes of the elastic system. Thus, the interaction of sea and swell of equal phase velocity.

■ 2.3.2 Microbarom radiation of the atmosphere-ocean interface

The fundamentals of the oceanic microbarom model assuming an ocean of infinite depth are first described by Longuet-Higgins [1950] and validated by Hasselmann [1963]. Brekhovskikh *et al.* [1973] extended the oceanic microbarom source model to obtain the atmospheric component by radiation from water into air. More recent, Waxler and Gilbert [2006] refined the atmospheric component, adding compressibility of the atmosphere to complete the second-order acoustics. The state-of-the-art infrasound microbarom radiation source model, assuming an infinite ocean depth [Waxler and Gilbert, 2006], has been validated by Walker [2012] and Stopa *et al.* [2012], studying ambient swell and hurricane induced microbaroms, respectively.

Longuet-Higgins [1950] developed the fundamentals of a finite-ocean microbarom source model, for oceanic microbaroms and microseisms, only many years later taken into account and applied by Kedar *et al.* [2008]. The effect of a finite ocean depth is added by Waxler *et al.* [2007], assuming an elastic sea floor, by interference of the up and down going oceanic signals in the (homogenous) water column.

Principle mechanism : vibrating interface

Consider a two-fluid model, a rare fluid (air) over a dense fluid (seawater). Let the source area S define the high-energetic ocean-atmosphere interface. The area is represented by multiple patches, each defining a water column of finite depth, enclosed by the interface and the sea floor, illustrated in Figure 2.16.

Non-linear interaction of counter propagating surface waves generates standing waves, which are harmonics of the ocean-atmosphere interface. The vibrating interface acts as a membrane, causing a velocity potential. This potential induces

a pressure oscillation in the water near the interface. Acoustic energy is radiated, normal to the interface in outward direction, at double the ocean wave frequency. Since the source is stationary (standing), acoustic radiation can be described by outward propagating plane waves normal to the interface. The velocity potential is defined by second-order perturbative terms in the expansion of the fluid dynamics equations (to the lowest non-zeroth order or Mach number), which are continuous at the interface between the two fluids [Brekhovskikh *et al.*, 1973]. Since motions of the fluids affect the motion of the interface, the second-order interface condition does contain the effects of non-linearities in air and water [Waxler and Gilbert, 2006]. Note that, in the linear approximation, the acoustic field is vertically evanescent so the source area does not radiate.

The interface radiates acoustic energy in the ocean ($z \leq \zeta$), propagating through the water column. At the top the water column, the signal radiates into the atmosphere ($z > \zeta$). In addition, the atmospheric component contains a signal due to compressibility of the air near the interface by the oscillation of the interface. At the bottom of the water column ($z = -D$), the signal reflects on the solid sea floor, partly coupling to the solid sea floor as seismic waves, which are body and surface waves and interface waves known as Scholte waves. Interference between the downward and upward propagating signals may lead to resonance of the water column. Although there is a significant impedance contrast between air and seawater ($(\rho_w c_w)/(\rho_a c_a) \sim 4.4 \cdot 10^3$), acoustic energy is radiated from the water column into the air. Since the interface is in motion, both fluids have approximately the same velocity, reducing the impedance contrast to a ratio of densities ($\rho_w/\rho_a \sim 10^3$).

Assumptions

The first-order Euler equation and second-order equation of continuity describe the second-order velocity potential of the interface. To obtain a solution for the velocity potential and corresponding pressure perturbation, some assumptions are required:

- Only sea state wave vectors of opposite direction and equal magnitude are considered. So, a statistical source description can be obtained from the Hasselmann integral, assuming ideal counter propagating waves. Since the stochastic sea state assumes an ambient mean sea, acoustic radiation by outward propagating plane waves normal to the interface is limited to vertical propagation only (near the air-water interface and within the water column). This reduces the outward velocity potential to a one-dimensional problem in the source region.
- Neighbouring patches of the area S are assumed independent, each radiating acoustic energy given a local energy spectrum. Hence, the interface radiates without horizontal spreading (see previous point). Consequently, resonance of the water column assumes a homogeneous ocean with a flat sea floor. Since surfaces are independent, the water column characteristics (e.g., sea floor depth, speed of sound or density) may vary one from another.
- In the sea wave frequency band, the acoustic wavelengths are much larger

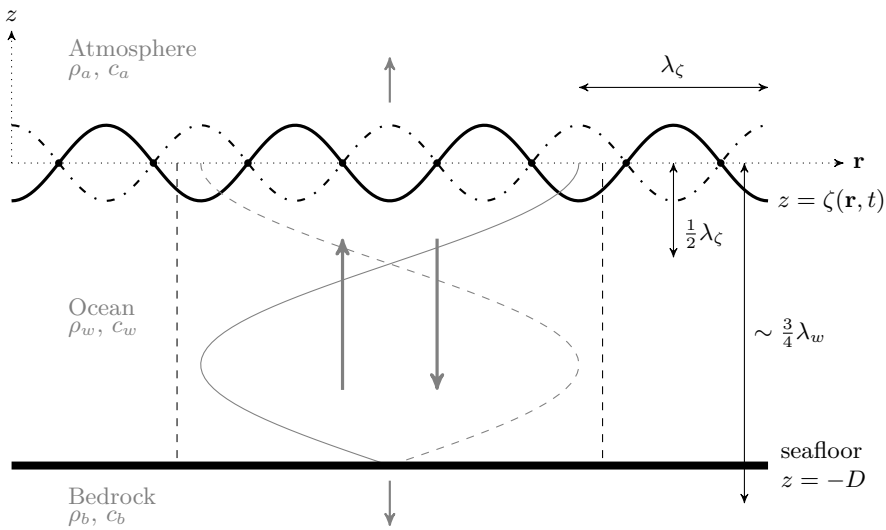


Figure 2.16: Microbarom radiation mechanism using a two-fluid model over a solid. Solid and dashed sinusoidal lines indicate the ocean surface harmonics. Vertical dashed lines indicate the homogeneous water column, enclosed by (top) a patch of the source area S and (bottom) the elastic sea floor of depth D .

than the ocean surface wavelength ($\lambda_\sigma \gg \lambda_c$). Assuming wave interaction at the typical peak of the ocean wave spectra the resulting acoustic frequency becomes 0.2 Hz. Corresponding acoustic wavelengths are 1700 m and 7500 m, assuming a speed of sound of 340 m s^{-1} for air and 1500 m s^{-1} in sea water, respectively. Hence, acoustic radiation of a source region at large distances can be considered as a radiating monopole field [Brekhovskikh *et al.*, 1973]. Accordingly, the received microbarom signal of multiple source regions can be obtained by incoherent superposition of radiating patches at the sea surface.

■ 2.3.3 Microbarom source spectrum for a finite ocean depth

The equation of motion of the vibrating interface yields a description for the velocity potential given a sea state wave vector, in agreement with the deep water dispersion relation of equation (2.3.4). A measure for the received microbarom is obtained by the Helmholtz-Kirchhoff integral theorem, relating the observed pressure fluctuation at a distance from the source area to the velocity potential of the source area. Propagation of sound through the medium is described by a Green's function G_σ , with σ representing the atmosphere (a) or water (w).

A measure for the received stochastic microbarom signal is given by the correlation of the received signal at two arbitrary points, \mathbf{x} and \mathbf{x}' , not part of the surface S

[*Brekhovskikh et al., 1973; Waxler and Gilbert, 2006*]

$$\langle \hat{P}_\sigma(\mathbf{x}, \omega_\sigma) \hat{P}_\sigma(\mathbf{x}', \omega_\sigma)^* \rangle_T = \int_S \mathcal{Q}_\sigma(\mathbf{x}, \mathbf{x}', \mathbf{r}, f_\sigma) \mathcal{D}_\sigma(f_\sigma) d\mathbf{r}, \quad (2.3.14)$$

with \hat{P}_σ the Fourier transform of the received pressure over a period T , \mathcal{D}_σ the microbarom source strength spectrum squared, and \mathcal{Q} the cross spectral density,

$$\mathcal{Q}_\sigma(\mathbf{x}, \mathbf{x}', \mathbf{r}, f_\sigma) = \langle \hat{G}_\sigma(\mathbf{x}, \mathbf{r}, \omega_\sigma) \hat{G}_\sigma(\mathbf{x}', \mathbf{r}, \omega_\sigma)^* \rangle_P, \quad (2.3.15)$$

obtained from the correlation of the Green's function for propagation from a point source at \mathbf{r} toward the receivers. Integration over the source area S is required since \mathcal{D}_σ , depending on two-dimensional variance spectrum (2.3.5), is not constant but slowly varies over the various patches. For a single sensor, equation (2.3.14) becomes the received power spectrum

$$\langle |\hat{P}_\sigma(\mathbf{x}, \omega_\sigma)|^2 \rangle_T = \int_S \mathcal{Q}_\sigma(\mathbf{x}, \mathbf{x}, \mathbf{r}, f_\sigma) \mathcal{D}_\sigma(f_\sigma) d\mathbf{r}, \quad (2.3.16)$$

The microbarom source energy spectrum [*Waxler et al., 2007*] is defined as

$$\mathcal{D}_\sigma(f_\sigma) = 4g^2\pi^4 f_\sigma^3 \mathcal{H}(f_\sigma) \begin{cases} \frac{\rho_w^2 A}{c_w^2 B} & z \leq \zeta \\ \frac{\rho_a^2}{c_a^2} \left(\frac{9g^2}{4\pi^2 c_a^2 f_\sigma^2} + \frac{c_a^2 A}{c_w^2 B} + \frac{3g}{2\pi c_w f_\sigma} \frac{C}{B} \right) & z > \zeta \end{cases} \quad (2.3.17)$$

with ocean wave frequency f_ζ , acoustic frequency $f_\sigma = 2f_\zeta$. Coefficients A , B , and C are the resonance terms because of the finite ocean,

$$\begin{aligned} A &= \mathcal{R}^2 \cos^2(\varphi) + \sin^2(\varphi) \\ B &= \cos^2(\varphi) + \mathcal{R}^2 \sin^2(\varphi) \\ C &= (1 - \mathcal{R}^2) \sin(\varphi) \cos(\varphi) \end{aligned}$$

with reflection coefficient $\mathcal{R} = (\rho_w c_w) / (\rho_b c_b)$, obtained from the continuity of pressure between water (w) and the solid sea floor (b). It is noted that c_b for the elastic interface is approximated by the shear velocity since the shear velocity is larger than the compressional velocity c_w [*Jensen et al., 2011; Brekhovskikh and Godin, 1990*].

Column resonance depends on the acoustic wavelength in water λ_w and the ocean depth D , assuming the microbaroms radiate on a direct path between surface and solid sea floor (bedrock) without spreading. As signals with the same frequency are combined, this results in an interference pattern caused by their superposition. The amount of interference depends of the phase difference $\varphi = 2\pi D/\lambda_w$ between the signals. Vertical resonance occurs when $D/\lambda_w = 1/4 + n/2$ for any integer n .

In the oceanic source spectral density ($z \leq \zeta$), ρ_w^2/c_w^2 states second-order radiation into the water [*Longuet-Higgins, 1950*]. For the atmosphere ($z > \zeta$), second-order

Table 2.1: *Microbarom source modelling environmental parameters [Jensen et al., 2011].*

Parameter	Symbol	Value
Seawater density	ρ_w	1000 kg m ⁻³
Speed of sound in seawater	c_w	1500 m s ⁻¹
Air density at sea level	ρ_a	1.2466 kg m ⁻³
Speed of sound in air	c_a	337.31 m s ⁻¹
Sea floor density	ρ_b	2700 kg m ⁻³
Shear wave velocity in sea floor	c_b	2500 m s ⁻¹

radiation from water into air is given by ρ_a^2/c_w^2 [Brekhovskikh et al., 1973] and second-order compression of air by $9g^2/(4\pi c_a^2 f_a^2)$ [Waxler and Gilbert, 2006].

Equation (2.3.17) becomes the microbarom source model for an infinitely deep ocean when $\mathcal{R} = 1$ (solid sea floor is water) such that the resonance terms become $A/B = 1$ and $C = 0$.

The ratio of atmospheric and oceanic source spectra, independent of the sea state, yields

$$\sqrt{\frac{\mathcal{D}_a}{\mathcal{D}_w}} \approx \frac{\rho_a c_w}{\rho_w c_a} \sqrt{\frac{c_a^2}{c_w^2}} = \frac{\rho_a}{\rho_w} \quad (2.3.18)$$

which is in agreement with the previously stated reduced impedance contrast. The ocean spectra is approximately a factor 10^3 stronger than the atmospheric signal.

■ 2.3.4 Implementation and examples

Implementation using ECMWF two-dimensional wave spectra

The sea state is described by two-dimensional wave spectra (2DFD) obtained from the ECMWF deterministic high-resolution ocean wave model (HRES-WAM) analysis. The wave model is coupled to the high-resolution atmosphere model (HRES) which allows two-way interaction between the ocean waves and the surface winds. Wave spectra, from January 2010 onward [Cycle 36r1 *ECMWF*, 2016], consist of 36 wave directions, from 5° to 355° in steps of 10°, and 36 wave frequencies increasing exponentially from 0.0345 Hz to 0.9695 Hz ($f_{\zeta, n+1} = 1.1f_{\zeta, n}$). Frequencies range from ~29 s to 1 s, spanning nearly the entire GW domain. Data is available every 6h, globally, with latitudes up to 85° and a horizontal resolution of 0.25° before March 2016 and 0.125° after. 2DFD data is implemented on the native reduced grid to avoid resampling and interpolation issues of the spectral data.

Global bathymetry data is obtained from either ETOPO1 [1 arc-minute, *Amante and Eakins*, 2009] or GEBCO [30 arc-seconds, *Weatherall et al.*, 2015]. The data is first down sampled applying a low pass cosine filter in the frequency domain followed by bilinear interpolation to obtain the ocean depth at the wave model grid points.

The environmental parameters used are listed in Table 2.1.

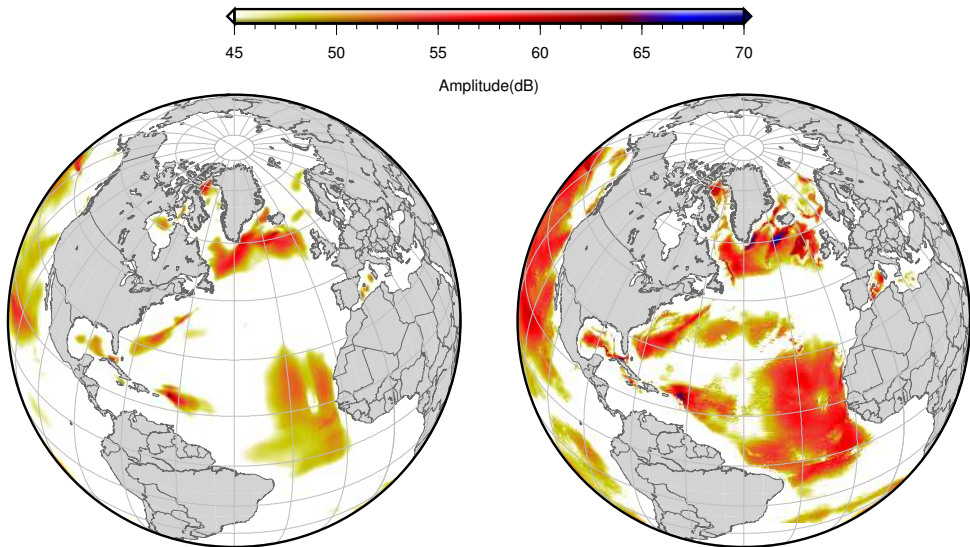


Figure 2.17: Microbarom source amplitude using the ECMWF operational HRES WAM analysis on 10 September 2017 (left) assuming an infinite ocean depth [Waxler and Gilbert, 2006] and (right) for a finite ocean depth [Waxler et al., 2007].

Examples

Figure 2.17 shows the spatial distribution of atmospheric microbarom source amplitude using two-dimensional wave spectra of the ECMWF operational HRES WAM analysis for both the infinite and the finite ocean depth source models. The microbarom source spectral density \mathcal{D}_a is integrated over the entire WAM frequency range. The intense source regions near Puerto Rico and The Bahamas correspond to hurricane induced microbaroms [e.g. *Stopa et al.*, 2011; *Blom et al.*, 2014] by tropical cyclones Jose and Irma, respectively. Including finite ocean depth resonances not only increases the mean source amplitude by ~ 10 dB but also triggers (e.g. Norwegian Sea) or damps (e.g. Hudson Bay) certain regions.

The distribution of atmospheric microbarom hotspots and corresponding frequencies are shown in Figure 2.18 and in Figure 2.19, assuming an infinite and finite ocean depth, respectively. Most prominent sources are located in the northern Atlantic Ocean, northern Pacific Ocean and Southern Ocean.

Figures 2.20 and 2.21 show the latitudinal variation of the stacked microbarom amplitudes, assuming an infinite and finite ocean depth, respectively. Figures 2.20 and 2.21 reveal typical resonance frequencies of the various oceans, with a clear minimum for the northern Atlantic Ocean. Both amplitude and frequency indicate a clear seasonal variation, which is most pronounced for the NH.

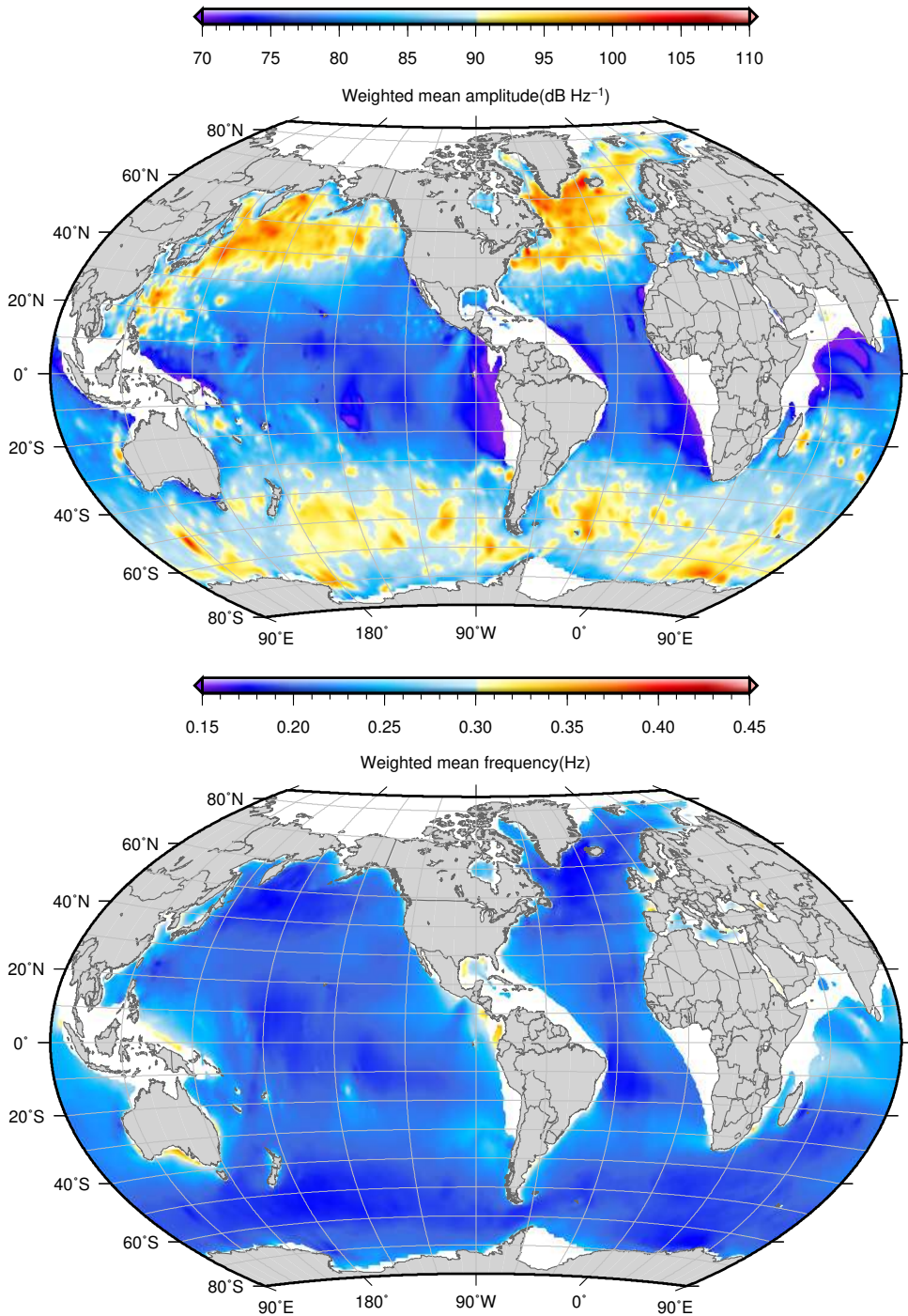


Figure 2.18: Map of 5 year stacked microbarom peak spectral amplitudes and frequencies assuming an infinite ocean depth [Waxler and Gilbert, 2006]. Source modelling is obtained using the ECMWF operational HRES WAM analysis, twice a day, from 2011 to 2015.

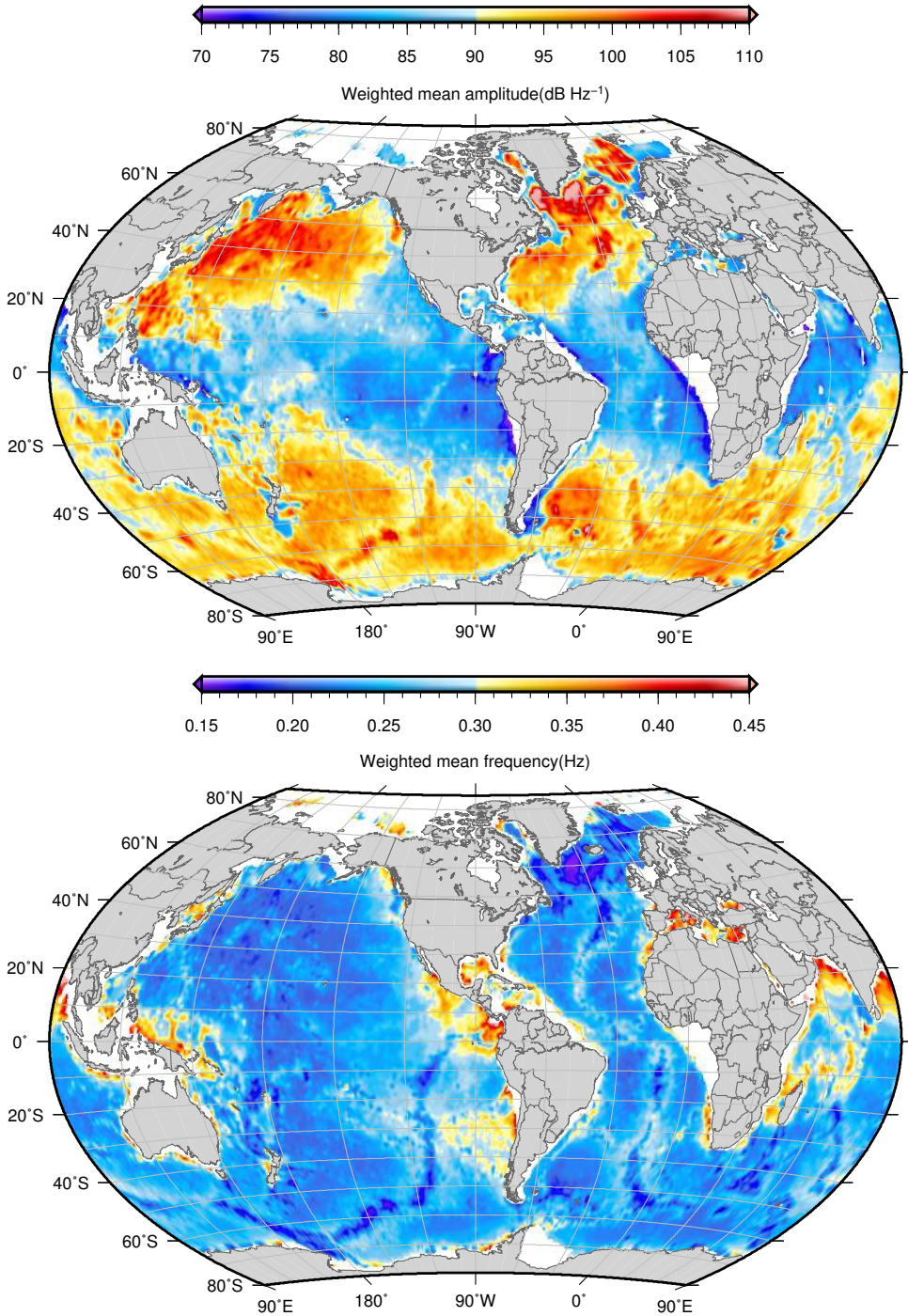


Figure 2.19: Similar to Figure 2.18, now for a finite ocean depth [Waxler et al., 2007].

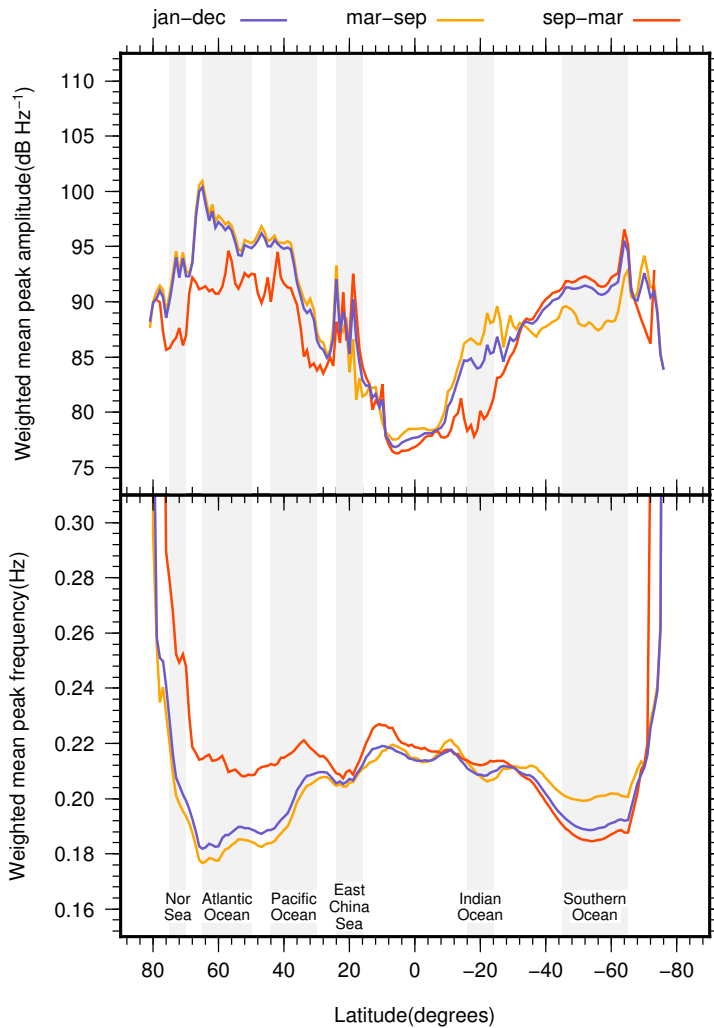


Figure 2.20: Latitude variation of 5 year longitudinally stacked microbarom peak spectral amplitudes and frequencies, for the entire period and (jan-dec) and summer/winter (mar-sep and sep-mar), assuming an infinite ocean depth [Waxler and Gilbert, 2006]. Source modelling is obtained using the ECMWF operational HRES WAM analysis, twice a day, from 2011 to 2015.

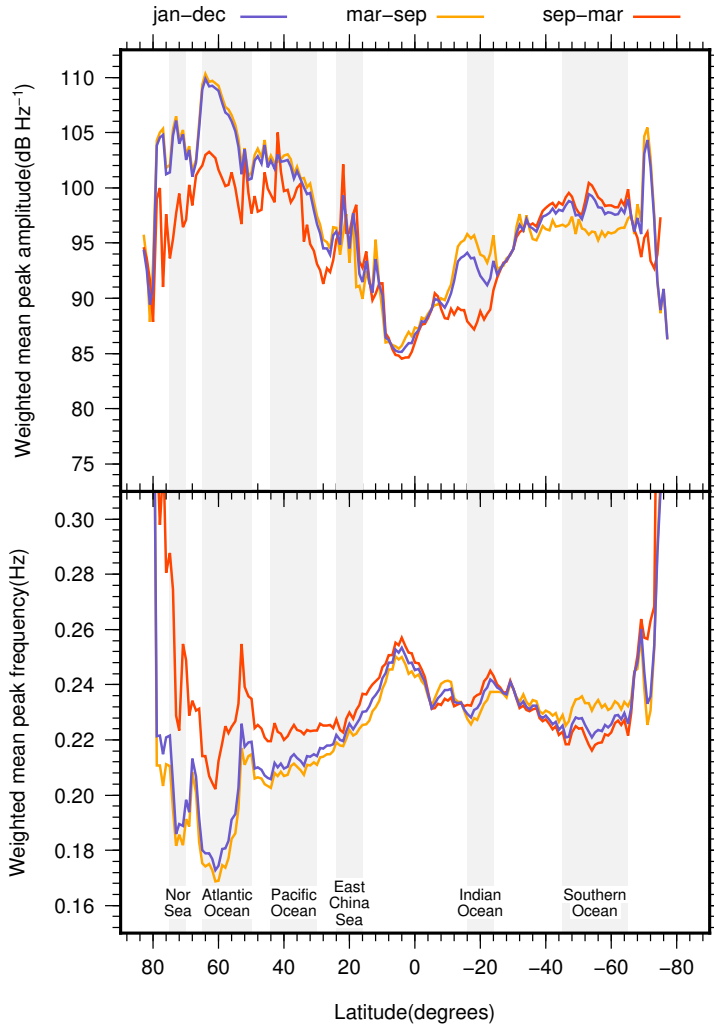


Figure 2.21: Similar to Figure 2.20, now for a finite ocean depth [Wasler et al., 2007].

3

The life cycle of a sudden stratospheric warming from infrasonic ambient noise observations

Abstract A method is presented to study the life cycle of a sudden stratospheric warming (SSW) using infrasonic ambient noise observations. The potential of infrasound is shown to provide the missing observations required by numerical weather prediction to better resolve the upper atmosphere. The 2009 major SSW is reanalyzed using the Evers and Siegmund (2009) data set. Microbarom observations are evaluated to identify detections that cannot be explained by the analysis of the European Centre for Medium-Range Weather Forecasts. Identified differences can be related to either the altitude limit of the analysis, not resolving thermospheric ducts, or to an actual error in the analysis. Therefore, a first-order model is used to relate observations with the analysis, existing of the *Waxler et al.* [2007] microbarom source model, including bathymetry to allow column resonances, and an atmospheric propagation model using three-dimensional ray tracing. Daily normalized spectral powers are proposed to distinguish stratospheric from thermospheric return height, based on the different signature of solar tidal amplitude fluctuations. It is shown that a SSW is not a smooth event as following from the analysis but a series of abrupt changes with a period of 10 to 16 days, increasing in intensity and duration. This is in agreement with the wave period of Rossby waves, interacting with the stratospheric circumpolar vortex. The type of vortex disturbance, split or reversal, can be deduced from the combined effect of the change in back-azimuth direction, solar tidal signature type, and/or phase variation of the amplitude variation of the observed microbaroms.

3.1 Introduction

An optimal estimate of the true state of the atmosphere, called the analysis, is widely used in many fields of research. The analysis is a product of the data assimilation system, given as input a set of observations and a first-guess field. The first-guess field is defined by the time integration of the model equations from the previous analysis. A good analysis, which is what everyone desires, requires both a good model and good observations. However, observations can be problematic, because a lot of them are required (in space and time) with resemblance with the model itself. If observations deviate too much from the first-guess, they are neglected.

Improving forecasts involves resolving the stratosphere and assimilating upper atmospheric data [Ramaswamy *et al.*, 2001; Gerber *et al.*, 2009]. Stratospheric and lower mesospheric temperature observations are dominated by Advanced Microwave Sounding Unit type A (AMSU-A) observations, available from more than a dozen satellites, and are directly assimilated in, e.g., the European Centre for Medium-Range Weather Forecasts (ECMWF) models.

In the stratosphere, global circulation is derived from only these temperature observations. The stratospheric circumpolar vortex is driven by a temperature gradient between the equator and the poles, resulting from the unequal solar insolation. The seasonal variation in the atmosphere's heat balance changes the direction of the circumpolar vortex around the vernal and autumnal equinoxes. For this induced geostrophic circulation, the Coriolis force balances the horizontal pressure gradient [Muench, 1965]. In summer, the circumpolar vortex is easterly, characterized by a stable stratospheric wind and temperature structure. In winter, however, the westerly circumpolar vortex is stronger but unstable. The latter is essentially the topographically induced instability of Rossby waves due to the conservation of the planetary vorticity [Chao, 1985]. This instability allows midwinter Sudden Stratospheric Warmings (SSWs), occurring approximately twice every three years [Charlton and Polvani, 2007]. Within a week the stratospheric temperature, poleward from 60° latitude, increases 25°C resulting in dramatic changes of the circumpolar vortex [McInturff, 1978]. Enhanced vertical propagation of planetary waves, consisting primarily of zonal wave numbers 1 and 2, from the troposphere into the stratospheric polar vortex can trigger a SSW [Matsumo, 1971; Andrews *et al.*, 1987; Kodera *et al.*, 2013] (see Subsection 1.1.3). Due to this large-scale phenomena, a SSW is the primary atmospheric variation, being the clearest and strongest proof of the dynamical coupling between the stratosphere and troposphere [Charlton and Polvani, 2007; Shaw and Shepherd, 2008]. Because the slow recovery of the polar vortex in the lowermost stratosphere following an SSW, there is a long influence of the lower stratosphere on the troposphere [Gerber *et al.*, 2009]. AMSU-A is capable of capturing the fast temperature variations related to the SSW. But due to the very rapid changes, the first-guess field and observations differ significantly resulting in a possible rejection of all AMSU-A data. Consequentially, the quality of the analysis, and thus the forecast, will reduce. To improve the analysis in times of a SSW, additional upper atmospheric observations are required.

Infrasound, used as a verification technique for the Comprehensive Nuclear-Test-

Ban Treaty (CTBT), has shown its ability to act as a passive remote sensing technique to probe the upper atmosphere [Donn and Rind, 1971; Le Pichon *et al.*, 2010; Green *et al.*, 2012; Assink *et al.*, 2012]. Infrasound propagates through the atmosphere, up to thermospheric altitudes, retaining information on the whole atmosphere in the passive observations at the surface [Drob *et al.*, 2003]. Previous studies have shown that infrasound can be used to monitor the seasonal change in direction of the stratospheric polar vortex around the equinoxes by looking at signals arriving from the opposite direction [Garcés *et al.*, 2004; Landès *et al.*, 2012] or changes in mean amplitude variations of ambient coherent noise [Rind and Donn, 1978]. Stratospheric changes of wind dedicated to a SSW can be monitored similarly, by looking at signals arriving from the opposite direction than expected under regular winter conditions [Evers and Siegmund, 2009; Hedlin *et al.*, 2010], or by looking at simultaneous arrivals from two stratospheric ducts [Assink *et al.*, 2014a]. Evers *et al.* [2012] studied the temperature effect of a hot stratosphere during a SSW on infrasound propagation, observing the shadow zone. During a SSW, the extent of the classical stratospheric shadow zone (~ 200 km) reduces by a factor of 2, leading to extremely small shadow zones. Although infrasound has clearly shown its potential in probing the upper atmosphere, with clear signatures of a SSW, it is not yet used, or known, for numerical weather prediction (NWP). So, in what extend can infrasound now contribute to NWP to better resolve a SSW?

Therefore, the 2009 SSW data set of Evers and Siegmund [2009] is reanalyzed to identify trends in infrasound ambient noise observations, due to a coherent signal from a finite source region in the oceans, that cannot be explained by the ECMWF analysis. Microbaroms are atmospheric pressure oscillations, radiated from ocean surface wave-wave interaction at double the ocean surface wave frequency [Gutenberg, 1939; Longuet-Higgins, 1950]. Large regions of high-energetic ocean waves, e.g., ocean swell and marine storms, radiate almost continuous acoustic energy well characterized by a radiation frequency of 0.2 ± 0.1 Hz. Because microbaroms vary in space and time, a source model is required. Microbaroms can be modelled using a two-fluid model, over air and seawater, and an ocean-atmosphere model providing the sea state [Waxler and Gilbert, 2006]. The Waxler and Gilbert [2006] infinite ocean microbarom radiation source model has been validated by Walker [2012] and Stopa *et al.* [2012], studying ambient swell and hurricane induced microbaroms, respectively. In this study, the Waxler *et al.* [2007] finite ocean microbarom radiation source model is used, not yet validated, which takes into account the effect of resonance due to bathymetry affecting the source location, amplitude, and frequency. The data set of Evers and Siegmund [2009] is limited to only the Arctic infrasound observations, containing the clearest infrasonic signature, to clarify this study. Similar analyses of more recent winters, using the same infrasound arrays, can be found in appendix B.

The chapter is organized as follows. The data used are explained in Section 3.2. The microbarom source model, atmospheric propagation model, and their combination to simulate the microbarom observations are described in Section 3.3. The results of the observations, microbarom source model, and the simulations are presented in Section 3.4. In that section, additional analysis is performed to determine

the atmospheric return height using only observed amplitude variations. Section 3.5 explains the life cycle of the 2009 SSW. Finally, discussion and concluding remarks are given in Section 3.6.

3.2 Data

■ 3.2.1 Arctic infrasound observations

Three months of infrasound recordings, from December 2008 to February 2009, of two (near) Arctic infrasound arrays is used. These stations are in place for the verification of the Comprehensive Nuclear-Test-Ban Treaty (CTBT) and are part of the International Monitoring System (IMS). The IMS is a global network providing infrasound, seismic, hydroacoustic and radionuclide recordings, designed to detect and locate nuclear explosions in the atmosphere, ocean, and solid earth [Dahlman *et al.*, 2009]. Infrasound is recorded using arrays, consisting of at least four microbarometers. The sensors have a flat frequency response in the pass band from 0.08 to 4 Hz and are sensitive to amplitudes of several mPa up to tens of pascals. Pressure fluctuations are sampled at 20 Hz. In 2009, two out of three (near) Arctic IMS infrasound arrays were operational: IS18 in Qaanaaq, Greenland (77.5°N 69.3°W), and IS53 in Fairbanks, Alaska (64.9°N 147.9°W). The station layouts and locations of the two operational stations are provided in Figure 3.1. Both arrays consist of eight elements and have an aperture of 1170 and 1980 m, respectively. The layout is designed such that the array response function has a circular response for the desired frequency range and suppresses unwanted side lobes to avoid spatial aliasing (see Subsection 2.1.1). To reduce wind noise, each array element is connected to a passive wind noise reduction system. This is a series of pipes with discrete inlets, spatially integrating the pressure field to increase the signal-to-noise ratio [Hedlin *et al.*, 2003; Walker and Hedlin, 2009].

Signals are filtered using a second-order Butterworth band-pass filter with corner frequencies of 0.1 and 0.5 Hz. Possible detections, coherent signals, are obtained applying the Fisher ratio (F) in the time domain [Melton and Bailey, 1957] with a moving window of 12.8 s (256 samples) with 50% overlap between successive windows. The Fisher ratio provides an estimate of the detection probability and is related to the signal-to-noise-ratio (SNR) assuming normal distributed uncorrelated noise: $F = N \cdot \text{SNR}^2 + 1$, with N the number of array elements (see Subsection 2.1.2). The slowness grid for the beamforming is defined from 0 to 360° for back azimuth (ϕ_b) and from 250 to 500 m s^{-1} for apparent velocity (c_{app}) with steps of 1° and 5 m s^{-1} . For each time window 18,360 beams are examined. Subsample time shifts are obtained by bicubic interpolation of the time signals. The maximum value of F corresponds to the best-beam and a possible detection. Let F_ϕ be the maximum F for each back azimuth angle ϕ_b . Multiple detections per time window are allowed by determining the local maxima of F_ϕ , applying a one-dimensional peak detection algorithm. For each detection the time signals of all sensor are aligned, based on the array response travel time delays, and averaged to obtain the best-beam signal. The energy spectrum or amplitude spectral density (ASD) of each best-beam with

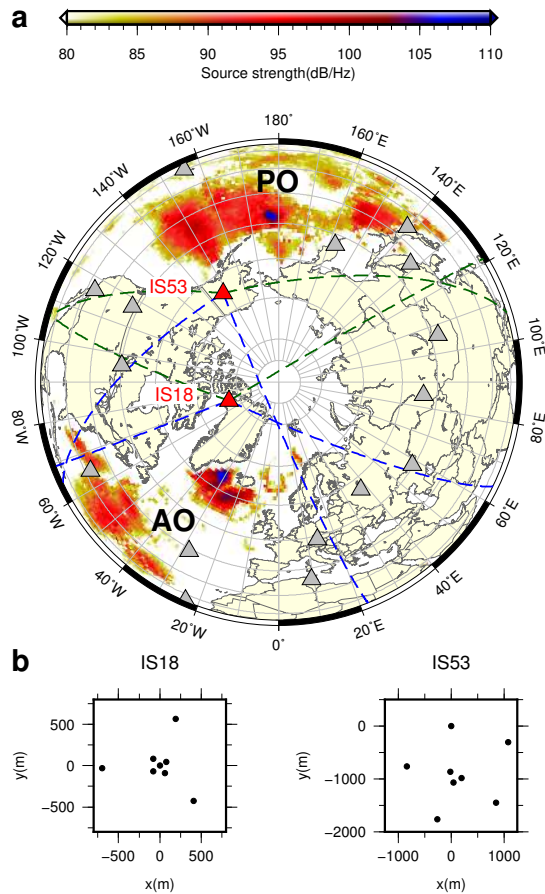


Figure 3.1: Map of infrasound arrays of the IMS for the verification of the CTBT on the NH at latitudes higher than 15° N. (a) Red triangles indicate the locations of the two (near) Arctic arrays used, IS18 and IS53, respectively. Grey triangles correspond with the remaining certified IMS infrasound locations for the period of the warming. Colour coded are the microbarom amplitudes in the Atlantic and Pacific Ocean corresponding to 19 January 2009 at 12 UT, applying the Waxler and Gilbert [2006] model including bathymetry [Waxler et al., 2007]. Dashed lines indicate the used back azimuth limits of the arrays toward the AO (blue) and PO (green). (b) The geometrical configurations of arrays IS18 and IS53 are given in the two bottom frames.

a length of 204.8 s (4096 samples) is determined by applying the fast Fourier transform (FFT) and a flat top taper window, to correct for amplitude leakage due to the finite signal. As the determination of the atmospheric return heights (see Subsection 3.4.2) makes use of variations in the observed spectral amplitudes, a shorter time window is used. The use of a much longer time window for the spectral analysis than for the beamforming ($4096 \gg 256$ samples) can result in an error in the array processing results, as the best-beam can include signals that can influence the SNR. For the energy spectrum shown in Figure 3.2 this is not a problem, as all directions are averaged for each hour. For the determination of the atmospheric return height, based on the spectral power, it is important as the signals of the Atlantic Ocean (AO) and the Pacific Ocean (PO) are separated. For the analysis of the observed amplitudes to determine the return height, the beamforming time window is used, 256 samples, elongated up to 4096 samples by adding zeros. This is done to achieve enough spectral resolution, while minimizing the error of including false signals.

■ 3.2.2 Ocean wave data

The European Centre for Medium-Range Weather Forecasts (ECMWF) operational high-resolution ocean wave model (HRES-WAM, Cy35r1, September 2008) is used as a sea state model for microbarom modelling, consisting of both model data and assimilated buoy and satellite data. The ocean wave model is coupled to the ECMWF high-resolution atmosphere model (HRES). This allows interaction between the ocean waves and the surface winds, which is important for microbarom simulations. The sea state is described by the two-dimensional wave spectra (2DFD), consisting of 30 steps for frequency and 24 for direction, respectively. Integration of the two-dimensional wave spectra over direction and frequency results in the significant wave height for each longitude and latitude (see Subsection 2.3.1). Wave periods (T) range from approximately 28.5 s down to 1.8 s, varying logarithmically ($T_0/T_n = 1.1^{n-1}$), with a maximum horizontal resolution of 0.36° [ECMWF, 2009]. 2DFD are available every 6 h, globally, with latitudes up to 85° .

■ 3.2.3 Atmospheric specifications

Atmospheric analyses are obtained from the ECMWF high-resolution atmospheric model (HRES, Cy35r1, September 2008) making use of the Integrated Forecast System (IFS). It is a global circulation model consisting of assimilated radiosonde, ground, and satellite based atmospheric observations by four-dimensional variational assimilation (4D-Var). HRES comprises of 91 levels with a horizontal resolution of T799 (~ 25 km) up to 1 Pa (~ 78 km). Analyses are available every 6 h. For this study, 6-hourly atmospheric specifications of wind (zonal, meridional, and vertical), temperature, humidity, and pressure are used with a grid resolution of 1° . The two upper levels are neglected. Those levels operate as a sponge layer, filtering wave reflections, which is required for model stability but provides an unrealistically representation of the atmosphere. Therefore, the maximum altitude is limited to 70 km. This is much lower than the thermospheric return height (~ 120 km). Consequently, thermospheric signals cannot be resolved using the ECMWF analysis.

3.3 Model

■ 3.3.1 Microbarom source model

Microbarom source regions are modelled by applying the finite ocean atmospheric microbarom radiation source strength model as described by *Waxler et al.* [2007] (see Section 2.3). The sea state $\zeta(\mathbf{x}, t)$, depending on horizontal position \mathbf{x} and time t , is described by the ECMWF ocean wave model. Altitude z is used to indicate the ocean ($z < \zeta$) or atmosphere ($z > \zeta$) source region, whereas D refers to the depth of the water column.

The fundamentals of the oceanic microbarom radiation model ($z < \zeta$) are first described by *Longuet-Higgins* [1950], proving that the source mechanism is radiation resulting of the interaction of counter propagating ocean waves. The pressure oscillations, due to acoustic radiation, are due to second-order perturbative terms in the expansion of the fluid dynamics equations. This results in a frequency doubling with respect to the surface waves. *Longuet-Higgins* [1950] developed the fundamentals of a finite-ocean microbarom source model, for oceanic microbaroms, only many years later taken into account and applied by *Kedar et al.* [2008]. The oceanic microbarom radiation model, assuming an infinitely deep ocean, was validated by *Hasselmann* [1963]. He related the source strength density to the density of counter propagating waves for a specific frequency, known as the Hasselmann integral (\mathcal{H}),

$$\mathcal{H}(f_\zeta) = \int_0^{2\pi} F(f_\zeta, \phi)F(f_\zeta, \phi - \pi)d\phi, \quad (3.3.1)$$

with F ($\text{m}^2\text{srad}^{-1}$) the directional spectral density function, depending on the ocean wave frequency f_ζ and direction ϕ . Note that the acoustic frequency is double the ocean wave frequency ($f_\sigma = 2f_\zeta$). The spectral density function is approximated by the discrete 2DFD of the ECMWF WAM. The oceanic microbarom radiation source strength spectrum squared is stated in equation (3.3.2) ($z \leq \zeta$).

To simulate the atmospheric component of microbarom radiation ($z > \zeta$), *Brekhovskikh et al.* [1973] extended the Longuet-Higgins microbarom source model with radiation from water into air. *Waxler and Gilbert* [2006] then refined this atmospheric component, including second-order compression of air. Finally, *Waxler et al.* [2007] assumed a finite ocean assuming an elastic sea floor, to take into account the effects of column resonance in the Longuet-Higgins and Brekhovskikh terms. The microbarom source strength spectrum squared, $\mathcal{D}_\sigma(f_\sigma)$, is defined as

$$\mathcal{D}_\sigma(f_\sigma) = 4g^2\pi^4 f_\sigma^3 \mathcal{H}(f_\zeta) \begin{cases} \frac{\rho_w^2 A}{c_w^2 B} & z \leq \zeta \\ \frac{\rho_a^2}{c_a^2} \left(\frac{9g^2}{4\pi^2 c_a^2 f_\sigma^2} + \frac{c_a^2 A}{c_w^2 B} + \frac{3g}{2\pi c_w f_\sigma} \frac{C}{B} \right) & z > \zeta \end{cases} \quad (3.3.2)$$

with gravity acceleration g , speed of sound c_σ , and density ρ_σ , with σ representing atmosphere (a), water (w), or seafloor (b), respectively. Coefficients A , B , and C

are the resonance terms because of the finite ocean,

$$\begin{aligned} A &= \mathcal{R}^2 \cos^2(\varphi) + \sin^2(\varphi) \\ B &= \cos^2(\varphi) + \mathcal{R}^2 \sin^2(\varphi) \\ C &= (1 - \mathcal{R}^2) \sin(\varphi) \cos(\varphi) \end{aligned}$$

with reflection coefficient $\mathcal{R} = (\rho_w c_w) / (\rho_b c_b)$, obtained from the continuity of pressure between water (w) and the solid sea floor (b).

Column resonance is determined by the frequency of the microbarom signal f_σ and the ocean depth D , assuming the microbaroms radiate on a direct path between surface and solid-seafloor without spreading. As microbarom signals are reflected on the solid seafloor, interaction occurs between the downward and upward propagating signals. As signals with the same frequency are combined, this results in an interference pattern caused by their superposition. The amount of interference depends of the phase difference φ between the signals, with $\varphi = 2\pi f_\sigma D / c_w$. The ocean depth is obtained from the General Bathymetric Chart of the Oceans (GEBCO) global 30 arc-second gridded bathymetry data set [Becker *et al.*, 2009], resampled using *grdsample* of Generic Mapping Tools (GMT) version 4.5 [Wessel and Smith, 1991] to match the ECMWF WAM grid.

Equation (3.3.2) becomes the microbarom source model for an infinitely deep ocean, as described in the paper of Waxler and Gilbert [2006], when $\mathcal{R} = 1$ (solid seafloor is water) such that resonance terms become $A/B = 1$ and $C = 0$.

■ 3.3.2 Atmospheric propagation

Sound propagation through the atmosphere is affected by the atmosphere itself, which may result in changes in the wave vector direction (e.g. reflection, refraction) and attenuation of the signal. The relation between density and pressure, affected by temperature (T), determines the adiabatic speed of sound (c_T) of the medium. It is noted that c_T is represented by c_a in equation (3.3.2). As the atmosphere is in motion, sound propagation is affected by the residual of the projected wind in the direction of propagation. Approximating the wave equation for infrasound in a horizontally stratified atmosphere, characterized by temperature and horizontal wind, results in the effective speed of sound c_{eff} [Gossard and Hooke, 1975]. Speed of sound, $c_T = \sqrt{\gamma RT}$, is defined by the ideal gas law with adiabatic conditions existing of the ratio of specific heats, for air $\gamma = c_p / c_v = 1.4$, the specific gas constant $R_{\text{air}} = 287 \text{ J kg}^{-1} \text{ K}^{-1}$, and temperature T depending on position and time. For a fixed horizontal position and time, c_{eff} is defined as

$$c_{\text{eff}}(z, \phi) = c_T(z) + \mathbf{w}_{xy}(z) \cdot \hat{\mathbf{n}}_{xy}(\phi), \quad (3.3.3)$$

with $\mathbf{w}_{xy} \cdot \hat{\mathbf{n}}_{xy}$ the projected horizontal wind in azimuth direction of the sound propagation ϕ at a specific altitude z . Note that all direction angles for the array processing are expressed in back azimuth $\phi_b = \phi \pm 180$, the arrival angle of the ray. The effective speed of sound ratio $c_{\text{eff, ratio}}$, indicating the refractivity of the atmosphere, is defined as the ratio of the effective speed of sound at an altitude z

and at the ground, at equal time and location,

$$c_{\text{eff, ratio}}(z, \phi) = \frac{c_{\text{eff}}(z, \phi)}{c_{\text{eff}}(0, \phi)}. \quad (3.3.4)$$

In order to have signals refracting back to the ground, the effective speed of sound ratio should be near to or greater than one. The effective speed of sound ratio is a useful indicator of infrasound propagation, but does not describe the actual propagation itself.

Infrasound propagation can be described by ray tracing, e.g., [Benamou, 1995; Blom and Waxler, 2012]. In this study, a self-developed ray code is used. Rays are obtained from a high frequency approximation of the wave equation. The wave equation, describing the disturbance of an infinitesimal volume of air in space-time, can be characterized by a surface in space-time, the eikonal, describing only the position of the wavefront instead of the full wave [Stone and Goldbart, 2009]. Therefore, amplitudes are no longer resolved. The eikonal operates as a high frequency approximation, with rays spanning this characteristic surface. Applying a canonical transformation to the eikonal results in the equations of motion, the ray equations for position and slowness.

Although ray tracing does not include amplitude information, amplitudes can be associated to each ray, described by the transport equation, based on geometrical spreading of the rays [Jensen *et al.*, 2011]. Geometrical spreading is obtained from the Jacobian determinant for ray coordinates azimuth and elevation. Atmospheric attenuation (α) includes incoherent transmission loss due to geometrical spreading from the rays and frequency dependent absorption by the atmosphere, described by Sutherland and Bass [2004]. Absorption depends upon variations in thermal conductivity, density, and viscosity throughout the medium and concentrations of chemical components.

Ray tracing is applied in spherical coordinates using three-dimensional atmospheric specifications, interpolated by cubic splines with a smooth kernel. Ray elevation angles range from 0 to 40° with steps of 1° and azimuth angles range from 0 to 358° with steps of 2°. Elevation angles larger than 40° do most likely refract beyond the stratosphere, but cannot be obtained using the ECMWF analysis. A source frequency of 0.2 Hz is assumed for all rays, as this only influences the atmospheric absorption, which is rather low for stratospheric returns and does not vary significantly due to small changes in source frequency. Only reflection points on the ground and sea surface are stored for the simulated microbarom observations. Due to the low frequencies, rays that refract close to the surface can also result in signals observable at the ground. Therefore, rays that refract close to the surface, at maximally 1.7 km above the earth surface (0.20 Hz times 340 m s⁻¹), will also result in a reflection point for the simulations.

■ 3.3.3 Simulated microbarom observations

The ECMWF analysis is evaluated, using ray tracing, to identify trends in stratospheric return height ambient noise observations that cannot be explained by the

analysis. A proper propagation path is described by the eigenray between a microbarom source and the array, resulting in a detectable amplitude. As many active microbarom regions can be potential microbarom sources, ray tracing is applied reversely to avoid determining all possible eigenrays of all possible source locations to the array. Using reverse ray tracing, infrasound propagation starts at the array (see Figure 3.1) and is propagated backward with reflection points being possible source locations. Each ray between receiver and possible source location is thus an eigenray, with the initial azimuth angle of the ray corresponding with the observed back azimuth angle. Reverse ray tracing is acquired by modifying the atmospheric profile, thus reversing the direction of the horizontal wind and changing the sign of the horizontal components of the metrical tensor for the atmospheric derivatives used in the ray and Jacobian equations. The use of reverse ray tracing with only a fixed set of rays does result in eigenrays, but these rays do not necessary correspond with the actual observed source. It is possible that a nearby, weaker source is reached.

Possible source locations, oceanic reflection points, are evaluated by a simple first-order coupling between the source and propagation model. Assume each reflection point behaves as an independent point source constant over the area S , then the simulated microbarom power becomes

$$A_{\text{sim}}^2 = \alpha \mathcal{D}_a S, \quad (3.3.5)$$

with the atmospheric attenuation α (m^{-2}), due to spreading and absorption, and the microbarom source energy spectrum \mathcal{D}_a ($\text{Pa}^2 \text{Hz}^{-1}$).

As the source area S is unknown, the normalized simulated microbarom power can be defined as [Waxler and Gilbert, 2006]

$$\hat{A}_{\text{sim}}^2 = \alpha \mathcal{D}_a. \quad (3.3.6)$$

The simulated microbarom spectral amplitude, A_{sim} , should be equal to the observed microbarom spectral amplitude, A_{obs} , such that the required source area S holds

$$S = A_{\text{obs}}^2 / \hat{A}_{\text{sim}}^2. \quad (3.3.7)$$

From equation (3.3.7) the corresponding source radius is calculated, assuming a perfect circular source area of constant amplitude. The source radius is used to validate the plausibility of the simulations, by identifying unrealistic source dimensions. Realistic source radii are limited to 1000 km, equivalent to half the northern Atlantic Ocean.

Microbarom spectral amplitudes are interpolated in space and time to obtain the source amplitude for each oceanic reflection point. Microbarom simulations are filtered by applying the following criteria. Only oceanic reflection points with an attenuation of 60 dB Re 1m and more are included. An attenuation smaller than 60 dB Re 1m over a distance of >1000 km most likely corresponds with a ray caustic, resulting in a minus infinite or unrealistically small attenuation.

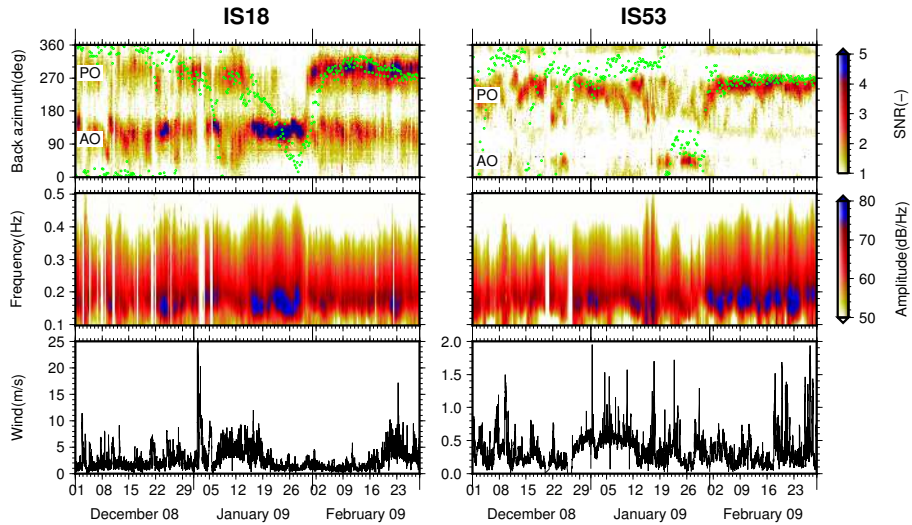


Figure 3.2: From top to bottom are shown, array processing results and wind observations at the array site for IS18 (left) and IS53 (right), respectively. (top) The maximum hourly signal-to-noise ratio for each back azimuth direction per hour as derived from the Fisher analysis. Only events with a $SNR > 1$ are used. The green dots represent the wind direction at 50 km altitude above the array, derived from the ECMWF HRES analysis model. (middle) The energy spectrum, averaged per hour. (bottom) The wind measured at the array site, low-pass filtered for a period of one hour.

3.4 Results

■ 3.4.1 Infrasonic observations

Figure 3.2 shows the infrasonic observations of arrays IS18 (left panes) and IS53 (right panes), respectively. Shown are processing results and array surface wind strength for the period of 1 December 2008 up to 28 February 2009. The energy spectrum shows a good correlation with the expected 0.2 ± 0.1 Hz band for microbaroms. The surface wind strength, from high-resolution sonic anemometers at the array central element, indicates the noise level at the array. Increased noise levels, resulting from strong surface winds, degrade the infrasonic detectability by reducing the signal coherency over the array [Walker and Hedlin, 2009]. This can be seen in the SNR. Surface winds are inversely related with SNRs, as F is coupled to the source activity and array coherency.

Figure 3.3 shows the comparison of the microbarom detections with the microbarom radiation model for amplitude and frequency. The microbarom observations and the source model agree well. Despite the influence of the atmospheric propagation, there is a good resemblance between observed and simulated amplitudes and frequencies as well as between the observed SNR and modelled amplitude. For

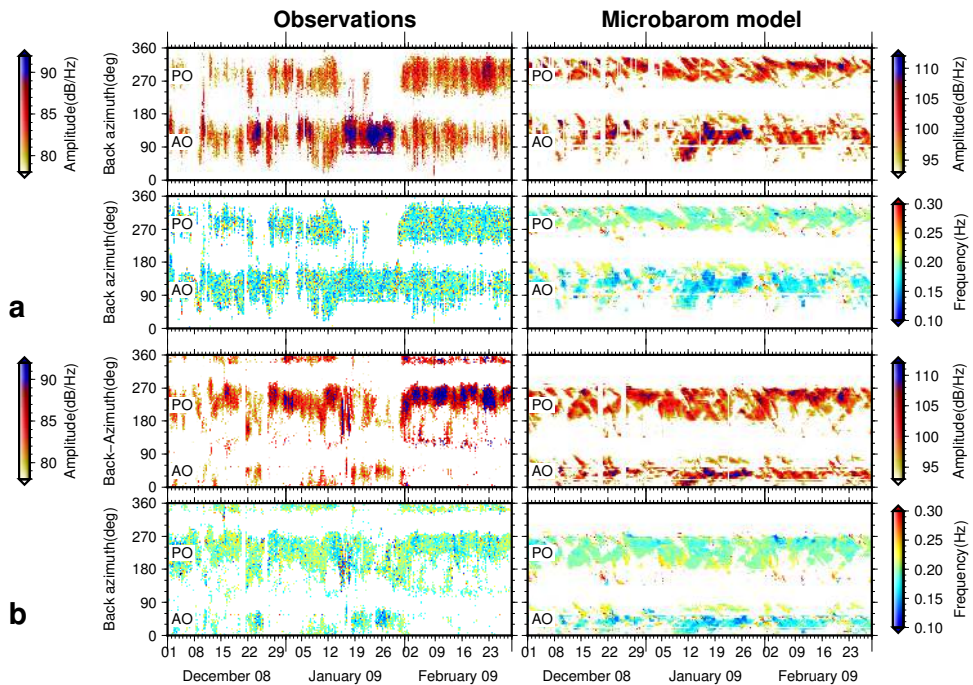


Figure 3.3: Comparison of the infrasound observations (left) and the microbarom source model (right), for (a) IS18 and (b) IS53, respectively. Each subfigure shows the spectral amplitude (top) with the corresponding frequency (bottom), per degree back azimuth for each hour for the observations and for each 6 h for the microbarom source model. For the observations, the spectral amplitude corresponding to the maximum SNR is shown, and for the microbarom source model, the maximum spectral amplitude. Gaps appearing in the array processing results due to high wind noise or data loss (see Figure 3.2) are recreated in the microbarom source model. Microbarom source specifications are obtained from the ECMWF HRES-WAM applying the Waxler et al. [2007] model for atmospheric radiation including bathymetry effects.

both arrays and both oceans, the back azimuth deviation is rather small, except for weaker detections at IS53 toward the north and south-east. Detections with back azimuth angles of $> 300^\circ$ and $120\text{--}150^\circ$ do not appear in the source model. These detections do most likely correspond with the modelled microbarom sources in Figure 3.3, but are affected by atmospheric propagation effects resulting in significant back azimuth deviations and lower SNR and amplitudes.

Table 3.1 presents the mean microbarom peak frequency, for the observations and the microbarom source model. Interesting is the difference in microbarom frequency between AO and PO, which is present in both the observations and source model. The lower frequencies for the AO can be explained by the deeper ocean, resulting in the resonance of lower frequency microbarom signals. This proves the added value of using the finite ocean microbarom source model of *Waxler et al.* [2007], allowing such bathymetry dependent variations. The observed frequencies (see Figure 3.3) show a relation with the direction of the stratospheric polar vortex above the array. Lowest frequencies are observed when the stratospheric duct is stable or in direction of the nearest ocean microbarom source region. IS53 in PO direction observes very low frequencies from 15 to 19 January 2009, with a broader energy spectrum. It is unclear if this is related to the microbarom source, although this does not appear in the microbarom source model, an atmospheric effect or due to wind noise at the array.

The SSW leaves a clear signature in the infrasound observations, as described by *Evers and Siegmund* [2009]. The back azimuth clearly shows the directional change of the stratospheric polar vortex. Both arrays indicate a stratospheric duct to the PO in regular winter conditions, changing to a stratospheric duct to the AO due to the SSW. This agrees with the stratospheric duct of the analysis in Figure 3.4. Before the warming, the stratospheric duct is unstable compared to the situation after, clearly noticeable in the SNR and energy spectrum in Figure 3.2. During 60 days after the onset of the warming, the stratospheric duct slowly descends into the lower stratosphere, followed by anomalous tropospheric weather regimes [*Baldwin and Dunkerton*, 2001]. The slow downward movement of the polar vortex is related to the offset mechanism of a SSW, which is more gradual than the SSW onset [*Limpasuwan et al.*, 2005]. The SSW onset is associated with stratospheric wind reduction anomalies produced by wave driving, which can be rapid. The SSW offset is associated with the radiative cooling of the polar cap, which happens more gradually.

Table 3.1: Mean microbarom peak frequencies, with one standard deviation range, per ocean for both the observations and the microbarom source model.

	AO	PO
IS18	0.187 ± 0.023 Hz	0.190 ± 0.022 Hz
IS53	0.185 ± 0.022 Hz	0.191 ± 0.025 Hz
Model	0.189 ± 0.031 Hz	0.200 ± 0.021 Hz

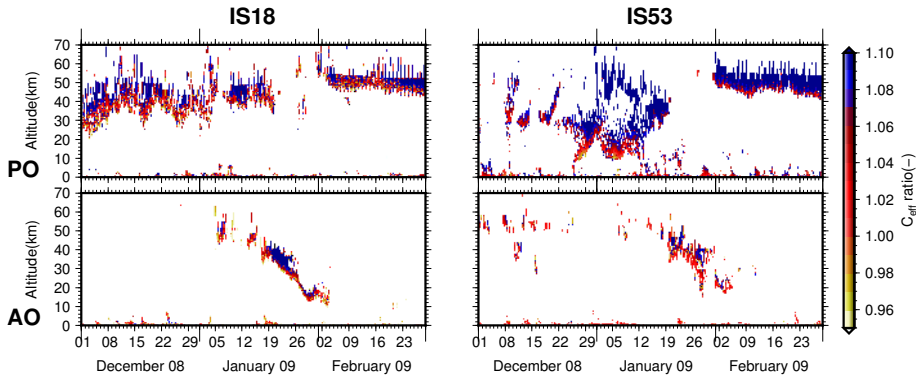


Figure 3.4: Effective speed of sound ratio for arrays (left) IS18 and (right) IS53 for mean back azimuth direction toward the Pacific Ocean (top) and the Atlantic Ocean (bottom).

Figure 3.4 does not explain the propagation of all observations due to the altitude limit of the analysis. IS18 almost continuously receives AO microbaroms, while IS53 almost continuously detects PO microbaroms, even when no stratospheric duct is present. During the warming, the SNR varies, increasing for the IS18 AO microbaroms and decreasing for the IS53 PO microbaroms. Interesting are the observed distant AO microbaroms around 22 December 2008 for IS53, while the analysis does not indicate the presence of a stratospheric duct. It is not yet clear if these detections, when no stratospheric duct is present, are related to either the not resolved thermospheric ducts or an error in the analysis. Therefore, additional information on the atmospheric return height is required.

■ 3.4.2 Stratospheric versus thermospheric return heights

As infrasound propagates through the atmosphere, the signal is continuously influenced by the atmosphere, resulting in an integrated effect at the surface [Drob *et al.*, 2003]. A different influence by the stratosphere and thermosphere will result in a different signature in the detections, allowing both signals to be distinguished. As the stratosphere and thermosphere are exposed differently to solar tidal fluctuations of temperature and wind, a different solar tidal signature is present in the observed microbaroms. In the stratosphere, the diurnal thermotidal oscillation is primarily excited due to water vapour heating in the troposphere. This remains true until the thermosphere, where viscosity, conductivity and electromagnetic damping may attenuate incoming waves [Lindzen and Chapman, 1969]. The thermosphere is characterized by high attenuation caused by the low density [Sutherland and Bass, 2004]. Therefore, thermospheric semidiurnal solar tides are excited to a greater degree due to the heat generated by the absorption of solar ultraviolet radiation by oxygen around 120 km altitudes. Irregular heating of the atmosphere results in a variation of the thermospheric return height, twice a day, due to the change in wind

strength and attenuation.

The typical signature is represented in the detection characteristics, for example, the number of detections, back azimuth angle, apparent velocity, bandwidth, and amplitude [Le Pichon *et al.*, 2005; Whitaker and Mutschlecner, 2008; Green *et al.*, 2012]. Assink *et al.* [2012] looked at travel time variations and its relation to return height variations associated with atmospheric tides. All studies make use of strong impulsive sources with a well known position, e.g., volcanoes, which makes it hard to implement the used methodologies on ambient noise. The studies of Donn and Rind [1971], Rind *et al.* [1973], Rind and Donn [1975], and Rind and Donn [1978] statistically relate observed microbarom amplitudes to solar tidal fluctuations using the mean amplitude per time of day (tod), \bar{A}_{tod} . However, the presented method involves long-period averaging, using several months of data, losing all small scale fluctuations of interest. Therefore, \bar{A}_{tod} is calculated for each day.

Atmospheric tides are found in the daily normalized spectral powers (see Figure 3.5) obtained from the best-beam peak spectral amplitudes in direction of the AO and PO for IS18 and IS53, respectively. For each half hour (one pixel), consisting of at least 15 detections with a SNR of 1.5 and more for IS18 and of 1.3 and more for IS53, the peak spectral power is averaged. The mean spectral amplitude per time of day (tod), \bar{A}_{tod} , in direction of the AO and PO, is computed following a method similar to the method described by Donn and Rind [1971]. Variations in the directional daily mean amplitude \bar{A}_{day} , shown below the normalized spectral powers, are in agreement with the expected return heights from the solar tidal signature. Higher daily mean amplitudes are observed for expected stratospheric return heights; for example, see Figure 3.5b in January during the SSW. The colour coded horizontal bar in Figure 3.5 roughly indicates periods with either diurnal or semidiurnal signatures, manually picked.

\bar{A}_{tod} for IS18 shows a clear semidiurnal variation in direction of the AO (Figure 3.5b), in agreement with Donn and Rind [1971], indicating mainly thermospheric return heights. A similar semidiurnal signature is shown by the normalized spectral powers, with periods in agreement with the lack of a stratospheric duct indicated by c_{eff} . In December, when the stratospheric duct is unstable, scattered signals are observed resulting in a rather unclear semidiurnal signature. When the AO duct becomes stratospheric, indicated by the green periods, the tidal signature becomes diurnal, with stronger daily mean amplitudes \bar{A}_{day} . After the warming, the atmosphere stabilizes resulting in a clear semidiurnal signature up to halfway February. From then on the number of detections decreases too much to clearly determine the tidal signature. In PO direction, the dominant signature is diurnal. In December, during the unstable stratospheric duct, the signature is very vague. After the warming, during the first half of February 2009, a weaker peak around 18h can be observed as well. This signature is most likely related to the interactions of the stratospheric and thermospheric tides, corresponding to mixed stratospheric-thermospheric propagation. In the modelling, described in the next subsection, these mixed propagation paths will be missing, similar to the detections related to pure thermospheric return heights.

\bar{A}_{tod} for IS53 in PO direction indicates a diurnal signature. The daily normal-

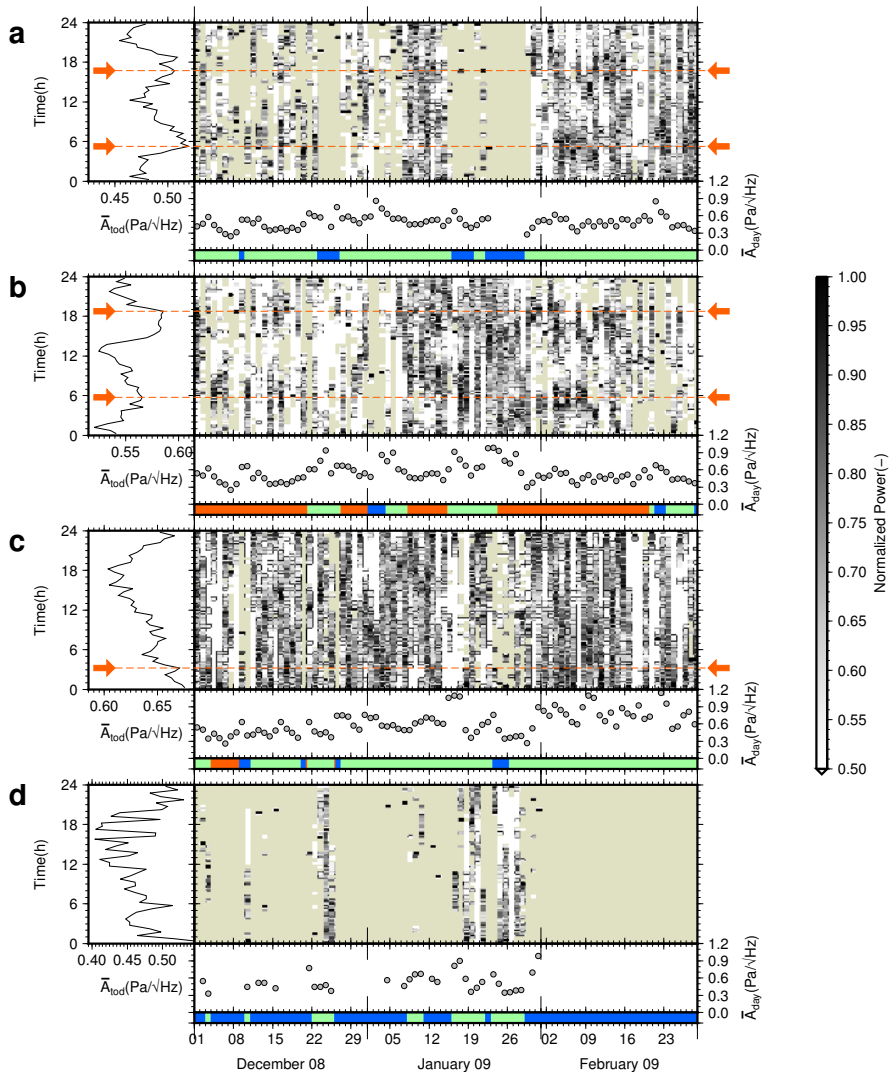


Figure 3.5: Directional time averaged spectral amplitude variations. From top to bottom are shown IS18 in direction of the (a) Pacific Ocean and (b) Atlantic Ocean, IS53 in direction of the (c) Pacific Ocean and (d) Atlantic Ocean. Each subfigure consists of a vertical graph (left) and an image (right) with below one horizontal graph and one colour coded bar. The vertical graph (left) shows the spectral amplitude averaged per time of day, \bar{A}_{tod} , for each half hour. The red arrows and dashed lines indicate the tidal peaks in the mean time of day amplitude, if present. The image (right) shows the half hour averaged spectral power, normalized per day. Each pixel column corresponds with one single day, while each row indicates the time of day. The horizontal graph shows the daily mean spectral amplitude \bar{A}_{day} . The colour coded bar roughly indicates manually picked periods with either no peak (blue), one peak (green) or two peaks (red) per day. Only detections are used with $SNR \geq 1.5$ for IS18 and $SNR \geq 1.3$ for IS53.

ized power reveals significant phase variations of the diurnal signature during the 3 month period. A weak semidiurnal signature is present in early December 2008, which is in agreement with the lack of a stable stratospheric duct in Figure 3.4. In AO direction \bar{A}_{tod} indicates a less pronounced diurnal signature. However, the signature becomes more clear for the normalized power, indicating a clear stratospheric duct at the time of the warming, in agreement with c_{eff} . The IS53 AO detections around 22 December 2008 show a diurnal signature with a maxima around 16 h (see Figure 3.5d) indicating a missing stratospheric duct in the analysis.

Interesting is the phase reversal of the IS53 AO diurnal maximum from approximately 20 h for 17 to 21 January 2009 to approximately 4 h for 23 to 28 January 2009. The reversed phase takes place during the vortex split of the stratospheric polar vortex with a significant directional change of the stratospheric wind. Due to the vortex split, the flow changes significantly but does not completely reverse. Consequentially, the AO duct changes, moving south, resulting in an observable phase change of the diurnal peak. Therefore, a phase change of the diurnal signal is an indicator of a significant directional change of the stratospheric vortex. A similar phenomena can be observed at IS18 in AO direction. During the vortex split, the tidal signature becomes semidiurnal, but less clear than after the SSW indicating a mixed stratospheric-thermospheric path, with a constant phase change due to the continuing directional change of the stratospheric wind.

■ 3.4.3 Simulated microbarom observations

Microbarom observations are simulated to verify the analysis with the expected stratospheric returns resulting from the spectral amplitude variations. Because the atmosphere is a four-dimensional problem (three-dimensional position and time), three-dimensional reverse ray tracing is used with 6 h discrete time steps, assuming the atmosphere is constant along this period, to determine source locations. This implicates a similar behaviour of the mean observed signal for this time window. The microbarom source model of *Waxler et al.* [2007] is used to filter out likely source locations, using the source amplitude, then validated calculating the required source area as described in Section 3.3.3.

The proposed simulation consists of limitations in both the used data and the methodology applied. A major limitation of the data is the vertical limit of the analysis. Therefore, thermospheric and combined stratospheric-thermospheric signals cannot be resolved. Ray tracing has some limitations as well. First of all, the limited number of rays spanning the wavefront results in a decreasing resolution with distance. As a result, some source regions cannot be reached, or correspond with a weaker microbarom region. Second, rays can become chaotic over very long distances, resulting in an unrealistic large attenuation. Finally, ray tracing is affected by caustics, resulting in singularities, enforced by the use of a three-dimensional atmospheric profile due to the increased number of directional changes of rays compared with one-dimensional ray tracing. The assumption of independent microbarom sources behaving as a point source with a circular area S will probably underestimates the radiated microbarom signals, resulting into too low observed

amplitudes¹.

Microbarom simulations for IS18 (see left-hand side of Figure 3.6), can be explained by two phases: before the SSW and from the warming onward. Before the SSW, only a sparse number of simulations in both AO and PO direction are obtained. This is as expected due to the semidiurnal signature present in AO direction and a weaker signature for the PO with an unstable and too northerly stratospheric duct, resulting in unresolved thermospheric and mixed stratospheric-thermospheric paths. From the warming onward, the correlation with the observations improves. Detections with an expected stratospheric return can be propagated using three-dimensional ray tracing and the ECMWF analysis, in AO direction during and in PO direction after the warming, respectively. As expected, the detections with the assumed thermospheric return heights, in AO direction after the warming, are missing. The density of the obtained PO simulations is low compared with the observations, which is most likely due to the too low number of rays. The most distant sources correspond with the very large attenuations and low source amplitudes compared with the peak source amplitude of Figure 3.3. This implies that ray chaos is present. During the warming, the closer AO is sampled much better, with the same number of rays, and results in more realistic simulated amplitudes. Both the simulated back azimuth and the amplitudes of the stratospheric predictions are in agreement with the observations. Two clear differences can be denoted that can be related to possible errors in the analysis. First, during the warming, from 14 to 21 January 2009, too many northerly simulations are present. From the observations, it holds that the warming onset and corresponding change of stratospheric polar vortex is much faster than in the ECMWF model, resulting in a clearer switch from PO to AO duct. Second, at the end of February the analysis tends to deviate slightly southerly, while the observations do not show this deviation. Simulations tend to be too much constrained by the direction of the circumpolar vortex compared with the observations, indicating an offset in the direction of stratospheric polar vortex in the analysis.

Simulations for IS53 (see right-hand side of Figure 3.6) show in general good agreement with the observations, as propagation is dominated by stratospheric return heights. Before the warming, the simulation is similar to IS18. The unstable stratospheric duct in PO direction results in only a few stratospheric simulations which do not reach the active microbarom areas. Although the stratospheric duct is unstable, observations with back azimuth angles of $>330^\circ$ are present, indicating the added value of three-dimensional propagation. After the warming, when the stronger and more constant stratospheric duct is more westerly, these predictions are missing. Only AO, stratospheric, simulations are present during the SSW as expected, with the exception of 22 December 2008. Although a clear stratospheric duct is present (see Figure 3.5), no stratospheric returns can be simulated. The simulations in AO direction from 19 January onward tend to be different from the observations, which are closer concentrated between 30 and 60° back azimuth. Despite the very high attenuation for these simulations, it seems that the core of the microbarom source region is reached, indicated by high source amplitudes. As these

¹As pointed out in Subsection 2.3.3.

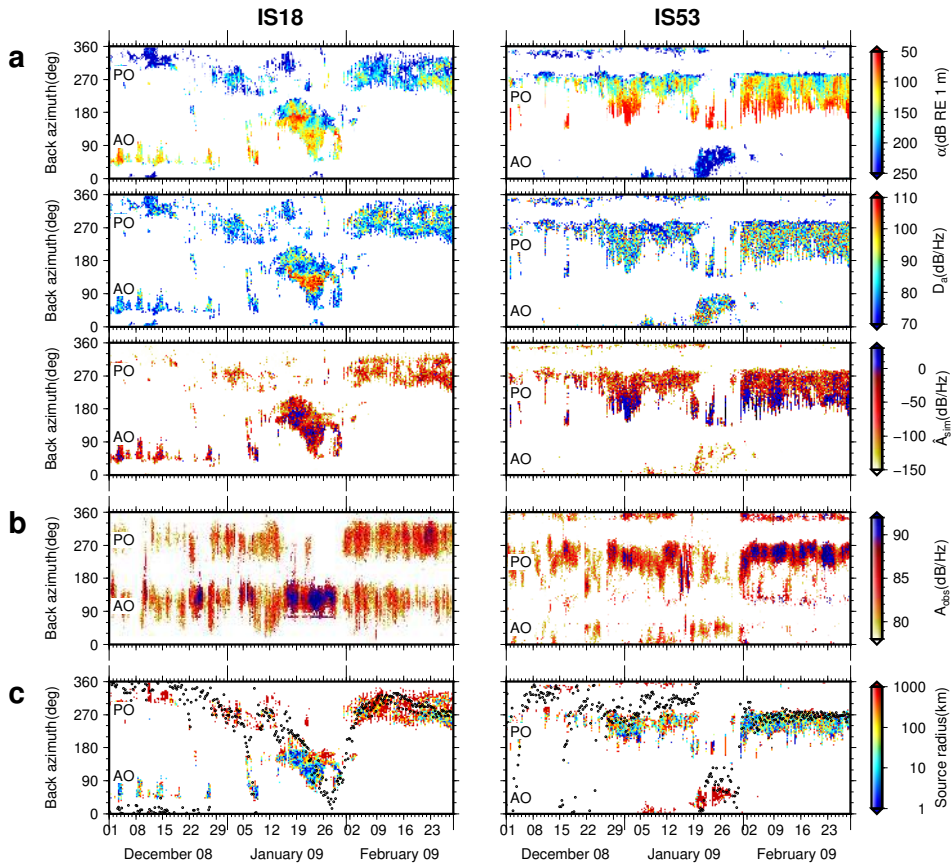


Figure 3.6: Results of the microbarom simulations (a) compared with the observed peak SNR spectral amplitudes (b) and the required source radius (c) of IS18 (left) and IS53 (right) per back azimuth angle in time, respectively. Each back azimuth angle corresponds with the eigenray with the highest microbarom source amplitude. (a) Colour coded are, from top to bottom, attenuation, source spectral amplitude, and simulated received spectral amplitude. (b) Observed amplitudes as shown in Figure 3.3. (c) Required source radius, with black dots representing the wind direction at 50 km altitude above the array derived from the ECMWF HRES analysis.

directions are in agreement with the observed amplitudes, the analysis performs well during the warming. At the SSW offset, from 26 January 2009 onward, a small, increasing, back azimuth deviation between simulations and observations occurs indicating a possible error. At the beginning of February 2009, the observed AO signals are missing in the simulations.

3.5 The life cycle of a SSW

The differences between the observed and simulated expected stratospheric return heights are mostly related with the SSW, indicating the loss of performance of the analysis due to the sudden warming. Most important is the completely missing stratospheric return height AO detections of IS53 at 22 December 2008 using the analysis. Also, during the warming halfway January 2009, the directional change of observed microbaroms for IS18 is much faster and from the opposite direction (northward instead of southward) than shown by the ECMWF analysis.

The analysis indicates a displaced westerly elongated vortex from 18 to 22 January 2009 and a vortex split from 24 to 28 January 2009, corresponding with two stratospheric vortices, followed by a recovery until 4 February 2009. First signatures of the warming are indicated by small variations around 22 December 2008 and 7–8 January 2009. Hemispheric 10 hPa (~ 31 km) wind analysis before, during, and after the SSW can be found in Appendix B (Figure B.1), clarifying the evolution of the stratospheric polar vortex during the 2009 SSW.

Figure 3.5 reveals additional information about the life cycle of the warming. The effect of the warming is most pronounced for IS53 as AO microbaroms with a $\text{SNR} \geq 1.3$ (see Figure 3.5(d)) are only expected in summer or in case of a SSW. Therefore, IS53 is used to describe the life cycle of the warming due to having the clearest signature. Observations reveal more abrupt changes, increasing in intensity and duration, and some differences in the onset and offset. Largest differences are the very clear AO stratospheric duct from 22 to 25 December 2008, completely missing in the analysis, indicating a vortex disturbance, and an earlier stratospheric vortex recovery, at 30 January 2009. The series of abrupt changes can be explained by Rossby wave breaking in the stratospheric polar vortex. Rossby waves, type 2 planetary, have a typical period of 10 to 16 days [Holton, 2004]. In winter, these waves can be forced up into the stratosphere, disturbing the circumpolar vortex via momentum dumping. At the beginning of the winter, in December 2008, the circumpolar vortex is strong but highly unstable, being very sensitive to any disturbance. Therefore, the polar vortex is easily influenced by the Rossby wave breaking, resulting in early SSW signatures on 3 and 10 December 2008 that are rather weak and short, observable in Figure 3.5d by the short periods with low spectral amplitudes. As the vortex is not yet critically disturbed it recovers fast. As the life cycle intensifies due to the repeated wave breaking, the stratospheric vortex weakens, resulting in more extended signatures [Limpasuvan *et al.*, 2004]. This can be denoted from 22 to 25 December 2008, where a clear AO stratospheric duct is present with peak amplitudes at approximately 16 h. Because the stratospheric vortex is not yet fully disturbed, PO detections and simulations are still present. Therefore, the strato-

spheric vortex recovers fast. On 8–9 January 2009, very small disturbances can be denoted, in agreement with the period of Rossby waves, differing from the analysis. The westerly vortex intensifies but displaces slightly as it becomes unstable. A stronger longer lasting disturbance takes place from 17 to 21 January 2009 with a displaced and elongated but rather unstable westerly polar vortex. This results in a stratospheric duct in AO direction and a diurnal maximum at approximately 14 h. The stratospheric vortex, highly disturbed, elongates even more until it splits into two stratospheric vortices from 23 to 28 January 2009, located above Canada and Russia. Due to the location of the vortices, no clear difference in back azimuth is observed. However, a signature of the split can be observed by the loss of the weak PO observations for IS18 and IS53, while the AO shows an amplitude and SNR variation for IS18 and a silence for IS53. This directional change can be denoted as well from the phase change of the diurnal signature, which changes from approximately 20 to 4 h for IS53, due to the different path of the infrasound through the atmosphere. The vortex split is clearly observable in the tidal signature of IS18 in AO direction, which is diurnal during the elongated displaced phase and changes to mixed diurnal and semidiurnal due to the vortex split. Because the two vortices displaces the semidiurnal peaks vary from 2 to 6 h and from 15 to 18 h, approximately. These vortices are mixed into the background flow at the end of January 2009, resulting in a normal winter situation. Because of the weak polar vortex, recovering slowly due to the gradually radiative cooling of the polar cap [Limpasuvan *et al.*, 2005], a stable continuous stratospheric duct in PO direction is present, clearly noticeable in the microbarom observations.

3.6 Discussion and conclusions

In this study, a method is presented to study the life cycle of a SSW using infrasonic ambient noise observations. The 2009 major SSW is used as a case study because of its very clear influence on infrasound propagation [Evers and Siegmund, 2009].

It is shown that the implemented Waxler *et al.* [2007] microbarom amplitude density model with bathymetry, using the ECMWF WAM coupled ocean–atmosphere model input, explains very well the observed microbaroms. The microbarom source model resolves observed ocean depth frequency difference, resulting in slightly lower frequency AO microbaroms. Therefore, infrasound ambient noise is an excellent source to probe the upper atmosphere that can be modelled well. Knowledge of the atmospheric ducting condition of the observed microbaroms is obtained from the infrasonic amplitudes, without any a priori atmospheric information. It is successfully shown that spectral amplitude variations of continuous microbarom observations can reveal whether the sound propagated through the stratosphere or thermosphere, based on the diurnal or semidiurnal signature. These findings are verified by simulations, using three-dimensional reverse ray tracing and the microbarom source model, with the known implications of a vertically limited atmospheric model. Although these limitations, regions of stratospheric propagation can be identified, confirming the amplitude variations method. Thermospheric signals of IS18 toward Atlantic Ocean, with distance of 2000 up to 3500 km (February 2009), can

be observed. This study shows the use of microbarom observations to validate the state of the atmosphere represented by the ECMWF analysis, indicating in general a good agreement but with clear differences dedicated to the SSW. It is shown that infrasound can provide additional information of the state of the atmosphere, with the potential to contribute to NWP, especially in case of a SSW. A vortex displacement and a vortex split leave a clear signature in the infrasound observations, resulting in a solar tidal signature type and or phase variation, which can be distinguished from each other. Maybe in the future infrasound can assist AMSU-A observations to force the first-guess field more toward the actual state of the rapidly varying atmosphere. The observed microbarom amplitudes show more details on the SSW life cycle, with differences in the warming onset and offsets, than present in the ECMWF analysis. Simulations are over constrained by the direction of the circumpolar vortex, whereas observations indicate some differences.

Some further investigation is required. Errors in array processing of simultaneous coherent signal detection, more specific the spectral amplitude estimate, have a significant impact on the amplitude variation method. Errors in separating AO from PO microbarom observations can lead to errors in the amplitude variations and thus tides. Although a larger window for the spectral analysis, filled with zeros, is used to minimize this problem, still other signals can be present in the best-beam, affecting the SNR. Simulated microbarom observations should be obtained as presented by [Waxler and Gilbert, 2006] and stated in Subsection 2.3.3, using the cross spectral density from Greens function as a propagation factor for the microbaroms. Accordingly, one needs to superpose all individual microbarom source patches span by the ray reflection points of interest (an area) instead of a single source for each bounce (a point). Infrasound propagation can be improved by increasing the number of rays significantly, or by adaptively starting new rays when the spreading is too large. The use of another atmospheric propagation model, that can resolve amplitudes, for example, PE or normal-mode, can improve the quality of the validation of the analysis. Some missing stratospheric return heights, assumed to be related to errors an the analysis, can probably be related to fine-scale structure in the wind and temperature and internal gravity waves generating additional arrivals [Kulichkov et al., 2010; Revelle, 2010; Chunchuzov et al., 2011] but are not resolved by the global circulation models as these are below the model resolution.

4

Sudden stratospheric warming forecast evaluation using infrasound

Abstract Accurate prediction of Sudden Stratospheric Warming (SSW) events is important for the performance of numerical weather prediction due to significant stratosphere-troposphere coupling. In this study, for the first time middle atmospheric numerical weather forecasts are evaluated using infrasound. A year of near-continuous infrasound from the volcano Mount Tolbachik (Kamchatka, Russian Federation) is compared with simulations using high-resolution deterministic forecasts of the European Centre for Medium-Range Weather Forecasts (ECMWF). For the entire time span the nowcast generally performs best, indicated by a higher continuity of the predicted wavefront characteristics with a minimal back azimuth difference. Best performance for all forecasts is obtained in summer. The difference between the infrasound observations and the predictions based on the forecasts is significantly larger during the 2013 SSW period for all forecasts. Simulations show that the SSW onset is better captured by the ten-day forecast while the recovery is better captured by the nowcast.

4.1 Introduction

The middle atmosphere has gained more and more importance for the purpose of weather and climate prediction, since increasing evidence indicates that the troposphere and stratosphere are more closely coupled than assumed before [Baldwin and Dunkerton, 2001; Charlton *et al.*, 2004; Shaw and Shepherd, 2008]. Significant effort has been made toward a more comprehensive representation of the atmosphere to better capture the stratospheric variability as well as the stratospheric-tropospheric interactions [Randel *et al.*, 2004; Charlton-Perez *et al.*, 2013].

The strongest manifestations of this stratosphere-troposphere coupling are Sudden Stratospheric Warmings (SSWs) [Charlton and Polvani, 2007; Gerber *et al.*, 2009]. SSWs are regularly occurring features of the winter stratosphere on the Northern Hemisphere (NH), characterized by dramatic changes in the stratospheric wind and temperature. The importance of accurately predicting SSWs is justified by the delayed impact of up to two months that such events have on the weather as experienced on the Earth's surface [Sigmond *et al.*, 2013]. However, significant discrepancies between numerical weather prediction models and the observations they assimilate may lead to rejection of good data by the data assimilation system which means that both the forecasts and analyses of SSWs will likely be inadequate. Recently, the European Centre for Medium-Range Weather Forecasts (ECMWF) has adapted its numerical scheme that reduces this problem, leading to an improved characterization of SSWs [Diamantakis, 2014]. Besides such numerical adaptations, further improvements in SSW predictions can be obtained from better resolving the stratosphere [Gerber *et al.*, 2009; Roff *et al.*, 2011] and mesosphere [Coy *et al.*, 2011] as well as assimilating data from these regions, which have been notoriously difficult to monitor [Ramaswamy *et al.*, 2001]. Only temperature can be resolved by satellites, dominated by Advanced Microwave Sounding Unit type A (AMSU-A) observations, available from more than a dozen satellites, and are directly assimilated in the European Centre for Medium-Range Weather Forecasts (ECMWF) models. In a recent study [Le Pichon *et al.*, 2015], colocated independent ground-based middle atmospheric wind and temperature measurements have been compared to both the ECMWF operational analyses and NASA's Modern Era Retrospective analysis for Research and Applications (MERRA) reanalyses. Significant discrepancies were identified in the region above 40 km in winter as well as for variability on shorter timescales (2–15 day period) above 30 km. Thus, SSWs are a good starting point to apply novel techniques based on infrasonic analysis.

Since the pioneering work of Donn and Rind [1972], there has been much development in the use of ground-based infrasound arrays for upper atmospheric remote sensing [Le Pichon *et al.*, 2005; Lalande *et al.*, 2012; Assink *et al.*, 2013; Fricke *et al.*, 2014; Chunchuzov *et al.*, 2015]. An important application of this technique is the evaluation of atmospheric analyses [Assink *et al.*, 2014b] and ensemble members [Smets *et al.*, 2015]. Recently, various passive acoustic remote sensing studies have focused on SSW events [Evers and Siegmund, 2009; Evers *et al.*, 2012; Assink *et al.*, 2014a; Smets and Evers, 2014].

Volcanoes represent valuable sources for passive acoustic remote sensing of the

atmosphere, as the source location is fixed and the source is relatively well understood [Fee *et al.*, 2010; Matoza *et al.*, 2011; Marchetti *et al.*, 2013]. Here a novel method for the evaluation of middle atmospheric weather forecasts is introduced, using near-continuous infrasound detections from Mount Tolbachik on the Kamchatka peninsula in Russian Federation (55.8°N, 160.3°E). The relative small wavelength and near-continuous character of the source leads to high spatiotemporal resolution evaluations and improved insight in the forecast capabilities in the middle atmosphere, in particular, during SSW events. In addition, it is demonstrated that infrasound can provide useful additional information on SSW onset and duration.

The chapter is organized as follows. Section 4.2 sets out the fundamentals of infrasound as an atmospheric remote sensing technique, including the signature of SSW events on infrasound recordings. Section 4.3 explains the methods in more detail, covering infrasound observations, propagation modelling, and the atmospheric forecasts. Section 4.4 describes the observations, followed by the evaluation of ECMWF forecasts in Section 4.5 with distinction between the entire observation period and the 2013 SSW. Discussion and conclusions are stated in Section 4.6.

4.2 Background

■ 4.2.1 The relationship between wind, temperature and infrasound

Infrasound, or low-frequency acoustic waves, is generated by movement of large volumes of air. Such movements can be created by natural or anthropogenic sources. Examples include interfering ocean waves, volcanic eruptions, (nuclear) explosions, and meteor explosions [Brachet *et al.*, 2010]. Infrasound can propagate efficiently over long ranges, since attenuation is relatively low. Moreover, several wave guides exist between the Earth's surface and the (upper) atmosphere that channel infrasonic energy.

One can distinguish between tropospheric, stratospheric, and thermospheric waveguides. The tropospheric waveguide is bound by the jet stream around the tropopause (~ 10 km). The stratospheric waveguide is formed by the temperature increase due to the presence of ozone and the circumpolar vortex. Generally, the stratospheric waveguide extends to ~ 50 km during the boreal summer. During SSWs, the top of the waveguide may descend into the lower stratosphere and may even extend into the lower mesosphere. The thermospheric waveguide exists due to the strong temperature gradient above the mesopause. However, infrasound is much attenuated at thermospheric altitudes [Assink *et al.*, 2012].

Sound propagation in the atmosphere is a function of wind \mathbf{w} and temperature T , which may vary strongly as a function of location and time. For a fixed source-receiver pair, changes in the mode of propagation (i.e., stratospheric to thermospheric) can be observed as horizontal wind and temperature change seasonally. Ray tracing (Figure 4.1) can be used to model the influence of three-dimensional temperature and three-component wind fields on infrasound propagation [Brekhovskikh and Godin, 1999].

It is instructive to consider a horizontally layered atmosphere to review basic concepts of infrasound propagation. The effective sound speed c_{eff} can be used to approximate to first order [Godin, 2002] the effects of temperature T and horizontal wind \mathbf{w}_{uv} in the direction of propagation ϕ :

$$\begin{aligned} c_{\text{eff}}(z) &= \sqrt{\gamma RT(z)} + |\mathbf{w}_{uv}(z)| \cos(\phi - \phi_{\mathbf{w}_{uv}}(z)), \\ &= c_T(z) + w_a(z). \end{aligned} \quad (4.2.1)$$

Here $\gamma = 1.4$ and $R = 286.9 \text{ J kg}^{-1} \text{ K}^{-1}$ are the ratio of specific heats and the specific gas constant for dry air, respectively. Note that both propagation azimuth ϕ and wind direction $\phi_{\mathbf{w}_{uv}}$ are clockwise relative to the north.

From Snell's law, it follows that positive vertical gradients of the effective sound speed lead to downward refraction, and vice versa. Acoustic waveguides are combinations of these gradients. The orientation of the source and receiver locations determine the propagation azimuth ϕ . This angle is used to estimate the along-track wind (w_a) and cross-wind (w_c) components, by rotating the zonal (w_u) and meridional (w_v) components of the horizontal wind vector \mathbf{w}_{uv} (see Figure 4.1d),

$$\begin{pmatrix} w_a \\ w_c \end{pmatrix} = \begin{pmatrix} \sin \phi & \cos \phi \\ \cos \phi & -\sin \phi \end{pmatrix} \begin{pmatrix} w_u \\ w_v \end{pmatrix}. \quad (4.2.2)$$

The quantities w_a and w_c each have a specific influence on infrasound propagation.

Infrasound is often measured with arrays of microbarometers (Figure 4.1b). Beam-forming techniques allow for the detection of coherent infrasound and the estimation of the *slowness vector* $\mathbf{p} = (p_x, p_y, p_z)$. The slowness vector describes the direction of propagation of a wavefront in three dimensions. The magnitude of three-dimensional slowness corresponds to the reciprocal of wave propagation speed c . The slowness vector can be converted into azimuth ϕ and apparent velocity c_{app} as

$$\phi = \arctan \frac{p_x}{p_y}, \quad (4.2.3)$$

$$c_{\text{app}} = \frac{1}{\|\mathbf{p}_{xy}\|} = \frac{1}{\|\mathbf{p}\| \cos \theta} = \frac{c}{\cos \theta}. \quad (4.2.4)$$

In observational studies, *back azimuth* $\phi_b = \phi \pm \pi$ is used instead of azimuth (equation (4.2.3)), taking the array as the point of reference. It is often found that significant deviations exist between the observed and theoretical back azimuth. Such deviations exist due to the influence of cross winds w_c and are like the crabbing of an airplane needed to fly along a constant bearing in a cross wind.

Back azimuth deviation is illustrated in Figure 4.1c, as the angle between the true azimuth (grey line) and the propagation azimuth (purple line) needed to arrive at the receiver location. Note that the propagation path is denoted by the dashed red line. At the receiver location, the observed back azimuth (orange line) does not point toward the source. Only in the case of zero cross wind, all four mentioned lines would align.

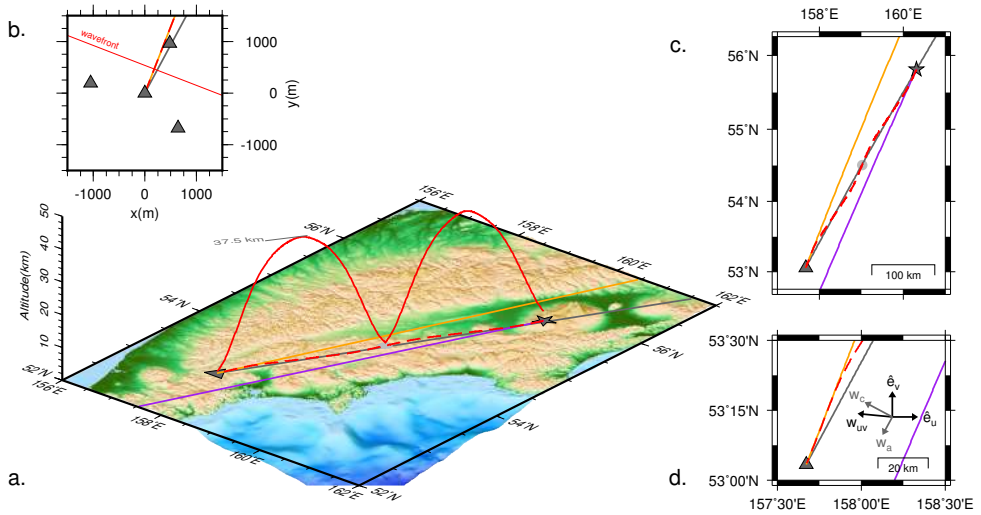


Figure 4.1: (a) Three-dimensional map of the Kamchatka peninsula in Russian Federation (55.8°N , 160.3°E), showing source (star) and receiver array (triangle) locations interconnected with an example eigenray (solid red line) and its horizontal projection (dashed red line). The purple, orange, and grey lines represent the azimuth, back azimuth, and theoretical back azimuth angles, respectively. (b) IS44 array elements layout (triangles) with theoretical, observed, and ray simulated back azimuth angles, all with respect to the array central element. The thin red line perpendicular to the observed back azimuth indicates the incoming planar wavefront. (c) Horizontal projection (top view) of Figure 4.1a with the grey circle indicating the reflection at the ground. (d) Zoom-in in Figure 4.1c, showing the receiver area with the observed and theoretical back azimuth angles. The black vectors indicate the zonal and meridional wind unit vectors \hat{e}_u and \hat{e}_v and the horizontal wind vector \mathbf{w}_{uv} at 37.5 km altitude. Its projection along the theoretical back azimuth, approximating the propagation direction, is given by the grey vectors resulting in the along-track w_a and cross-wind w_c components. The purple and orange lines change due to variations in the atmosphere while the solid grey line is constant.

Apparent velocity (equation (4.2.4)) is the horizontal projection of the propagation velocity vector and describes the horizontal propagation speed of a wavefront with grazing angle θ . This quantity is of interest observationally, as infrasound arrays are typically constructed horizontally. For a layered medium, apparent velocity is an invariant [Pierce, 1981].

Finally, return height z_R is defined as an altitude at which sound refracts down from the upper atmosphere toward the Earth's surface. From the definition of apparent velocity and its invariance, it follows that the apparent velocity equals the effective sound speed at the return height. This relationship allows one to identify return heights from an effective sound speed profile. A range of return heights may exist, but z_R is necessarily smaller or equal to the top of the acoustic waveguide. For the ray shown in Figure 4.1a, z_R is estimated to be around 37.5 km.

In summary, ignoring vertical wind, in-plane atmospheric specifications (temperature, along-track wind) determine effective sound speed and therefore apparent velocity, while the cross-track winds determine the back azimuth deviation. Thus, a complementary set of infrasound observations exist that are sensitive to temperature and horizontal wind.

■ 4.2.2 Signature of SSW events on infrasound recordings

Infrasound has a long history as a method to monitor changes in the stratospheric polar vortex wind direction dedicated to SSWs. Already in the early 1970s, various pioneering studies of Donn and Rind describe the infrasonic signature of a SSW [Donn and Rind, 1971, 1972; Rind and Donn, 1975, 1978]. Using ambient coherent noise, microbaroms, as a continuous natural mechanism for probing the upper atmosphere, they relate abnormal winter amplitude intensities to SSW events. However, these studies came to a stop when nuclear tests were diverted to the subsurface under the Limited or Partial Test Ban Treaty. Recently, with the Comprehensive Nuclear-Test-Ban Treaty opened for signature, the use of infrasound as a passive atmospheric probe gained renewed attention. More recently, Evers and Siegmund [2009] used coherent ambient noise to identify signals arriving from the opposite direction than expected under regular winter conditions to characterize the infrasonic signature of the 2009 major SSW, whereas Assink *et al.* [2014a] identified simultaneous arrivals from two stratospheric ducts due to the 2011 minor SSW. The temperature effect of a hot stratosphere during a SSW on infrasound propagation is studied by Evers *et al.* [2012]. During the 2010 SSW, the extent of the classical stratospheric shadow zone (~ 200 km) reduces by a factor of 2, leading to extremely small shadow zones. Smets and Evers [2014] demonstrated the use of ambient noise amplitude variations to describe the life cycle of the 2009 major SSW. Similar to the earlier study of Donn and Rind [1972], amplitude variations allow to estimate the return height. In addition, Smets and Evers [2014] demonstrate that the combined signature of the change in back azimuth direction, solar tidal signature type, and/or phase variation of the amplitude variation of the observed microbaroms reveals the type of vortex disturbance, either split or reversal.

4.3 Methods

In this work, simulated and observed infrasound wavefront parameters are compared, i.e., back azimuth and apparent velocity. The theoretical basis of this method relies on the assertion that sound propagates through a particular atmospheric state. The atmospheric state that is closest to reality will then lead to simulated values that are closest to the observed values. Experimental evidence for the validity of this method has been provided by various earlier studies [e.g., *Le Pichon et al.*, 2005; *Assink et al.*, 2014b; *Smets et al.*, 2015].

For this study, infrasound propagation is simulated from the volcano Mount Tolbachik to a regional infrasound station at 347 km distance (Figure 4.1), for comparison with observations. The remainder of this section describes the observations, the propagation method, and the atmospheric forecasts that are used.

■ 4.3.1 Infrasound observations

Observations from infrasound station IS44 (Kamchatka, Russian Federation) are used. IS44 is part of the International Monitoring System (IMS). The IMS is a global network of infrasound, seismic, hydroacoustic, and radionuclide stations for the verification of the Comprehensive Nuclear- Test-Ban Treaty (CTBT) [*Dahlman et al.*, 2009]. Today, 45 out of 60 infrasound stations have been installed and certified, providing continuous recordings of infrasound worldwide.

IS44 consists of four MB2000 microbarometers [*Ponceau and Bosca*, 2010] that measure small pressure fluctuations on the order of mPa up to tens of pascals. The microbarometers have a flat response over the frequency band spanning from 0.08 to 4 Hz and are sampled at 20 Hz. Wind noise filters are used to reduce noise levels over the infrasonic frequency band, by spatially averaging the pressure field in the vicinity of an infrasound sensor. Infrasound detection bulletins are provided by the International Data Centre (IDC) of the CTBT Organization (CTBTO). The bulletins include infrasound waveform parameters (including their uncertainties) as a function of time, such as back azimuth, apparent velocity, and dominant frequency. The bulletins correspond to average values of grouped detections in time-frequency space [*Brachet et al.*, 2010]. The parameters used to filter the relevant detections from the raw IDC bulletins are given in Table 4.1.

■ 4.3.2 Propagation modelling

For the evaluation, an in-house developed ray tracing algorithm (cast in spherical coordinates) is used that takes into account the full effect of the three-dimensional inhomogeneous wind and temperature fields. A detailed description is given in Section 2.2. See Figure 4.2 as an example of stratospheric infrasound propagation using three-dimensional ray theory. For every atmospheric model, eigenrays (connecting source and receiver, see Figure 4.1a) are considered for further analysis. Given the aperture of IS44, rays that pass within 1 km of the center of the array are counted as eigenrays. For every eigenray, apparent velocity and back azimuth deviation values are stored, for comparison with the observed values.

Table 4.1: Parameters used to filter the relevant detections of Mount Tolbachik from the raw IDC bulletins [Brachet *et al.*, 2010].

Parameter	Range
Mean frequency	0.5–3.5 Hz
Back azimuth ψ	$28.11 \pm 12^\circ$
σ_ψ	$< 2.0^\circ$
Apparent velocity c_{app}	310–450 m s ⁻¹
$\sigma_{c_{\text{app}}}$	< 25.0 m s ⁻¹
Consistency	< 0.15 s

Except for the limitations that are inherent to the ray theory approximation [Brekhovskikh and Godin, 1999], namely, that the variations in atmospheric wind and temperature are small over an acoustic wavelength, the theory is exact. Thus, the propagation effects such as diffraction and scattering from small-scale structure (e.g., from gravity waves) [Chunchuzov *et al.*, 2015] are neglected. These effects are included in full-wave modelling [e.g., Assink *et al.*, 2014b]. Typically, such computations are limited to in-plane effects, because of the additional high computational load for out-of-plane effects.

■ 4.3.3 Atmospheric forecasts

In this study, ECMWF’s operational high resolution forecasts (HRES), part of the Integrated Forecast System (IFS) cycle 38r1 (June 2012) and cycle 38r2 (June 2013) are used. The IFS consists of a general circulation model and assimilates radiosonde-, ground-, and satellite- based atmospheric observations by four-dimensional variational assimilation (4D-Var). HRES is the deterministic and highest spatial resolution member of the IFS with a resolution of T_L1279L91 (a horizontal resolution of ~ 16 km or 0.125° and 91 vertical levels up to 0.01 hPa, increased to 137 levels in June 2013). See ECMWF [2016] for the evolution of the IFS. Forecasts are available every 12 h with a forecast step up to ten days. For this study, three-dimensional atmospheric specifications of wind, temperature, humidity, and pressure are used every 12 h for the nowcast, five and ten-day forecasts. All specifications are vertically resampled to 500 m levels from ground up to 70 km. Consequentially, infrasound propagation above 70 km cannot be simulated using the ECMWF IFS. To obtain mesospheric and thermospheric returns, the ECMWF forecasts are extended above 70 km by splining a one-dimensional wind and temperature profile obtained from the Horizontal Wind Model (HWM) and Mass Spectrometer and Incoherent Radar Model (MSIS) semi-empirical models [Drob *et al.*, 2008; Picone *et al.*, 2002], for the midpoint between source and receiver.

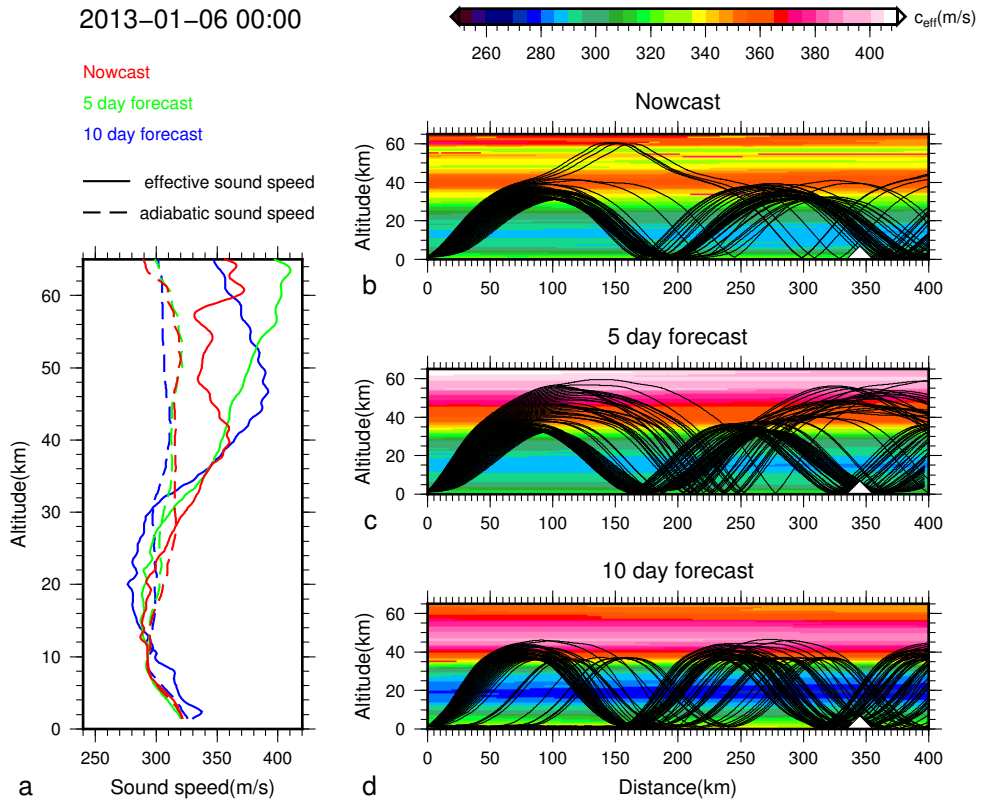


Figure 4.2: (a) Sound speed profiles derived from ECMWF HRES forecasts for 6 January 2013 at 00 UTC indicating the (dashed) adiabatic and (solid) effective sound speed at the source. While the largest variability between the forecasts is found in the upper stratosphere, the ten-day forecast is different throughout the troposphere and lower stratosphere as well. The three panels on the right show three-dimensional ray trace infrasound propagation over 400 km using three different ECMWF HRES forecasts: (b) nowcast, (c) five-day forecast, and (d) ten-day forecast. The background corresponds to the effective sound speed, and the white triangle indicates the array distance. The temperature and wind variability in the profiles are reflected in the far-field infrasound predictions.

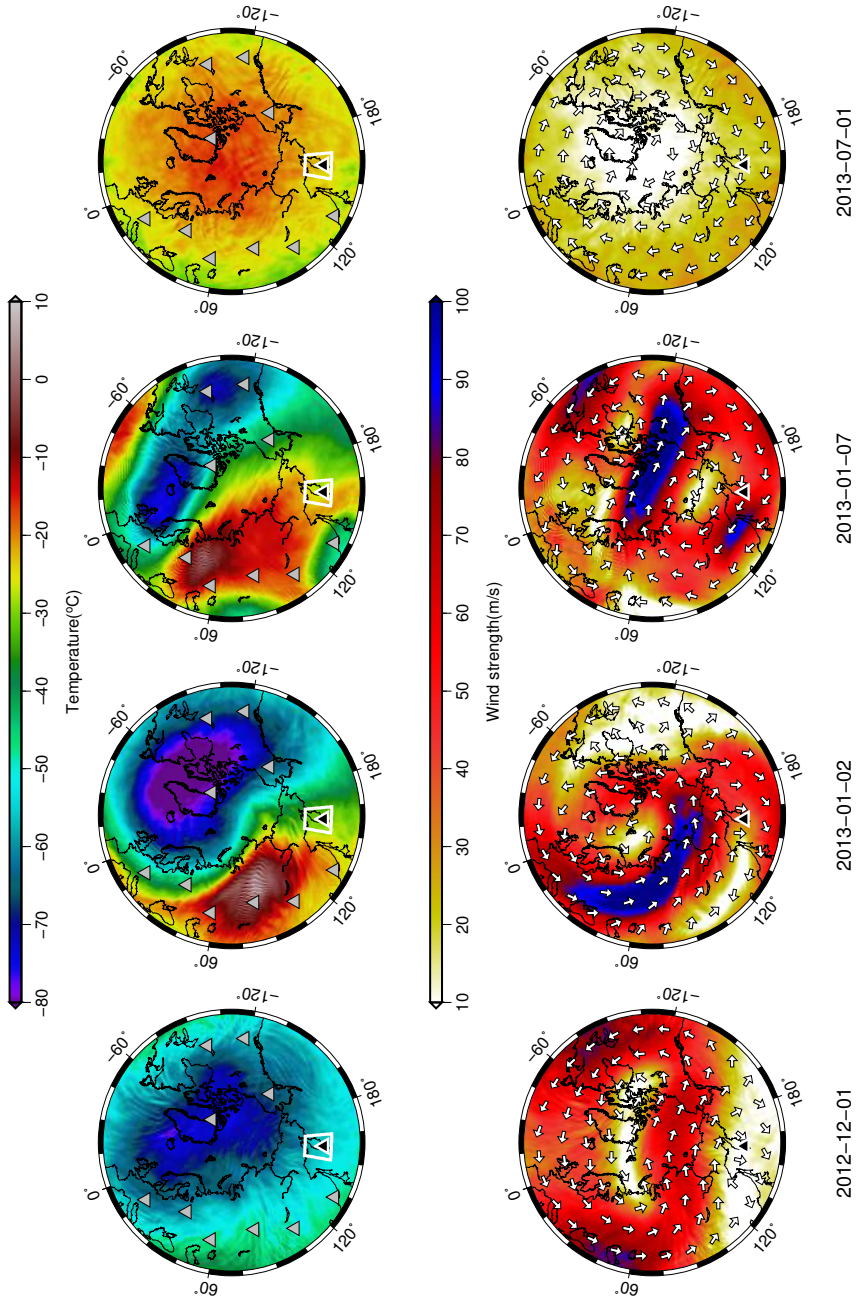


Figure 4.3: (top row) Temperature and (bottom row) horizontal wind specifications from ECMWF analysis at 5.0 hPa (around 36 km altitude) (first column) before, (second and third columns) during, and (fourth column) after the SSW, which directly influence the detectability of Mount Tolbachik on IS44 (white rectangle).

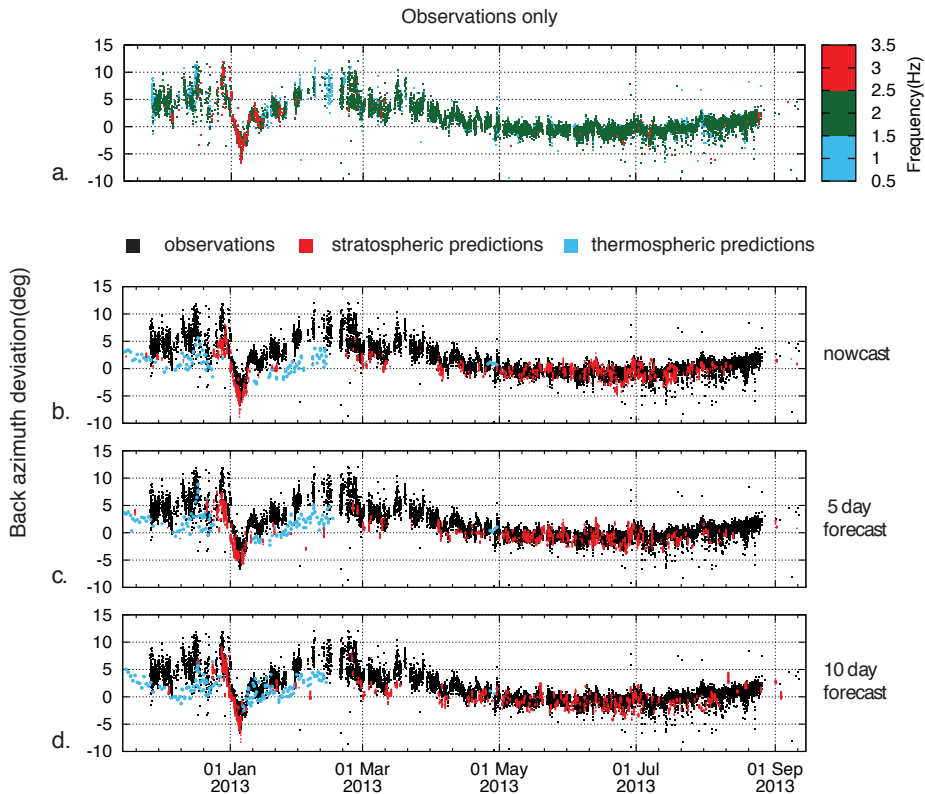


Figure 4.4: (a) Back azimuth deviation values from Mount Tolbachik infrasound detections, for which apparent velocity values are shown in Figure 4.5a. (b–d) Comparisons between observations (black dots) and three-dimensional ray tracing results (red dots) as a function of time, using three different ECMWF HRES forecasts: (Figure 4.4b) nowcast, (Figure 4.4c) five-day forecast, and (Figure 4.4d) ten-day forecast. The blue dots correspond to simulated arrivals that have propagated through the mesosphere and lower thermosphere, for which the MSIS and HWM climatologies have been used.

4.4 Observations

Figure 4.3 shows four states of the analysis temperature and wind field in the NH at 5.0 hPa (about 36 km altitude), prior to the 2013 major SSW (first column), during the SSW (second and third columns), and during the summer of 2013 (fourth column).

Prior to the SSW, the circumpolar vortex flows eastward around the Arctic region, thereby sustaining a cold Arctic stratosphere. This typical winter situation is disturbed during the first week of January 2013. As a result of upward propagat-

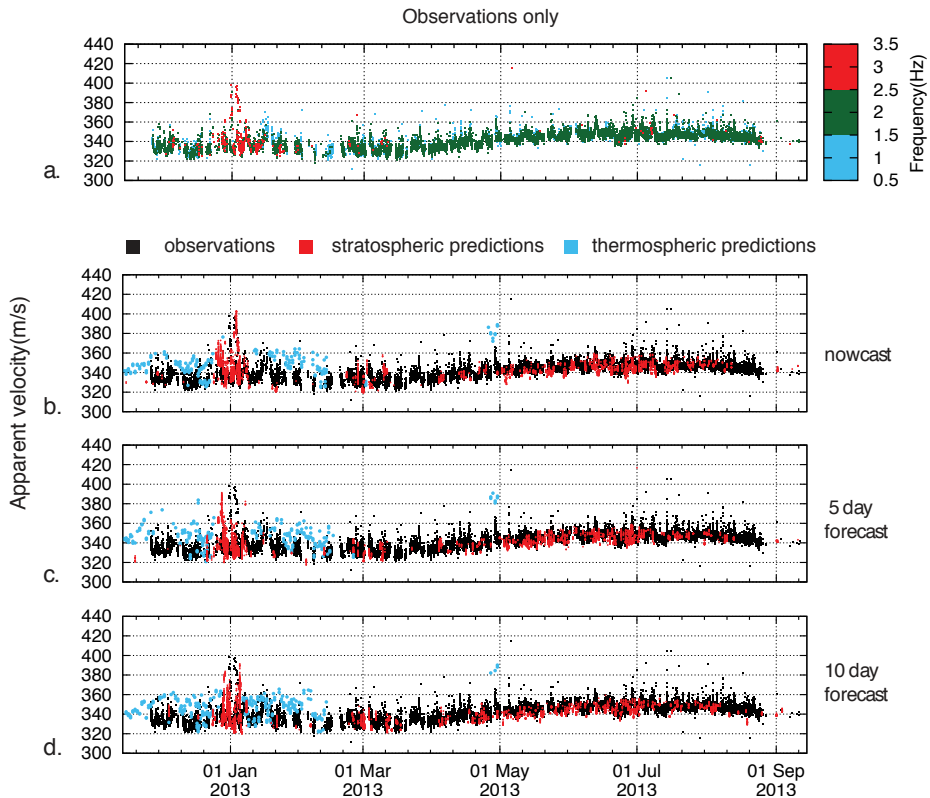


Figure 4.5: (a) Apparent velocity values from Mount Tolbachik infrasound detections. (b–d) Comparisons between observations (black dots) and three-dimensional ray tracing results (red dots) as a function of time, using three different ECMWF HRES forecasts: (Figure 4.5b) nowcast, (Figure 4.5c) five-day forecast, and (Figure 4.5d) ten-day forecast. The blue dots correspond to simulated arrivals that have propagated through the mesosphere and lower thermosphere, for which the MSIS and HWM climatologies have been used.

ing planetary waves, e.g., Matsuno [1971] and Baldwin and Dunkerton [2001], the circumpolar vortex weakens and destabilizes, migrates south of 65°N , and finally is split into two daughter vortices. As a result, the vortex direction is reversed for various regions. Additionally, the Arctic stratosphere warms up to 50°C within a few days, classifying the warming as major. After 18 January 2013, the stratosphere on the NH returns to its more common winter state until the final warming (March), after which the stratosphere transforms into its summer state, featuring a westward circumpolar vortex.

Nearly 36 years after its last eruption, Mount Tolbachik began erupting again

on 27 November 2012, leading to the largest basaltic eruption in Kamchatka during historic times. The volcanic activity remained high for nine months and finally weakened at the end of August 2013 [Albert *et al.*, 2015]. Infrasound detections at IS44, at 347 km distance from Mount Tolbachik, provide a near-continuous record of the eruption sequence (Figures 4.4a and 4.5a). The relative position of Mount Tolbachik to IS44 as well as the stratospheric dynamics is paramount in understanding the observations. While more volcanoes are present in the area, we assume that infrasound detections for the parameters given in Table 4.1 correspond to Mount Tolbachik. This seems justified based on activity reports [GVP, 2013]. Moreover, we assume that the source has a constant spectral content.

During the winter period, not including the warming period, infrasound is detected with a relatively large back azimuth offset of $+5^\circ$, when compared to the summer observations (Figure 4.4a). Taking into account the direction of the winter circumpolar vortex, this suggests that these signals have likely returned from the lower thermosphere instead of the stratopause. After the transition to the summer stratosphere, the back azimuth offset is small and of opposite sign, due to the presence of a westward circumpolar vortex, that creates a stratospheric waveguide. Apparent velocities show the expected seasonal signature (Figure 4.5a) on the basis of higher boundary layer temperatures in summer than in winter, with lower velocities in winter and higher in during summer. During the SSW, a strong westward vortex is present above the region (Figure 4.3). As a result, three particularities can be noted. First, the back azimuth deviation rapidly reverses and reaches a much higher value than during the summer. This is in accord with the much stronger westward vortex, i.e., the cross wind causing the back azimuth deviation. Second, the apparent velocities are higher than usual and even reach values of 400 m s^{-1} , likely due to the increased temperature and along-track wind. Third, the dominant frequency is significantly higher during the warming period, when compared to the summer. This may be explained by the lower return height during the warming period (30 km as opposed to 45 km; see Figure 4.6), important for propagation efficiency, resulting in reduced geometrical spreading in combination with reduced absorption of higher frequencies [Lonzaga *et al.*, 2015].

4.5 Evaluating ECMWF forecasts

Figure 4.2 shows an example of stratospheric infrasound propagation, using three-dimensional ray theory, for three different ECMWF forecasts for 6 January 2013. Typically, IS44 is reached after one bounce. Figure 4.2a shows the effective sound speed (combining the effect of wind and temperature on infrasound propagation) profiles for the different forecast steps. The largest variability between the different forecasts is found in the upper stratosphere, except for the ten-day forecast, which is different throughout the troposphere and stratosphere as well. The sensitivity of infrasound propagation to the variations in forecast steps is essential in this evaluation work.

ECMWF forecasts are evaluated by forward modelling the propagation of infrasound from Mount Tolbachik toward IS44 every 12 h for the entire observation

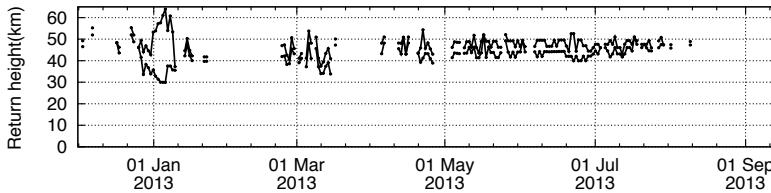


Figure 4.6: Return height range computed from vertical wind and temperature profiles over IS44 (53° N, 158° E), for propagation from Mount Tolbachik to IS44. During the SSW period, the return heights are lower when compared to the summer (30 km versus 45 km). Lower return height correlates with the higher frequencies observed during the SSW period.

period by three-dimensional ray theory using the various forecast steps. These wavefront simulations are compared to the array observations in order to validate the atmospheric specifications of each forecast step. Significant inconsistencies or lack of simulated returns indicate a possible difference between the true state of the atmosphere and the consulted forecast in the vicinity of the return height.

As mesospheric and thermospheric specifications are missing using the ECMWF IFS, comparison of predictions and observations can be misleading. To explain mesospheric and thermospheric returns, all forecasts are extended with semi-empirical wind and temperature profiles (see Section 4.3.3). In general, observations from mesospheric and thermospheric return heights correspond to observations within the lower frequency range of 0.5–1.5 Hz (see Figures 4.4 and 4.5). For these arrivals, there appears to be a near-constant offset of $\pm 2.5^{\circ}$ (Figures 4.4), similar to earlier findings by *Le Pichon et al.* [2005]. In their study, the bias between the measurements and the results of simulation is explained by undervalued wind speeds by HWM in the upper atmosphere. Apparent velocity values are generally overestimated by 10 to 20 m s^{-1} (Figure 4.5).

Comparisons of the observed and simulated wavefront characteristics for the entire period of observation, using different forecast steps, are shown in Figures 4.4 and 4.5, for back azimuth and apparent velocity, respectively. Figures 4.7 and 4.8 zoom-in on the period of the SSW. For the sake of brevity, the discussion here is mainly focused on back azimuth deviations although most conclusions hold for the apparent velocity observations as well.

The estimated difference between the observed and predicted back azimuth, an indication of the forecast uncertainty, is shown in Figure 4.9. For each forecast the difference is calculated between the observations (black dots) and predictions (red dots) in Figures 4.4b–4.4d. All observations are averaged using 12 h time bins and contain at least six detections (on average, every bin contains 50 detections). In general, uncertainty values of observed back azimuth (horizontal dashed black line in Figure 4.9) and apparent velocity are dependent on the detection slowness, the planarity of the waveform, and the signal-to-noise level [*Szuberla and Olson*, 2004].

For IS44 95% uncertainty values up to 2° and 10 m s^{-1} are possible. In this study we estimate typical uncertainty values for IS44 of 1° and 5 m s^{-1} .

■ 4.5.1 Entire observation period

For the entire observation time span the nowcast performs best out of all forecast steps (see Figures 4.4, 4.5, and 4.9a), indicated by a higher continuity of the simulated characteristics and smaller back azimuth differences. The estimated average back azimuth difference shows a clear seasonal variation with a minimum in summer and differences frequently below the 1° estimated observational uncertainty.

Summer observations, related to the stable summer stratospheric waveguide, are, in general, well simulated by all forecasts up to approximately 10 July 2013. After 10 July 2013, only the nowcast is able to provide continuous predictions (see Figure 4.9a). Smaller deviations are occasionally obtained using the five or ten-day forecasts, though these forecasts do not adequately predict continuous values after 10 July 2013. Despite that the ten-day forecast yields the worst performance, based on the density and continuity of the simulations, it still does provide some sparse predictions until the end of August.

In winter, the stratospheric waveguide is rather unstable, resulting in an increased back azimuth difference almost consistently above the 1° estimated observational uncertainty for all forecasts (see Figure 4.9a).

■ 4.5.2 2013 SSW

Zooming-in on the period of the SSW, see Figures 4.7 and 4.8, midwinter stratospheric predictions of back azimuth and apparent velocity can only occur due to the dramatic changes in the stratospheric wind and temperature of a SSW. For these unusual winter stratospheric predictions (and during equinox periods), the prediction performance is significantly lower and clearly different for all three forecast steps when compared to the summer predictions (Figure 4.9a). The local infrasonic signature of the 2013 SSW observed at IS44 is highlighted in Figures 4.7 and 4.8 by the gray rectangle and in Figure 4.9a by the green rectangle. The rectangle points to the continuous high-frequency infrasound observations interpreted as low stratospheric altitude returns ($<40 \text{ km}$ return altitude). In addition, these low stratospheric returns are characterized by a sudden reversal in the back azimuth deviation and an increase in apparent velocity. Therefore, these low stratospheric returns are interpreted to be due to the SSW indicating the assumed warming onset (28 December 2012) and recovery (16 January 2013).

All forecasts are able to reproduce the general SSW characteristics, including the sudden reversal of the back azimuth deviation (Figures 4.4 and 4.7) as well as the sudden increase in apparent velocity (Figures 4.5 and 4.8). Nevertheless, the performance skill during the SSW is much more variable when compared to the summer predictions.

- The warming onset (28 December 2012) is well predicted by all three forecasts, both the nowcast and five-day forecast predict the same warming onset

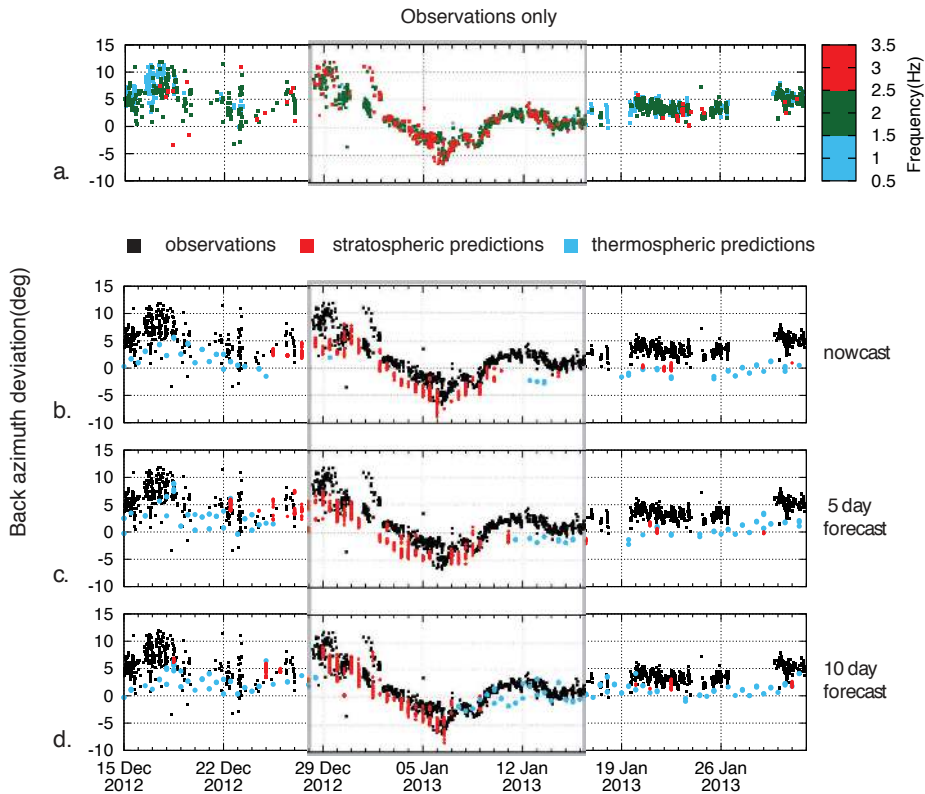


Figure 4.7: Zoom-in of Figure 4.4, focusing on the SSW period. The gray rectangle points to the continuous high-frequency infrasound observations interpreted as low stratospheric altitude returns (<40 km return altitude). These low stratospheric returns with sudden reversal in back azimuth are interpreted to be due to the SSW.

followed 12 h later by the ten-day forecast. Though, the ten-day appears to be more accurate in predicting the larger back azimuth deviations and corresponding apparent velocities during the first days of the warming. The resemblance in timing of the predicted and observed stratospheric returns using the ten-day forecast is better as well.

- During the vortex displacement phase of the major warming (before 7 January 2013), the ten-day forecast most accurately predicts the varying back azimuth deviation, including a sudden wind direction change around 2 January 2013 with corresponding increase in apparent velocity (Figure 4.8). Note that the difference in back azimuth prediction of both the nowcast and ten-day forecast is below the array uncertainty. Yet the large difference of the five-day forecast

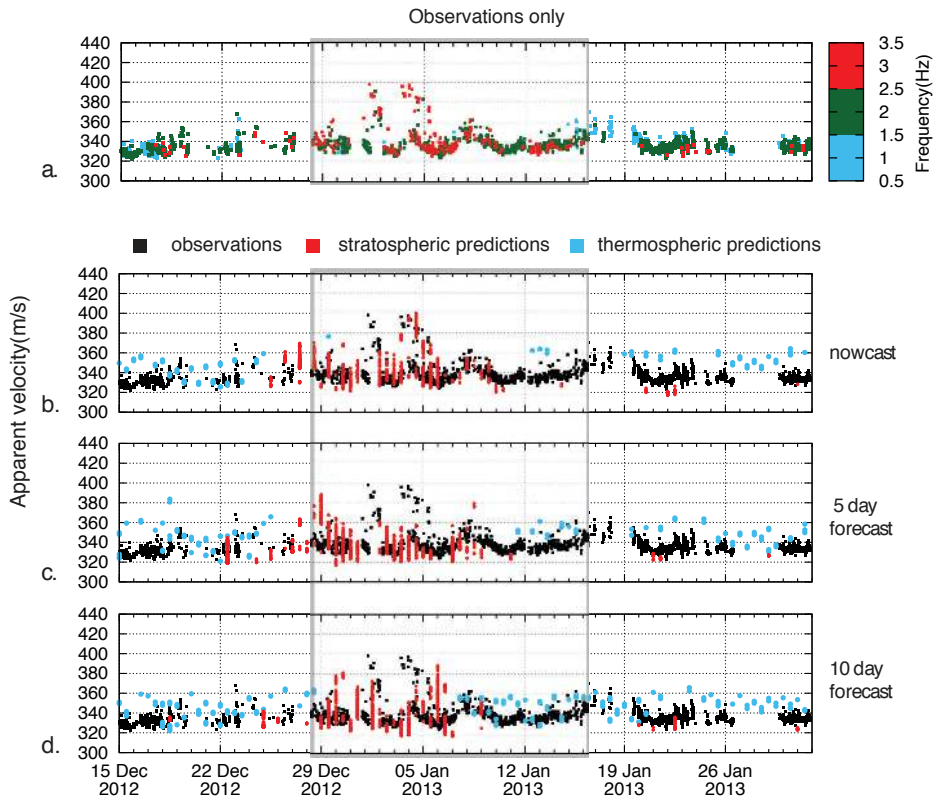


Figure 4.8: Zoom-in of Figure 4.5, focusing on the SSW period.

when compared to the nowcast and ten-day forecast is remarkable.

- When the vortex splits (around 7 January 2013) the ten-day forecast does no longer predict stratospheric returns, while the five-day forecast and nowcast continue, respectively, two and four days with a quasi similar back azimuth difference.
- All forecasts have difficulties in predicting the stratospheric observations up to the expected warming recovery (16 January 2013). Predictions for all forecast steps indicate a too-early recovery. The ten-day forecast predicts a difference of about nine days with respect to the moment that no stratospheric arrivals are expected anymore (8 January 2013). The recovery is best captured by the nowcast model, continuously predicting up to 11 January 2013.

This relative performance is illustrated in Figure 4.9b, presenting a minimal mean difference between the observed and modeled back azimuth. All forecasts indicate

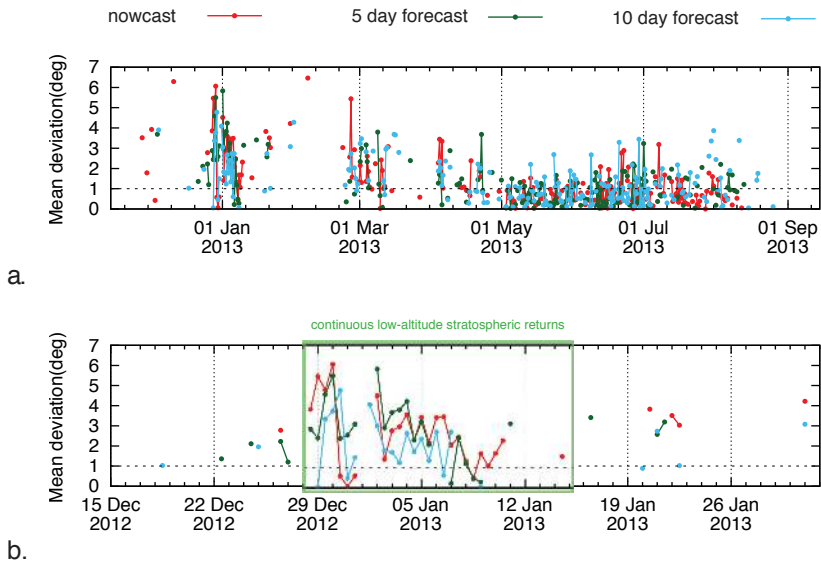


Figure 4.9: (a) Estimated root-mean-square deviation between the observed and predicted back azimuth of all returns over the full time span of observation. Observations are averaged for 12h time bins and contain at least six detections. The different colours correspond to the different ECMWF forecasts that are used in the simulations. The lines connecting the dots indicate the continuity of the predictions. The horizontal dashed black line is indicative of the uncertainty due to infrasound array configuration. (b) Similar as Figure 4.9a, but focusing on the midwinter with the SSW period (green rectangle).

a reduction in back azimuth difference when the vortex migration evolves. Minimal back azimuth differences are obtained using the ten-day forecast, while the nowcast yields the highest continuity of the predictions. Least performance is obtained by the five-day forecast.

Ray simulations based on the analysis (see Figure 4.10) do not indicate a significant improvement during the SSW compared to the nowcast.

4.6 Discussion and Conclusions

For the discussion of our results it is important to establish that the nowcast is most constrained by the data assimilation whereas the ten-day forecast tends to be quasi free running, with the five-day forecast positioned somewhere in between. For a typical forecast, more forecast skill is expected for a shorter forecast step, as it is closer to the data assimilation. This is observed during summer (Figure 4.9), where the nowcast performs best. Surprisingly, in winter the ten-day forecast appears

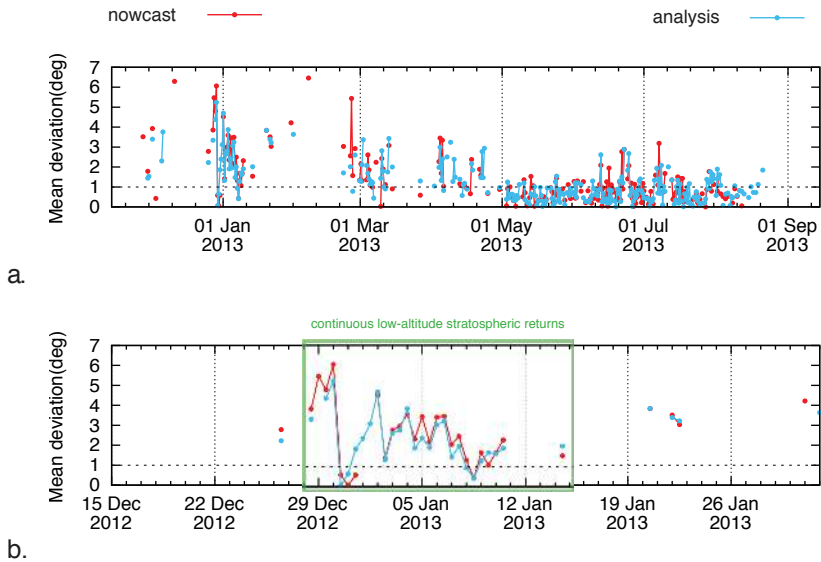


Figure 4.10: Similar to Figure 4.9, now comparing the root-mean-square deviation between the observed and predicted back azimuth using the nowcast (red) and analysis (blue) over (a) the full timespan of observation and (b) focusing on the SSW period with the continuously observed low-altitude stratospheric returns (green rectangle).

to be most accurate in predicting the first phase of the warming. For validation, comparison of the nowcast with the subsequent analysis, often applied in NWP, reveals only a small improvement in absolute deviation compared to the nowcast (see Figure 4.10). Our interpretation is that the ten-day forecast is able to obtain sufficient information from the small a priori warming signatures with enough time to propagate through the atmosphere, to predict the warming including the sudden recovery around 2 January 2013. Once data have to be assimilated during the warming, the ten-day forecast loses a lot of forecast skill. At this stage, data gets most likely rejected or modified by the data assimilation system leading to inaccurate initialization as addressed by *Diamantakis* [2014]. The nowcast is affected similarly but recovers approximately at once with the data assimilation system such that it predicts best the SSW duration and recovery.

An ECMWF IFS cycle update has been implemented to address spurious data assimilation issues that occur during SSW events [*Diamantakis*, 2014]. For future research, it would be useful to evaluate the effects of this cycle update (Cy41r1, May 2015), including the consideration of the ensemble forecasts [*Smets et al.*, 2015], using our technique. Moreover, it would be of interest to study the uncertainties due to unresolved small-scale structure, involving three-dimensional full-wave modelling.

Detailed analyses between the various forecasts are needed, for example, by considering differences in polar cap-averaged stratospheric zonal wind and temperature.

For the first time, weather forecasts for different forecast steps are evaluated using infrasound. The high spatiotemporal resolution of infrasound is explained by the relative small wavelength of infrasound (< 500 m) compared with the characteristic length scales of atmospheric features (> 500 m). The high temporal resolution is due to the use of a near-continuous infrasound source (typical resolution of minutes; compared with 6-hourly atmospheric specifications). The proposed method in this study for the evaluation of middle atmospheric weather forecasts using near-continuous infrasound detections can directly be applied to similar setups, making use of other IMS or even national infrasound arrays. The method presented here relies on an active source like the volcano used. However, source-independent techniques are being developed based on interferometry of the ambient noise field [Fricke *et al.*, 2013, 2014].

This study demonstrates that infrasound can provide useful additional information in regions where data coverage is sparse, such as in the upper stratosphere. The frequency content of the observed infrasound suggests a six day longer duration of the 2013 SSW than predicted by the ECMWF nowcast.

Validation of atmospheric analysis and forecast products, in particular in regions above 30 km altitude, is important for numerical weather prediction applications, as the interaction between the stratosphere and the troposphere cannot be neglected. Due to the delayed impact of a warming on the weather at the ground, evaluating the forecast in the middle atmospheric can act as an early indicator of a possible upcoming loss of forecast skill in the troposphere. As atmospheric specifications in the lower and middle atmosphere are routinely used in a wide variety of atmospheric sciences and applications, the validation is relevant to a broad community and a wide variety of applications, such as the verification of the Comprehensive Nuclear-Test-Ban Treaty, in which infrasound is used as a verification technique.

5

Using stratospheric variability for advanced infrasound propagation

5.1 Probabilistic infrasound propagation using realistic atmospheric perturbations

Abstract This study demonstrates probabilistic infrasound propagation modelling using realistic perturbations. The ensembles of perturbed analyses, provided by the European Centre for Medium-Range Weather Forecasts (ECMWF), include error variances of both model and assimilated observations. Ensemble spread profiles indicate a yearly mean effective sound speed variation of up to 8 m s^{-1} in the stratosphere, exceeding occasionally 25 m s^{-1} for a single ensemble set. It is shown that errors in point estimates of effective sound speed are dominated by variations in wind strength and direction. One year of large mining explosions in the Aitik mine, northern Sweden, observed at infrasound array IS37 in northern Norway are simulated using three-dimensional ray tracing. Probabilistic propagation modelling using the ensembles demonstrates that small-scale fluctuations are not always necessary to improve the match between predictions and observations.

■ 5.1.1 Introduction

The state of the atmosphere is of utmost importance for infrasound propagation. In infrasound propagation modelling, still, the true state of the atmosphere is usually represented by the analysis. The analysis is the best deterministic estimate of the atmosphere using a data assimilation system consisting of a general circulation model (GCM).

Section 5.1 is published as: Smets, P. S. M., L. G. Evers, S. P. Näsholm, and S. J. Gibbons (2015), Probabilistic infrasound propagation using realistic atmospheric perturbations, *Geophys. Res. Lett.*, 42, 6510–6517.

Note that minor changes have been introduced to make the text consistent with the other chapters.

GCMs are advanced numerical models describing the physical state of the atmosphere and/or ocean, simulating the response of the global climate system. GCMs are smooth, designed to suppress unbalanced motion associated with, e.g., internal gravity waves, to allow longer time steps [Shutts *et al.*, 2011]. In general, GCMs have to deal with two disadvantages: parameterisation and feedback mechanisms of different processes [Houghton *et al.*, 1997]. GCMs are limited in resolution relative to the scale for most impact assessments, e.g., clouds or gravity waves. Therefore, the effects of smaller length scale processes must be averaged over larger regions. This is referred to as parameterisation. Feedback mechanisms become an issue at the boundary of the model, where signals will be damped to avoid unwanted reflections. This results in a less physical representation but enhancement in model stability. Consequentially, GCM limitations influence the simulation of infrasound propagation, resulting in the lack of simulated arrivals due to fine-scale structure in wind and temperature [Chunchuzov *et al.*, 2005, 2011; Kulichkov *et al.*, 2008, 2010; Revelle, 2010] or due to discrepancies in the analysis related to large-scale phenomena, for example, the equinox [Assink *et al.*, 2014b] or a sudden stratospheric warming [Smets and Evers, 2014]. A current trend in improving infrasound propagation modelling is adding fine-scale structure and nonresolved gravity waves to one dimensional vertical profiles of horizontal wind [e.g. Drob *et al.*, 2013]. As these modifications do not obey the physical laws acting in the atmosphere, for example, between wind and temperature, such adaptations are avoided in here.

However, the analysis excludes error variances of both model and observations. Therefore, we propose to model infrasound propagation based on an ensemble of realistically perturbed analyses provided by the European Centre for Medium-Range Weather Forecasts (ECMWF).

Infrasound, used as a verification technique for the Comprehensive Nuclear-Test-Ban Treaty (CTBT), has shown its ability to act as a passive technique to probe the upper atmosphere, e.g., [Donn and Rind, 1971; Le Pichon *et al.*, 2010; Green *et al.*, 2012; Assink *et al.*, 2012, 2014a,b; Smets and Evers, 2014]. Both the treaty verification as well as atmospheric probing, e.g., inversion studies, make significant use of infrasound propagation modelling that still relies on the deterministic estimate of the atmosphere. Usually, the analysis is used, but occasionally modelling is based on free running atmospheric models that are not constrained by assimilating atmospheric observations. Therefore, this study contributes to improving the treaty verification and future atmospheric probing studies.

■ 5.1.2 Realistic atmospheric perturbations

The analysis is a product of the data assimilation system, given as input an initial estimate field and a set of observations, defined by the time integration of the model equations from the previous analysis. However, the analysis provides a deterministic estimate of the true atmosphere, which can be off from the truth due to both model and observation errors.

At the European Centre for Medium-Range Weather Forecasts (ECMWF) the probability density function (PDF) of the atmosphere is sampled by an ensemble set of realistic perturbed analyses using the Ensemble Data Assimilation (EDA)

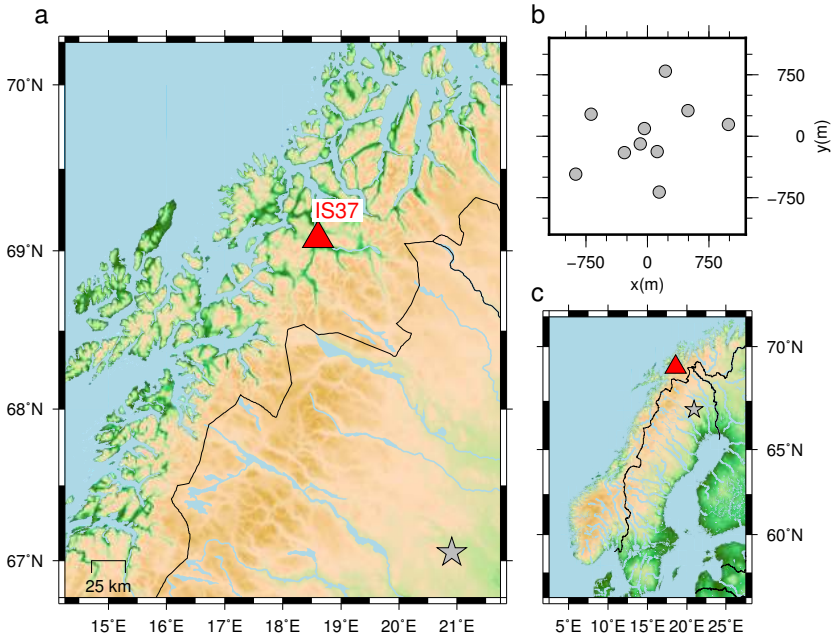


Figure 5.1: (a) Regional map indicating the location of IMS infrasound array IS37 (red triangle) in northern Norway and the location of the Aitik mine near Gällivare (gray star), northern Sweden: the site of large mining explosions. (b) Station layout of IS37. (c) Map of Norway and Sweden.

system [Buizza *et al.*, 1999]. The ensembles are obtained by randomly perturbing the observations consistent with observational error statistics [Houtekamer *et al.*, 1996; Houtekamer and Mitchell, 2005], in combination with a stochastic backscatter scheme to simulate the effect of model uncertainties with amplitudes comparable to analysis error estimates [Shutts, 2005; Berner *et al.*, 2009]. For each observation apart from cloud-track winds, perturbations have been defined by randomly sampling a Gaussian distribution with zero mean and standard deviation defined by the observation error standard deviation [Buizza *et al.*, 2008]. Each perturbed analysis is produced using the same background error statistics in the four-dimensional variational data assimilation cycles [Bonavita *et al.*, 2012].

The ECMWF EDA ensemble of perturbed analyses with cycle 38r1 of the Integrated Forecasting System (IFS) consists of 25 ensemble members plus the unperturbed analysis, with a resolution of T_L1279L137 (horizontal resolution of ~ 16 km and 137 vertical levels up to 0.01 hPa). For infrasound propagation modelling, atmospheric specifications are used with a horizontal resolution of 0.1° which are vertically resampled to 500 m levels from ground up to 70 km. Ensembles of perturbed analyses are available every 12 h at noon and midnight UTC, respectively.

■ 5.1.3 Infrasound propagation modelling

Sound is a pressure disturbance propagating through a medium, for example, air. Sound propagation through the medium is affected by the medium itself, which may result in changes in the wave vector direction (e.g. reflection, refraction) and attenuation of the signal. The relation between density and pressure, affected by temperature (T), determines the adiabatic speed of sound (c) of the medium. Speed of sound is defined by the ideal gas law with adiabatic conditions, $c_T(\mathbf{x}) = \sqrt{\gamma RT(\mathbf{x})}$, with the ratio of specific heats for air $\gamma = c_p/c_v = 1.4$, the specific gas constant $R = 287 \text{ J kg}^{-1} \text{ K}^{-1}$, and position vector \mathbf{x} inside the medium. The medium itself can be in motion, e.g., as wind in the atmosphere. Sound propagation is approximated by ray tracing, e.g., *Blom and Waxler* [2012]. In this study, a self-developed three-dimensional ray code for spherical coordinates is used (see Section 2.2). Ray equations for position \mathbf{x} and slowness \mathbf{p} are obtained from a canonical transformation of the high-frequency approximation of the wave equation using the eikonal,

$$\dot{\mathbf{x}} = \mathbf{w} \left(1 - \mathbf{w} \cdot \mathbf{p} \right) + c_T^2 \mathbf{p}, \quad (2.2.53a)$$

$$\dot{\mathbf{p}} = -c_T \frac{\partial c_T}{\partial \mathbf{x}} \left(\mathbf{p} \cdot \mathbf{p} \right) + \left(1 - \mathbf{w} \cdot \mathbf{p} \right) \left(-\mathbf{p} \cdot \frac{\partial \mathbf{w}}{\partial \mathbf{x}} \right), \quad (2.2.53b)$$

with three-component wind vector \mathbf{w} .

Along each ray the atmospheric attenuation (α) is obtained, including incoherent transmission loss due to geometrical spreading from the rays and frequency dependent absorption by the atmosphere, which becomes more important with increasing altitude. Absorption, described by [*Sutherland and Bass*, 2004], depends on variations in thermal conductivity, density, viscosity, and relaxation throughout the medium and varying concentrations of chemical components. Incoherent transmission loss is described by the transport equation, based on the Jacobian determinant for ray coordinates azimuth and elevation [*Jensen et al.*, 2011].

Ray tracing is applied using full three-dimensional atmospheric specifications, interpolated by cubic splines with a smooth kernel. Eigenrays are obtained using a ray grid search method, evaluating all rays with elevation angles ranging from 0.0 to 45.0° with the horizontal in steps of 0.1° and azimuth angles ranging from 325.0 to 343.0° north with steps of 0.1°. Eigenrays are defined as a ray approaching the array within 1.5 km Euclidean distance from the array center coordinate. Rays do not necessarily need to reflect at the surface but may refract close to the ground. Only stratospheric eigenrays are used, defined as eigenrays with a minimal ray refraction altitude of 20 km and a transmission loss below 100 dB Re 1 km.

■ 5.1.4 Case study: 1 year of reference events

Probabilistic infrasound propagation modelling is demonstrated by simulating 1 year of observed infrasound at array IS37 in Norway, part of the International Monitoring System (IMS) for verification of the Comprehensive Nuclear-Test-Ban Treaty (CTBT). Observed infrasound corresponds to mining activity in Aitik, e.g., blasting, near Gällivare, northern Sweden, at approximately 245 km distance. The location

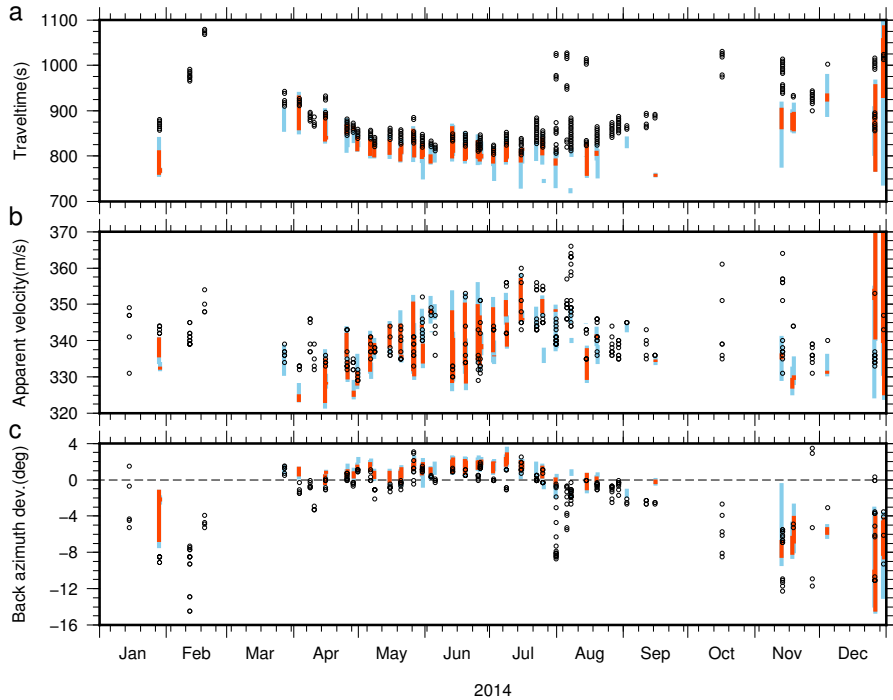


Figure 5.2: (a) Travel time, (b) apparent velocity, and (c) bearing deviation of all infrasound events for IS37 corresponding with mining blasts at Aitik near Gällivare in northern Sweden in 2014. Each panel shows (black circles) the observed signals, as well as the range of (vertical bar) the simulated signal characteristics obtained using (red) the analysis and (blue) the perturbations. Only stratospheric eigenrays within 1.5 km of the array central point are used.

of the infrasound array IS37, its layout, and the location of the open pit mine are shown in Figure 5.1.

Locations and origin times are obtained from ground truth or GT events. A seismic signal with a known source is unambiguously associated with GT events using correlation detectors [Gibbons and Ringdal, 2006] and Empirical Matched Field Processing [Harris and Kvaerna, 2010], which are so-called pattern detectors. The uncertainty in the source location is limited to the dimensions of the mine (of the order of a couple of kilometers) [Evers et al., 2012], and the origin time of each explosion can be determined to within approximately 1 s. All explosions take place at approximately 19:30 central European time (CET). Infrasound signals are detected by performing a channel-to-channel correlation procedure [cf. Brown et al., 2002] using 10 s long segments of data in the 1–4 Hz band pass with 60% overlap. Figure 5.2 shows 358 associated observations of 46 events or mining explosions for 2014 in terms of travel time, apparent velocity, and bearing deviation with respect

to the back azimuth angle between IS37 and the ground truth source location. All associated events take place at approximately 19:30 CET.

To evaluate the added value of using realistic atmospheric perturbations, each of the associated events is simulated by three-dimensional ray tracing, see Section 5.1.3. Conventional deterministic model predictions are obtained using the unperturbed analysis. Probabilistic infrasound predictions are described by a Monte Carlo method, aggregating the ray trace simulations of each individual ensemble member, sampling the PDF of the atmosphere. As the ensembles are only available every 12 h, eigenrays are simulated using the atmospheric specifications before and after the event to avoid temporal interpolation.

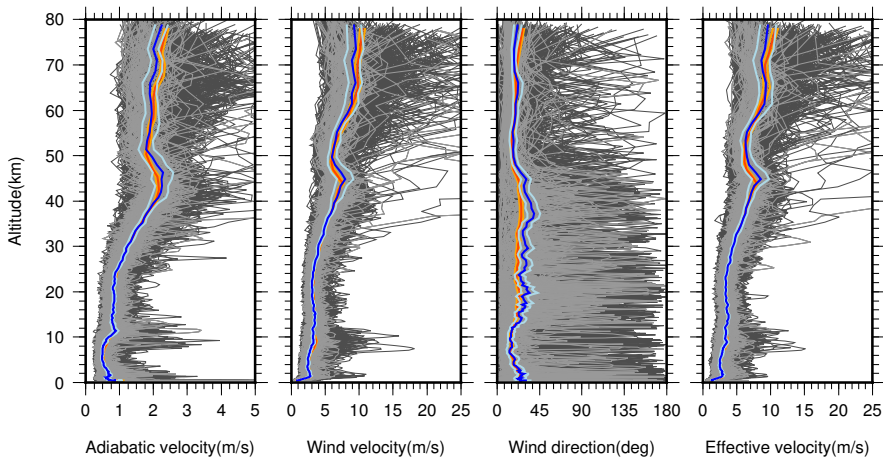


Figure 5.3: Ensemble spread at IS37 indicating error variance profiles for the year 2014 with 12h interval sampling. The profiles for the times at which signals from the Aitik events were observed are in light gray with profiles for all other times in dark grey. The mean error variance per level is shown in dark blue for the times of Aitik observations and red for all other times, and the 95% confidence intervals for times of observations and all other times are light blue and orange respectively.

■ 5.1.5 Atmospheric error variance profiles

Figure 5.3 shows 1 year of semidiurnal atmospheric ensemble spread profiles, an approximation of the error variance, for temperature (in terms of sound speed), wind direction and velocity, and effective sound speed in the direction from Gällivare. Vertical profiles correspond to the ensemble spread for the model grid point the nearest to the IS37 central coordinate. Figure 5.3 indicates an error increasing with height, in accordance with an increasing model and observational uncertainty as expected. At the stratopause, a sharp decrease in variation is present which could denote the lack of assimilated observations. However, this decrease in variance

could also be physical (related to the reduced propagation of waves) or related to the ensemble perturbation scheme. Below 25 km the variances for both wind and temperature are small and rather constant. Only the tropopause induces an increase in the temperature mean variance. Up to this altitude, still many data points using diverse observations techniques are assimilated [Bouttier and Kelly, 2001]. From 25 km and up to roughly 44 km, data assimilation is dominated by satellite based sounding, for example, nadir microwave sounding by Advanced Microwave Sounding Unit-A or limb sounding using GPS radio occultation. Distributions of temperature or other atmospheric properties, such as humidity or ozone content, are derived from radiative signals (see, for example, Rodgers, 1976; Healy and Thépaut, 2006). From 44 km up to 52 km the mean error variance is reduced significantly. This can be explained by the sudden decrease in the number of assimilated observations and the variety of the remote sensing techniques used. Consequentially, the atmospheric model is no longer constrained by observations but by climatology, resulting in a lower variance. Improving the analysis, and thus forecasts, involves resolving the stratosphere and assimilating upper atmospheric data [Ramaswamy et al., 2001; Gerber et al., 2009].

Effective sound speed variances are dominated by the error in wind strength and direction. The error variance for wind strength is approximately four times larger than the error variance for temperature. Ensemble spread profiles at the array indicate a yearly mean effective sound speed variation up to 8 m s^{-1} in the stratosphere, exceeding occasionally 25 m s^{-1} for a single ensemble set. In the mesosphere, the variation around the yearly mean sound speed error, of approximately 10 m s^{-1} , is significantly larger.

■ 5.1.6 Deterministic versus probabilistic simulations

Figure 5.2 shows the characteristics of the observed infrasound from the Aitik events, together with the ranges of signal characteristics predicted from the eigenrays using both the analysis and the ensemble of perturbed analyses. The performance of the model predictions is determined by the hit rate or probability of detection, defined by the number of observations correctly predicted divided by the total number of observations. An individual hit corresponds to an observed signal characteristic that falls within the range of the predicted signal characteristic. Similarly, a combined hit is evaluated, indicating an agreement of all three signal characteristics. False alarms are ignored. Hits and hit rates for the deterministic and the probabilistic simulations are listed in Table 5.1.

Model predictions using the analysis explain the general trend of the observations in summer. Between March and July most of the predictions agree with the observations. Some few predictions are obtained around the equinoxes, in winter, or in case of large back azimuth deviations. Prediction hit rates increase significantly when using EDA-based perturbations, as can be seen in Figure 5.2. In summer, almost all stratospheric observations coincide with the simulations, including the vernal equinox. Still, the overall performance is rather poor. Predicted travel times are predominantly lower than the observed travel times, and the observed bearing deviations are predominantly lower (more negative) than the predicted. The travel

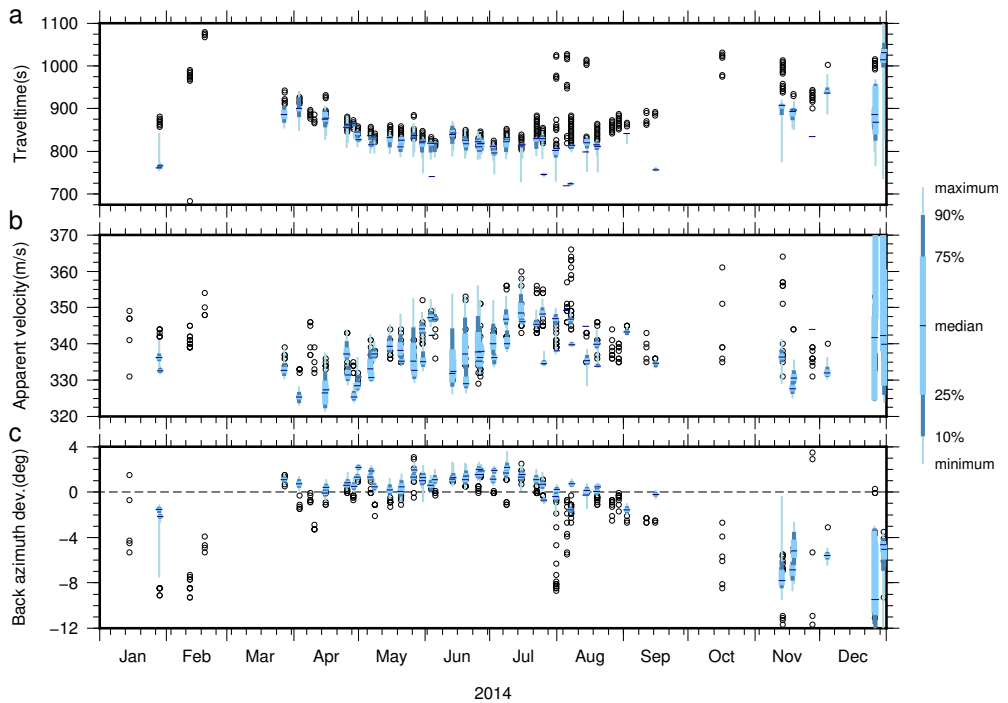


Figure 5.4: Percentile distribution of simulated events obtained using the atmospheric perturbations for signal characteristics (a) travel time, (b) apparent velocity, and (c) bearing deviation. (black circles) Observed events at IS37 are shown in the background. For each simulated event the percentile distribution indicates the minimum, 10th centile, 25th centile, median, 75th centile, 90th centile, and the maximum.

Table 5.1: Number of hits and corresponding hit rates (percentage) between all 358 observations and the deterministic (analysis) and probabilistic (ensemble) ray predictions. Signal characteristics apparent velocity (c_{app}), bearing deviation ($\Delta\phi$), and travel time (tt) are compared individually as well as combined (all).

	c_{app}	$\Delta\phi$	tt	c_{app}	$\Delta\phi$	tt
		count		percentage	percentage	
Deterministic (analysis)	94	82	84	26.3%	22.9%	23.5%
Probabilistic (perturbations)	185	152	127	51.7%	42.5%	35.5%
Improvement	+91	+70	+43	+96.8%	+85.4%	+51.2%

time prediction bias is most likely dominated by ray tracing issues. Late arrivals are probably a scattering or ray trace resolution issue, while the early predictions correspond with rays partly trapped in a tropospheric duct, which are not likely to be realistic. This results in a low probability of detection for travel time and, consequently, a low hit rate for all combined characteristics. The Monte Carlo method using 26 ensembles generates a large number of predictions such that a probability distribution of the predicted signal characteristics can be determined. This is shown in Figure 5.4 by the percentile distribution for each predicted signal characteristic. The obtained likelihood can be used to evaluate the performance of the simulated observations. Similarly, the percentile distribution is of importance to validate the atmospheric GCM, in this case including model and observational error variances.

An example is provided in Figure 5.5, which illustrates a day when the analysis fails to simulate the observed event while one of the ensemble members does succeed.

■ 5.1.7 Discussion and Conclusions

In this study, the use of ensembles of realistically perturbed analyses for infrasound propagation modelling is successfully demonstrated. Although GCMs have limitations, a significant improvement in propagation modelling is obtained without the need of adding small-scale fluctuations. Error variance profiles at the array shown that the yearly mean effective sound speed variation can reach up to 8 m s^{-1} in the stratosphere, exceeding occasionally 25 m s^{-1} for a single ensemble set. The latter value is in the order of what has been proposed previously to explain infrasound observations, often dedicated to missing small-scale fluctuations and gravity waves [Green *et al.*, 2011; Hedlin *et al.*, 2012; Drob *et al.*, 2013] or model discrepancies [Assink *et al.*, 2014b].

Not all observations can be predicted, neither using the analysis nor by the ensemble of perturbed analyses, due to multiple reasons. First of all, neither upper mesospheric nor thermospheric observations can be simulated due to the altitude limit of the atmospheric model. Second, events originate around 19:30 CET, which is in the middle of two consecutive atmospheric realizations. As the analysis and perturbations before and after the event are used, with a time offset of 6 h, the atmosphere can be changed significantly during this time span. The time offset can be reduced using probabilistic forecasts provided by the Ensemble Prediction System (EPS) with 1 h steps. Third, a simulation can be missing due to limitations of the applied propagation modelling, ray tracing, which cannot penetrate the acoustic shadow zone as full wave models can, e.g., parabolic equation model [Jensen *et al.*, 2011]. Fourth, the ensemble of analyses can be off from the true state of the atmosphere. The bearing deviation prediction bias indicates that a bias in the analysis or ensemble can be present. At last, differences can be related to the lack of physically plausible but unresolved small-scale fluctuations. Future research is required to determine whether or not the probabilistic approach will work as well for shorter source-to-station ranges, where simulations suggest that finite-frequency effects related to scattering from small-scale inhomogeneities generate much of the observed signal [Kulichkov, 2009].

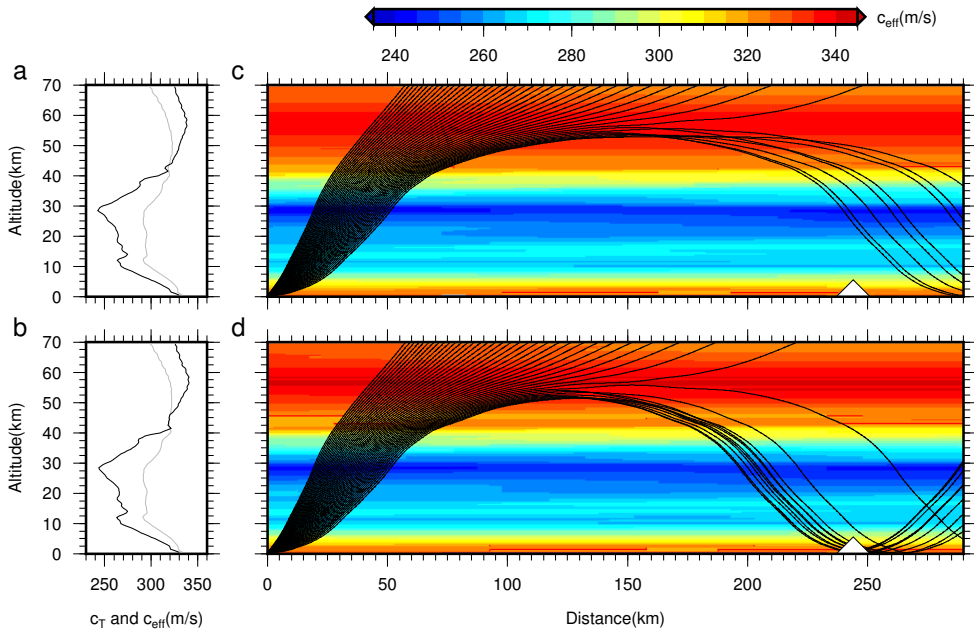


Figure 5.5: Example when the analysis fails to simulate the observed event while one of the ensemble members does succeed. (left) Vertical profiles indicate (gray) the adiabatic sound speed and (black) the effective sound speed at the source in direction of IS37 on 27 March 2014 for (a) the analysis and (b) the best ensemble member. (right) Simulated rays for equal elevation and azimuth angles using (c) the analysis and (d) the best ensemble member.

5.2 On the infrasound detected from the 2013 and 2016 DPRK's underground nuclear tests

Abstract The underground nuclear tests by the Democratic People's Republic of Korea (DPRK) generated atmospheric infrasound, both in 2013 and 2016. Clear detections were made in the Russian Federation (IS45) and Japan (IS30) in 2013 at stations from the International Monitoring System. Both tropospheric and stratospheric refractions arrived at the stations. In 2016, only a weak return was potentially observed at IS45. Data analysis and propagation modelling shows that the noise level at the stations and the stratospheric circumpolar vortex were different in 2016 compared to 2013. As the seismic magnitude of the 2013 and 2016 nuclear test explosions was comparable, we hypothesize that the 2016 test occurred at least 1.5 times deeper. In such a case, less seismic energy would couple through the lithosphere-atmosphere interface, leading to less observable infrasound. Since explosion depth is difficult to estimate from seismic data alone, this motivates a synergy between seismics and infrasonics.

■ 5.2.1 Introduction

Sources of seismic energy in the subsurface can generate low-frequency acoustic waves in the atmosphere, i.e., infrasound. Examples of such sources are earthquakes and explosions [Donn and Posmentier, 1964]. There are various mechanisms through which seismic waves in the subsurface can couple to infrasonic waves in the atmosphere, at the lithosphere-atmosphere interface. Previous studies with earthquake recordings have shown: (1) epicentral infrasound, (2) topographical infrasound and (3) evanescently coupled infrasound. (1) Epicentral infrasound is the direct coupling of seismic-to-infrasonic energy at the earthquake's epicenter, due to the movement of the earth surface [Mutschlecner and Whitaker, 2005]. (2) Topographical infrasound can be generated away from the epicentral region by the movement of mountain ranges [Le Pichon et al., 2006] or steep slopes, like a cliff [Green et al., 2009]. Here also the movement of the earth surface due to seismic waves is the source of infrasonic waves [Walker et al., 2013]. (3) Evanescently coupled infrasound has been observed from an earthquake under the ocean. Secondary sources in the water column generated hydro-acoustical waves. The ocean-atmosphere interface became anomalously transparent, since the underwater source depths were within one acoustic wavelength, generating infrasound in the atmosphere [Evers et al., 2014].

When a source in the subsurface is capable of generating infrasound, there is no guarantee that the infrasound generated will be detected at a distant station. This strongly depends on the source-receiver distance, the atmospheric winds and temperature and noise levels at the receiver due to wind and turbulence. In long-range infrasound propagation, i.e., over distances of more than 100 km, the state of

Section 5.2 is published as: J. D. Assink, G. Averbuch, P. S. M. Smets, and L. G. Evers (2016), On the infrasound detected from the 2013 and 2016 DPRK's underground nuclear tests, *Geophys. Res. Lett.*, 43, 3526–3533. All authors contributed equally.

Note that minor changes have been introduced to make the text consistent with the other chapters.

the stratosphere [Assink *et al.*, 2014b; Waxler *et al.*, 2015] and to a lesser extent the thermosphere determine the (un)favorable conditions for detection.

The Democratic People’s Republic of Korea (DPRK) has tested four nuclear devices over the last years (2006, 2009, 2013 and 2016) [Selby, 2010; Wen and Long, 2010]. All four tests took place at the Punggye-ri Nuclear Test Site in the northeast of the country (see Figure 5.6). It is a mountainous area, mainly consisting of granite. Details on the source are listed in Table 5.2 and are derived with seismic stations from the global International Monitoring System (IMS). The IMS is in place for the verification of the Comprehensive Nuclear-Test-Ban Treaty (CTBT). Next to seismic stations, the IMS also consists of radionuclide, hydro-acoustic and infrasonic measurement devices [Dahlman *et al.*, 2009]. Recordings from the latter will be used in this study. The closest IMS infrasonic stations to the Punggye-ri site are in the Russian Federation (IS45) and Japan (IS30), as shown in Figure 5.6. Infrasound has not been detected on IMS infrasonic stations from the 2006 and 2009 test. Non-IMS infrasound stations will not be considered here [Che *et al.*, 2009]. A suggested fifth test in 2010 is disputed and will not be discussed, as it would have had a too small yield to be detected with infrasound [Zhang and Wen, 2015].

In this study, it is discussed why infrasound from the 2013 DPRK nuclear test was clearly detected and why the 2016 test left a less clear signature on ground-based microbarometers. Although the source strengths were comparable, the source depth, the state of the upper atmosphere and receiver noise levels appear to have played an important role in the detectability of infrasound. Since the depth of an explosion is difficult to estimate from seismic data alone [Bowers and Selby, 2009], this motivates a synergy between the seismic and infrasound technologies to improve on the depth estimation of (nuclear) explosions.

■ 5.2.2 Atmospheric propagation of infrasound in 2013 and 2016

Infrasound can travel over long ranges, because of its low frequency content and since several wave guides exist in the atmosphere, in which acoustic energy can be trapped. Three wave guides between the earth’s surface and upper atmosphere exist. (1) The

Table 5.2: Details from the DPRK’s nuclear tests using the IMS

Date	Time (UTC)	Lat (deg)	Lon (deg)	Uncertainty (km ²)	Mb	Yield ^a (kT TNT)
2006.10.09	01:35:27.58	41.3119	129.0189	880	4.1	~1
2009.05.25	00:54:42.80	41.3110	129.0464	265	4.5	~5
2013.02.12	02:57:50.80	41.3005	129.0652	181	4.9	~10
2016.01.06	01:30:00.49	41.3039	129.0481	193	4.8	<10

^a Yield estimates were obtained from NORSAR, as published at <http://www.norsar.no/norsar/about-us/News/North-Korea-nuclear-test-on-6-January-2016>, last accessed 2016.01.21.

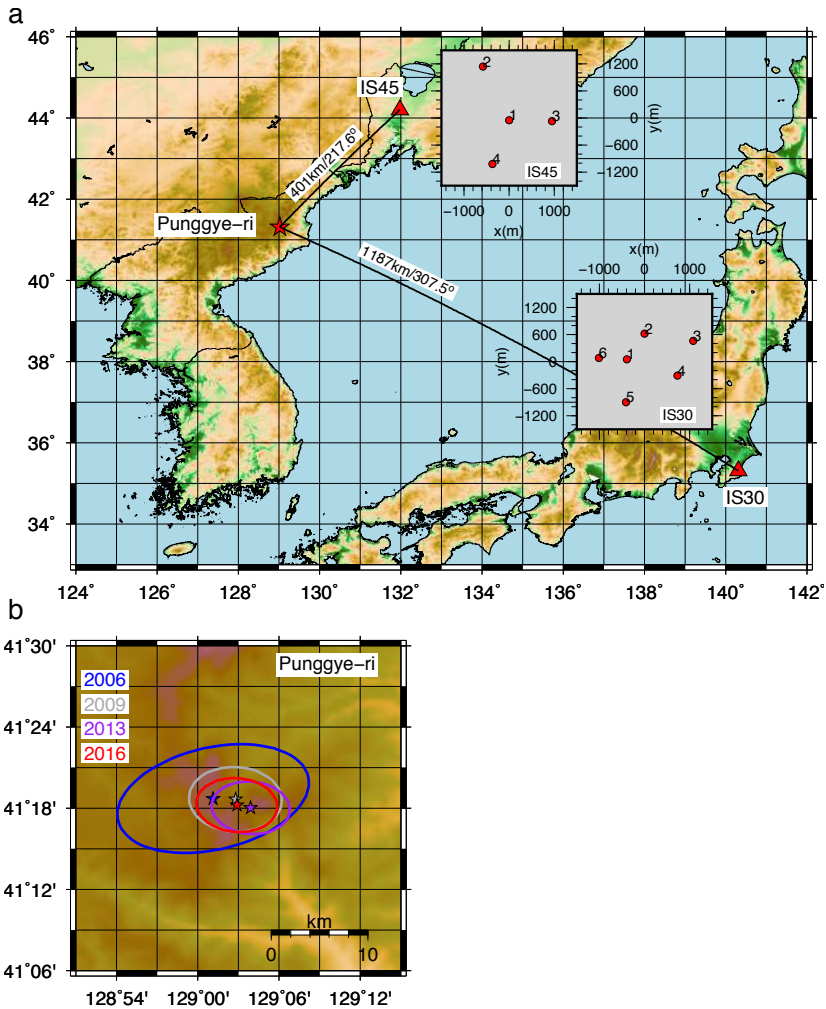


Figure 5.6: (a) Map showing the DPRK's Punggye-ri Nuclear Test Site in the northeast of the country. The IMS infrasound arrays, and their configurations of microbarometers are also shown, being IS45 in the Russian Federation and IS30 in Japan. Element 2 from IS45 was missing in 2013 and element 3 from IS30 in 2016. (b) Map showing the locations of the nuclear test at the Punggye-ri site from 2006, 2009, 2013 and 2016. The uncertainty ellipses are also shown, as derived from IMS seismic recordings (see Table 5.2 for details).

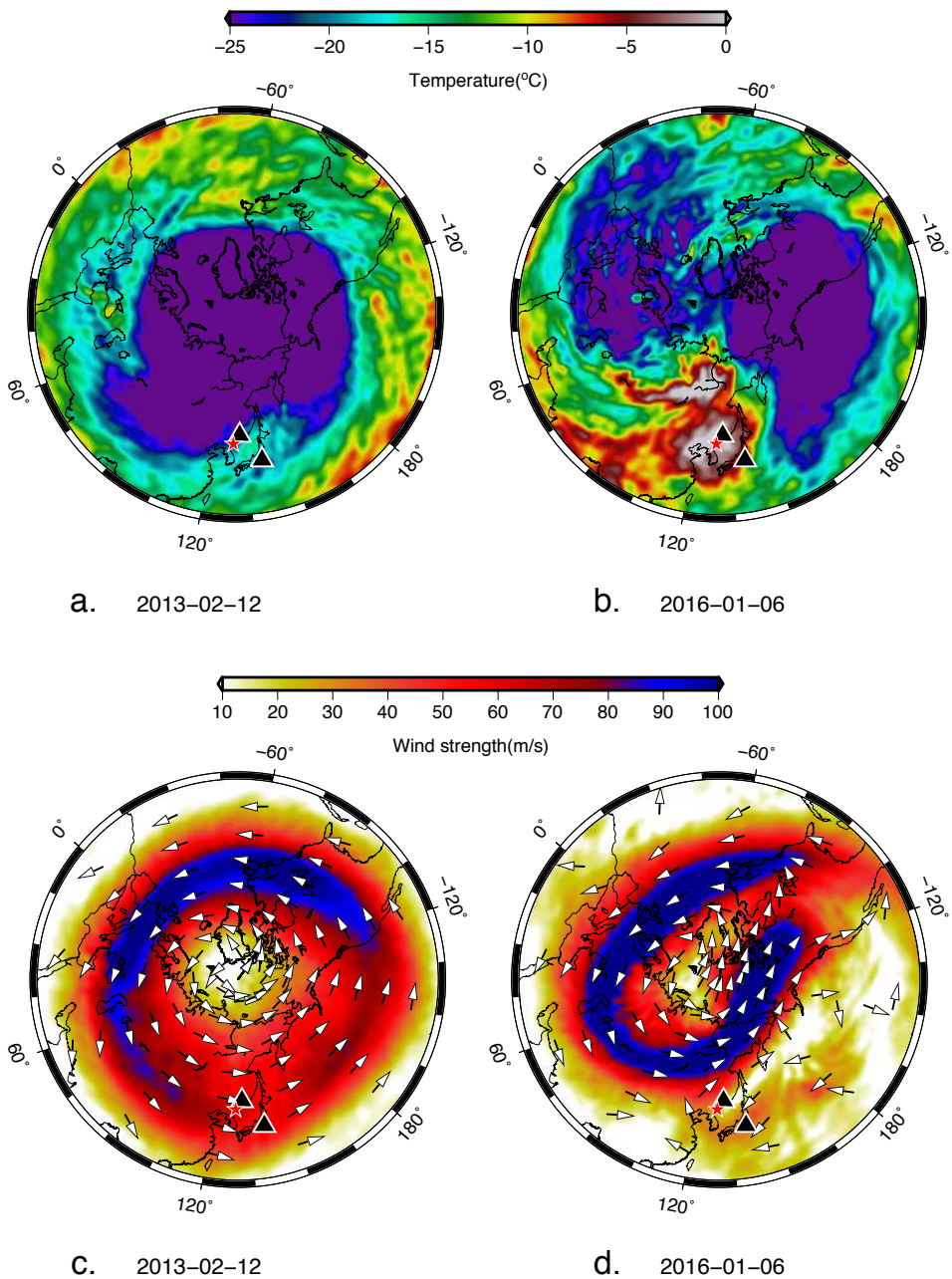


Figure 5.7: The wind and temperature at 1.5 hPa (~ 45 km) from ECMWF atmospheric specifications. IMS infrasound stations are indicated with the black triangles, being IS45 to the north of Punggye-ri (star) and IS30 to the east. The temperatures are given in the top frames, for (a) 2013-02-12 03:00 UTC and (b) 2016-01-06 02:00 UTC. The wind strength and direction are shown in the bottom frames for (c) 2013 and (d) 2016.

tropospheric wave guide with its upper bound in the tropopause (~ 10 km), caused by the jet stream. Winds at a lower level and temperature inversions can also form a tropospheric wave guide. (2) The stratospheric wave guide with its upper limit around the stratopause (~ 50 km), formed by the temperature increase due to the presence of ozone and the circumpolar vortex. (3) The thermospheric wave guide from the mesopause (~ 90 km) and upwards, due to the increase in temperature. However, infrasonic waves are much attenuated at these altitudes in the highly rarefied atmosphere.

The wind strength and direction, as a function of altitude, make the atmosphere a highly anisotropic medium for the propagation of infrasound. Typically, infrasound is detected in the down-wind direction. The westerly jet stream near the tropopause directs the infrasound to the east, while the direction of circumpolar vortex changes direction between the equinoxes. On the Northern Hemisphere, the polar vortex is directed to the east in winter and west in summer. The summer stratosphere is stable, but in winter planetary waves from the troposphere can propagate into the stratosphere. Interaction of such waves with the polar vortex can lead to Sudden Stratospheric Warmings (SSWs). Even bi-directional wave guides can be formed under such circumstances [Assink *et al.*, 2014a]. These SSWs occur every winter and can be minor or major. In the latter case, stratospheric winds reverse and the temperature increases with tens of degrees Celsius in only a few days. These conditions strongly affect infrasound propagation [Evers and Siegmund, 2009; Evers *et al.*, 2012; Smets and Evers, 2014].

Infrasonic propagation can be modeled in a high frequency approach by applying raytracing. However, such an approach does not cover full wave effects like scattering and diffraction. Therefore other methods, such as the Parabolic Equation (PE) method are used, which account for full wave phenomena [Collins, 1993]. Inputs necessary for the propagation modelling are atmospheric specifications of density, temperature and wind. Especially, the latter two are highly variable as a function of altitude, time and geographical location. The European Centre for Medium-Range Weather Forecasts (ECMWF) provides hourly global atmospheric specifications with a spatial resolution of 0.125 degree, up to 0.01 hPa (~ 79 km altitude).

Figure 5.7 shows the ECMWF's wind and temperature specifications near the stratopause (1.5 hPa or ~ 45 km). In February 2013, there was a well developed circumpolar vortex around the cold Arctic stratosphere. In contrast, in January 2016, the vortex was displaced from its circumpolar trajectory and a warm stratosphere was present over the area of interest. The eastward vortex, as in 2013, is no longer present and a mixture of eastward and westward wind directions is visible over the area of interest. Such a state of the stratosphere is formed in the early stages of a SSW. The results of infrasound propagation structure through the different wind and temperature conditions, for the 2013 and 2016 events, are shown in Figure 5.8.

A well formed tropospheric and stratospheric wave guide is present for IS45 in 2013. Both wave guides exist due the strong winds near the tropopause and stratopause. Comparing the adiabatic and effective sound speed, which takes into account the wind effect, shows that the jet stream and circumpolar vortex, respectively, lead

Table 5.3: Transmission loss in dB re. to 1 km at 1.0 Hz, for tropospheric (I_w) and stratospheric (I_s) refractions

2013	I_w	I_s
IS45	-37.7	-47.9
IS30	-53.4	-53.4
2016		
IS45	-38.1	-53.0
IS30	-50.6	-67.5

to a downward refracting atmosphere. In 2016, tropospheric and weak stratospheric refractions are predicted to reach IS45. The stratospheric paths interact with the troposphere, but have a relative large transmission loss, due to the weaker vortex. Tropospheric refractions are predicted for IS30 in both 2013 and 2016, which are caused by the jet stream. A weak stratospheric return might be observed in 2013. However, the partly counteracting circumpolar vortex in 2016 will prevent such a stratospheric refraction. In 2016, the refraction altitude is higher than in 2013, which leads to a stronger attenuation. Furthermore, the strong jet stream hardly allows refractions to reach the earth's surface. A so-called elevated wave guide has formed. The transmission losses at each array are given in Table 5.3.

■ 5.2.3 Infrasound detections of the 2013 and 2016 tests

Infrasound is measured with arrays of microbarometers (see Figure 5.6), which are sensitive in the frequency range of at least 0.02 to 4 Hz. Within this range, small-sized atmospheric nuclear tests of about 1 kT TNT can be detected, as these are expected to generate infrasound of 0.1 to 0.2 Hz. Underground tests can generate higher frequencies in the atmosphere, as the seismic wavefield contains more higher frequencies. The advantage of measuring with arrays is twofold. (1) The noise due to wind and turbulence is reduced by summing the signals of the individual microbarometers. Those are spaced at such a distance that the wind field leaves an incoherent pressure field, while the long wave lengths of the infrasound are coherent. (2) The apparent velocity of the infrasonic wave can be estimated, being a measure of the angle of incidence of the wave. Furthermore, the direction of arrival or back azimuth can be obtained. In order to do so, beamforming is applied to the individual recordings, by time delaying and summing the recordings.

Continuous infrasonic recordings are processed based on the signal coherency, with a sliding window approach. An increase in signal coherency over the array indicates the presence of an infrasonic wave. The Fisher ratio is a sensitive measure of the signal coherency or signal-to-noise ratio (SNR) [Melton and Bailey, 1957].

Array processing results are shown for the IS45 and IS30 infrasonic recordings in 2013 and 2016, in Figure 5.9. IS45 clearly detects both tropospheric (I_w) and stratospheric (I_s) refractions in 2013. A intermediate return (I_{ws}) is also identified, which is a signal that has leaked from the troposphere into the stratosphere (see

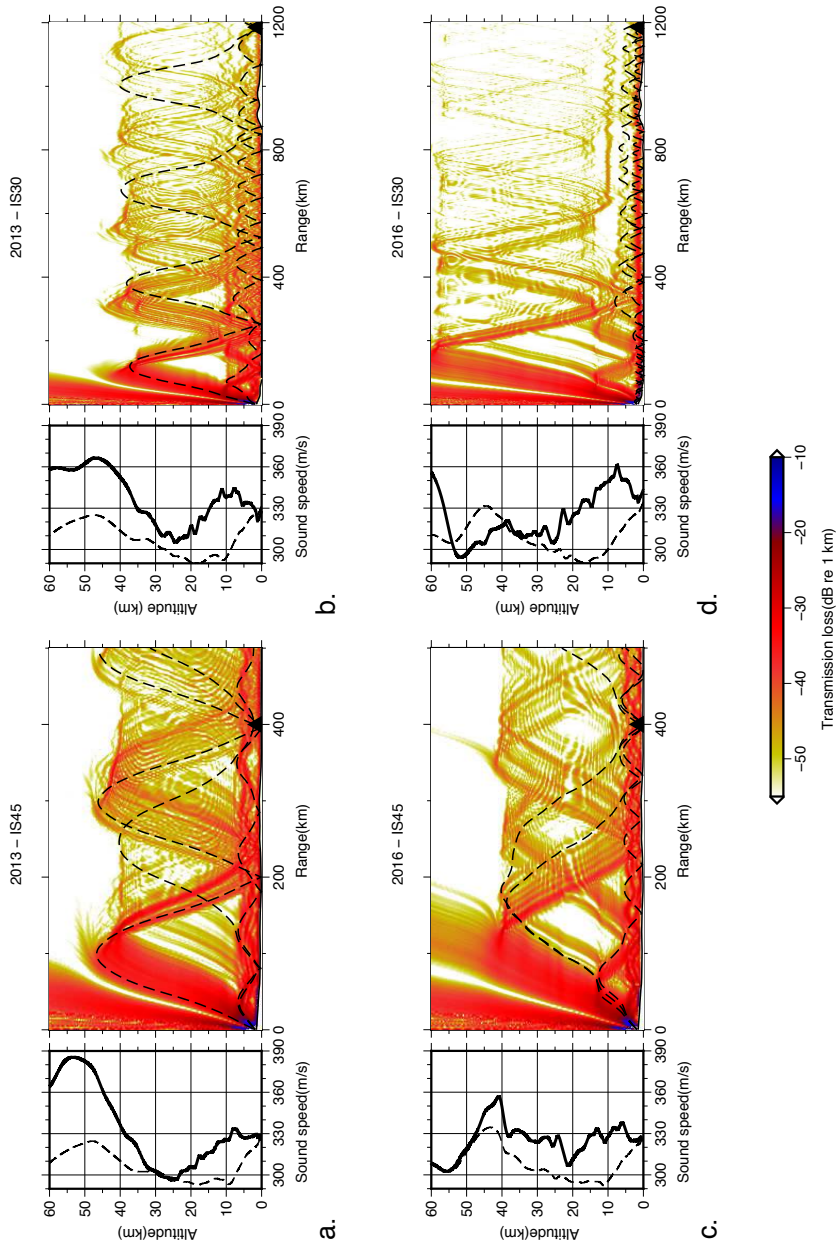


Figure 5.8: The propagation of infrasound from the Punggye-ri Nuclear Test Site to the IMS infrasound stations, for IS45 in (a) 2013 and (c) 2016 and for IS30 in (b) 2013 and (d) 2016. The transmission loss is shown as a function of distance and altitude at 1.0 Hz. The eigenrays that connect the source and receiver are shown as dashed lines. The adiabatic (dashed line) and effective sound speeds (solid line) are given in separate frames, to the left of each propagation frame. These profiles are taken at the mid-point between source and receiver. In Table 5.3 the exact transmission loss values are given.

also Figure 5.8). The expected arrival time, back azimuth and apparent velocity (blue dots) from raytracing and the observations (red dots) are in agreement. The increase in apparent velocity as a function of time is representative for the increase in refractions altitude. Furthermore, the celerities (horizontal distance divided by traveltime), as given in the SNR-frame, correspond to the expected values for tropospheric and stratospheric returns [Brown *et al.*, 2002]. Other local impulsive sources with a high SNR are visible throughout the recording. In 2016, only one arrival is potentially identified at IS45. This arrival can be associated with the tropospheric and both stratospheric propagation paths (Figure 5.8c), considering the observations and the modeled parameters. The detection is very weak and its identification is much dependent on the processing parameters. In that sense, it is a rather unstable detection that might be missed with different settings for the binsize, overlap and corner frequencies of the bandpass filter. The local noise levels in 2016 are higher than those in 2013, as can be seen from the high spectral values in the spectrograms, outside the times signal is present. ECMWF surface winds are 2.4 m s^{-1} in 2016 and 0.9 m s^{-1} in 2013, which are consistent with higher noise levels.

Tropospheric returns are not observed in IS30 neither in 2013 nor in 2016. The only refractions that could be identified is a stratospheric return in 2013. Noise levels from the spectral amplitudes seem not to differ too much. The surface winds in 2016 are only slightly higher than those in 2013, i.e., 1.9 versus 1.6 m s^{-1} .

■ 5.2.4 Discussion and conclusions

The underground nuclear tests conducted by the DPRK in 2013 and 2016 both generated observable atmospheric infrasound. Clear signatures were obtained in the Russian Federation, by IMS array IS45, and in Japan by IS30 in 2013. At IS45 both a tropospheric and stratospheric refraction were identified from the 2013 test. In 2016, only a weak tropospheric return could potentially be found at IS45. The stratospheric refraction detected at IS30 in 2013 was not observed in 2016.

The following explanations are postulated, based on observations and modelling.

- [1] The 2016 stratosphere was disturbed by planetary waves interacting with the circumpolar vortex, i.e. a possible early stage SSW. Propagation of infrasound through the stratosphere was unfavourable for IS30. This also follows from the transmission loss modelling (see Table 5.3).
- [2] The local noise levels at IS45 due to wind were higher in 2016 than 2013, which can obscure a clear detection.
- [3] It should be noted that the detection capability of IS45 was higher in 2016 than in 2013, since one of the microbarometers (element 2) was missing in 2013.
- [4] The size of the nuclear test, in terms of yield, might be somewhat smaller in 2016 (m_b 4.8) than in 2013 (m_b 4.9), based on IMS magnitudes. Therefore, less energy was possibly coupled into the atmosphere. However, it should be

noted that this difference in magnitudes falls within the typical range of uncertainties. Indeed, comparable seismic moment magnitudes have been estimated for the 2013 ($M_w = 4.7$) and 2016 ($M_w = 4.71$) events [IRIS, 2013, 2016], as well.

It should be noted that we have not considered scattering off small-scale structure, such as caused by sub-grid scale gravity waves [e.g. *Kulichkov et al.*, 2010], which could likely further enhance the stratospheric propagation efficiency, in particular for the 2016 case.

The lack of detections of tropospheric refractions at IS30 can only be explained by the fact that the wave guide is very thin and its continuity can be disrupted by wind and turbulence.

The fact that (1) tropospheric propagation towards IS45 was similar in 2013 and 2016 and no clear detection could be made at IS45 in 2016, (2) no stratospheric returns were identified at IS45, though possible from the transmission loss calculations and (3) the seismic magnitudes of the 2013 and 2016 test explosions were comparable, motivates us to hypothesize that the 2016 test was at a greater depth than the 2013 test.

Based on a preliminary analysis of relative source depths of the 2013 and 2016 explosions for two cases of stratospheric propagation (Appendix C), we estimate that the 2016 test took place at least 1.5 times deeper than the 2013 test. Assuming a minimum source depth of 450 m for the 2013 test, based on hydrodynamic simulation results [*Rougier et al.*, 2011] and the 2013 yield estimate of 10 kT TNT (Table 5.3), this would imply that the 2016 explosion would have occurred at least 225 m deeper.

Such an explanation could indeed explain the reduced coupling of seismic energy through the lithosphere-atmosphere interface. However, this hypothesis should be further tested, to investigate the effects of differences in rock conditions as well as uncertainties in yield estimates and atmospheric structure.

Future studies, involving a more extensive observational dataset and numerical modelling that accounts for lithosphere-atmosphere coupling and varying geological conditions, will be conducted to further test this hypothesis and to provide quantitative constraints on the source depth.

As the depth of an explosion is difficult to estimate from seismic data alone [*Bowers and Selby*, 2009], infrasound may thus provide useful complementary information.

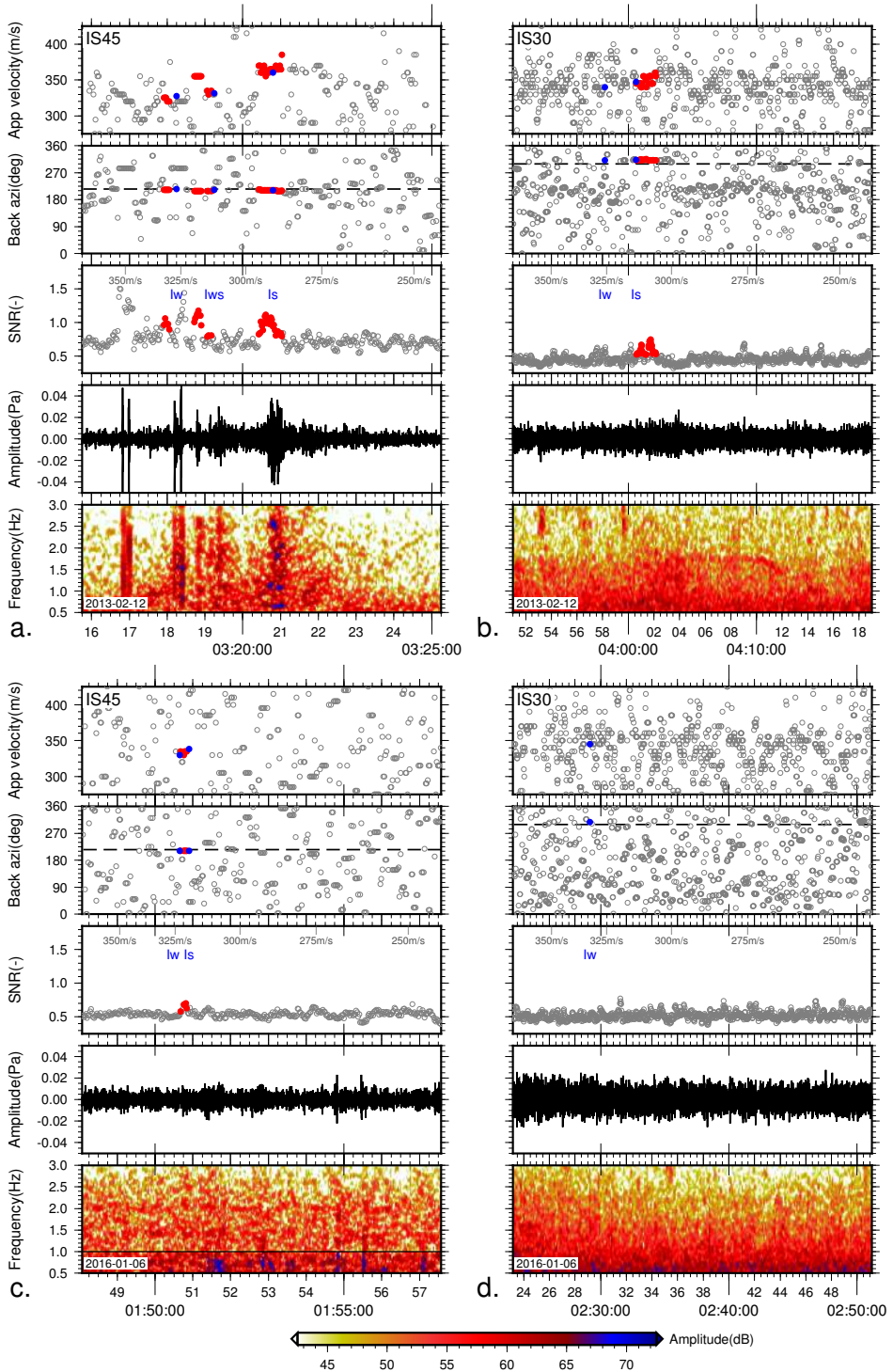


Figure 5.9 (preceding page): Results from array processing the infrasonic recording of IS45 in (a) 2013 and (c) 2016 and those for IS30 in (b) 2013 and (d) 2016. For each array and date, a set of four frames is shown to characterize the signals. Shown are subsequently: the spectral contents, the bestbeam, the signals-to-noise ratio (SNR), the back azimuth (with the true back azimuth as dashed line) and the apparent velocity, from bottom to top and as a function of time. The celerities are given in $m s^{-1}$ in the SNR-frame. The red dots indicate events of interest which are also labeled as I_w , I_{ws} and I_s , for respectively tropospheric, combined tropospheric-stratospheric and stratospheric refractions. The blue dots follow from three-dimensional raytracing (in spherical coordinates) through ECMWF atmospheric specifications. The following settings were used to obtain these results: binsize 256 samples, overlap 224 samples, 2nd order Butterworth filter with two passes and corner frequencies of 0.5 to 3.0 Hz (for IS45 2016 1.0 to 3.0 Hz).

6

Conclusions and recommendations

In this final chapter, the conclusions of the previous chapters will be summarized and recommendations will be given to support the path towards infrasound data assimilation as well as an outlook for future research.

6.1 Conclusions

In this thesis, the synergy between stratospheric variability and infrasound has been presented. Knowledge on stratospheric variability appeared equally important for numerical weather prediction and infrasound monitoring purposes. Validation of atmospheric analysis and forecast products, in particular in regions above 30 km altitude, is important for numerical weather prediction applications, as the interaction between the stratosphere and the troposphere cannot be neglected. Due to the delayed impact of a warming on the weather in the troposphere, evaluating the forecast in the middle atmosphere can act as an early indicator of a possible upcoming loss of forecast skill in the troposphere. As atmospheric specifications in the lower and middle atmosphere are routinely used in a wide variety of atmospheric sciences and applications, the validation is relevant to a broad community and a wide variety of applications, such as the verification of the Comprehensive Nuclear-Test-Ban Treaty, in which infrasound is used as a verification technique. In this thesis, a clear transition can be denoted from observing anomalous signatures towards the use of the infrasound signals to study anomalies in atmospheric conditions, for example. It is shown that infrasound can provide additional information of the state of the atmosphere, with the potential to contribute to NWP, especially during a SSW. In this thesis, observed and simulated infrasound wavefront parameters are compared, i.e., back azimuth. The theoretical basis of this method relies on the assertion that sound propagates through a particular atmospheric state. The atmospheric state that is closest to reality will then lead to simulated values that are closest to the observed values.

■ Conclusions from Chapter 2 on processing and modelling

The fundamental theory used throughout this thesis is explained in Chapter 2. Firstly, Chapter 2 explains the detection of coherent infrasound signals by array processing. Relevant wavefront information is extracted from the continuous waveform recordings using beamforming and the Fisher coherence analysis. Throughout the thesis, extracted wavefront parameters, for example, back azimuth, apparent velocity, or travel time, are simulated by ray theory using various atmospheric conditions.

Secondly, Chapter 2 describes propagation modelling of infrasound in a dynamical atmosphere. Kinematic or geometric propagation of a wavefront is described by the eikonal, a high-frequency approximation of the wave equation, which is solved asymptotically by ray tracing. Transmission is defined by the impedance variation along a ray and the Jacobian, describing the geometrical spreading. Although ray theory does not include full wave phenomena such as scattering and diffraction, ray theory is exact. Hence, long-range propagation in a complex three-dimensional atmosphere using ray theory implemented in spherical coordinates can be computed more efficiently. This allows bulk processing using various atmospheric conditions, of importance for the diverse case studies throughout this thesis when using for example ensemble representation of the atmosphere.

Thirdly, Chapter 2 describes the dominant ambient infrasound source, microbaroms. Interacting large regions of high-energetic ocean waves of similar frequency with opposite directions, e.g., ocean swell and marine storms, radiate almost continuous acoustic energy well characterized by a radiation frequency of 0.2 ± 0.1 Hz. Microbarom source modelling is obtained using a two-fluid model, over air and seawater, and a coupled ocean-wave model providing the sea state [Hasselmann, 1963; Brekhovskikh *et al.*, 1973]. Air-sea coupling is crucial due to the two-way interaction of surface winds and ocean waves [Janssen, 2009]. The state-of-the-art infrasound microbarom radiation source model [Waxler *et al.*, 2007] takes into account the effect of resonance due to bathymetry, affecting the source location, amplitude, and frequency (applied in Chapter 3).

■ Conclusions from Chapter 3 on the life cycle of a warming

The use of ambient noise as a passive atmospheric probe is demonstrated in Chapter 3. Microbarom observations are evaluated to identify detections that cannot be explained by the analysis of the European Centre for Medium-Range Weather Forecasts. A first-order model is used to relate observations with the analysis, comprising of the Waxler *et al.* [2007] microbarom source model and an atmospheric propagation model using linear three-dimensional ray tracing. Knowledge of the atmospheric ducting condition for the observed microbaroms is obtained from the infrasonic amplitudes, without any a priori atmospheric information. It is successfully shown that daily normalized spectral powers can be used to distinguish stratospheric from thermospheric return height, based on the different signature of solar tidal amplitude fluctuations. The observed microbarom amplitudes show more details on the life cycle of a sudden stratospheric warming, with differences in the

warming onset and offsets, than present in the ECMWF analysis. Chapter 3 shows that a SSW is not a smooth event as following from the analysis but a series of abrupt changes with a period of 10 to 16 days, increasing in intensity and duration. This is in agreement with the wave period of Rossby waves, interacting with the stratospheric circumpolar vortex. The type of vortex disturbance, split or reversal, can be deduced from the combined effect of the change in back-azimuth, solar tidal signature type, and/or phase variation of the amplitude variation of the observed microbaroms.

■ Conclusions from Chapter 4 on stratospheric forecast evaluation

In Chapter 4, for the first time, middle atmospheric numerical weather forecasts are evaluated using infrasound. A year of near continuous infrasound from the volcano Mount Tolbachik (Kamchatka, Russian Federation) is compared with simulations using high-resolution deterministic ECMWF forecasts. For the entire time span the nowcast generally performs best, indicated by a higher continuity of the predicted wavefront characteristics with a minimal back azimuth difference. Best performance for all forecasts is obtained in summer. The difference between the infrasound observations and the predictions based on the forecasts is significantly larger during the 2013 SSW period for all forecasts. Simulations show that the SSW onset is better captured by the ten-day forecast while the recovery is better captured by the nowcast. The proposed method in Chapter 4 for the evaluation of middle atmospheric weather forecasts using near-continuous infrasound detections can directly be applied to similar setups, making use of other IMS or national infrasound arrays. Chapter 4 demonstrates that infrasound can provide useful additional information in regions where data coverage is sparse, such as in the upper stratosphere. The frequency content of the observed infrasound suggests a six-day longer duration of the 2013 SSW than predicted by the ECMWF nowcast.

■ Conclusions from Chapter 5 on advanced infrasound propagation

The use of knowledge on stratospheric variability for advanced infrasound propagation is applied in Chapter 5. In this chapter, two applications are given.

First, Chapter 5 demonstrates probabilistic infrasound propagation modelling using realistic atmospheric perturbations. One year of large mining explosions in the Aitik mine, northern Sweden, observed at infrasound array IS37 in northern Norway are simulated using three-dimensional ray tracing. In this study, the use of ensembles of realistically perturbed analyses for infrasound propagation modelling is successfully demonstrated. Although GCMs have limitations, a significant improvement in propagation modelling is obtained without the need of adding small-scale fluctuations. Error variance profiles at the array show that the yearly mean effective sound speed variation can reach up to 8 m s^{-1} in the stratosphere, exceeding occasionally 25 m s^{-1} for a single ensemble set. The latter value is in the order of what has been proposed previously to explain infrasound observations, often dedicated to small-scale fluctuations and gravity waves [Green *et al.*, 2011; Hedlin *et al.*, 2012; Drob *et al.*, 2013] or model discrepancies [Assink *et al.*, 2014b].

Second, Chapter 5 explains the observed atmospheric infrasound generated by the 2013 and 2016 underground nuclear tests conducted by the Democratic People's Republic of Korea (DPRK). Clear detections were made in the Russian Federation (IS45) and Japan (IS30) in 2013 at stations from the International Monitoring System. Both tropospheric and stratospheric refractions arrived at the stations. In 2016, only a weak return was potentially observed at IS45. Data analysis and propagation modelling shows that the noise level at the stations and the stratospheric circumpolar vortex were different in 2016 compared to 2013. As the seismic magnitude of the 2013 and 2016 nuclear test explosions was comparable, we hypothesize that the 2016 test occurred at least 1.5 times deeper. In such a case, less seismic energy would couple through the lithosphere-atmosphere interface, leading to less observable infrasound. Since explosion depth is difficult to estimate from seismic data alone, this motivates a synergy between seismics and infrasonics.

6.2 Recommendations and outlook

Infrasound has a long history in monitoring SSWs, introduced in Chapter 1. Several pioneering studies have focused on the various effects of a major warming on the propagation of infrasound [*Donn and Rind, 1972; Rind and Donn, 1978; Evers and Siegmund, 2009; Evers et al., 2012; Assink et al., 2014a*]. Over the last decade, a clear transition can be denoted from observing anomalous signatures towards the use of these signals to study anomalies in atmospheric conditions [*Smets and Evers, 2014; Smets et al., 2016*]. A final goal in the next 10 to 20 years is the implementation of infrasound, and other ARISE instruments, for weather and climate monitoring [*Smets et al., 2014*]. However, assimilation of new observations requires a long pathway with the need of developing costly assimilation routines or even new atmospheric models. This thesis contributes to the development of methods to allow infrasound to be used for model validation by weather and climate prediction centres, and raising awareness of the utility of infrasound recordings making the first pathway to assimilation.

■ Extrapolation of forecast evaluation

In a next step, the method of Chapter 4 for the evaluation of middle atmospheric weather forecasts using near-continuous infrasound detections can directly be applied to similar setups, making use of other IMS and national infrasound arrays. The demonstrated forecast evaluation method relies on an active volcano. However, the same methodology can be applied to other sources, for example, microbaroms, as partly shown in Chapter 3 for the analysis. Partially, as the proposed first-order point source model is in fact invalid. The actual source area is significantly larger than the assumption of radiating patches. A more realistic approach would be obtained by using the cross spectral density from Green's functions as propagation factor for the microbarom sources. Ray tracing is still an option, in order to provide the transmission loss, but it is essential to integrate over the entire active source area. In fact, any source whose characteristics are constrained is of

potential interest. Hence, the entire infrasound wavefield is of potential interest to evaluate atmospheric conditions. Interesting natural sources to explore further are lightning, aurora, earthquakes, and meteors. In addition, the development of source-independent techniques by interferometry can contribute to utilization of the entire ambient infrasound spectrum [Fricke *et al.*, 2013, 2014].

Microbaroms from multiple source regions commonly arrive at the same time at a given array. It is therefore desirable to be able to measure multiple slowness vectors accurately. In this thesis, overlapping Atlantic and Pacific Ocean sources are resolved by beamforming in a specific direction. Alternative methods besides conventional (fk) or adaptive (Capon) beamforming are deconvolution enhanced direction of arrival estimation (CLEAN) as applied in astronomy [Högbon, 1974], aeroacoustics [Sijtsma, 2007] and geophysics [Gal *et al.*, 2016] or multiple signal classification (MUSIC) for super-resolution, used in acoustics [Gruber *et al.*, 2004], radar signal processing [Schmidt, 1986], electromagnetic imaging [Chen and Agarwal, 2008], and biology [Agarwal and Macháň, 2016].

Also, the forecast evaluation method (Chapter 4) needs to be applied to ensemble forecasting (Section 5.1), which has a larger impact on NWP than the high-resolution deterministic forecast. In addition, it is crucial to explore further the uncertainty and bias behaviour of the observations.

■ Extensive collaboration

The fundamental method of validating atmospheric conditions using infrasound is through propagation modelling. Improving propagation modelling by benchmarking experiments is desired. Inter-comparison of various infrasound propagation methods and implementations is of great importance. Ray propagation used in the thesis can be improved by implementation in meteorological coordinates, operating on the native atmospheric model grids. This limits the need for resampling and interpolation. In addition, collaboration with numerical weather prediction is stimulated. Combining ray theory with full waveform techniques as Parabolic Equations can provide cost-efficient three-dimensional propagation effects (rays) with accurate transmission loss estimates (full waveform).

In future, direct implementation of infrasound propagation modelling by NWP centres themselves is recommended. Hence, this allows the use of the entire variety of atmospheric modelling products and at much smaller time steps (in the order of several minutes). The next step towards the use of infrasound for numerical weather prediction demands joint case studies with weather and climate prediction centres. Specifically, infrasound as a service, with relevant case studies defined by NWP to address their needs. Such relevant collaborative work stimulates the interest of both the infrasound and NWP communities. In addition, this contributes to the development of a user community, the key element to guarantee long-term existence [Smets *et al.*, 2014].

■ Toward a real global stratospheric signature

It is shown that infrasound is capable of providing detailed insight into the state of the atmosphere, which is of great value during a SSW. Nevertheless, it is essential to evolve towards a global comprehensive signature. Expanding towards ambient noise observations provides the ability to probe larger parts of the stratosphere. This is highly important for NWP, since improved knowledge of the global stratosphere induces a gain in tropospheric forecast skill but only when incorporating global observations [Lee *et al.*, 2018]. An intermediate step along the path towards assimilation of global infrasound data is to invert for the stratospheric zonal-mean-zonal-wind from the observed ambient noise. In NWP, this parameter is important for the evaluation of stratospheric variability, used as a definition of a SSW in model space [Charlton and Polvani, 2007]. Accordingly, a simple yet robust first order comparison of infrasound and numerical weather prediction on a global scale is obtained. More importantly, this comparison will encourage the infrasound community to speak the common language of weather and climate modelling.

A

Additional theory

A.1 Ideal signal-to-noise ratio increase using array measurements

Assume an array of N receivers with positions \mathbf{r}_n . Let recording $y_n(t)$ be the sum of the background noise $\epsilon(t)$ and signal $a(t)$,

$$y_n(t) = a(t) + \epsilon(t),$$

where n denotes the array element at time t . Signal-to-noise ratio SNR_n for an individual receiver n is denoted as

$$\text{SNR}_n = \frac{a}{\epsilon}.$$

The sum of all array elements for the time-shifted window y_n yields

$$y_N(t) = \sum_{n=1}^N y_n(t + \tau_n),$$

with time shift $\tau_n = \mathbf{r}_n \cdot \mathbf{s}$ assuming signal s propagates according to a plane wave with slowness \mathbf{s} . Assuming that noise is incoherent and signal is coherent and not attenuated, thus identical at each receiver, the sum can be written as

$$y_N(t) = Na(t) + \sum_{n=1}^N \epsilon_n(t + \tau_n).$$

Noise ϵ is assumed to be normal distributed with zero mean and variance σ^2 at all N receiver sites. The variance of noise of the array sum yields,

$$\sigma_N^2 = N\sigma^2,$$

with standard deviation,

$$\sigma_N = \sqrt{N}\sigma,$$

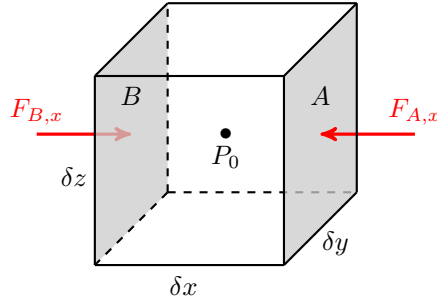


Figure A.1: Pressure gradient for an infinitesimal volume of air, $\delta V = \delta x \delta y \delta z$.

and signal-to-noise-ratio,

$$\text{SNR}_N = \frac{N}{\sqrt{N}} \frac{a}{\epsilon}.$$

Signal summation for an array of N receivers ideally leads to an increased signal-to-noise-ratio by \sqrt{N} ,

$$\frac{\text{SNR}_N}{\text{SNR}_n} = \sqrt{N}.$$

A.2 Pressure gradient force

Assume an infinitesimal volume of air, $\delta V = \delta x \delta y \delta z$, with pressure P_0 in the center, as shown in Figure A.1. The pressure at the edges of the volume in x-direction, respectively surfaces A and B , with respect to the pressure at the centre of the volume P_0 can be expressed in terms of a first order Taylor expansion:

$$P_A = P_0 + \frac{\partial p}{\partial x} \frac{\delta x}{2},$$

$$P_B = P_0 - \frac{\partial p}{\partial x} \frac{\delta x}{2}.$$

Pressure force is the product of pressure over the area of interest. The pressure force at surfaces A and B is,

$$F_{A,x} = -P_A \delta y \delta z,$$

$$F_{B,x} = P_B \delta y \delta z,$$

where $\delta y \delta z$ equals the area of surfaces A and B . The net x component of the pressure force acting on the volume V equals,

$$F_x = F_{A,x} + F_{B,x} = -\frac{\partial P}{\partial x} \delta x \delta y \delta z.$$

Because the net force is proportional to the derivative of the pressure in the direction of the force, it is referred to as the *pressure gradient force*. Rewriting the net x component for the infinitesimal volume $\delta V = \delta x \delta y \delta z$, the pressure gradient force per unit volume is,

$$\frac{F_x}{V} = -\frac{\partial p}{\partial x}.$$

Similarly the y and z components of the pressure gradient force can be derived as

$$\frac{F_y}{V} = -\frac{\partial p}{\partial y} \quad \text{and} \quad \frac{F_z}{V} = -\frac{\partial p}{\partial z}.$$

The total pressure gradient force per unit volume can be denoted as

$$\frac{\mathbf{F}}{V} = -\nabla P. \tag{A.2.1}$$

A.3 Hamilton's canonical equations

Recall Hamilton's principal functional \mathcal{S} , which is a function of the Lagrangian \mathcal{L} ,

$$\mathcal{S}(\mathbf{x}, t) = \int \mathcal{L}(\mathbf{x}, \dot{\mathbf{x}}, t) dt, \tag{2.2.46}$$

describing the time evolution of the dynamic system for position \mathbf{x} and time t . Repeating Fermat's principle,

$$\delta \mathcal{S} = 0,$$

which is only valid when,

$$\int \delta \mathcal{L} dt = 0,$$

known as Hamilton's stationary principle. The extremal of the Lagrangian functional $\delta \mathcal{L}$ is obtained by calculus of variations, which is related to the total differential,

$$d\mathcal{L} = \frac{\partial \mathcal{L}}{\partial \mathbf{x}} \cdot d\mathbf{x} + \frac{\partial \mathcal{L}}{\partial \dot{\mathbf{x}}} \cdot d\dot{\mathbf{x}} + \frac{\partial \mathcal{L}}{\partial t} dt,$$

for a virtual displacement $\delta \mathbf{x}$ and a zero time increment $\delta t = 0$ as the extremal is a stationary point. The variational of the Lagrangian yields,

$$\delta \mathcal{L} = \frac{\partial \mathcal{L}}{\partial \mathbf{x}} \cdot \delta \mathbf{x} + \frac{\partial \mathcal{L}}{\partial \dot{\mathbf{x}}} \cdot \delta \dot{\mathbf{x}},$$

with,

$$\delta \dot{\mathbf{x}} = \delta \frac{d\mathbf{x}}{dt} = \frac{d}{dt} \delta \mathbf{x},$$

so that,

$$\int \delta \mathcal{L} dt = \int \left(\frac{\partial \mathcal{L}}{\partial \mathbf{x}} \cdot \delta \mathbf{x} + \frac{\partial \mathcal{L}}{\partial \dot{\mathbf{x}}} \cdot \frac{d}{dt} \delta \mathbf{x} \right) dt = 0.$$

Rewriting yields,

$$\frac{\partial \mathcal{L}}{\partial \dot{\mathbf{x}}} \cdot \delta \mathbf{x} \int dt + \int \left(\frac{\partial \mathcal{L}}{\partial \mathbf{x}} - \frac{d}{dt} \frac{\partial \mathcal{L}}{\partial \dot{\mathbf{x}}} \right) \cdot \delta \mathbf{x} dt = 0.$$

For a virtual displacement it holds $\delta \mathbf{x} \rightarrow 0$ wherefore the first integral always becomes zero anywhere. However, the second integral will only be definitely zero when the integrand itself is zero,

$$\frac{\partial \mathcal{L}}{\partial \mathbf{x}} - \frac{d}{dt} \frac{\partial \mathcal{L}}{\partial \dot{\mathbf{x}}} = 0, \quad (\text{A.3.1})$$

which yields the Euler–Lagrange equation.

The Hamiltonian \mathcal{H} is related to the Lagrangian \mathcal{L} by its Legendre transform

$$\mathcal{H} = \dot{\mathbf{x}} \cdot \frac{\partial \mathcal{L}}{\partial \dot{\mathbf{x}}} - \mathcal{L} = \dot{\mathbf{x}} \cdot \mathbf{p} - \mathcal{L}, \quad (\text{A.3.2})$$

with conjugate moment definition,

$$\frac{\partial \mathcal{L}}{\partial \dot{\mathbf{x}}} = \frac{\partial S}{\partial \dot{\mathbf{x}}} = \mathbf{p}.$$

The total differential of the Hamiltonian (A.3.2) yields,

$$\begin{aligned} d\mathcal{H} &= \frac{\partial \mathcal{H}}{\partial \mathbf{x}} \cdot d\mathbf{x} + \frac{\partial \mathcal{H}}{\partial \mathbf{p}} \cdot d\mathbf{p} + \frac{\partial \mathcal{H}}{\partial t} dt, \\ &= \dot{\mathbf{x}} \cdot d\mathbf{p} + \mathbf{p} \cdot d\dot{\mathbf{x}} - \frac{\partial \mathcal{L}}{\partial \mathbf{x}} \cdot d\mathbf{x} - \frac{\partial \mathcal{L}}{\partial \dot{\mathbf{x}}} \cdot d\dot{\mathbf{x}} - \frac{\partial \mathcal{L}}{\partial t} dt. \end{aligned}$$

Substituting the Euler–Lagrange equation (A.3.1) and the conjugate moment definition gives,

$$\begin{aligned} \frac{\partial \mathcal{H}}{\partial \mathbf{x}} \cdot d\mathbf{x} + \frac{\partial \mathcal{H}}{\partial \mathbf{p}} \cdot d\mathbf{p} + \frac{\partial \mathcal{H}}{\partial t} dt \\ = \dot{\mathbf{x}} \cdot d\mathbf{p} - \dot{\mathbf{p}} \cdot d\mathbf{x} - \frac{\partial \mathcal{L}}{\partial t} dt. \end{aligned}$$

Rearranging for each coefficient yields Hamilton’s canonical equations describing the motion of particles in terms of time rates of change for position $\dot{\mathbf{x}}$ and slowness $\dot{\mathbf{p}}$,

$$\dot{\mathbf{x}} = \frac{\partial \mathcal{H}}{\partial \mathbf{p}}, \quad \dot{\mathbf{p}} = -\frac{\partial \mathcal{H}}{\partial \mathbf{x}}, \quad \text{and} \quad \frac{\partial \mathcal{H}}{\partial t} = -\frac{\partial \mathcal{L}}{\partial t}, \quad (\text{A.3.3})$$

whereas the latter indicates,

$$\frac{\partial}{\partial t} (\mathbf{p} \cdot \dot{\mathbf{x}}) = 0. \quad (\text{A.3.4})$$

A.4 Ray equations in spherical coordinates

Assume the Earth is a perfect sphere. The transformation matrix or metrical tensor \mathcal{Q} denotes,

$$\mathcal{Q} = \begin{pmatrix} \sin \lambda \cos \varphi & \sin \lambda \sin \varphi & \cos \lambda \\ \cos \lambda \cos \varphi & \cos \lambda \sin \varphi & -\sin \lambda \\ -\sin \varphi & \cos \varphi & 0 \end{pmatrix}. \quad (\text{A.4.1})$$

Hence, converting from Cartesian coordinates $\mathbf{x}(x, y, z)$ to spherical coordinates $\mathbf{r}(r, \lambda, \varphi)$ yields,

$$\mathbf{r} = \mathcal{Q}\mathbf{x}, \quad (\text{A.4.2})$$

with r the radial component, λ the polar angle from the vertical and φ the azimuthal angle. The inverse transform is defined as

$$\mathbf{x} = \mathcal{Q}^T \mathbf{r}. \quad (\text{A.4.3})$$

As such, the tensor is orthogonal satisfying $\mathcal{Q}\mathcal{Q}^T = I$, with I the identity matrix. Derivative $d\mathbf{r}$ yields,

$$d\mathbf{r} = \left(dr \quad r d\lambda \quad r \sin \lambda d\varphi \right)^T. \quad (\text{A.4.4})$$

Let $\mathbb{C} = \text{diag}(1, r, r \sin \lambda)$, the coefficients of Equation (A.4.4). Wind and slowness vectors in spherical coordinates are defined as $\mathbf{w}_r = \mathbb{C}^{-1}\mathbf{w}$, and $\mathbf{p}_r = \mathbb{C}\mathbf{p}$. Note the opposite exponent sign for slowness.

The kinematic ray equations for position and slowness in spherical coordinates for time rates of change denote,

$$\dot{\mathbf{r}} = \mathbf{w}_r \left(1 - \mathbf{p}_r \cdot \mathbf{w}_r \right) + c_T^2 \mathbb{C}^{-2} \mathbf{p}_r, \quad (\text{A.4.5a})$$

$$\begin{aligned} \dot{\mathbf{p}}_r &= c_T^2 \left(\mathbf{p}_r^T \mathbb{C}^{-3} \frac{\partial \mathbb{C}}{\partial \mathbf{r}} \mathbf{p}_r \right) - c_T \left(\mathbf{p}_r^T \mathbb{C}^{-2} \mathbf{p}_r \right) \frac{\partial c_T}{\partial \mathbf{r}}, \\ &+ \left(1 - \mathbf{p}_r \cdot \mathbf{w}_r \right) \left(-\mathbf{p}_r \cdot \frac{\partial \mathbf{w}_r}{\partial \mathbf{r}} \right), \end{aligned} \quad (\text{A.4.5b})$$

with initial conditions,

$$\mathbf{r}(t=0) = \mathbf{r}_0 \quad \text{and} \quad \mathbf{p}_r(t=0) = \mathbf{p}_{r,0} = \frac{\hat{\mathbf{n}}}{c_0} \mathbb{C}_0. \quad (\text{A.4.6})$$

Remark that initial phase speed $c_0 = \|\mathbf{w} \cdot \mathbf{n} + c_T\| = \|\mathbf{w}_r \cdot \mathbf{n} \mathbb{C} + c_T\|$.

Ray equations in terms of time rates of change of elevation yield,

$$\begin{aligned} \partial_\phi \dot{\mathbf{r}} &= \frac{d}{dt} \frac{\partial \mathbf{r}}{\partial \phi} = \frac{\partial \mathbf{w}_r}{\partial \mathbf{r}} \frac{\partial \mathbf{r}}{\partial \phi} \left(1 - \mathbf{w}_r \cdot \mathbf{p}_r \right) - \mathbf{w}_r \left(\mathbf{p}_r \cdot \frac{\partial \mathbf{w}_r}{\partial \mathbf{r}} \frac{\partial \mathbf{r}}{\partial \phi} + \mathbf{w}_r \cdot \frac{\partial \mathbf{p}_r}{\partial \phi} \right) \\ &+ c_T^2 \left(\mathbb{C}^{-2} \frac{\partial \mathbf{p}_r}{\partial \phi} - 2\mathbb{C}^{-3} \frac{\partial \mathbb{C}}{\partial \mathbf{r}} \frac{\partial \mathbf{r}}{\partial \phi} \mathbf{p}_r \right) \\ &+ 2c_T \mathbb{C}^{-2} \mathbf{p}_r \frac{\partial c_T}{\partial \mathbf{r}} \frac{\partial \mathbf{r}}{\partial \phi} \end{aligned}, \quad (\text{A.4.7})$$

for position, and,

$$\begin{aligned}
\partial_\phi \dot{\mathbf{p}}_{\mathbf{r}} &= \frac{d}{dt} \frac{\partial \mathbf{p}_{\mathbf{r}}}{\partial \phi} = 2c_T \left(\mathbf{p}_{\mathbf{r}}^T \mathbb{C}^{-3} \frac{\partial \mathbb{C}}{\partial \mathbf{r}} \mathbf{p}_{\mathbf{r}} \right) \frac{\partial c_T}{\partial \mathbf{r}} \frac{\partial \mathbf{r}}{\partial \phi} + 2c_T^2 \left(\mathbf{p}_{\mathbf{r}}^T \mathbb{C}^{-3} \frac{\partial \mathbb{C}}{\partial \mathbf{r}} \frac{\partial \mathbf{p}_{\mathbf{r}}}{\partial \phi} \right) \\
&\quad - 3c_T^2 \left(\mathbf{p}_{\mathbf{r}}^T \mathbb{C}^{-4} \frac{\partial^2 \mathbb{C}}{\partial \mathbf{r}^2} \frac{\partial \mathbf{r}}{\partial \phi} \mathbf{p}_{\mathbf{r}} \right) + c_T^2 \left(\mathbf{p}_{\mathbf{r}}^T \mathbb{C}^{-3} \frac{\partial^2 \mathbb{C}}{\partial \mathbf{r}^2} \frac{\partial \mathbf{r}}{\partial \phi} \mathbf{p}_{\mathbf{r}} \right) \\
&\quad - c_T \frac{\partial^2 c_T}{\partial \mathbf{r}^2} \frac{\partial \mathbf{r}}{\partial \phi} \left(\mathbf{p}_{\mathbf{r}}^T \mathbb{C}^{-2} \mathbf{p}_{\mathbf{r}} \right) - 2c_T \left(\mathbf{p}_{\mathbf{r}}^T \mathbb{C}^{-2} \frac{\partial \mathbf{p}_{\mathbf{r}}}{\partial \phi} \right) \frac{\partial c_T}{\partial \mathbf{r}} \\
&\quad + 4c_T \left(\mathbf{p}_{\mathbf{r}}^T \mathbb{C}^{-3} \frac{\partial \mathbb{C}}{\partial \mathbf{r}} \frac{\partial \mathbf{r}}{\partial \phi} \mathbf{p}_{\mathbf{r}} \right) \frac{\partial c_T}{\partial \mathbf{r}} \\
&\quad + \left(\mathbf{p}_{\mathbf{r}} \cdot \frac{\partial \mathbf{w}_{\mathbf{r}}}{\partial \mathbf{r}} \right)^2 \frac{\partial \mathbf{r}}{\partial \phi} + \left(\mathbf{p}_{\mathbf{r}} \cdot \frac{\partial \mathbf{w}_{\mathbf{r}}}{\partial \mathbf{r}} \right) \left(\mathbf{w}_{\mathbf{r}} \cdot \frac{\partial \mathbf{p}_{\mathbf{r}}}{\partial \phi} \right) \\
&\quad - \left(1 - \mathbf{w}_{\mathbf{r}} \cdot \mathbf{p}_{\mathbf{r}} \right) \frac{\partial \mathbf{p}_{\mathbf{r}}}{\partial \phi} \cdot \frac{\partial \mathbf{w}_{\mathbf{r}}}{\partial \mathbf{r}} - \left(1 - \mathbf{w}_{\mathbf{r}} \cdot \mathbf{p}_{\mathbf{r}} \right) \mathbf{p}_{\mathbf{r}} \cdot \frac{\partial^2 \mathbf{w}_{\mathbf{r}}}{\partial \mathbf{r}^2} \frac{\partial \mathbf{r}}{\partial \phi}
\end{aligned} \tag{A.4.8}$$

for slowness.

In terms of time rates of change of azimuth the ray equations become,

$$\begin{aligned}
\partial_\theta \dot{\mathbf{r}} &= \frac{d}{dt} \frac{\partial \mathbf{r}}{\partial \theta} = \frac{\partial \mathbf{w}_{\mathbf{r}}}{\partial \mathbf{r}} \frac{\partial \mathbf{r}}{\partial \theta} \left(1 - \mathbf{w}_{\mathbf{r}} \cdot \mathbf{p}_{\mathbf{r}} \right) - \mathbf{w}_{\mathbf{r}} \left(\mathbf{p}_{\mathbf{r}} \cdot \frac{\partial \mathbf{w}_{\mathbf{r}}}{\partial \mathbf{r}} \frac{\partial \mathbf{r}}{\partial \theta} + \mathbf{w}_{\mathbf{r}} \cdot \frac{\partial \mathbf{p}_{\mathbf{r}}}{\partial \theta} \right) \\
&\quad + c_T^2 \left(\mathbb{C}^{-2} \frac{\partial \mathbf{p}_{\mathbf{r}}}{\partial \theta} - 2\mathbb{C}^{-3} \frac{\partial \mathbb{C}}{\partial \mathbf{r}} \frac{\partial \mathbf{r}}{\partial \theta} \mathbf{p}_{\mathbf{r}} \right) \\
&\quad + 2c_T \mathbb{C}^{-2} \mathbf{p}_{\mathbf{r}} \frac{\partial c_T}{\partial \mathbf{r}} \frac{\partial \mathbf{r}}{\partial \theta}
\end{aligned} \tag{A.4.9}$$

for position, and,

$$\begin{aligned}
\partial_\theta \dot{\mathbf{p}}_{\mathbf{r}} &= \frac{d}{dt} \frac{\partial \mathbf{p}_{\mathbf{r}}}{\partial \theta} = 2c_T \left(\mathbf{p}_{\mathbf{r}}^T \mathbb{C}^{-3} \frac{\partial \mathbb{C}}{\partial \mathbf{r}} \mathbf{p}_{\mathbf{r}} \right) \frac{\partial c_T}{\partial \mathbf{r}} \frac{\partial \mathbf{r}}{\partial \theta} + 2c_T^2 \left(\mathbf{p}_{\mathbf{r}}^T \mathbb{C}^{-3} \frac{\partial \mathbb{C}}{\partial \mathbf{r}} \frac{\partial \mathbf{p}_{\mathbf{r}}}{\partial \theta} \right) \\
&\quad - 3c_T^2 \left(\mathbf{p}_{\mathbf{r}}^T \mathbb{C}^{-4} \frac{\partial^2 \mathbb{C}}{\partial \mathbf{r}^2} \frac{\partial \mathbf{r}}{\partial \theta} \mathbf{p}_{\mathbf{r}} \right) + c_T^2 \left(\mathbf{p}_{\mathbf{r}}^T \mathbb{C}^{-3} \frac{\partial^2 \mathbb{C}}{\partial \mathbf{r}^2} \frac{\partial \mathbf{r}}{\partial \theta} \mathbf{p}_{\mathbf{r}} \right) \\
&\quad - c_T \frac{\partial^2 c_T}{\partial \mathbf{r}^2} \frac{\partial \mathbf{r}}{\partial \theta} \left(\mathbf{p}_{\mathbf{r}}^T \mathbb{C}^{-2} \mathbf{p}_{\mathbf{r}} \right) - 2c_T \left(\mathbf{p}_{\mathbf{r}}^T \mathbb{C}^{-2} \frac{\partial \mathbf{p}_{\mathbf{r}}}{\partial \theta} \right) \frac{\partial c_T}{\partial \mathbf{r}} \\
&\quad + 4c_T \left(\mathbf{p}_{\mathbf{r}}^T \mathbb{C}^{-3} \frac{\partial \mathbb{C}}{\partial \mathbf{r}} \frac{\partial \mathbf{r}}{\partial \theta} \mathbf{p}_{\mathbf{r}} \right) \frac{\partial c_T}{\partial \mathbf{r}} \\
&\quad + \left(\mathbf{p}_{\mathbf{r}} \cdot \frac{\partial \mathbf{w}_{\mathbf{r}}}{\partial \mathbf{r}} \right)^2 \frac{\partial \mathbf{r}}{\partial \theta} + \left(\mathbf{p}_{\mathbf{r}} \cdot \frac{\partial \mathbf{w}_{\mathbf{r}}}{\partial \mathbf{r}} \right) \left(\mathbf{w}_{\mathbf{r}} \cdot \frac{\partial \mathbf{p}_{\mathbf{r}}}{\partial \theta} \right) \\
&\quad - \left(1 - \mathbf{w}_{\mathbf{r}} \cdot \mathbf{p}_{\mathbf{r}} \right) \frac{\partial \mathbf{p}_{\mathbf{r}}}{\partial \theta} \cdot \frac{\partial \mathbf{w}_{\mathbf{r}}}{\partial \mathbf{r}} - \left(1 - \mathbf{w}_{\mathbf{r}} \cdot \mathbf{p}_{\mathbf{r}} \right) \mathbf{p}_{\mathbf{r}} \cdot \frac{\partial^2 \mathbf{w}_{\mathbf{r}}}{\partial \mathbf{r}^2} \frac{\partial \mathbf{r}}{\partial \theta}
\end{aligned} \tag{A.4.10}$$

for slowness.

The initial conditions of Equations (A.4.7) and (A.4.9) for \mathbf{r}_0 yield,

$$\partial_\phi \mathbf{r}_0 = 0 \quad \text{and} \quad \partial_\theta \mathbf{r}_0 = 0, \quad (\text{A.4.11})$$

since the initial ray coordinates do not yet change by the ray angles elevation and azimuth. The initial conditions for (A.4.8) and (A.4.10) result from the derivative of initial slowness \mathbf{p}_0 for ϕ and θ ,

$$\partial_\phi \mathbf{p}_0 = -\frac{\hat{\mathbf{n}}}{c_0^2} \mathbb{C}_0 \frac{\partial c_0}{\partial \phi} \quad \text{and} \quad \partial_\theta \mathbf{p}_0 = -\frac{\hat{\mathbf{n}}}{c_0^2} \mathbb{C}_0 \frac{\partial c_0}{\partial \theta}. \quad (\text{A.4.12})$$

whereas $\partial_\phi \mathbb{C}_0 = 0$ and $\partial_\theta \mathbb{C}_0 = 0$.

B

Additional spectral amplitude variations for the 2010–2014 winters

Figure B.1 shows the hemispheric 10 hPa (~ 31 km) wind velocity and direction obtained from the ECMWF analysis before, during, and after the SSW for specific time frames clarifying the evolution of the stratospheric polar vortex during the 2009 SSW.

Figures B.2 to B.6 show additional directional time averaged spectral amplitude variations for winters of 2010, 2011, 2012, 2013, and 2014 for infrasound arrays IS18 and IS53, respectively.

For 2012 no results are present for IS53 due to station unavailability. The data of December 2009 and winter 2014 has not yet been requested.

During the winters of 2010, 2011 and 2013 signatures of a SSW can be denoted, comparable to the analysis made in Section 3.4.2. Amplitude variations do not indicate signatures of a vortex split, in agreement with these known minor warming events. In 2012 and 2014 no clear signature related to a SSW can be observed.

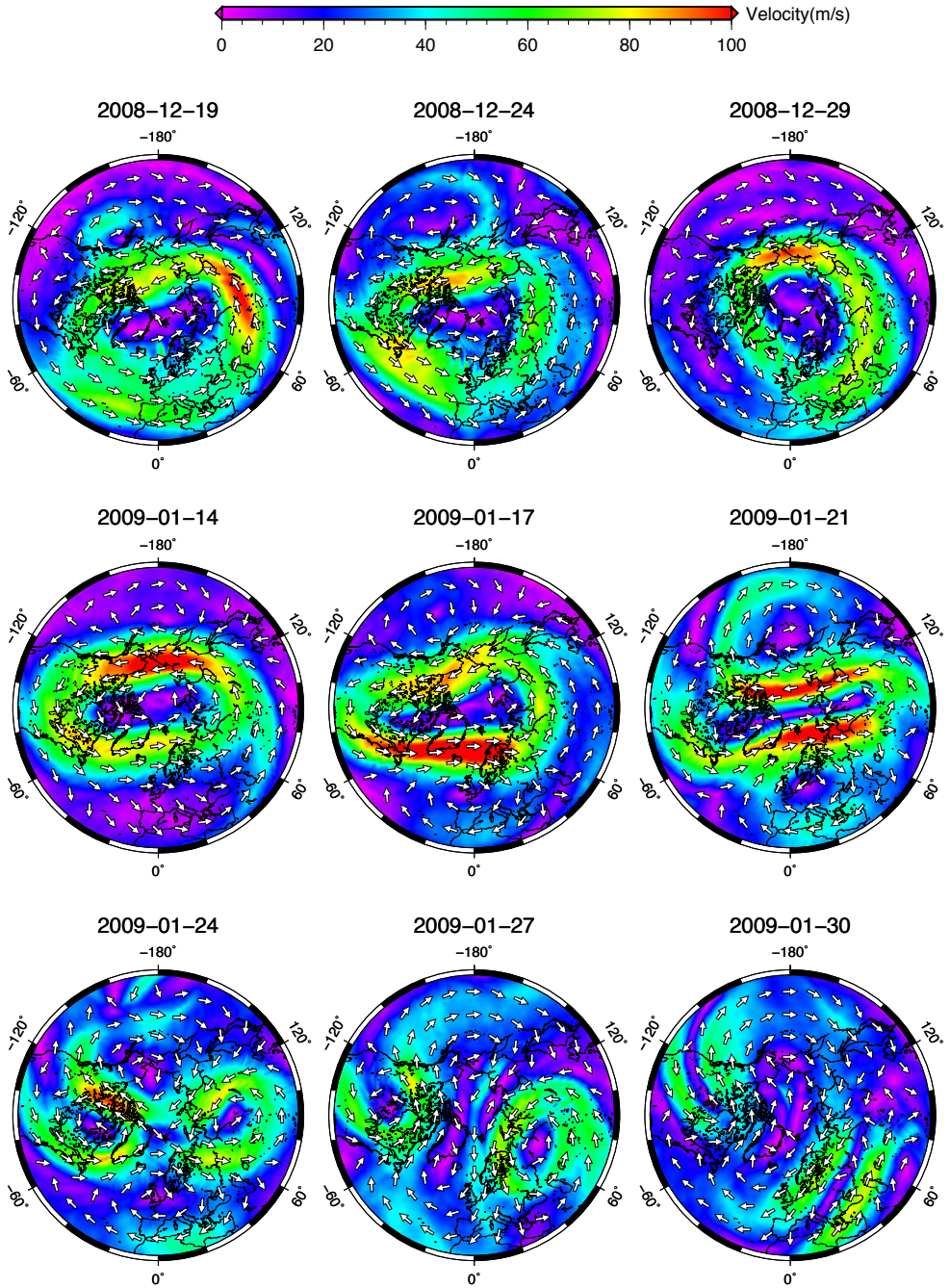


Figure B.1: Hemispheric ECMWF analysis for wind velocity and direction at 10hPa (~ 31 km) at midnight.

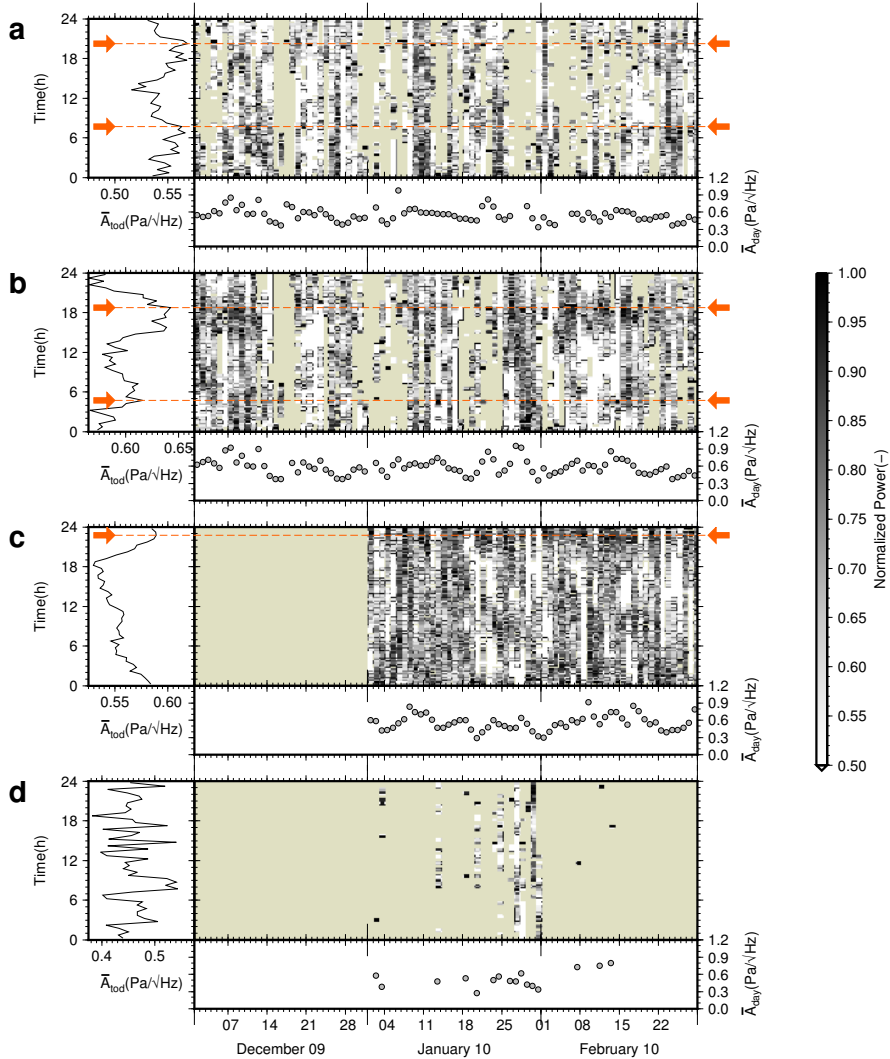


Figure B.2: Directional time averaged spectral amplitude variations for the 2010 winter. From top to bottom are shown, IS18 in (a) Atlantic Ocean and (b) Pacific Ocean direction and IS53 in (c) Pacific Ocean and (d) Atlantic Ocean direction. Each subfigure consists of (left) spectral amplitude averaged per time of day for each half hour, (right) half hour averaged spectral power, normalized per day, and (below) the daily mean spectral amplitude. Red arrows and dashed lines indicate the tidal peaks in the mean time of day amplitude, if present. Only detections are used with $\text{SNR} \geq 1.5$ for IS18 and $\text{SNR} \geq 1.3$ for IS53.

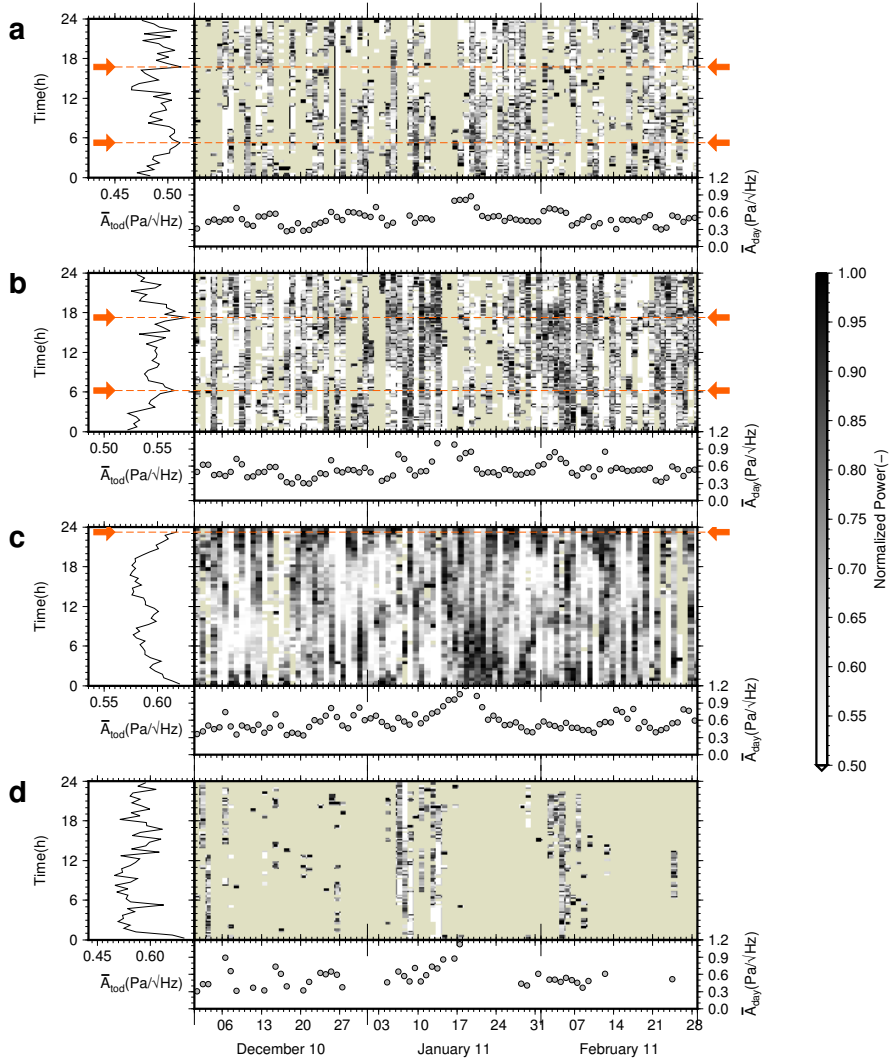


Figure B.3: Directional time averaged spectral amplitude variations for the 2011 winter. From top to bottom are shown, IS18 in (a) Atlantic Ocean and (b) Pacific Ocean direction and IS53 in (c) Pacific Ocean and (d) Atlantic Ocean direction. Each subfigure consists of (left) spectral amplitude averaged per time of day for each half hour, (right) half hour averaged spectral power, normalized per day, and (below) the daily mean spectral amplitude. Red arrows and dashed lines indicate the tidal peaks in the mean time of day amplitude, if present. Only detections are used with $\text{SNR} \geq 1.5$ for IS18 and $\text{SNR} \geq 1.3$ for IS53.

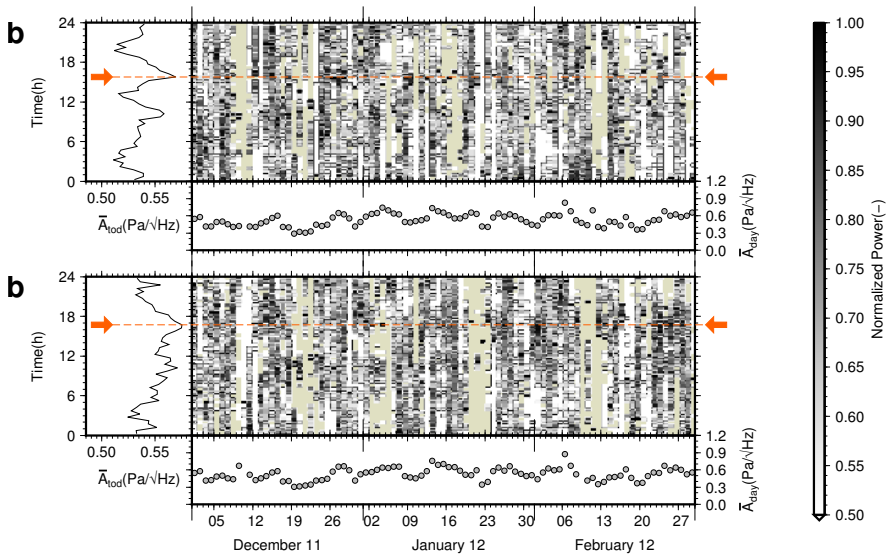


Figure B.4: Directional time averaged spectral amplitude variations for the 2012 winter. From top to bottom are shown, IS18 in (a) Atlantic Ocean and (b) Pacific Ocean direction. Each subfigure consists of (left) spectral amplitude averaged per time of day for each half hour, (right) half hour averaged spectral power, normalized per day, and (below) the daily mean spectral amplitude. Red arrows and dashed lines indicate the tidal peaks in the mean time of day amplitude, if present. Only detections are used with $\text{SNR} \geq 1.5$.

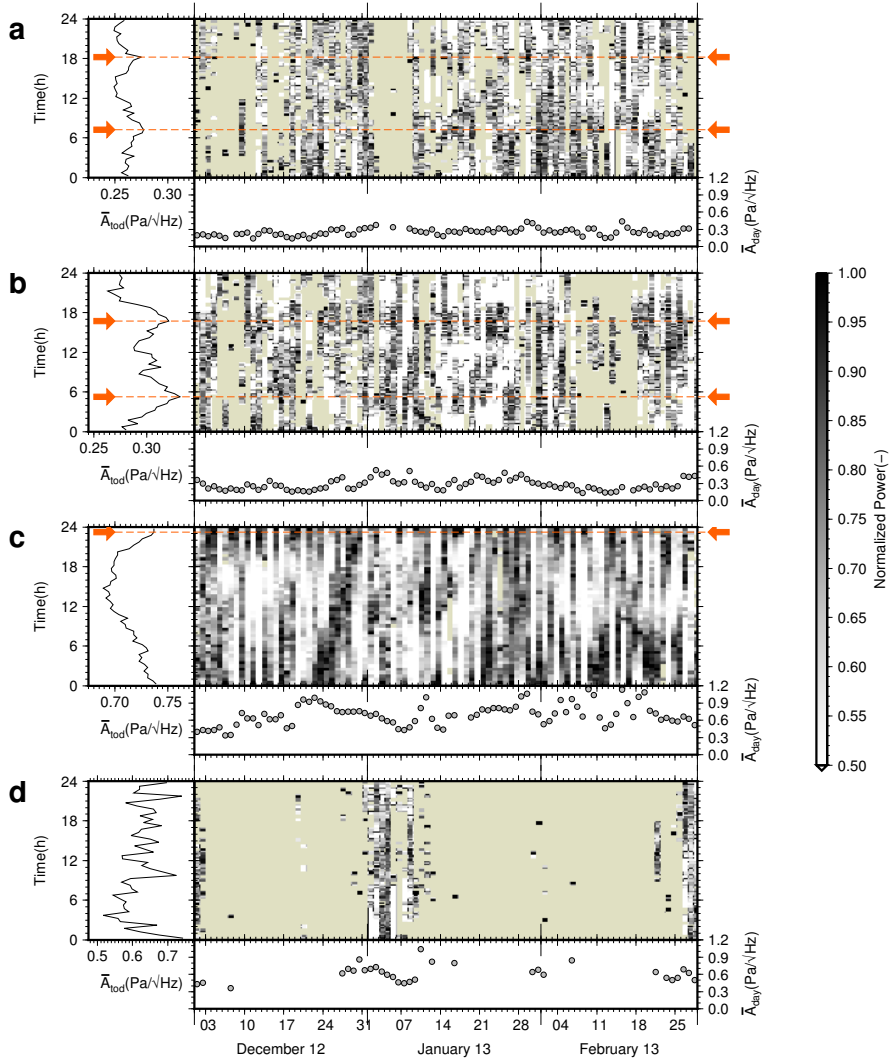


Figure B.5: Directional time averaged spectral amplitude variations for the 2013 winter. From top to bottom are shown, IS18 in (a) Atlantic Ocean and (b) Pacific Ocean direction and IS53 in (c) Pacific Ocean and (d) Atlantic Ocean direction. Each subfigure consists of (left) spectral amplitude averaged per time of day for each half hour, (right) half hour averaged spectral power, normalized per day, and (below) the daily mean spectral amplitude. Red arrows and dashed lines indicate the tidal peaks in the mean time of day amplitude, if present. Only detections are used with $\text{SNR} \geq 1.5$ for IS18 and $\text{SNR} \geq 1.3$ for IS53.

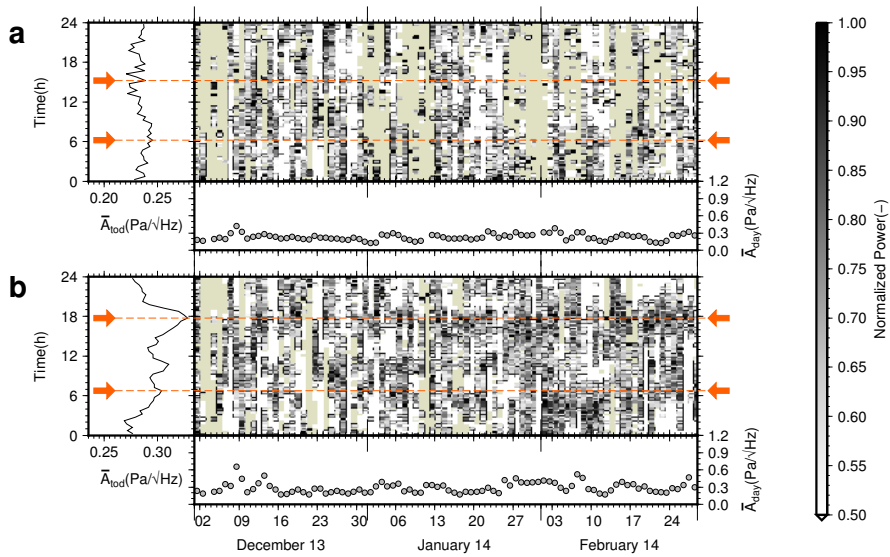


Figure B.6: Directional time averaged spectral amplitude variations for the 2014 winter. From top to bottom are shown, IS18 in (a) Atlantic Ocean and (b) Pacific Ocean direction. Each subfigure consists of (left) spectral amplitude averaged per time of day for each half hour, (right) half hour averaged spectral power, normalized per day, and (below) the daily mean spectral amplitude. Red arrows and dashed lines indicate the tidal peaks in the mean time of day amplitude, if present. Only detections are used with $\text{SNR} \geq 1.5$.

C

Preliminary analysis of the relative source depth of DPRK's 2013 and 2016 underground nuclear tests

In here an expression for the relative depth of the 2016 underground test is derived, using the 2013 test as a reference. The expression is a function of the ratio of measured pressures in the far field and the relative propagation efficiency. The expression assumes a constant impedance contrast between ground and air as well as constant source amplitude. The expression is evaluated for two cases of stratospheric propagation in 2013 and 2016.

C.1 Propagation efficiency and pressure ratios

Recall that transmission loss (TL) due to propagation in a medium [Jensen *et al.*, 2011] is defined as

$$\text{TL} = -20 \log_{10} \left(\frac{p_r}{p_s} \right). \quad (2.2.69)$$

Here, p_r and p_s correspond to the signal root mean square pressure at receiver and source positions. Consider the two following equations relating source and receiver power levels,

$$\text{TL}_{2013} = -20 \log_{10} \left(\frac{p_{r,2013}}{p_{s,2013}} \right), \quad (C.1.1)$$

and,

$$\text{TL}_{2016} = -20 \log_{10} \left(\frac{p_{r,2016}}{p_{s,2016}} \right). \quad (C.1.2)$$

Combining equations (C.1.1) and (C.1.2) yields

$$\Delta\text{TL} = -20 \log_{10} \left[\left(\frac{p_{r,2016}}{p_{s,2016}} \right) / \left(\frac{p_{r,2013}}{p_{s,2013}} \right) \right] \quad (\text{C.1.3})$$

Here, $\Delta\text{TL} = \text{TL}_{2016} - \text{TL}_{2013}$. This leads, after some straightforward algebra, to

$$\mathcal{P} \equiv \frac{p_{s,2013}}{p_{s,2016}} = 10^{\frac{\Delta\text{TL}}{-20}} \times \frac{p_{r,2013}}{p_{r,2016}} = Q \times \frac{p_{r,2013}}{p_{r,2016}}. \quad (\text{C.1.4})$$

This relation expresses the ratio of amplitudes in the near field (s) as a function of ratio of amplitudes in the far field (r). In general, propagation factor Q scales the two ratios. It follows immediately that if $\Delta\text{TL} = 0 \rightarrow Q = 1$. In this case, there is no difference in propagation efficiency, and thus the ratio of far field pressures equals the ratio of near field pressures. In other cases, propagation efficiency factor Q must be taken into account.

C.2 Stratospheric propagation

Consider the stratospheric propagation losses for propagation towards I45RU, as listed in Table 5.3. We find that $\text{TL}_{2016} = 53.0$ dB, $\text{TL}_{2013} = 47.9$ dB and hence $\Delta\text{TL} = 5.1$ dB ($Q \approx 0.6$).

From Figure 5.9, it follows that $p_{r,2013} \approx 0.02$ Pa. As no stratospheric arrival is clearly detected in 2016, this means that the stratospheric pressure has not exceeded the noise level. This implies an upper limit $p_{r,2016} \leq 0.005$ Pa. Substituting these numbers in equation (C.1.4) yields $\mathcal{P} \geq 2.2$.

C.3 Estimating relative depth from the pressure ratio

Also recall the impedance condition [*Jensen et al.*, 2011] for a plane wave with pressure p and vertical particle velocity ν , in a medium with density ρ_0 and sound speed c ,

$$p = \rho_0 c \nu. \quad (\text{C.3.1})$$

Now, the ratio of source pressures \mathcal{P} can be expressed as a ratio of particle velocities in the air,

$$\mathcal{P} = \frac{p_{s,2013}}{p_{s,2016}} = \frac{\rho_{0,2013} c_{2013} \nu_{2013}}{\rho_{0,2016} c_{2016} \nu_{2016}}. \quad (\text{C.3.2})$$

Because of the continuity of vertical particle velocity, the particle velocity in the air can be related to the particle velocity in the ground, through transmission coefficient \mathcal{T} . We also consider that the particle velocity ν in the ground is in the near-field [*Lay and Wallace*, 1995], and is due to a source with amplitude p at distance d ,

$$\mathcal{P} = \frac{\rho_{0,2013} c_{2013} \mathcal{T}_{2013} p_{2013} d_{2013}^{-2}}{\rho_{0,2016} c_{2016} \mathcal{T}_{2016} p_{2016} d_{2016}^{-2}}. \quad (\text{C.3.3})$$

Next, it is assumed **assume** that the characteristic impedances $\rho_0 c$ are invariant over 2013 and 2016 (so $\mathcal{T}_{2013} = \mathcal{T}_{2016}$). This is justified as the source is in the same region in 2013 and 2016. Moreover, it is **assumed** that the amplitude factor $p_{2013} = p_{2016}$. We justify this, based on the moment tensor solution; comparable seismic moment magnitudes have been estimated for the 2013 ($M_w = 4.7$) and 2016 ($M_w = 4.71$) test explosions. A more complete analysis of the source parameters can be found on the IRIS event summary pages [IRIS, 2013, 2016]. Now, equation (C.3.3) reduces to

$$\mathcal{P} = \frac{d_{2013}^{-2}}{d_{2016}^{-2}} = \frac{d_{2013}^{-2}}{(d_{2013} + \Delta d)^{-2}}. \quad (\text{C.3.4})$$

Solving for Δd ,

$$\Delta d = -d_{2013} \pm d_{2013} \sqrt{\mathcal{P}} \quad (\text{C.3.5})$$

which equals,

$$\frac{d_{2016}}{d_{2013}} = \pm \sqrt{\mathcal{P}} = \sqrt{10^{\frac{\Delta TL}{-20}} \times \frac{p_{r,2013}}{p_{r,2016}}}. \quad (\text{C.3.6})$$

Recalling that $\mathcal{P} \geq 2.2$, we find,

$$\frac{d_{2016}}{d_{2013}} \geq 1.5. \quad (\text{C.3.7})$$

Following this analysis, it is estimated that the 2016 test took place at least 1.5 times deeper than the 2013 test. Assuming a minimum source depth of 450 m for the 2013 test, based on hydrodynamic simulation results [Rougier *et al.*, 2011] and the 2013 yield estimate of 10 kT TNT (Table 5.3), this would imply that the 2016 explosion would have occurred at least 225 m deeper.

Bibliography

- Agarwal, K., and R. Macháň (2016), Multiple signal classification algorithm for super-resolution fluorescence microscopy, *Nature Communications*, *7*, 13,752+, doi:10.1038/ncomms13752.
- Albert, S., D. Fee, P. Firstov, E. Makhmudov, and P. Izbekov (2015), Infrasound from the 2012–2013 Plosky Tolbachik, Kamchatka fissure eruption, *J. Volcanol. Geotherm. Res.*, *307*, 68–78, doi:10.1016/j.jvolgeores.2015.08.019.
- Amante, C., and B. W. Eakins (2009), ETOPO1 1 Arc-Minute Global Relief Model: Procedures, Data Sources and Analysis., *Tech. rep.*, National Geophysical Data Center, Boulder, Colorado, doi:10.7289/V5C8276M.
- Andrews, D. G., C. B. Leovy, and J. R. Holton (1987), *Middle Atmosphere Dynamics, International Geophysics Series*, vol. 40, Academic Press, San Diego, California.
- Arnold, V. I. (1989), *Mathematical Methods of Classical Mechanics, Graduate Texts in Mathematics*, vol. 60, second ed., Springer-Verlag, New York, NY, USA.
- Assink, J., R. Waxler, and D. Velea (2017), A wide-angle high Mach number modal expansion for infrasound propagation, *J. Acoust. Soc. Am.*, *141*(3), 1781–1792, doi:10.1121/1.4977578.
- Assink, J. D., R. Waxler, and D. Drob (2012), On the sensitivity of infrasonic traveltimes in the equatorial region to the atmospheric tides, *J. Geophys. Res.*, *117*, D01,110+, doi:10.1029/2011JD016107.
- Assink, J. D., R. Waxler, W. G. Frazier, and J. Lonzaga (2013), The estimation of upper atmospheric wind model updates from infrasound data, *J. Geophys. Res. Atmos.*, *118*, 10,707–10,724, doi:10.1002/jgrd.50833.
- Assink, J. D., R. Waxler, P. Smets, and L. G. Evers (2014a), Bidirectional infrasonic ducts associated with sudden stratospheric warming events, *J. Geophys. Res.*, *119*, 1140–1153, doi:10.1002/2013jd021062.
- Assink, J. D., A. L. Pichon, E. Blanc, M. Kallel, and L. Khemiri (2014b), Evaluation of wind and temperature profiles from ECMWF analysis on two hemispheres using volcanic infrasound, *J. Geophys. Res.*, *119*(14), 8659–8683, doi:10.1002/2014jd021632.
- Assink, J. D., G. Averbuch, P. S. M. Smets, and L. G. Evers (2016), On the infrasound detected from the 2013 and 2016 DPRK’s underground nuclear tests, *Geophys. Res. Lett.*, *43*, 3526–3533, doi:10.1002/2016gl068497.

- Baldwin, M. P., and T. J. Dunkerton (2001), Stratospheric Harbingers of Anomalous Weather Regimes, *Science*, *294*, 581–584, doi:10.1126/science.1063315.
- Becker, J. J., D. T. Sandwell, W. H. F. Smith, J. Braud, B. Binder, J. Depner, D. Fabre, J. Factor, S. Ingalls, S. H. Kim, R. Ladner, K. Marks, S. Nelson, A. Pharaoh, R. Trimmer, J. Von Rosenberg, G. Wallace, and P. Weatherall (2009), Global Bathymetry and Elevation Data at 30 Arc Seconds Resolution: SRTM30 PLUS, *Marine Geodesy*, *32*, 355–371, doi:10.1080/01490410903297766.
- Benamou, J.-D. (1995), Big Ray Tracing: Multivalued Travel Field Computation using Viscosity Solutions of the Eikonal Equation, *Tech. rep.*, Unité de recherche INRIA Rocquencourt, Le Chesnay Cedex (France).
- Berner, J., G. J. Shutts, M. Leutbecher, and T. N. Palmer (2009), A Spectral Stochastic Kinetic Energy Backscatter Scheme and Its Impact on Flow-Dependent Predictability in the ECMWF Ensemble Prediction System, *J. Atmos. Sci.*, *66*, 603–626, doi:10.1175/2008jas2677.1.
- Blom, P., and R. Waxler (2012), Impulse propagation in the nocturnal boundary layer: Analysis of the geometric component, *J. Acoust. Soc. Am.*, *131*, 3680–3690, doi:10.1121/1.3699174.
- Blom, P., and R. Waxler (2017), Modeling and observations of an elevated, moving infrasonic source: Eigenray methods, *J. Acoust. Soc. Am.*, *141*(4), 2681–2692, doi:10.1121/1.4980096.
- Blom, P., R. Waxler, W. Frazier, and C. Talmadge (2014), Observations of the Refraction of Microbaroms Generated by Large Maritime Storms by the Wind Field of the Generating Storm, *J. Geophys. Res. Atmos.*, doi:10.1002/2014jd021795.
- Bonavita, M., L. Isaksen, and E. Hólm (2012), On the use of EDA background error variances in the ECMWF 4D-Var, *Q.J.R. Meteorol. Soc.*, *138*, 1540–1559, doi:10.1002/qj.1899.
- Bouttier, F., and G. Kelly (2001), Observing-system experiments in the ECMWF 4D-Var data assimilation system, *Q.J.R. Meteorol. Soc.*, *127*, 1469–1488, doi:10.1002/qj.49712757419.
- Bowers, D., and N. D. Selby (2009), Forensic Seismology and the Comprehensive Nuclear-Test-Ban Treaty, *Annu. Rev. Earth Planet. Sci.*, *37*(1), 209–236, doi:10.1146/annurev.earth.36.031207.124143.
- Brachet, N., D. Brown, R. L. Bras, Y. Cansi, P. Mialle, and J. Coyne (2010), *Monitoring the Earth's atmosphere with the global IMS infrasound network*, chap. 3, pp. 77–118, Springer, New York.
- Brekhovskikh, I. M., V. V. Goncharov, V. M. Kurtepov, and K. A. Naugol'nykh (1973), The radiation of infrasound into the atmosphere by surface waves in the ocean, *Atmos. Oceanic Phys.*, *9*, 899–907.
- Brekhovskikh, L., and O. Godin (1990), Geometrical Acoustics. WKB Approximation, in *Acoustics of Layered Media I, Springer Series on Wave Phenomena*, vol. 5, pp. 165–178, Springer Berlin Heidelberg, doi:10.1007/978-3-642-52369-4_8.
- Brekhovskikh, L. M., and O. A. Godin (1999), *Acoustics of Layered Media II: Point Sources and Bounded Beams, Springer Series on Wave Phenomena*, vol. 10, 2 ed., 524+ pp., Springer, Berlin.
- Brown, D. J., C. N. Katz, R. Le Bras, M. P. Flanagan, J. Wang, and A. K. Gault (2002), Infrasonic Signal Detection and Source Location at the Prototype International Data Centre, *Pure Appl. Geophys.*, *159*(5), 1081–1125, doi:10.1007/s00024-002-8674-2.
- Buizza, R., M. Milleer, and T. N. Palmer (1999), Stochastic representation of model uncertainties in the ECMWF ensemble prediction system, *Q.J.R. Meteorol. Soc.*, *125*, 2887–2908, doi:10.1002/qj.49712556006.

- Buizza, R., M. Leutbecher, and L. Isaksen (2008), Potential use of an ensemble of analyses in the ECMWF Ensemble Prediction System, *Q.J.R. Meteorol. Soc.*, *134*, 2051–2066, doi:10.1002/qj.346.
- Chao, W. C. (1985), Sudden Stratospheric Warmings as Catastrophes, *J. Atmos. Sci.*, *42*, 1631–1646.
- Charlton, A. J., and L. M. Polvani (2007), A new look at stratospheric sudden warmings. Part I: Climatology and modeling benchmarks, *J. Climate*, *20*, 449–469, doi:10.1175/JCLI3996.1.
- Charlton, A. J., A. O’neill, W. A. Lahoz, and A. C. Massacand (2004), Sensitivity of tropospheric forecasts to stratospheric initial conditions, *Q.J.R. Meteorol. Soc.*, *130*(600), 1771–1792, doi:10.1256/qj.03.167.
- Charlton-Perez, A. J., M. P. Baldwin, T. Birner, R. X. Black, A. H. Butler, N. Calvo, N. A. Davis, E. P. Gerber, N. Gillett, S. Hardiman, J. Kim, K. Krüger, Y.-Y. Lee, E. Manzini, B. A. McDaniel, L. Polvani, T. Reichler, T. A. Shaw, M. Sigmond, S.-W. Son, M. Toohey, L. Wilcox, S. Yoden, B. Christiansen, F. Lott, D. Shindell, S. Yukimoto, and S. Watanabe (2013), On the lack of stratospheric dynamical variability in low-top versions of the CMIP5 models, *J. Geophys. Res. Atmos.*, *118*, 2494–2505, doi:10.1002/jgrd.50125.
- Charney, J. G., and P. G. Drazin (1961), Propagation of planetary-scale disturbances from the lower into the upper atmosphere, *J. Geophys. Res.*, *66*, 83–109, doi:10.1029/jz066i001p00083.
- Che, I. Y., J. Myung-Soon, and J. Jeong-Soo (2002), Analysis of local seismo-acoustic events in the Korean Peninsula, *Geophys. Res. Lett.*, *29*, 1589+, doi:10.1029/2001gl014060.
- Che, I.-Y., T. S. Kim, J.-S. Jeon, and H.-I. Lee (2009), Infrasound observation of the apparent North Korean nuclear test of 25 May 2009, *Geophys. Res. Lett.*, *36*(22), L22,802+, doi:10.1029/2009gl041017.
- Chen, X., and K. Agarwal (2008), MUSIC Algorithm for Two-Dimensional Inverse Problems With Special Characteristics of Cylinders, *IEEE Trans. Antennas Propag.*, *56*(6), 1808–1812, doi:10.1109/tap.2008.923333.
- Chunchuzov, I., S. Kulichkov, A. Otrezov, and V. Perepelkin (2005), Acoustic pulse propagation through a fluctuating stably stratified atmospheric boundary layer, *J. Acoust. Soc. Am.*, *117*, 1868–1879, doi:10.1121/1.1862573.
- Chunchuzov, I., S. Kulichkov, V. Perepelkin, O. Popov, P. Firstov, J. D. Assink, and E. Marchetti (2015), Study of the wind velocity-layered structure in the stratosphere, mesosphere, and lower thermosphere by using infrasound probing of the atmosphere, *J. Geophys. Res. Atmos.*, *120*(17), 2015JD023,276–8840, doi:10.1002/2015jd023276.
- Chunchuzov, I. P., S. N. Kulichkov, O. E. Popov, R. Waxler, and J. Assink (2011), Infrasound scattering from atmospheric anisotropic inhomogeneities, *Izv. Atmos. Ocean. Phys.*, *47*, 540–557, doi:10.1134/s0001433811050045.
- Collins, M. D. (1993), A split-step Padé solution for the parabolic equation method, *J. Acoust. Soc. Am.*, *93*(4), 1736–1742, doi:10.1121/1.406739.
- Coy, L., S. D. Eckermann, K. W. Hoppel, and F. Sassi (2011), Mesospheric Precursors to the Major Stratospheric Sudden Warming of 2009: Validation and Dynamical Attribution Using a Ground-to-Edge-of-Space Data Assimilation System, *J. Adv. Model. Earth Syst.*, *3*(4), M10,002+, doi:10.1029/2011ms000067.
- Dahlman, O., S. Mykkeltveit, and H. Haak (2009), *The Treaty*, chap. 4, pp. 83–98, Springer Netherlands, Dordrecht, doi:10.1007/978-1-4020-6885-0_4.

- De Angelis, S., D. Fee, M. Haney, and D. Schneider (2012), Detecting hidden volcanic explosions from Mt. Cleveland Volcano, Alaska with infrasound and ground-coupled airwaves, *Geophys. Res. Lett.*, *39*, L21,312+, doi:10.1029/2012gl053635.
- de Groot-Hedlin, C., M. A. H. Hedlin, and K. Walker (2011), Finite difference synthesis of infrasound propagation through a windy, viscous atmosphere: application to a bolide explosion detected by seismic networks, *Geophys. J. Int.*, *185*(1), 305–320, doi:10.1111/j.1365-246x.2010.04925.x.
- de Groot-Hedlin, C. D. (2016), Long-range propagation of nonlinear infrasound waves through an absorbing atmosphere, *J. Acoust. Soc. Am.*, *139*(4), 1565–1577, doi:10.1121/1.4944759.
- de Groot-Hedlin, C. D., and M. A. H. Hedlin (2014), Infrasound detection of the Chelyabinsk meteor at the USArray, *Earth Planet. Sci. Lett.*, *402*, 337–345, doi:10.1016/j.epsl.2014.01.031.
- Denholm-Price, J. C. W., and J. M. Rees (1999), Detecting Waves Using an Array of Sensors, *Mon. Wea. Rev.*, *127*(1), 57–69, doi:10.1175/1520-0493(1999)127<%3C0057:dwuaao>%3E2.0.co;2.
- Diamantakis, M. (2014), Improving ECMWF forecasts of sudden stratospheric warmings, *ECMWF Newsletter*, *141*, 30–36.
- Donn, W. L., and E. S. Posmentier (1964), Ground-coupled air waves from the Great Alaskan Earthquake, *J. Geophys. Res.*, *69*(24), 5357–5361, doi:10.1029/jz069i024p05357.
- Donn, W. L., and D. Rind (1971), Natural Infrasound as an Atmospheric Probe, *Geophys. J. R. Astron. Soc.*, *26*, 111–133, doi:10.1111/j.1365-246x.1971.tb03386.x.
- Donn, W. L., and D. Rind (1972), Microbaroms and the Temperature and Wind of the Upper Atmosphere, *J. Atmos. Sci.*, *29*, 156–172, doi:10.1175/1520-0469(1972)029<%3C0156:mattaw>%3E2.0.co;2.
- Drob, D. P., J. M. Picone, and M. Garcés (2003), Global morphology of infrasound propagation, *J. Geophys. Res.*, *108*, 4680+, doi:10.1029/2002jd003307.
- Drob, D. P., J. T. Emmert, G. Crowley, J. M. Picone, G. G. Shepherd, W. Skinner, P. Hays, R. J. Niciejewski, M. Larsen, C. Y. She, J. W. Meriwether, G. Hernandez, M. J. Jarvis, D. P. Sipler, C. A. Tepley, M. S. O'Brien, J. R. Bowman, Q. Wu, Y. Murayama, S. Kawamura, I. M. Reid, and R. A. Vincent (2008), An empirical model of the Earth's horizontal wind fields: HWM07, *J. Geophys. Res.*, *113*(A12), A12,304+, doi:10.1029/2008ja013668.
- Drob, D. P., D. Broutman, M. A. Hedlin, N. W. Winslow, and R. G. Gibson (2013), A method for specifying atmospheric gravity wavefields for long-range infrasound propagation calculations, *J. Geophys. Res. Atmos.*, *118*, 3933–3943, doi:10.1029/2012jd018077.
- Drob, D. P., J. T. Emmert, J. W. Meriwether, J. J. Makela, E. Doornbos, M. Conde, G. Hernandez, J. Noto, K. A. Zawdie, S. E. McDonald, J. D. Huba, and J. H. Klenzing (2015), An update to the Horizontal Wind Model (HWM): The quiet time thermosphere, *Earth and Space Science*, *2*(7), 2014EA000,089+, doi:10.1002/2014ea000089.
- ECMWF (2009), IFS documentation - Cy33r1 Operational implementation 3 June 2008. PART VII: ECMWF WAVE MODEL, *Tech. rep.*, European Centre for Medium-Range Weather Forecasts, Reading, United Kingdom.
- ECMWF (2016), *Changes in ECMWF model*, European Centre for Medium-Range Weather Forecasts, <http://www.ecmwf.int/en/forecasts/documentation-and-support/changes-ecmwf-model>.
- Edwards, W. N., and D. N. Green (2012), Effect of interarray elevation differences on infrasound beamforming, *Geophys. J. Int.*, *190*, 335–346, doi:10.1111/j.1365-246x.2012.05465.x.

- Evers, L. G. (2008), The inaudible symphony: on the detection and source identification of atmospheric infrasound, Ph.D. thesis, Delft University of Technology.
- Evers, L. G., and P. Siegmund (2009), Infrasonic signature of the 2009 major sudden stratospheric warming, *Geophys. Res. Lett.*, *36*, L23,808+, doi:10.1029/2009gl041323.
- Evers, L. G., A. R. J. van Geyt, P. Smets, and J. T. Fricke (2012), Anomalous infrasound propagation in a hot stratosphere and the existence of extremely small shadow zones, *J. Geophys. Res.*, *117*, D06,120+, doi:10.1029/2011jd017014.
- Evers, L. G., D. Brown, K. D. Heaney, J. D. Assink, P. S. M. Smets, and M. Snellen (2014), Evanescent wave coupling in a geophysical system: Airborne acoustic signals from the Mw 8.1 Macquarie Ridge earthquake, *Geophys. Res. Lett.*, *41*, 1644–1650, doi:10.1002/2013gl058801.
- Fee, D., A. Steffke, and M. Garces (2010), Characterization of the 2008 Kasatochi and Okmok eruptions using remote infrasound arrays, *J. Geophys. Res.*, *115*(D2), D00L10+, doi:10.1029/2009jd013621.
- Fee, D., R. Waxler, J. Assink, Y. Gitterman, J. Given, J. Coyne, P. Mialle, M. Garces, D. Drob, D. Kleinert, R. Hofstetter, and P. Grenard (2013), Overview of the 2009 and 2011 Sayarim Infrasound Calibration Experiments, *J. Geophys. Res. Atmos.*, *118*, 6122–6143, doi:10.1002/jgrd.50398.
- Fleming, E. L., S. Chandra, J. J. Barnett, and M. Corney (1990), Zonal mean temperature, pressure, zonal wind and geopotential height as functions of latitude, *Adv. Space Res.*, *10*(12), 11–59, doi:10.1016/0273-1177(90)90386-e.
- Fricke, J. T., N. E. Allouche, D. G. Simons, E. N. Ruigrok, K. Wapenaar, and L. G. Evers (2013), Infrasonic interferometry of stratospherically refracted microbaroms – A numerical study, *J. Acoust. Soc. Am.*, *134*, 2660–2668, doi:10.1121/1.4819117.
- Fricke, J. T., L. G. Evers, P. S. M. Smets, K. Wapenaar, and D. G. Simons (2014), Infrasonic interferometry applied to microbaroms observed at the Large Aperture Infrasound Array in the Netherlands, *J. Geophys. Res.*, *119*, 9654–9665, doi:10.1002/2014jd021663.
- Fritsch, F. N., and R. E. Carlson (1980), Monotone Piecewise Cubic Interpolation, *SIAM J. Numer. Anal.*, *17*(2), 238–246.
- Gal, M., A. M. Reading, S. P. Ellingsen, K. D. Koper, R. Burlacu, and S. J. Gibbons (2016), Deconvolution enhanced direction of arrival estimation using one- and three-component seismic arrays applied to ocean induced microseisms, *Geophys. J. Int.*, *206*(1), 345–359, doi:10.1093/gji/ggw150.
- Garcés, M., M. Willis, C. Hetzer, A. Le Pichon, and D. Drob (2004), On using ocean swells for continuous infrasonic measurements of winds and temperature in the lower, middle, and upper atmosphere, *Geophys. Res. Lett.*, *31*, L19,304+, doi:10.1029/2004gl020696.
- Gerber, E. P., C. Orbe, and L. M. Polvani (2009), Stratospheric influence on the tropospheric circulation revealed by idealized ensemble forecasts, *Geophys. Res. Lett.*, *36*, L24,801+, doi:10.1029/2009gl040913.
- Gibbons, S. J., and F. Ringdal (2006), The detection of low magnitude seismic events using array-based waveform correlation, *Geophys. J. Int.*, *165*, 149–166, doi:10.1111/j.1365-246x.2006.02865.x.
- Godin, O. A. (2002), An effective quiescent medium for sound propagating through an inhomogeneous, moving fluid, *J. Acoust. Soc. Am.*, *112*(4), 1269–1275, doi:10.1121/1.1504853.
- Gossard, E. E., and W. H. Hooke (1975), *Waves in the atmosphere : atmospheric infrasound and gravity waves : their generation and propagation*, *Developments in Atmospheric Science*, vol. 2, 456 pp., Elsevier Scientific Pub. Co., Amsterdam, New York.

- Green, D. N., J. Guilbert, A. Le Pichon, O. Sebe, and D. Bowers (2009), Modelling Ground-to-Air Coupling for the Shallow ML 4.3 Folkestone, United Kingdom, Earthquake of 28 April 2007, *Bull. Seismol. Soc. Am.*, *99*(4), 2541–2551, doi:10.1785/0120080236.
- Green, D. N., J. Vergoz, R. Gibson, A. Le Pichon, and L. Ceranna (2011), Infrasound radiated by the Gerdec and Chelophechene explosions: propagation along unexpected paths, *Geophys. J. Int.*, *185*, 890–910, doi:10.1111/j.1365-246x.2011.04975.x.
- Green, D. N., R. S. Matoza, J. Vergoz, and A. Le Pichon (2012), Infrasonic propagation from the 2010 Eyjafjallajökull eruption: Investigating the influence of stratospheric solar tides, *J. Geophys. Res.*, *117*, D21,202+, doi:10.1029/2012jd017988.
- Gruber, F. K., E. A. Marengo, and A. J. Devaney (2004), Time-reversal imaging with multiple signal classification considering multiple scattering between the targets, *J. Acoust. Soc. Am.*, *115*(6), 3042–3047, doi:10.1121/1.1738451.
- Gutenberg, B. (1939), The velocity of sound waves and the temperature in the stratosphere in southern California, *Bull. Am. Meteorol. Soc.*, *20*, 192–201.
- GVP (2013), *Global Volcanism Program*, Smithsonian Institution, <http://www.volcano.si.edu/world>.
- Harris, D. B., and T. Kvaerna (2010), Superresolution with seismic arrays using empirical matched field processing, *Geophys. J. Int.*, *182*, 1455–1477, doi:10.1111/j.1365-246x.2010.04684.x.
- Hasselmann, K. (1963), A statistical analysis of the generation of microseisms, *Rev. Geophys.*, *1*, 177–210, doi:10.1029/rg001i002p00177.
- Healy, S. B., and J. N. Thépaut (2006), Assimilation experiments with CHAMP GPS radio occultation measurements, *Q.J.R. Meteorol. Soc.*, *132*, 605–623, doi:10.1256/qj.04.182.
- Hedlin, M. A. H., B. Alcoverro, and G. D’Spain (2003), Evaluation of rosette infrasonic noise-reducing spatial filters, *J. Acoust. Soc. Am.*, *114*(4), 1807–1820.
- Hedlin, M. A. H., D. Drob, K. Walker, and C. de Groot-Hedlin (2010), A study of acoustic propagation from a large bolide in the atmosphere with a dense seismic network, *J. Geophys. Res.*, *115*, B11,312+, doi:10.1029/2010jb007669.
- Hedlin, M. A. H., C. de Groot-Hedlin, and D. Drob (2012), A Study of Infrasound Propagation Using Dense Seismic Network Recordings of Surface Explosions, *B. Seism. Soc. of Am.*, *102*, 1927–1937, doi:10.1785/0120110300.
- Högbom, J. A. (1974), Aperture Synthesis with a Non-Regular Distribution of Interferometer Baselines, *Astron. Astrophys. Suppl.*, *15*, 417–426.
- Holton, J. R. (2004), *An Introduction to Dynamic Meteorology*, fourth ed., Elsevier Academic Press, Oxford.
- Houghton, J. T., L. Gylvan Meira Filho, D. J. Griggs, and K. Maskell (1997), An Introduction to Simple Climate Models used in the IPCC Second Assessment Report, *Tech. rep.*, Intergovernmental Panel on Climate Change, Geneva, Switzerland.
- Houtekamer, P. L., and H. L. Mitchell (2005), Ensemble Kalman filtering, *Q.J.R. Meteorol. Soc.*, *131*, 3269–3289, doi:10.1256/qj.05.135.
- Houtekamer, P. L., L. Lefaivre, J. Derome, H. Ritchie, and H. L. Mitchell (1996), A System Simulation Approach to Ensemble Prediction, *Mon. Wea. Rev.*, *124*, 1255–1242, doi:10.1175/1520-0493(1996)124<3C1225:assate>%3E2.0.co;2.

- IRIS (2013), Special Event: North Korea nuclear explosion, Incorporated Research Institutions for Seismology, Washington, D. C. [Available at <http://ds.iris.edu/ds/nodes/dmc/specialevents/2013/02/12/north-korea-nuclear-explosion/>, accessed 16 March 2016.].
- IRIS (2016), Special Event: 2016 North Korean nuclear test, Incorporated Research Institutions for Seismology, Washington, D. C. [Available at <https://ds.iris.edu/ds/nodes/dmc/specialevents/2016/01/05/2016-north-korean-nuclear-test/>, accessed 16 March 2016.].
- Jacobson, M. J. (1957), Analysis of a Multiple Receiver Correlation System, *J. Acoust. Soc. Am.*, *29*, 1342–1347, doi:10.1121/1.1908806.
- Janssen, P. (2009), *The Interaction of Ocean Waves and Wind*, 1 ed., Cambridge University Press.
- Jensen, F. B., W. A. Kuperman, M. B. Porter, and H. Schmidt (2011), *Computational Ocean Acoustics (Modern Acoustics and Signal Processing)*, second ed., Springer, New York.
- Jung, T., M. J. Miller, and T. N. Palmer (2010), Diagnosing the Origin of Extended-Range Forecast Errors, *Mon. Wea. Rev.*, *138*(6), 2434–2446, doi:10.1175/2010mwr3255.1.
- Källén, E. (2008), Special issue with manuscripts related to ESA's Atmospheric Dynamics Mission/Aeolus, *Tellus A: Dynamic Meteorology and Oceanography*, *60*(2), 189–190, doi:10.1111/j.1600-0870.2007.00296.x.
- Kedar, S., M. Longuet-Higgins, F. Webb, N. Graham, R. Clayton, and C. Jones (2008), The origin of deep ocean microseisms in the North Atlantic Ocean, *Proc. R. Soc. A*, *464*, 777–793, doi:10.1098/rspa.2007.0277.
- Keys, R. G. (1981), Cubic convolution interpolation for digital image processing, *IEEE Trans Acoust.*, *29*, 1153–1160.
- Kodera, K., H. Mukougawa, and A. Fujii (2013), Influence of the vertical and zonal propagation of stratospheric planetary waves on tropospheric blockings, *J. Geophys. Res.*, *118*, 8333–8345, doi:10.1002/jgrd.50650.
- Komen, G. J., L. Cavaleri, M. Donelan, K. Hasselmann, S. Hasselmann, and P. A. E. M. Janssen (1996), *Dynamics and Modelling of Ocean Waves*, reprint ed., Cambridge University Press.
- Krauss, W. (1973), *Dynamics of the Homogeneous and the Quasihomogeneous Ocean, Methods and Results of Theoretical Oceanography*, vol. 1, ed., 302 pp., Gebrüder Borntraeger, Berlin, Germany.
- Kriester, B. (1972), Large scale circulation patterns of the stratosphere, *Space Sci. Rev.*, *13*(2), 258–273, doi:10.1007/bf00175315.
- Kulichkov, S. (2009), On the prospects for acoustic sounding of the fine structure of the middle atmosphere, in *Infrasound Monitoring for Atmospheric Studies*, edited by A. Le Pichon, E. Blanc, and A. Hauchecorne, chap. 16, pp. 511–540, Springer, New York, NY, USA, doi:10.1007/978-1-4020-9508-5_16.
- Kulichkov, S. N., I. P. Chunchuzov, G. A. Bush, and V. G. Perepelkin (2008), Physical modeling of long-range infrasonic propagation in the atmosphere, *Izv. Atmos. Ocean. Phys.*, *44*, 175–186, doi:10.1134/s0001433808020059.
- Kulichkov, S. N., I. P. Chunchuzov, and O. I. Popov (2010), Simulating the influence of an atmospheric fine inhomogeneous structure on long-range propagation of pulsed acoustic signals, *Izv. Atmos. Ocean. Phys.*, *46*, 69–77, doi:10.1134/S0001433810010093.

- Labitzke, K. G., and H. van Loon (1999), *The Stratosphere*, 179 pp., Springer-Verlag, Berlin, Heidelberg, doi:10.1007/978-3-642-58541-8.
- Lalande, J. M., O. Sèbe, M. Landès, P. Blanc-Benon, R. S. Matoza, A. Le Pichon, and E. Blanc (2012), Infrasound data inversion for atmospheric sounding, *Geophys. J. Int.*, *190*, 687–701, doi:10.1111/j.1365-246x.2012.05518.x.
- Landès, M., L. Ceranna, A. Le Pichon, and R. S. Matoza (2012), Localization of microbarom sources using the IMS infrasound network, *J. Geophys. Res.*, *117*, D06,102+, doi:10.1029/2011jd016684.
- Lay, T., and T. C. Wallace (1995), *Modern Global Seismology*, vol. 58, 612 pp., Academic Press, San Diego, USA.
- Le Pichon, A., E. Blanc, D. Drob, S. Lambotte, J. X. Dessa, M. Lardy, P. Bani, and S. Vergnolle (2005), Infrasound monitoring of volcanoes to probe high-altitude winds, *J. Geophys. Res.*, *110*, D13,106+, doi:10.1029/2004jd005587.
- Le Pichon, A., L. Ceranna, M. Garcés, D. Drob, and C. Millet (2006), On using infrasound from interacting ocean swells for global continuous measurements of winds and temperature in the stratosphere, *J. Geophys. Res.*, *111*, doi:10.1029/2005jd006690.
- Le Pichon, A., J. Vergoz, P. Herry, and L. Ceranna (2008), Analyzing the detection capability of infrasound arrays in Central Europe, *J. Geophys. Res.*, *113*(D12), D12,115+, doi:10.1029/2007jd009509.
- Le Pichon, A., J. Vergoz, E. Blanc, J. Guilbert, L. Ceranna, L. Evers, and N. Brachet (2009), Assessing the performance of the International Monitoring System's infrasound network: Geographical coverage and temporal variabilities, *J. Geophys. Res.*, *114*, D08,112+, doi:10.1029/2008jd010907.
- Le Pichon, A., E. Blanc, and A. Hauchecorne (Eds.) (2010), *Infrasound Monitoring for Atmospheric Studies*, first ed., 1–735 pp., Springer Netherlands, Dordrecht.
- Le Pichon, A., J. D. Assink, P. Heinrich, E. Blanc, A. Charlton-Perez, C. F. Lee, P. Keckhut, A. Hauchecorne, R. Rüfenacht, N. Kämpfer, D. P. Drob, P. S. M. Smets, L. G. Evers, L. Ceranna, C. Pilger, O. Ross, and C. Claud (2015), Comparison of co-located independent ground-based middle atmospheric wind and temperature measurements with numerical weather prediction models, *J. Geophys. Res. Atmos.*, *120*(16), 2015JD023,273–8331, doi:10.1002/2015jd023273.
- Lee, C. F., P. S. M. Smets, A. J. Charlton-Perez, L. G. Evers, R. G. Harrison, and G. Marlton (2018), *The potential impact of upper stratospheric measurements on sub-seasonal forecasts in the extra-tropics*, Springer, Dordrecht, submitted book chapter.
- Limpasuvan, V., D. W. J. Thompson, and D. L. Hartmann (2004), The Life Cycle of the Northern Hemisphere Sudden Stratospheric Warmings, *J. Clim.*, *17*, 2584–2596, doi:10.1175/1520-0442(2004)017\%3C2584:TLCOTN\%3E2.0.CO;2.
- Limpasuvan, V., D. L. Hartmann, D. W. J. Thompson, K. Jeev, and Y. L. Yung (2005), Stratosphere-troposphere evolution during polar vortex intensification, *J. Geophys. Res.*, *110*, doi:10.1029/2005jd006302.
- Lindzen, S. R., and S. Chapman (1969), Atmospheric Tides, *Space Sci. Rev.*, *10*, 3–188, doi:10.1007/BF00171584.
- Lingevitch, J. F., M. D. Collins, D. K. Dacol, D. P. Drob, J. C. W. Rogers, and W. L. Siegmann (2002), A wide angle and high Mach number parabolic equation, *J. Acoust. Soc. Am.*, *111*, 729–734, doi:10.1121/1.1430683.

- Longuet-Higgins, M. S. (1950), A theory of the origin of microseisms, *Phil. Trans. R. Soc. A*, *243*, 1–35, doi:10.1098/rsta.1950.0012.
- Lonzaga, J. B., R. M. Waxler, J. D. Assink, and C. L. Talmadge (2015), Modelling waveforms of infrasound arrivals from impulsive sources using weakly non-linear ray theory, *Geophys. J. Int.*, *200*(3), 1347–1361, doi:10.1093/gji/ggu479.
- Mack, H., and E. A. Flinn (1971), Analysis of the Spatial Coherence of Short-Period Acoustic-Gravity Waves in the Atmosphere, *Geophys. J. Roy. Astron. Soc.*, *26*, 255–269, doi:10.1111/j.1365-246x.1971.tb03399.x.
- Marchetti, E., M. Ripepe, D. Delle Donne, R. Genco, A. Finizola, and E. Garaebiti (2013), Blast waves from violent explosive activity at Yasur Volcano, Vanuatu, *Geophys. Res. Lett.*, *40*(22), 2013GL057,900+, doi:10.1002/2013gl057900.
- Matoza, R. S., J. Vergoz, A. Le Pichon, L. Ceranna, D. N. Green, L. G. Evers, M. Ripepe, P. Campus, L. Liszka, T. Kvaerna, E. Kjartansson, and A. Höskuldsson (2011), Long-range acoustic observations of the Eyjafjallajökull eruption, Iceland, April–May 2010, *Geophys. Res. Lett.*, *38*(6), L06,308+, doi:10.1029/2011gl047019.
- Matsuno, T. (1971), A Dynamical Model of the Stratospheric Sudden Warming, *J. Atmos. Sci.*, *28*, 1479–1494, doi:10.1175/1520-0469(1971)028<1479:admots>3E2.0.co;2.
- McInturf, R. M. (1978), *Stratospheric warmings: Synoptic, dynamic and general-circulation aspects*, NASA reference publication, vol. 1017, National Aeronautics and Space Administration, Scientific and Technical Information Office, Washington.
- McIntyre, M. E., and T. N. Palmer (1983), Breaking planetary waves in the stratosphere, *Nature*, *305*, 593–600.
- McIntyre, M. E., and T. N. Palmer (1984), The 'surf zone' in the stratosphere, *J. Atmos. Terr. Phys.*, *46*(9), 825–849, doi:10.1016/0021-9169(84)90063-1.
- McKisic, J. M. (1996), Infrasound and the Infrasonic Monitoring or Atmospheric Nuclear Explosions: An Annotated Bibliography, *Tech. rep.*, DOE/Phillips Laboratory.
- Melton, B. S., and L. F. Bailey (1957), Multiple signal correlators, *Geophysics*, *22*, 565–588, doi:10.1190/1.1438390.
- Muench, H. S. (1965), On the Dynamics of the Wintertime Stratosphere Circulation, *J. Atmos. Sci.*, *22*, 349–360, doi:10.1175/1520-0469(1965)022<349:otdotw>3E2.0.co;2.
- Mutschlecner, J. P., and R. W. Whitaker (2005), Infrasound from earthquakes, *J. Geophys. Res.*, *110*(D1), D01,108+, doi:10.1029/2004jd005067.
- Olson, J. V. (2004), Infrasound signal detection using the Fisher F-statistic, *Inframatrics*, *6*.
- Picone, J. M., A. E. Hedin, D. P. Drob, and A. C. Aikin (2002), NRLMSISE-00 empirical model of the atmosphere: Statistical comparisons and scientific issues, *J. Geophys. Res.*, *107*(A12), 1468+, doi:10.1029/2002ja009430.
- Pierce, A. D. (1981), *Acoustics - An Introduction to Its Physical Principles and Applications*, McGraw-Hill Series in Mechanical Engineering, McGraw-Hill, New York.
- Ponceau, D., and L. Bosca (2010), *Low-noise broadband microbarometers*, chap. 4, pp. 119–140, Springer, New York.
- Posmentier, E. S. (1967), A Theory of Microbaroms, *Geophys. J. Roy. Astron. Soc.*, *13*, doi:10.1111/j.1365-246x.1967.tb02301.x.

- Ramaswamy, V., M. L. Chanin, J. Angell, J. Barnett, D. Gaffen, M. Gelman, P. Keckhut, Y. Koshelkov, K. Labitzke, J. J. R. Lin, A. O'Neill, J. Nash, W. Randel, R. Rood, K. Shine, M. Shiotani, and R. Swinbank (2001), Stratospheric temperature trends: Observations and model simulations, *Rev. Geophys.*, *39*, 71–122, doi:10.1029/1999rg000065.
- Randel, W., P. Udelhofen, E. Fleming, M. Geller, M. Gelman, K. Hamilton, D. Karoly, D. Ortland, S. Pawson, R. Swinbank, F. Wu, M. Baldwin, M.-L. Chanin, P. Keckhut, K. Labitzke, E. Remsberg, A. Simmons, and D. Wu (2004), The SPARC Intercomparison of Middle-Atmosphere Climatologies, *J. Climate*, *17*, 986–1003, doi:10.1175/1520-0442(2004)017\%3C0986:tsiomc\%3E2.0.co;2.
- Revelle, D. O. (2010), Modified ray-mode (phase) theory: Understanding counter-wind propagation effects from atmospheric explosions, *J. Atmos. Sol.-Terr. Phys.*, *72*, 241–261, doi:10.1016/j.jastp.2009.11.017.
- Rind, D., and W. L. Donn (1975), Further Use of Natural Infrasond as a Continuous Monitor of the Upper Atmosphere, *J. Atmos. Sci.*, *32*, 1694–1704, doi:10.1175/1520-0469(1975)032\%3C1694:fuonia\%3E2.0.co;2.
- Rind, D., W. L. Donn, and E. Dede (1973), Upper Air Wind Speeds Calculated from Observations of Natural Infrasond, *J. Atmos. Sci.*, *30*, 1726–1729, doi:10.1175/1520-0469(1973)030\%3C1726:uawscf\%3E2.0.co;2.
- Rind, D. H., and W. L. Donn (1978), Infrasond Observations of Variability During Stratospheric Warmings, *J. Atmos. Sci.*, *35*, 546–553, doi:10.1175/1520-0469(1978)035\%3C0546:ioovds\%3E2.0.co;2.
- Rodgers, C. D. (1976), Retrieval of atmospheric temperature and composition from remote measurements of thermal radiation, *Rev. Geophys.*, *14*, 609–624, doi:10.1029/rg014i004p00609.
- Roff, G., D. W. J. Thompson, and H. Hendon (2011), Does increasing model stratospheric resolution improve extended-range forecast skill?, *Geophys. Res. Lett.*, *38*(5), L05,809+, doi:10.1029/2010gl046515.
- Rougier, E., H. J. Patton, E. E. Knight, and C. R. Bradley (2011), Constraints on burial depth and yield of the 25 May 2009 North Korean test from hydrodynamic simulations in a granite medium, *Geophysical Research Letters*, *38*(16), n/a+, doi:10.1029/2011gl048269.
- Schmidt, R. (1986), Multiple emitter location and signal parameter estimation, *IEEE Trans. Antennas Propag.*, *34*(3), 276–280, doi:10.1109/tap.1986.1143830.
- Seibert, G. (2006), *The history of sounding rockets and their contribution to European Space Research*, ESA Publications.
- Selby, N. D. (2010), Relative Locations of the October 2006 and May 2009 DPRK Announced Nuclear Tests Using International Monitoring System Seismometer Arrays, *Bull. Seismol. Soc. Am.*, *100*(4), 1779–1784, doi:10.1785/0120100006.
- Shaw, T. A., and T. G. Shepherd (2008), Raising the roof, *Nature Geosci.*, *1*, 12–13, doi:10.1038/ngeo.2007.53.
- Shumway, R. H. (1971), On Detecting a Signal in N Stationarily Correlated Noise Series, *Technometrics*, *13*(3), 499–519.
- Shutts, G. (2005), A kinetic energy backscatter algorithm for use in ensemble prediction systems, *Q.J.R. Meteorol. Soc.*, *131*, 3079–3102, doi:10.1256/qj.04.106.
- Shutts, G., M. Leutbecher, A. Weisheimer, T. Stockdale, L. Isaksen, and M. Bonavita (2011), Representing model uncertainty: stochastic parametrizations at ECMWF, *ECMWF Newsletters*, *129*, 19–24.

- Sigmond, M., J. F. Scinocca, V. V. Kharin, and T. G. Shepherd (2013), Enhanced seasonal forecast skill following stratospheric sudden warmings, *Nature Geoscience*, *6*, 98–102, doi:10.1038/ngeo1698.
- Sijtsma, P. (2007), CLEAN Based on Spatial Source Coherence, *Int. J. Aeroacoust.*, *6*(4), 357–374, doi:10.1260/147547207783359459.
- Smart, E., and E. A. Flinn (1971), Fast Frequency-Wavenumber Analysis and Fisher Signal Detection in Real-Time Infrasonic Array Data Processing, *Geophys. J. Roy. Astron. Soc.*, *26*, 279–284, doi:10.1111/j.1365-246x.1971.tb03401.x.
- Smets, P. S. M., and L. G. Evers (2014), The life cycle of a sudden stratospheric warming from infrasonic ambient noise observations, *J. Geophys. Res.*, *119*, 12,084–12,099, doi:10.1002/2014jd021905.
- Smets, P. S. M., L. G. Evers, A. J. Charlton-Perez, C. F. Lee, and R. G. Harrison (2014), Roadmap on the use of ARISE data for weather and climate monitoring in Europe – D5.5, *Tech. rep.*, Atmospheric dynamics Research InfraStructure in Europe – ARISE – project, FP7 Grant Agreement nr 284387.
- Smets, P. S. M., L. G. Evers, S. P. Näsholm, and S. J. Gibbons (2015), Probabilistic infrasound propagation using realistic atmospheric perturbations, *Geophys. Res. Lett.*, *42*(15), 2015GL064,992–6517, doi:10.1002/2015gl064992.
- Smets, P. S. M., J. D. Assink, A. Le Pichon, and L. G. Evers (2016), ECMWF SSW forecast evaluation using infrasound, *J. Geophys. Res. Atmos.*, *121*(9), 2015JD024,251–4650, doi:10.1002/2015jd024251.
- Stone, M., and P. Goldbart (2009), *Mathematics for Physics: A Guided Tour for Graduate Students*, first ed., Cambridge University Press, Cambridge.
- Stopa, J. E., K. F. Cheung, M. A. Garcés, and D. Fee (2011), Source of microbaroms from tropical cyclone waves, *Geophys. Res. Lett.*, *38*, doi:10.1029/2010gl046390.
- Stopa, J. E., K. F. Cheung, M. A. Garcés, and N. Badger (2012), Atmospheric infrasound from nonlinear wave interactions during Hurricanes Felicia and Neki of 2009, *J. Geophys. Res.*, *117*, doi:10.1029/2012jc008257.
- Straume, A. G., A. Elfving, D. Wernham, A. Culoma, L. Mondin, F. de Bruin, T. Kanitz, D. Schuettemeyer, F. Buscaglione, and A. Dehn (2016), ESA’s Spaceborne Lidar Mission ADM-Aeolus; Recent Achievements and Preparations for Launch, *EPJ Web of Conferences*, *119*, 01,001+, doi:10.1051/epjconf/201611901001.
- Sutherland, L. C., and H. E. Bass (2004), Atmospheric absorption in the atmosphere up to 160 km, *J. Acoust. Soc. Am.*, *115*, 1012–1032, doi:10.1121/1.1631937.
- Szuberla, C. A. L., and J. V. Olson (2004), Uncertainties associated with parameter estimation in atmospheric infrasound arrays, *J. Acoust. Soc. Am.*, *115*, 253–258, doi:10.1121/1.1635407.
- Tailpied, D., A. Le Pichon, E. Marchetti, J. Assink, and S. Vergnolle (2017), Assessing and optimizing the performance of infrasound networks to monitor volcanic eruptions, *Geophys. J. Int.*, *208*(1), 437–448, doi:10.1093/gji/ggw400.
- Tripathi, O. P., M. Baldwin, A. Charlton-Perez, M. Charron, S. D. Eckermann, E. Gerber, R. G. Harrison, D. R. Jackson, B.-M. Kim, Y. Kuroda, A. Lang, S. Mahmood, R. Mizuta, G. Roff, M. Sigmond, and S.-W. Son (2014), The predictability of the extratropical stratosphere on monthly time-scales and its impact on the skill of tropospheric forecasts, *Q.J.R. Meteorol. Soc.*, *141*(689), doi:10.1002/qj.2432.

- Tripathi, O. P., A. Charlton-Perez, M. Sigmond, and F. Vitart (2015), Enhanced long-range forecast skill in boreal winter following stratospheric strong vortex conditions, *Environ. Res. Lett.*, *10*(10), 104,007+, doi:10.1088/1748-9326/10/10/104007.
- Walker, K. T. (2012), Evaluating the opposing wave interaction hypothesis for the generation of microbaroms in the eastern North Pacific, *J. Geophys. Res.*, *117*, C12,016+, doi:10.1029/2012jc008409.
- Walker, K. T., and M. A. H. Hedlin (2009), A Review of Wind-Noise Reduction Methodologies, in *Infrasound Monitoring for Atmospheric Studies*, chap. 5, pp. 141–182, Springer Netherlands, Dordrecht, doi:10.1007/978-1-4020-9508-5_5.
- Walker, K. T., A. L. Pichon, T. S. Kim, C. de Groot-Hedlin, I.-Y. Che, and M. Garcés (2013), An analysis of ground shaking and transmission loss from infrasound generated by the 2011 Tohoku earthquake, *J. Geophys. Res. Atmos.*, *118*(23), 12,831–12,851, doi:10.1002/2013jd020187.
- Waxler, R., and K. E. Gilbert (2006), The radiation of atmospheric microbaroms by ocean waves, *J. Acoust. Soc. Am.*, *119*, 2651–2664, doi:10.1121/1.2191607.
- Waxler, R., K. Gilbert, C. Talmadge, and C. Hetzer (2007), The effects of the finite depth of the ocean on microbarom signals, in *8th International Conference on Theoretical and Computational Acoustics (ICTCA)*, European Acoustics Association (EAA), Crete, Greece.
- Waxler, R., L. G. Evers, J. Assink, and P. Blom (2015), The stratospheric arrival pair in infrasound propagation, *J. Acoust. Soc. Am.*, *137*(4), 1846–1856, doi:10.1121/1.4916718.
- Weatherall, P., K. M. Marks, M. Jakobsson, T. Schmitt, S. Tani, J. E. Arndt, M. Rovere, D. Chayes, V. Ferrini, and R. Wigley (2015), A new digital bathymetric model of the world's oceans, *Earth and Space Science*, *2*(8), 331–345, doi:10.1002/2015ea000107.
- Wen, L., and H. Long (2010), High-precision Location of North Korea's 2009 Nuclear Test, *Seismol. Res. Lett.*, *81*(1), 26–29, doi:10.1785/gssrl.81.1.26.
- Wessel, P., and W. H. F. Smith (1991), Free software helps map and display data, *Eos. Trans. AGU*, *72*, 441–446, doi:10.1029/90eo00319.
- Whitaker, R. W., and J. P. Mutschlecner (2008), A comparison of infrasound signals refracted from stratospheric and thermospheric altitudes, *J. Geophys. Res.*, *113*, D08,117+, doi:10.1029/2007jd008852.
- WMO (2013), *Guide to the global observing system*, WMO-No. 488, World Meteorological Organization, Geneva, Switzerland.
- Zhang, M., and L. Wen (2015), Seismological Evidence for a Low-Yield Nuclear Test on 12 May 2010 in North Korea, *Seismol. Res. Lett.*, *86*(1), 138–145, doi:10.1785/02201401170.

List of symbols and abbreviations

Symbols

The principal symbols used are alphabetically listed. Symbols formed by adding overbars, primes or indices are not listed separately. Boldface type indicates vector quantities.

Symbol	Description	Units
α	Atmospheric attenuation	m^{-2}
Γ	Horizontal xy -receiver plane	
γ	Ratio of specific heats	-
Δ	Sample rate	Hz
ϵ	Background noise	Pa
θ	Grazing or elevation angle	$^{\circ}$
κ	Isentropic bulk modulus	-
λ	Wavelength	m
	Polar angle of a spherical system	rad
μ	Array signal average	Pa
ν	Vertical particle velocity	m s^{-1}
ζ	Sea state	-
ρ	Volumetric mass density	kg m^3
σ	Standard deviation	-
τ	Wave front	s
	Delay time	s
Φ	Phase functional	rad
	Geopotential	$\text{m}^2 \text{s}^{-2}$
ϕ	Azimuth, clockwise relative to the north	$^{\circ}$

Symbol	Description	Units
ϕ_b	Back azimuth, clockwise relative to the north	$^\circ$
Ω	Ray tube surface	
ω	Angular frequency	rad
φ	Phase	rad
	Azimuthal angle of a spherical system	rad
A	Amplitude	Pa
	Microbarom radiation resonance term	-
\mathbf{a}	Acceleration vector	m s^{-2}
a	Acoustic pressure	Pa
B	Microbarom radiation resonance term	-
C	Spherical coordinates coefficient matrix	
C	Microbarom radiation resonance term	-
c	Phase velocity or absolute speed of sound	m s^{-1}
c_{app}	Apparent velocity	m s^{-1}
c_{eff}	Effective speed of sound	m s^{-1}
c_P	Specific heat capacity at constant pressure	J K^{-1}
c_T	Adiabatic speed of sound	m s^{-1}
c_V	Specific heat capacity at constant volume	J K^{-1}
\mathcal{D}	Microbarom source strength spectrum	$\text{Pa}^2 \text{ Hz}^{-1}$
D	Water column depth	m
d	Distance	m
E	Spectral power	Pa^2
	Energy	J
E_{kin}	Kinetic energy	J
E_{pot}	Potential energy	J
\mathcal{F}	Two-dimensional wavenumber spectral density function	$\text{m}^2 \text{ s rad}^{-1}$
\mathbf{F}	Force vector	N
F	Fisher ratio	-
	Two-dimensional variance density spectrum	$\text{m}^2 \text{ s rad}^{-1}$
f	Frequency	Hz
f_ζ	Ocean surface wave frequency	Hz
f_N	Nyquist frequency	Hz
g	Gravitational acceleration constant	m s^{-2}
\mathcal{H}	Hasselmann integral	$\text{m}^4 \text{ s}^2$
	Hamiltonian function	J
H_S	Significant wave height	m
h	Geometric height	m

Symbol	Description	Units
I	Sound intensity	W m^{-2}
\mathbf{k}	Wavenumber vector	-
k	Phase difference	-
\mathcal{L}	Lagrangian	J
L	Characteristic space scale of the atmospheric parameter variation	m
l	Euclidian distance between source and receiver	m
M_b	Seismic moment	J
M_w	Seismic moment magnitude scale	-
m	Mass	kg
N	Amount of moles	-
	Total number of array elements	-
$\hat{\mathbf{n}}$	Three-dimensional unit normal vector	-
n	Array element	-
\mathcal{P}	Root mean square pressure ratio	-
P	Absolute pressure	Pa
P_0	Ambient pressure	Pa
\mathbf{p}	Three-dimensional slowness vector	s m^{-1}
p	Root mean square amplitude	Pa
Q	Propagation factor	-
q	Specific humidity	-
\mathcal{R}	Reflection coefficient	-
R	Array response	-
	Specific gas constant	$\text{J kg}^{-1} \text{K}^{-1}$
R^*	Universal gas constant	$\text{J kg}^{-1} \text{mol}^{-1}$
\mathbf{r}	Two-dimensional position vector	m
	Spherical coordinate vector	
r	Radial component of a spherical system	m
\mathcal{S}	Hamilton's principle functional or action	
S	Entropy	J K^{-1}
	Microbarom source area	m
\mathbf{s}	Horizontal two-dimensional slowness vector	s m^{-1}
s	Signal	
\mathcal{T}	Transmission coefficient	-
T	Absolute temperature	K
	Period	s
T_v	Virtual temperature	K

Symbol	Description	Units
T_{ζ}	Ocean surface wave period	s
TL	Transmission loss	dB re 1m
t	Time	s
V	Volume	m^3
\mathbf{v}	Velocity vector	m s^{-2}
\mathbf{w}	Wind velocity vector	m s^{-1}
w	Array recording window	Pa
w_a	Horizontal along-track wind	m s^{-1}
w_c	Horizontal cross-wind	m s^{-1}
w_u	Zonal wind	m s^{-1}
w_v	Meridional wind	m s^{-1}
\mathbf{x}	Three-dimensional position vector	m
x	Eastward coordinate of a Cartesian system	m
Y	Fourier transform of the recording y	Pa
y	Array element recording	Pa
	Northward coordinate of a Cartesian system	m
Z	Acoustic impedance ratio	-
Z	Acoustic impedance	$\text{kg m}^{-2} \text{s}^{-1}$
Z_g	Geopotential height	m
z	Vertical coordinate of a Cartesian system	m

Abbreviations

2DFD	Two-dimensional wave spectra
4D-Var	Four-dimensional variational data assimilation
ADM-Aeolus	Atmospheric Dynamics Mission Aeolus
AIRS	Atmospheric Infrared Sounder
AMSU-A	Advanced Microwave Sounding Unit type A
ARISE	Atmosphere Research dynamics Infrastructure in Europe
ASD	Amplitude spectral density
AO	Atlantic Ocean
ATMS	Advanced Technology Microwave Sounder
CET	Central European Time
CMA	China Meteorological Administration
CIRA-86	COSPAR International Reference Atmosphere 1986
COSPAR	Committee on Space Research
CTBT	Comprehensive Nuclear-Test-Ban Treaty
CTBTO	Comprehensive Nuclear-Test-Ban Treaty Organization
CrIS	Crosstrack Infrared Sounder
DALR	Dry adiabatic lapse rate
DBN	KNMI's infrasound array at De Bilt, The Netherlands
DEM	Digital Elevation Model
DPRK	Democratic People's Republic of Korea
ECMWF	European Centre for Medium-Range Weather Forecasts
EDA	Ensemble of Data Assimilations
ELR	Environmental Lapse Rate
EOM	Equations of motion
ESA	European Space Agency
F	Fisher (analysis)
FFT	Fast Fourier transform
FY-3	FengYun-3
G2S	Ground-to-space
GCM	General Circulation Model
GEBCO	General Bathymetric Chart of the Oceans
GMT	Generic Mapping Tools
GPS	Global Positioning System
GT	Ground truth
GW	Gravity waves
HRES	High-resolution atmospheric model
HWM	Horizontal Wind Model

IASI	Infrared Atmospheric Sounding Interferometer
IDC	International Data Centre
IFS	Integrated Forecast System
IMS	International Monitoring System
IRIS	Incorporated Research Institutions for Seismology
ISA	International Standard Atmosphere
KNMI	Royal Netherlands Meteorological Institute
LOFAR	Low-Frequency Array
MERRA	Modern Era Retrospective analysis for Research and Applications
MSIS	Mass Spectrometer and Incoherent Radar Model
Mt.	Mount
NASA	National Aeronautics and Space Administration
NH	Northern Hemisphere
NPP	National Polar-orbiting Partnership
NRL	Naval Research Laboratory
NSMC	National Satellite Meteorological Center
NWP	Numerical Weather Prediction
NOAA	National Oceanic and Atmospheric Administration
NORSAR	Norwegian Seismic Array
NPOESS	National Polar-orbiting Operational Environmental Satellite System
ODE	Ordinary differential equation
PDE	Partial differential equation
PDF	Probability density function
PO	Pacific Ocean
REB	Reviewed Event Bulletin
RK4	Classical Runge-Kutta integration
RMS	Root mean squared
SNR	Signal-to-noise ratio
SH	Southern Hemisphere
SSW	Sudden stratospheric warming
UTC	Universal Time Coordinated
TL	Transmission loss
TEX	KNMI's infrasound array at Texel, The Netherlands
TNT	Trinitrotoluene
WAM	Wave Model
WMO	World Meteorological Organisation

Curriculum Vitæ

Pieter Steven Maarten Smets

15-01-1988 Born in Wilrijk, Belgium.

Education

2000–2006 Grammar school
Sint-Michielscollege, Brasschaat.

2006–2010 B.Sc. Aerospace Engineering
Delft University of Technology, Delft.

2009–2011 M.Sc. Aerospace Engineering, Earth and Planetary Observation
Delft University of Technology, Delft.

Thesis: Observation of the sudden stratospheric warming in
the southern hemisphere of 2010 using infrasound

Promotor: Prof. dr. D. G. Simons

Professional Experience

2012–2014 Project researcher at the Royal Netherlands Meteorological
Institute (KNMI) on the Atmospheric dynamics Research
InfraStructure in Europe (ARISE) design study project,
Seventh Framework Programme (FP7, grant number 284387).

2015–2017 Project researcher at the Royal Netherlands Meteorological
Institute (KNMI) on the Atmospheric dynamics Research
InfraStructure in Europe (ARISE2) project, Horizon 2020
Programme (H2020, grant number 653980).

List of publications

■ Peer-reviewed articles of this thesis

- [5] **Smets, P. S. M.**, J. D. Assink, and L. G. Evers (2018), *The study of sudden stratospheric warmings using infrasound*, Chap. 23 in: Le Pichon A., Blanc E., Hauchecorne A. (eds) *Infrasound Monitoring for Atmospheric Studies: Challenges and New Perspectives*, Springer, Dordrecht. Chapter 1 of this thesis
- [4] **Smets, P. S. M.**, J. D. Assink, A. Le Pichon, and L. G. Evers (2016), *ECMWF SSW forecast evaluation using infrasound*, *J. Geophys. Res.*, 121, 4637–4650. Chapter 4 of this thesis
- [3] Assink¹, J. D. , G. Averbuch, **P. S. M. Smets**, and L. G. Evers (2016), *On the infrasound detected from the 2013 and 2016 DPRK's underground nuclear tests*, *Geophys. Res. Lett.*, 43, 3526–3533. Section 5.2 of this thesis
- [2] **Smets, P. S. M.**, L. G. Evers, S. P. Näsholm, and S. J. Gibbons (2015), *Probabilistic infrasound propagation using realistic atmospheric perturbations*, *Geophys. Res. Lett.*, 42, 6510–6517. Section 5.1 of this thesis
- [1] **Smets, P. S. M.** and L. G. Evers (2014), *The Life Cycle of a Sudden Stratospheric Warming from Infrasonic Ambient Noise Observations*, *J. Geophys. Res.*, 119, 12,084–12,099. Chapter 3 of this thesis

Note that minor changes have been introduced to make the text consistent with the other chapters.

■ Full publication record

An up-to-date record of peer-reviewed publications and selected conference presentations is available at <http://www.pietersmets.eu>.

¹All authors contributed equally

